The Interplay of Lattice, Spin, and Charge Degrees of Freedom in Layered Cobaltates

Matthias Cwik

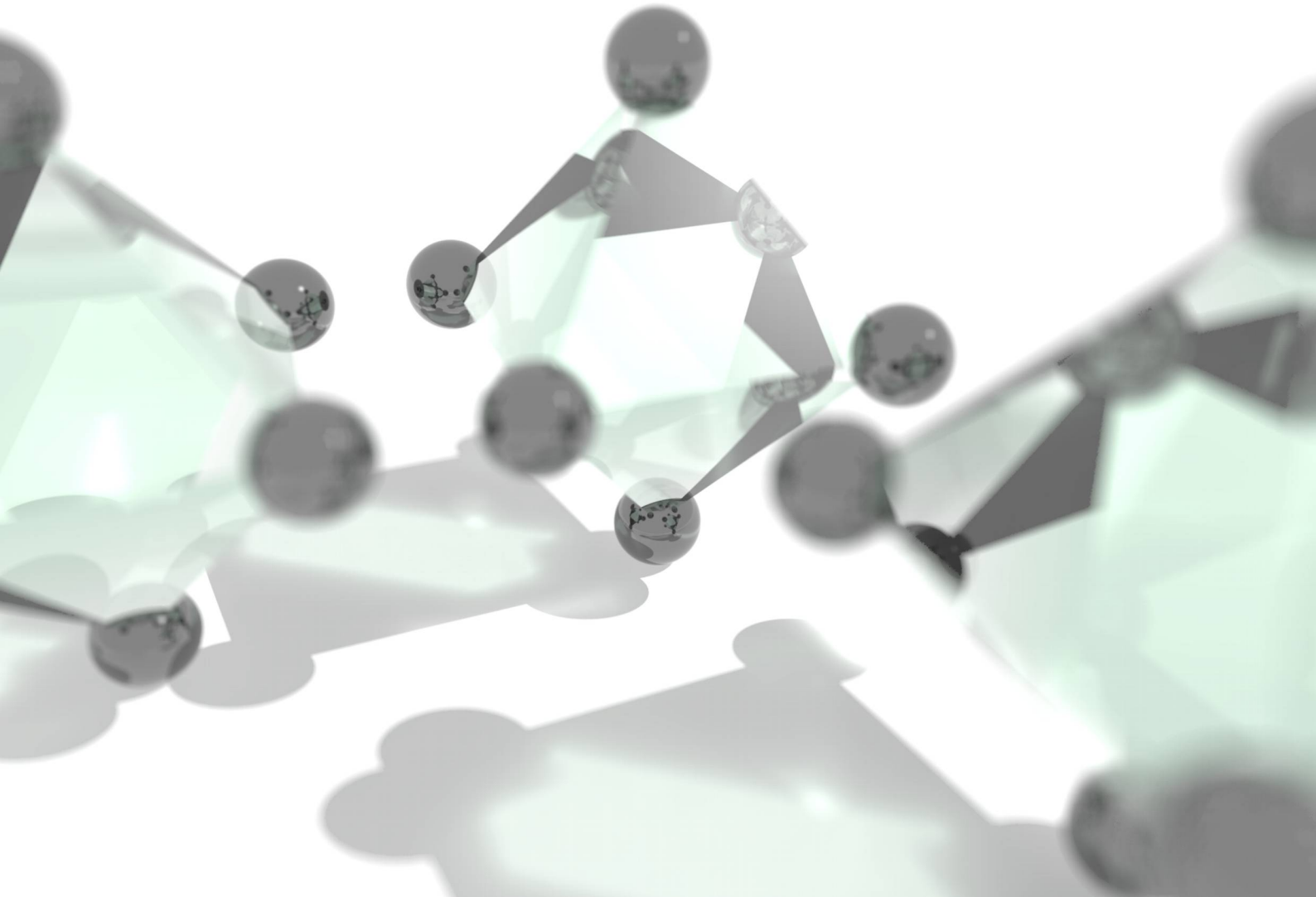

The Interplay of Lattice, Spin, and Charge Degrees of Freedom in Layered Cobaltates

I n a u g u r a l - D i s s e r t a t i o n
zur
Erlangung des Doktorgrades
der Mathematisch-Naturwissenschaftlichen Fakultät
der Universität zu Köln

vorgelegt von
Matthias Cwik
aus Osnabrück (Niedersachsen)

Köln, 3. Mai 2007

Berichterstatter:	Prof. Dr.	M. Braden
	Prof. Dr.	L. H. Tjeng
Vorsitzender der Prüfungskommision:	Prof. Dr.	L. Bohatý
Tag der mündlichen Prüfung	03.07.2007	

Geschrieben steht: Im Anfang war der Sinn. Bedenke wohl die erste Zeile, daß deine Feder sich nicht übereile! Ist es der Sinn, der alles wirkt und schafft? Es sollte stehn: Im Anfang war die Kraft!

(J. W. von Goethe, Faust - Der Tragödie erster Teil [1])

Contents

1. Introduction

Doped $3d$ transition metal oxides with a single-layered perovskite structure of the K_2NiF_4 type [2] have attracted much attention not only since the discovery of high-temperature superconductivity by Bednorz and Müller in 1986 [3] but also due to a variety of unusual ordering phenomena. Examples are the periodical modulation of antiferromagnetically coupled spins and charges, *e.g.* stripe-like order in cuprates [4] and nickelates [5], the CE-ordered phase in manganites [6], and the checkerboard-like charge order in the half-doped compounds [7–9]. In these systems with strongly-correlated electrons, the analysis of the interplay between lattice, spin, and charge degrees of freedom gives an insight to the outstanding physical phenomena of this material class. In general, the complexity of the phase diagram hinders this analysis. However, there are generic properties in the family of single-layered perovskites. In the layered transition metal oxides $La_2MO_{4+\delta}$ (M = Co, Ni, Cu), MO_6 octahedra-tilt distortions, charge-segregation instabilities, three-dimensional Néel states, spin-glass phases, and metal-insulator transitions appear depending on the chemical composition and can be modeled with a small set of microscopic parameters. The substitution of threevalent ions by divalent ions induces chemical pressure, alters the electronic bandwidth, and leads to a mixed-valence transition-metal system.

Starting from the high-temperature tetragonal (HTT) structure of the ideal single-layered perovskite with K_2NiF_4-type structure, the systems $La_2MO_{4+\delta}$ (M = Co, Ni, Cu) exhibit MO_6 octahedra tilt instabilities resulting in low-temperature orthorhombic (LTO) and low-temperature tetragonal (LTT) phases. These instabilities are induced by a so-called bond-length mismatch depending on the relative radii of the cations [10]. The phase transition into the LTO phase has been characterized as a classical soft-mode phase transition using a two-component order parameter. Long-range antiferromagnetic order on a square lattice can be realized by a finite MO_2 interlayer coupling or an Ising-type anisotropy [11]. Assuming high-spin states due to the small crystal-field splitting in comparison to intra-atomic Hunds rule coupling, the total spin increases with decreasing ionic radius from Cu^{2+} $3d^9$ $S = 1/2$ to Ni^{2+} $3d^8$ $S = 1$ and Co^{2+} $3d^7$ $S = 3/2$. Magnetic moments lie within the MO_2 layers, parallel to the orthorhombic tilt axis for La_2CuO_4 or perpendicular for La_2NiO_4 and La_2CoO_4. The magnetic propagation vector is defined by the spin arrangement of adjacent MO_2 layers. While long-range order in the 2D S=1/2 Heisenberg model system La_2CuO_4 is stabilized through a finite interlayer coupling, the long-range order in La_2NiO_4 and La_2CoO_4 is at finite temperatures described through an Ising-type anisotropy. Since in a body-centered structure every spin is symmetrically

surrounded by two equivalent spin pairs in adjacent layers, the interlayer coupling is frustrated. Considering the Zaanen-Sawatzky-Allen [12] scheme, the systems are located in the charge-transfer regime [13, 14]. Hole doping with earth-alkaline ions on A sites in the A_2BX_4 structure or interstitial incorporated excess oxygen removes electrons from the $2p$ band, destroys the three-dimensional antiferromagnetic ordering, and reduces the bond-length mismatch. Doping-induced charge carriers exhibit an instability to a spatially modulated charge density, forming so-called stripes, where spin moments are ordered antiferromagnetically across a stripe. Stripe instabilities are well studied in cuprates and nickelates, while they are not yet investigated in cobaltates. A comparative study of these model systems is important to unfold the relevant microscopic mechanisms for spin-glass behavior, charge and spin segregation, and at last, for high-temperature superconductivity. However, the sample quality, the homogeneity range in the phase diagram, and the availability of large samples are often limiting factors. Fortunately, solid solutions of doped single-layered cobaltates $La_{2-x}Sr_xCoO_4$ are stable between ($0 \leq x \leq 2$) using a variety of preparation methods [15–26]. In single-layered cobaltates interesting physics arises especially from the magnetic degree of freedom, since the Co^{3+} ion can be found in different spin states depending on the doping level and the temperature. The analysis of structural changes, spin-, and charge-ordering phenomena in doped single-layered cobaltates gives insight in this additional degree of freedom.

The major part of this thesis is devoted to the detailed analysis of structural instabilities, charge order, and magnetic coupling schemes in $La_{2-x}Sr_xCoO_4$ by means of x-ray diffraction and neutron scattering. As mentioned above, $La_{2-x}Sr_xCoO_4$ is less studied in the literature in comparison to $La_{2-x}Sr_xCuO_4$ (LSCuO) and $La_{2-x}Sr_xNiO_4$ (LSNiO). The parent compound La_2CoO_4 is a long-range ordered antiferromagnet with a Neel-temperature of $T_N = 275$ K in the LTO distorted phase [11]. Nearest neighbors of Co^{2+} spins are coupled antiferromagnetically and the spin arrangement is similar to La_2NiO_4 in the LTO phase. Hole doping with Sr suppresses long-range magnetic order [27] and lifts the orthorhombic distortion [28]. At half doping $x = 0.5$ with the nominal Co-valence $v = 2 + x = 2.5$, and thus an equal ratio of Co^{2+} and Co^{3+} ions, short-range charge and spin order with transition temperatures T_{co} and T_{so}, respectively, have been found [7, 8]. The large difference in the transition temperatures $T_{so} \ll T_{co}$ was attributed to the decoupling of both phenomena. A Co^{2+} spin frustration was proposed by an equal strength of two-dimensional antiferromagnetic coupling between nearest and next-nearest neighbors of Co^{2+} ions. A detailed analysis of the magnetic coupling scheme has not been reported in literature up to now. Non-magnetic Co^{3+} ions were proposed to bridge between magnetic Co^{2+} ions, providing an effective antiferromagnetic coupling. While a Co^{2+} high-spin state $t_{2g}^5 e_g^2$ ($S = 3/2$) is stabilized due to Hunds rule coupling [11], the influence of the Co^{3+} spin degree of freedom in the whole series is discussed controversially in the literature [18, 27, 29–31]. The possibility of a Co^{3+} spin-state transition is well known from the three-dimensional analogue $ACoO_3$. Susceptibility and

thermal expansion measurements [32] of $LaCoO_3$ indicate a thermally driven transition from a non-magnetic insulator with Co^{3+} in the low-spin state ($t_{2g}^6 e_g^0$, $S = 0$) to a paramagnetic insulator with Co^{3+} in the intermediate-spin ($t_{2g}^5 e_g^1$, $S = 1$) or high-spin state ($t_{2g}^4 e_g^2$, $S = 2$). Whether the intermediate-spin state or high-spin state is realized is still discussed controversially [33–36]. Unlike the high-spin state, the intermediate-spin state with partially filled e_g orbitals is Jahn-Teller active [37], which motivates detailed structural investigations.

The present thesis is organized as follows: In Chapter 2, a brief introduction to the physical properties of $La_{2-x}Sr_xCoO_4$ and related systems is given. Chapter 3 introduces the experimental setup. In Chapter 4 the structural aspects of $La_{2-x}Sr_xCoO_4$, the bond-lengths anisotropies, and phase instabilities are discussed. The results are analyzed in the terms of steric ionic-radii effects, hole doping, and a possible Co^{3+} spin-state transition. In Chapter 5 we discuss the charge ordering in the system near half doping determined by neutron single-crystal diffraction. In Chapter 6, static and dynamic spin correlations and their coupling to lattice degrees of freedom are discussed for several doping levels. An antiferromagnetic coupling scheme is developed and compared to the closely related cuprates and nickelates. In Chapter 7, the findings are summarized in a new phase diagram of the single-layered cobaltate and a Co^{3+} spin-state transition from the high-spin to the low-spin state is proposed.

2. $La_{2-x}Sr_xCoO_4$ and Related Systems

This chapter includes the basic physical properties of $La_{2-x}Sr_xCoO_4$ and of chemically, structurally, magnetically, and electronically closely related systems. The structural distortions and doping dependence of the atomic parameters in this single-layered perovskite system can be related to those in the well investigated non-layered perovskite. Therefore, we will introduce these distortions briefly and discuss their relation to the symmetry reduction in the Ruddlesden-Popper series. Offstoichiometry, due to the incorporation of excess oxygen in the sample, has a great influence on the structural and magnetic properties and will be compared with the isostructural $La_{2-x}Sr_xCuO_4$ and $La_{2-x}Sr_xNiO_4$ system. Investigations on charge order and spin correlations in $La_{2-x}Sr_xCoO_4$ will be presented below.

2.1. Basic Structural Aspects and Distortions in Layered and Non-Layered Perovskites

$La_{2-x}Sr_xCoO_4$ exhibits a K_2NiF_4-type single-layered perovskite structure. First, the basic perovskite has to be examined. In addition to a great number of high-temperature superconductors, a variety of other transition metal oxides can structurally be ascribed to the perovskite-type [38]. Due to the relative small set of structural degrees of freedom, the perovskite system is an ideal model to study the influence of chemical pressure, charge carrier doping, and temperature on the physical properties. Within a purely ionic picture, the ideal perovskite structure has the sum formula ABX_3, where A and B are cations and X are anions. B cations are coordinated by six X anions, forming a net corner-sharing octahedron. A cations complete the resulting interstices (see Fig. 2.1) and are twelvefold coordinated by X. With perfect close packing, the ideal perovskite structure exhibits cubic symmetry ($Pm\overline{3}m$ space group No. 221); a close-packed stacking of rigid spheres accords to the three-dimensional arrangement with the highest density.

Distortions, which are induced by the tilt and rotation of BX_6 octahedra or by a cooperative change of the intraoctahedral $\overline{BX}$ bond lengths, are common in perovskite systems. For example, $GdFeO_3$-type distortions [39, 40] and Jahn-Teller distortions [41, 42] accompanied by an orbital order-disorder transition [43, 44] reduce the lattice symmetry. A classification of the group-subgroup connections caused by rotation and tilts of the octahedra is described by Megaw [45], Glazer [46, 47], and Woodward [48, 49]. Through the corner-sharing connection of BX_6 octahedra in three dimensions, the tilt of

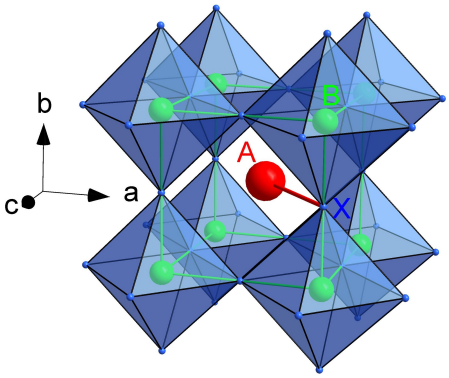

Figure 2.1.: Cubic unit cell of the ideal perovskite structure ABX_3 with corner-sharing BX_6-octahedra (space group $Pm\bar{3}m$ No. 221). The bond length $\overline{AX}$ is by a factor $\sqrt{2}$ larger than the bond length $\overline{BX}$ for the perfect close-packed stacking.

one octahedron can determine the distortion pattern of the whole octahedra arrangement. In general, the octahedral tilt and rotational degrees of freedom are strongly reduced in the three-dimensional network of nearly undistorted rigid octahedra [48]. In perovskites, 23 so-called Glazer tilt systems describing octahedra tilting modes exist.

To structurally separate the electronically or magnetically induced distortions of the ideal perovskite structure, the mismatch of ionic radii for close-packed stacking is a good starting point. An empirical prediction of the occurring strains and resulting distortions on the basis of ionic radii is included in the Goldschmidt tolerance factor t [50], defined by:

$$t = \frac{r_A + r_X}{\sqrt{2}(r_B + r_X)}. \tag{2.1}$$

The bond length $(r_A + r_X)$ of cation A with ionic radius r_A has to be $\sqrt{2}$ times larger than the bond length $(r_B + r_X)$ of cation B with ionic radius r_B to the anion X for the ideal closed packing. A stable perovskite structure is limited to the values $0.78 < t < 1.05$ [51]. For $0.78 < t < 0.9$ orthorhombic crystal symmetry and for $0.9 < t < 1$ rhombohedral symmetry are favored [52]. Even though other structural distortions are neglected, a first consideration of the distortion type and the constriction of the space group through the Glazer classification is helpful for many compounds [53]. On the basis of the ionic radii from Shannon [54], the tolerance factor for $LaCoO_3$, with Co^{3+} in the high-spin state as a lower limit, is $t = 0.97$. The expected rhombohedral symmetry $R\bar{3}c$ with octahedra tilt system $a^-a^-a^-$ was experimentally verified [55]. a represents octahedral tilts of equal magnitude around the cubic [100], [010], and [001] axis. The superscript denotes the relative tilt of consecutive octahedra along one direction. Therefore, '$-$' indicates anticooperative tilts. In general, the so-called bond-length mismatch between $A - X$ and $B - X$ bonds for a closed packed stacking of atoms in perovskites induces structural strains. Those can be reduced by the tilt and rotation of BX_6 octahedra, by octahedron distortions or by an instability to off-stoichiometry. The structural degrees of freedom to lessen the internal strain in perovskites are constricted through the three-dimensional

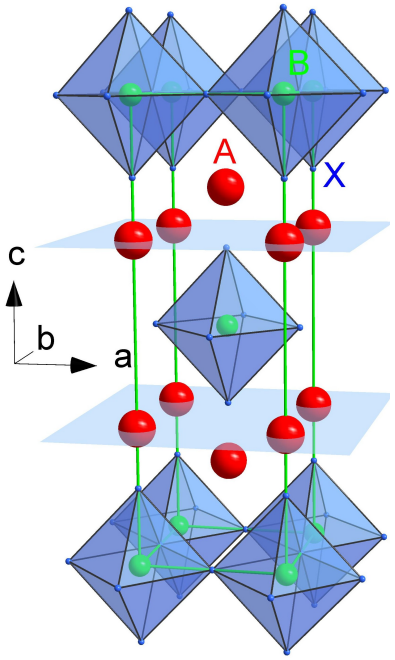

Figure 2.2.: Tetragonal unit cell of the ideal single-layered perovskite structure A_2BX_4 with corner-sharing BX_6-octahedra in the ab-plane (space group $I4/mmm$ No. 139). Neighboring BX_2-planes are staggered by $(\frac{1}{2}, \frac{1}{2}, \frac{1}{2})$ through the body centering and are separated by two AX planes. Within the Ruddlesden-Popper series $(AX)(ABX_3)_n$ the single-layered structure is classified by $n = 1$: ABX_3-units are separated by AX-interplanes.

interconnection of BX_6 octahedra.

Beside the rotation and the tilt of the BX_6-octahedra, the lattice symmetry can be lowered by a cooperative distortion of the octahedra induced by the Jahn-Teller effect or spin-orbit coupling. According to the Jahn-Teller theorem, every non-linear molecule with degenerate electronic ground state is unstable and lowers its free energy by a structural distortion to a system with lower symmetry and lifted degeneracy [56]. Since the present work is restricted to the physics of transition metal oxides, the properties of d electrons are discussed in the following. In the one-electron approximation the fivefold degenerate electronic state of the free d ion is split into a doublet state e_g and a triplet state t_{2g} by the anisotropic crystal field of the six oxygen ions. The further splitting of the energetically lower lying t_{2g}-multiplet by the shortening of the BO_6-octahedra along one direction by x results in a linear energy gain under preservation of the center of gravity. Concurrently, the elastic energy increases quadratically with x, whereby a finite structural distortion is always favored. All possible Jahn-Teller active modes for d ions with different electronic configurations, derived from group theory, can be found in Ref. [57]. The Co^{3+} ion spin states crucially differ in the strength of possible Jahn-Teller active modes. The Co^{3+} intermediate-spin state is expected to mediate the strongest Jahn-Teller distortion due to electronic energy gain in the e_g-orbitals in comparison to the t_{2g}-orbitals. This will be important for the doping dependence of Co-O bond lengths discussed in Section 4.3.

The transition from the ideal perovskite structure ABX_3 to the layered perovskite

$A_{n+1}B_nX_{3n+1} = (AX)(ABX_3)_n$ is classified in the Ruddlesden-Popper series [58, 59] through the inclusion of AX interplanes between perovskite-like ABX_3-units with a thickness of n octahedra. For $n = 1$ a tetragonal crystal structure (space group $I4/mmm$ or D_{4h}^{17} No. 139) follows, the so-called single-layered perovskite, see Fig. 2.2. Corner-sharing BX_6 octahedra form by $(\frac{1}{2},\ \frac{1}{2},\ \frac{1}{2})$ staggered planes, each separated by AX-interplanes. The ideal perovskite is the upper limit of the Ruddlesden-Popper series with $n = \infty$. Through the reduced dimensionality of the transition metal compounds with $n < \infty$ and the resulting anisotropy electronic correlations increase [60]. They are accompanied by unusual properties like high-temperature superconductivity [3, 61], stripe-like charge-order [4, 5, 62], and interlayer spin frustration. Structurally, we may expand the model of bond-length-mismatch induced structural strains to single-layered perovskites. The number of structural degrees of freedom is increased due to the decoupling of BX_6 octahedra into two-dimensional layers. First, the system may reduce internal strains by the variation of the c/a ratio, where a denotes an in-plane and c an out-of-plane lattice constant. This accounts for a shift of adjacent layers. Second, the system may reduce the strain by tilt and rotational instabilities of the BX_6 octahedra. The different tilt arrangements for single-layered perovskites depend on the in-plane corner-bonding. Third, a BX_6 octahedron distortion may be induced, where the apical oxygen displacement in both, an octahedra-tilted or not-tilted phase, reduces the strain. Fourth, the system may allow the incorporation of excess anions X to minimize the strain. All four mechanisms of strain reduction are present in single-layered perovskites.

2.1.1. Orthorhombic Distortion in Single-Layered Perovskites

All single-layered perovskite systems, $La_{2-x}Sr_xCoO_4$, $La_{2-x}Sr_xNiO_4$, and $La_{2-x}Sr_xCuO_4$, exhibit structural distortions from the K_2NiF_4-type structure at low Sr doping levels and sufficiently low temperatures. The undoped parent compound, La_2CoO_4, of the $La_{2-x}Sr_xCoO_4$ system stabilizes a low-temperature orthorhombic (LTO) distorted (space group $Bmab$[1], fully written $B\ 2/m\ 2_1/a\ 2/b$ or D_{2h}^{18} No. 64) structure [64] already at room temperature [11, 17, 22, 28, 65–69]. This distortion of the ideal single-layered structure is induced by a tilt of the corner-sharing CoO_6-octahedra along the [110]-direction of the high-temperature tetragonal (HTT) unit cell (see Fig. 2.3). The rotations of adjacent octahedra in the $[1\bar{1}0]$-direction are antiferrodistortive. This tilt pattern is common for undoped, single layered transition metal oxides like La_2MO_4 (M = Cu [70], Ni [71]), where the phase transition from the HTT to LTO phase is of second order [72, 73]. However, a subtle monoclinic distortion due to the out-of-plane oxygen ions displacement may be present for pure and lightly Sr doped samples [74].

[1] To keep in-plane and out-of-plane crystallographic axis systematic for LTT, LTO, and HTT phases, $Bmab$ is used for space group No. 64 instead of the standard setting $Cmca$. The often used standard setting of the orthorhombic space group No. 64 with the lattice vectors $\vec{a}$, $\vec{b}$, and $\vec{c}$ can be transformed by the permutation $a\bar{c}b$ of the lattice vectors [63].

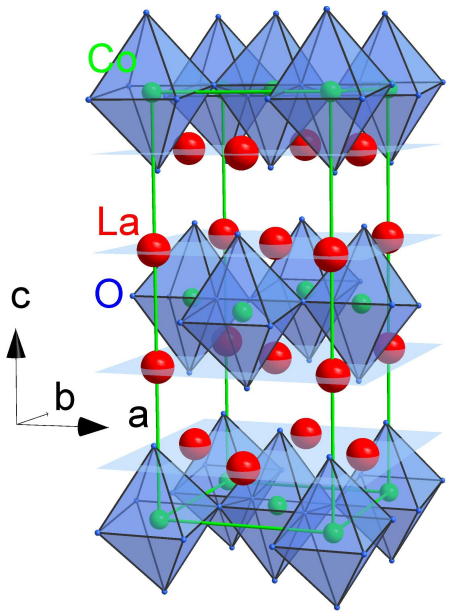

Figure 2.3.: Orthorhombic unit cell (space group *Bmab* No. 64) of the crystal structure of La_2CoO_4 at room temperature (atomic positions are taken from [65]) with figurative tilted CoO_6-octahedra in the *b*-direction (in $I4/mmm$-notation the [110]-direction).

In the simple picture presented above, the origin of the CuO_6-octahedra tilt distortions in cuprates is attributed to a bond-length mismatch between La-O and Cu-O, needed for quasi close-packed atoms in the ideal single-layered perovskite structure [10, 75]. On the one hand, this approach neglects the additional structural degrees of freedom of the layered perovskite system and gives only a qualitative understanding of the occurring distortions. On the other hand, quantitative predictions are subtle in an ionic model. In contrast to the ABX_3 perovskites, there are no close-packed A_2X_4 layers in A_2BX_4 [76]. Starting from the given AX_3 perovskite building blocks, a closed A_2X_4 layer would lead to adjacent A atoms and therefore to a considerable electrostatic repulsion.

In the bond-valence sum approach only one equilibrium bond length exists for a given pair of bonded atoms with regard to the coordination and valency. A deviation from this bond length in a purely ionic model results in structural strain. Already in the HTT phase, structural strain can be reduced by a D_{4h} distortion of the CuO_6 octahedra, without tilt or rotational instabilities. Because of the different thermal expansion of La-O and Cu-O bond lengths, the mismatch increases with decreasing temperature [77]. In comparison to three-dimensional perovskites, the octahedra-tilting angle cannot be easily attributed to the bond-length mismatch accounting additional structural degrees of freedom for the reduced dimensionality in single-layered perovskites. Through this, both the Cu-O bond length anisotropy and the La-O coordination polyhedron, see Fig. 2.5, must be taken into account to describe the LTO phase instability.

The Ginzburg-Landau theory gives an insight into the observed structural instabilities as a function of doping [78], hydrostatic pressure [79], and temperature. The order

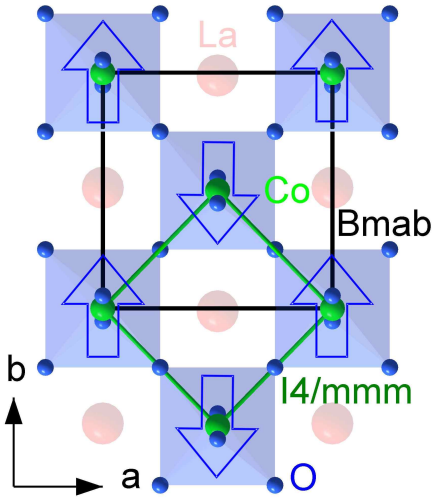

Figure 2.4.: Scheme of the LTO distortion of La_2CoO_4. Corner sharing CoO_6-octahedra are tilted in the direction of the face diagonal of the HTT units cell in $I4/mmm$ setting. The alternating tilt direction leading to an antiferrodistortive arrangement is represented by blue arrows. An expected shortening of the orthorhombic $\vec{b}$-axis in $Bmab$ setting is overcompensated through the cooperative D_{4h} octahedron distortion resulting in $a < b < c$.

parameter **Q** for the orthorhombic distortion is composed of two components Q_1 and Q_2 representing the octahedra tilts in [1, $\bar{1}$, 0] and [1, 1, 0] direction of the HTT phase; for cuprates, this method was developed by Axe *et al.* [80]. The expansion of the Ginzburg-Landau free energy near the phase transition, in terms of the order parameter, can be constructed in the form

$$F_Q = \alpha(T - T_0)(Q_1^2 + Q_2^2) + \frac{\beta}{2}(Q_1^2 + Q_2^2)^2 + 4\gamma Q_1^2 Q_2^2 + \ldots, \tag{2.2}$$

where T_0 denotes the transition temperature and α, β, and γ are temperature independent constants [81, 82]. Considering the total elastic energy $F_e = \sum 1/2 c_{ij}\eta_i\eta_j$ with elastic constants c_{ij} and the coupling of the lattice strains η_i to the order parameter given by

$$F_c = A_1(Q_1^2 + Q_2^2)(\eta_1 + \eta_2) + A_3(Q_1^2 + Q_2^2)\eta_3 + A_6(Q_1^2 - Q_2^2)\eta_6 + \ldots \tag{2.3}$$

with coupling constants A_i and lattice strains η_i, one can calculate interrelations between strains and the order parameter via a minimization of the total free energy. In particular, $\eta_6 = (a-b)/2a_{tetr}$ represents the orthorhombic shear strain. Therefore, the total Landau free energy, calculated for the HTT/LTO states, is $F = F_Q + F_e + F_c$ [83]. The stress free equilibrium state leads to

$$\frac{a-b}{2a_{tetr}} \propto (Q_1^2 - Q_2^2). \tag{2.4}$$

The transition from HTT with $Q_1 = Q_2 = 0$ to LTO is characterized by $Q_1 = 0$, $Q_2 \neq 0$. In Cu- and Ni-based single-layered perovskites a re-entrance of a tetragonal phase at low temperatures (LTT) with $P4_2/ncm$ symmetry ascribed to $Q_1 = Q_2 \neq 0$ was

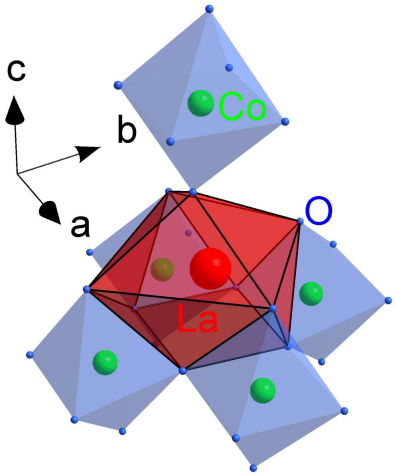

Figure 2.5.: Anisotropic La^{3+}-ion coordination in La_2CoO_4 with *Bmab* notation at room temperature (atomic positions are taken from [65]). The ninefold coordination polyhedron is asymmetrically distorted by the CoO_6 octahedra tilt and the shift of the La^{3+} ion from the symmetry position (0, 0, z) in the b-direction. The number of distinguishable La-O bond lengths is increased from 3 to 6 by the HTT-LTO transition.

observed. The octahedral tilting angle is nearly constant across this first order phase transition and only the tilt direction changes discontinuously by 45 degrees. Group-subgroup relations induced by octahedra tilt distortions in A_2BX_4 structures were investigated [84–86]. The LTO-LTT transition in La_2CoO_4 is presumably caused by the re-entrance of a tetragonal phase at $T = 132$ K [11], but a detailed structural analysis is missing.

2.1.2. Alternative Layered Structure Types and Related Cobaltates

A comparison of structural and magnetic properties of the single-layered cobaltates with other structurally related layered cobaltates provides valuable information about the influence of dimensionality and coordination on the physical properties.

In general, the K_2NiF_4-type structure is not the only possible ionic arrangement for a layered tetragonal oxide like in R_2CuO_4. The ionic radius of the rare earth ion R has a critical influence towards different structural modifications [87, 88]. Depending on the coordination polyhedra of the transition metal ion, or rather the oxygen arrangement in the crystallographic cell, one can distinguish three basic tetragonal structures: a sixfold coordination in the T, a pyramidal coordination in the T^*, and a fourfold square-planar coordination in the T' phases. This is of importance for the comparison of hole-doped and electron-doped cuprates.

For $A_{n+1}Co_nX_{3n+1}$, the crystal structure with $n = 1$ exists over a wide homogeneity range for a variety of alkaline earth doping on the A-site with La, Sr, Ca, Ba, Nd, Gd, Y [20, 26, 68, 89–92] and B-site co-doping with Ni, Ru, Cu [93–96]. Due to the additional degrees of freedom, the Goldschmidt tolerance factor t can only be limitedly transferred to layered perovskites concerning the stability of the crystal structure; the range of $0.85 \leq t \leq 1.02$ is given in literature [97]. Also the existence of further members of the Ruddlesden-Popper series for B = Co was reported in literature, e.g. $n = 2$ [98]

and $n = 3$ [99]. A systematical comparison of the influence of chemical pressure, different valencies, and the reduction of the number of AX_2 interlayers in the crystal structure was not reported up to now.

As alternatives to the Ruddlesden-Popper series, a number of perovskite based cobaltate compounds with interesting magnetic coupling schemes and charge ordering phenomena were synthesized. For example, $Bi_2Sr_2CoO_{6+\delta}$ is the structural analogon of the high-temperature superconductor $Bi_2Sr_2CuO_{6+\delta}$. In comparison to the layered perovskite system with $n = 1$, two additional BiO_2 layers are inserted between two adjacent SrO_2 layers [100, 101]. Due to the reduced Co-ion interlayer coupling, the evolution of ferromagnetism and antiferromagnetism in the system is interesting in the light of the magnetic properties of $La_{2-x}Sr_xCoO_4$, as discussed in Chap. 6. Oxygen deficient perovskites-like $Ln BaCo_2O_{5+\delta}$ (Ln = lanthanoid) exhibit interesting electronic and magnetic properties related to Co ions in pyramidal and octahedral oxygen coordination with respect to the spin degree of freedom [102–110]. Starting from the compound $Ln BaCo_2O_5$, the structure is based on corner-sharing CoO_5 square pyramids. Additional oxygen δ is incorporated in Ln layers forming CoO_6 octahedra. Magnetic and transport properties are driven by the mixed valence of cobalt ions (Co^{2+}:Co^{3+} or Co^{4+}:Co^{3+} depending on δ) [111].

2.1.3. Intercalation of Excess Oxygen δ in $La_{2-x}Sr_xMO_{4+\delta}$

Excess oxygen in the single-layered perovskite structure has a great influence on the structural, magnetic, and transport properties of the system, since the mobile hole concentration is varied and oxygen ions perturb the local crystal structure. The intercalation of molecular oxygen in the crystal structure of the parent compound $La_2CoO_{4+\delta}$ [11, 65, 67, 112] and the strontium doped compounds [28, 113–116] is well-established and must be taken into account using standard preparation techniques like the floating-zone method. As observed from oxygen kinetics, the diffusion coefficient is anomalously high and La_2CoO_4 is not stable at ambient pressure at room temperature [66]. The structural strains induced by a bond-length mismatch can be reduced through excess oxygen incorporation on interstitial sites. Chemical inhomogeneities in $La_{2-x}Sr_xCoO_{4+\delta}$ are of particular importance for the synthesis and the sample characterization, when taking this room-temperature topotactic oxidation found in La_2CoO_4 into account. An early work reports on La deficient phases [117] for which we found no indications. The orthorhombic splitting, c-axis length, and magnetic correlations strongly depend on the dopant.

Due to the not completely characterized phase diagram of cobaltates, the discussion of oxygen doping is restricted to cuprates and nickelates. Drastic changes of the structural, physical, and chemical properties are observed in $La_{2-x}Sr_xNiO_{4+\delta}$ when adding two holes per excess oxygen atom. Although the phase diagram of the oxygen-doped samples is relatively complex with a set of miscibility gaps and oxygen-ordered phases in comparison

to Sr doping [118], some similarities can be identified. Long-range antiferromagnetic order is suppressed and a spin-glass phase is induced [119, 120].

The orthorhombic strain $\epsilon = (a-b)/(a+b)$ decreases with increasing hole concentration $p = x + 2\delta$ and vanishes around $p = 0.12$, where the HTT phase is stabilized. In addition, the c-axis length depends only on p. Local perturbations induced by randomly distributed ions of different ionic radii, as in the case of alkaline-earth substitution and the disordered intercalation of excess oxygen, suggest the destruction of three-dimensional cooperative MO_6-octahedra tilting. In comparison to the substitution of alkaline-earth ions, the interstitial oxygen ions are mobile and order for critical hole concentrations [73, 121–124]. In the doping region ($0.13 \leq x \leq 0.18$), excess oxygen is incorporated as an interstitial oxygen defect near ($\frac{1}{4}$, $\frac{1}{4}$, $\frac{1}{4}$,) in an orthorhombic Fmmm structure [125]. The maximum amount of excess oxygen δ_{max} decreases if the strontium content increases up to $x = 0.3$ [126]. In La_2NiO_4, the Ni spins are aligned along the [100] direction parallel to the antiferromagnetic propagation vector in $Bmab$ setting. While the antiferromagnetic structure of $La_2NiO_{4+\delta}$ with δ=0.067 remains identical to the stoichiometric compound $\delta = 0$ [127], the Néel-temperature decreases upon doping (for $x \leq 0.06$ and $\delta = 0.06, 0.074, 0.105$) [119–121].

La_2CuO_4 becomes superconducting not only by Sr or Ba doping but also by the intercalation of excess oxygen [128]. As in LSNiO, the oxygen-doped La_2CuO_4 exhibits instabilities towards phase separation [129]. The dopant mobilities are expected to be quite different in this layered perovskite: While Sr^{2+} ions are immobile in the solid solution, the excess oxygen dopants are mobile and can order for a critical δ. Not minding these differences, the magnetic excitations in the La_2CuO_4 based compounds appear to be independent from the type of dopant, the crystallographic arrangement of the dopants, and the extent of disorder in the crystal [130]. In cuprates, oxygen ions order in layers, the so-called staging behavior, which was verified via neutron diffraction [131, 132]. For a given Sr doping, oxygen co-doping can enhance superconducting properties [133]. With increasing excess oxygen, δ in $LaCoO_{4+\delta}$, the orthorhombic splitting is vanishing [65]. Again, the maximum of incorporable oxygen (δ_{max}) systematically decreases in $La_{2-x}Sr_xCuO_4$ with increasing x [134], as the bond-length mismatch is reduced.

2.2. Charge Transport in $La_{2-x}Sr_xCoO_4$

Spin and charge order are observed in the half-doped cobaltate $La_{1.5}Sr_{0.5}CoO_4$ [7, 8] with a nominal equal ratio of Co^{2+} and Co^{3+} ions. We will discuss the characteristics in Chapter 5. Charge order instabilities affect the charge transport in the system. Generally, the transport properties of a system are defined by the charge-carrier excitation process. Insulating and metallic properties of transition metal oxides with strongly correlated electrons can be classified in the Zaanen-Sawatzky-Allen scheme through the relative strength of the Coulomb repulsion U and the charge transfer energy Δ [12]. In a transition

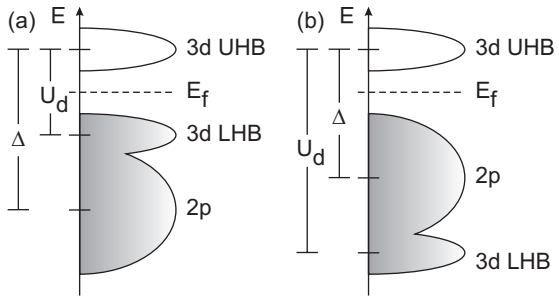

Figure 2.6.: Classification of the insulating properties of transition metal oxides within the single-particle picture. (a) The on-site Coulomb repulsion U leads to a separation of the upper (UHB) and lower Hubbard band (LHB). If Δ denotes the charge-transfer energy, a Mott-Hubbard insulator is given for $\Delta = \varepsilon_d - \varepsilon_p > U_d$ and (b) a charge-transfer insulator for $\Delta < U_d$.

metal oxide, the cation excitation process $d^n + d^n \rightarrow d^{n+1} + d^{n-1}$ from the lower to the upper Hubbard band costs the on-site repulsion energy $U = E(d^{n+1}) + E(d^{n-1}) - 2E(d^n)$ and the excitation from the oxygen $2p$ band to the upper Hubbard band costs the charge-transfer energy $\Delta = E(d^{n-1}) - E(d^n) + E(p^{m+1}) - E(p^m)$. The Mott-Hubbard insulator is characterized by $U < \Delta$ and the charge-transfer insulator by $U > \Delta$. La_2CoO_4 and $LaSrCoO_4$ are classified as charge-transfer insulators with energy gaps $E_g = 5 - 6$ eV and $E_g = 1$ eV, respectively [13, 14]. Therefore, Sr-doping induces holes in the O-2p band instead of in the Co-3d band. Via a strong p-d hybridization, the oxygen hole may be bound to the Co site. Since hybridization leaves the local symmetry unaffected, an effective mixed-valence approach may still be appropriate for the system.

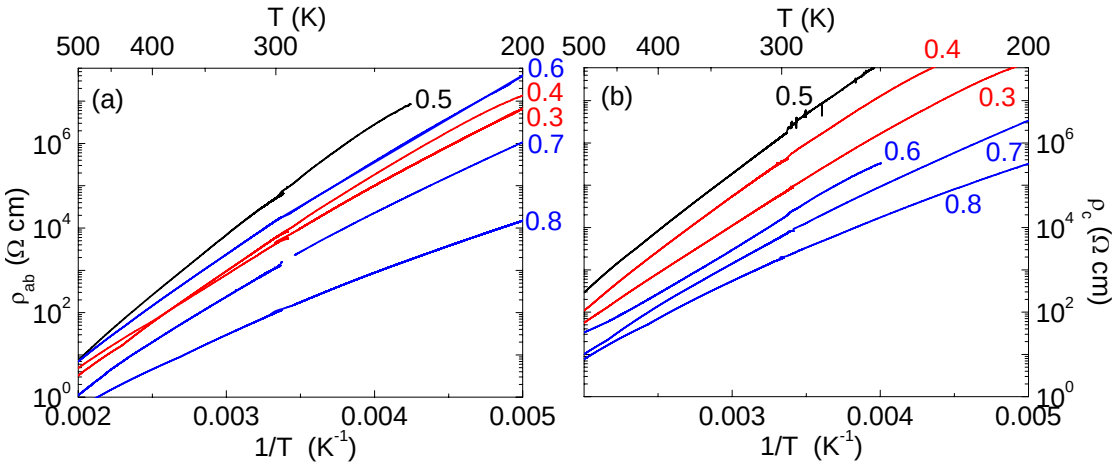

Figure 2.7.: Arrhenius-plot of the electric resistivity of $La_{2-x}Sr_xCoO_4$ within the CoO_2-planes (a) or perpendicular to these (b). Experimental data were determined by M. Benomar [135].

The system $La_{2-x}Sr_xCoO_4$ exhibits a semiconducting thermally-activated behavior with an activation energy of ∼0.5 eV in the doping range $0.3 \leq x \leq 0.8$. Although holes are induced by Sr doping, the system remains insulating. Fig. 2.7 shows the Arrhenius-plot of the in-plane (a) and out-of-plane (b) resistivity. Note that deviations from linearity may be caused by more complex conduction mechanisms, where the dimension of the conduction framework is reflected by the conductivity [136, 137]. For variable range hopping, one electron propagates through intermediate localized orbitals in a random potential and the conductivity follows $\sigma \propto exp(-(T_o/T)^{(1/(n+1))})$ with dimensionality n. We may restrict the discussion to the comparison of the doping dependence of the in-plane and out-of-plane conductivity, using the data measured by Benomar [135]. As expected, the observed energy gap, deduced from the resistivity ρ, is smaller than the gap obtained from optical spectroscopy data. On the one hand, the estimation of an electronic gap from ρ accounts only for transitions from the Fermi energy bisecting the real energy gap in the idealized scheme. On the other hand, the impurity contribution to the electronic resistivity of an insulator can be a crucial factor. Both the in-plane and the out-of-plane resistivities increase systematically with increasing strontium doping level up to $x = 0.5$ and decrease upon further hole doping. This suggests the localization of charge carries in accordance with the charge ordering at half doping.

2.2.1. Spin-state Scenarios from Macroscopic Magnetic Properties

The Co^{3+} spin-state degree of freedom is well known from the $LaCoO_3$ perovskite and is of particular importance in single-layered cobaltates, for which different spin-state scenarios are discussed.

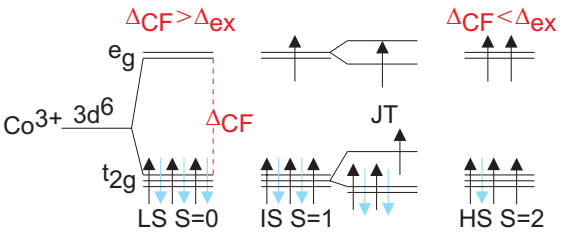

Figure 2.8.: Schematic representation of possible Co^{3+} spin states in $LaCoO_3$. Depending on the exchange energy Δ_{ex}, due to Hund's rule coupling, the crystal field splitting energy Δ_{CF}, and hybridization, three spin states are realizable: the low-spin (LS), intermediate-spin (IS), and high-spin (HS) state. A cooperative Jahn-Teller distortion was investigated by Maris *et al.* [37] and ascribed to the intermediate-spin excitation.

The unusual magnetic properties of the cobaltate perovskite $LaCoO_3$ were already investigated in the 60s [138]. $LaCoO_3$ exhibits a thermally induced spin-state transition from a non-magnetic insulator to a paramagnetic insulator near $T = 100$ K and an

insulator-metal transition near $T = 500$ K [139–141]. The spin-state degree of freedom is caused by the interplay of the intraatomic exchange interaction, *i.e.* Hund's rule coupling, Jahn-Teller distortion, crystal-field splitting, and hybridization. The possible Co^{3+} spin states for the octahedrally coordinated ion are shown in Fig. 2.8. While the stabilization of the Co^{3+} low-spin state ($3d^6$, $t_{2g}^6 e_g^0$, $S = 0$) in the octahedral oxygen coordination is widely accepted [142–147], the nature of the excited state is controversially discussed. In a purely ionic picture, the interplay between Hund's rule coupling (exchange energy Δ_{ex}) and crystal field splitting (crystal field energy Δ_{CF}) will always populate the high-spin state ($t_{2g}^4 e_g^2$, $S = 2$) for $\Delta_{ex} > \Delta_{CF}$. Korotin *et al.* proposed an energetically lower lying intermediate-spin state ($t_{2g}^5 e_g^1$, $S = 1$) by covalence effects using local density approximation plus Hubbard U LDA+U calculations [148]. From an experimental point of view, both high-spin [147, 149, 150] and intermediate-spin [32, 35] excitations were proposed for $LaCoO_3$. The combined analysis of the thermal expansion and the magnetic susceptibility in a thermally activated two-state model suggests an onset of orbital order at the spin-state transition, which vanishes at the insulator-metal transition, and an intermediate-spin population with an energy gap $\Delta \backsimeq 185$ K [32]. These findings propose a strong influence of the Jahn-Teller active intermediate-spin state. $LaCoO_3$ exhibits a pseudo cubic ABX_3 perovskite structure with corner-sharing CoO_6 octahedra, see Fig. 2.1. The crystal structure symmetry is reduced by a tilt of CoO_6 octahedra to rhombohedral $R\bar{3}c$, where Co-O bond lengths are not differentiated. A study of the temperature dependence of the lattice parameters by neutron diffraction brought no evidence for a symmetry reduction [55, 151]. A cooperative Jahn-Teller distortion is incompatible with the space group. The reduction of the $R\bar{3}c$ symmetry to a monoclinic subgroup $I2/a$ was proposed by Maris *et al.* [37]. The difference between long and short bond lengths increases with temperature and reaches ~ 6 % at room temperature. Since the monoclinic distortion is found already at $T = 20$ K and the low-spin state is not Jahn-Teller active, this ascription is inconsistent with the thermal population of the intermediate-spin state. Recent investigations found evidence for a low-spin to high-spin state transition, so that the intermediate-spin scenarios in $LaCoO_3$ have to be rejected. A direct neutron spectroscopic evidence of the high-spin excitation was proposed by Podlesnyak *et al.* [152]. Investigations on the spin-state transition in $LaCoO_3$ by soft x-ray absorption spectroscopy and magnetic circular dichroism are proposed to fully explain the existing magnetic susceptibility, electron spin resonance, and inelastic neutron data in a scenario with the high-spin state as the first excited state [33].

Transferring the idea of the spin-state degree of freedom to single-layered cobaltates, the analysis of the Co^{3+} spin-state degree of freedom in an anisotropic mixed-valence system is a challenging task: on the basis of the magnetic susceptibility and calculations of effective magnetic moments, different Co^{3+} spin-state transitions were proposed for $La_{2-x}M_xCoO_4$ (M = Ca, Sr, Ba). In Ca-doped samples, the effective magnetic moments decrease from 4.0 μ_B to 3.0 μ_B between $0.5 \leq x \leq 0.8$ [153]. These changes were

ascribed to a transition from a high-spin to an intermediate-spin state. In analogy, Moritomo *et al.* analyzed the Sr-doped samples and compared the results with a reduction of the in-plane resistivity [27]. They propose a similar HS-IS transition upon doping near $x \sim 0.6$. Because of a smaller crystal-field splitting, the Co^{3+} high-spin state should be dominant in the Ba doped cobaltate. The deviations from a linear Curie-Weiss behavior of the magnetic susceptibility and the two-dimensional character of the system make the analysis of effective magnetic moments for single-layered cobaltates, however, questionable. Up to now, there are no further indications for the proposed spin-state transitions in other physical properties. Controversially, a ferromagnetic, metallic state was proposed from nuclear magnetic resonance studies for $La_{2-x}Sr_xCoO_4$ ($x \geq 0.6$) [19]. Itoh *et al.* found evidence from the ^{59}Co Knights shift that $La_{2-x}Sr_xCoO_4$ ($0.5 \leq x \leq 1.0$) compounds are paramagnetic. Like Moritomo *et al.*, they conclude a spin-state-transition from high spin to intermediate spin near $x \sim 0.75$ from a comparison of the Knights shift, magnetic susceptibility, and the hyperfine coupling constant [30]. Wang *et al.* calculated the magnetic properties within unrestricted Hatree-Fock approximation and propose an antiferromagnetic high-spin state for $0 < x < 0.39$, a ferromagnetic high-spin state for $0.39 \leq x < 0.52$ and a ferromagnetic high-spin-low-spin ordered state for $0.52 \leq x \leq 1.1$ [29]. Overall, the Co^{3+} spin-state transition in $La_{2-x}Sr_xCoO_4$ is difficult to explain using only magnetic data. To investigate static and dynamic spin correlations, we used elastic and inelastic neutron scattering experiments, see Chapter 6.

2.3. Magnetic Susceptibility

In a first characterization of the magnetic properties of our samples, the magnetic susceptibility was investigated. The field-cooled magnetic susceptibility χ of $La_{2-x}Sr_xCoO_4$ in fields of $H = 0.25$ T applied parallel and perpendicular to the CoO_2 planes is shown in Figure 2.9. N. Hollmann performed the measurements [154] in a vibrating sample magnetometer on single crystals grown by M. Benomar [135]. No long-range Néel type order is found in the given doping region, as hole doping is expected to suppress the antiferromagnetic order present in the parent compound La_2CoO_4 [11, 155]. A comparison of field-cooled and zero-field-cooled measurements for $La_{2-x}Sr_xCoO_4$ in the same doping region was also done by N. Hollmann [154]. The drop of the zero-field curve for $H \| ab$ at low temperature, unlike the virtually constant magnetization for the field-cooled curve, agrees with a frustrated spin-glass behavior [156, 157]. Spin-glasses are defined as mixed-interacting, magnetic systems characterized by a random yet co-operative freezing of spins below a typical freezing temperature. Cooling a spin-glass below T_f produces a magnetically metastable, irreversible state without long-range order. A clear anisotropy $\chi_{ab} > \chi_c$ is found at low temperatures. Only for $x = 0.5$, the onset of short-range two-dimensional antiferromagnetic order is indicated by the decrease in χ_{ab} with decreasing temperature. Our results are similar to those of Moritomo *et al.* [27], and again the

inverse susceptibility differs from a simple Curie-Weiss behavior.

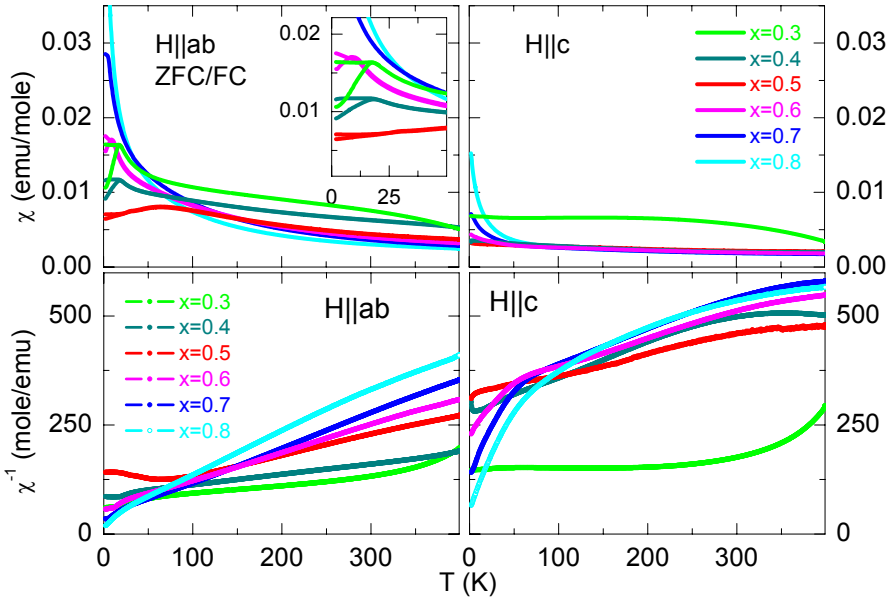

Figure 2.9.: Field-cooled magnetic susceptibility of $La_{2-x}Sr_xCoO_4$ within the *ab*-plane or perpendicular in *c*-direction with $H = 0.25$ T after measurements from Hollmann [154].

The magnetic anisotropy $\chi_{ab} > \chi_c$ was analyzed by Hollmann *et al.* [154] in terms of a cluster calculation: the anisotropic crystal field and spin-orbit coupling was calculated with respect to a Co^{2+} high-spin state and the Co^{3+} spin degree of freedom. To account magnetic interactions for an initially independent cluster, a mean-field correction was applied on the data. The difference of the Co^{2+}/Co^{3+} high-spin state anisotropies suggests a Co^{3+} low-spin state at higher doping levels. In contrast, a reduced anisotropy for $x = 0.3$ may suggest a spin-state transition to a Co^{3+} high-spin state. Interesting questions arise, as what causes the spin-glass frustration at half doping, and how do the spin correlations evolve with respect to the Co^{3+} spin-state change.

The magnetic properties of $La_{2-x}A_xCoO_4$ (A = Ca, Ba) were studied by Horigane *et al.* [153]. For all doping levels, Curie-paramagnetism is found in polycrystalline $La_{2-x}Ba_xCoO_4$ ($0.5 \leq x \leq 0.9$) and the field-cooled susceptibility of $La_{2-x}Ca_xCoO_4$ $x = 0.5, 0.6$ single crystals suggests the onset of short-range antiferromagnetic order within CoO_2 planes below $T = 67$ K. Effective magnetic moments were calculated via a Curie-Weiss description of the inverse susceptibility by the authors. However, taking the anisotropy of the single-layered perovskite into account, the validity of the Curie-Weiss law is questionable.

2.4. Spin- and Charge-Stripe Order in Single-Layered Perovskites

The spatial correlations of charge and spin in single-layered perovskites will be of particular importance for the discussion of static spin correlations in hole-doped $La_{2-x}Sr_xCoO_4$. The occurrence of a so-called stripe-phase was not reported for the single-layered cobaltate, but observed in the closely related systems $La_{2-x}Sr_xCuO_4$ and $La_{2-x}Sr_xNiO_4$. The undoped parent compounds of these systems La_2MO_4 (M= Co, Ni, Cu) are antiferromagnetic insulators with spin moments within the MO_2 layer [11]. To illustrate the idea of stripe formation, one may oversimplify the present spin correlations to just one effective nearest-neighbor coupling J on an ideal two-dimensional square lattice. The resulting spin arrangement with antiparallel spin directions for neighboring transition metal sites is shown in Fig. 2.10 (a). The enlargement of the magnetic unit cell in comparison to the chemical one induces the superstructure reflection $(\frac{1}{2}, \frac{1}{2})$. Hole doping in the MO_2 may induce a localization of charges at a critical concentration x_c in one-dimensional lines. A diagonal charge order found in $La_{5/3}Sr_{1/3}NiO_4$ is shown in Fig. 2.10 (c). The so-called charge stripes represent antiphase domain boundaries and modulate the spin order. This modulation induces satellite reflections in reciprocal space with the distance $\epsilon = 1/3$ away from $(\frac{1}{2}, \frac{1}{2})$. The magnetic twin structure rotated by 90° in real space is energetically equivalent in case of an ideal square lattice and induces the concomitant rotated satellite reflections. The commensurate diagonal stripe order for $x = 1/3$ in $La_{2-x}Sr_xNiO_4$ is found to be very stable [158]. Hole concentrations $n_h = x$ below or above $x = 1/3$ induce an incommensurate modulation of the static spin arrangement. The linearity of $\epsilon \sim n_h$ suggests that all holes contribute to the stripe formation. The incommensurate stripe modulation in $La_{2-x}Sr_xCuO_4$ changes with doping from a diagonal to a parallel arrangement along tetragonal axes by a rotation of 45° near the onset of superconductivity at $x \sim 0.05$ [159].

This is the basic idea of site-centered stripe-order and its geometrical aspects for the modulated spin-arrangement. A wide range of layered cuprates and nickelates exhibit stripe order instability. Stripe order in cuprates is believed to be closely related to high-temperature superconductivity [4]. The physics of dynamic and static stripe correlations is complex and the reason for stripes is controversially discussed from the theoretical side. Article reviews on the experimental techniques and the theoretical ideas of stripes in cuprates and nickelates can be found in Refs. [160–162]. A description of the Fourier analysis of displacive and density modulations and the calculated satellite reflections can be found in Refs. [163–166]. The static antiferromagnetic spin correlations in $La_{2-x}Sr_xCoO_4$ were studied over a wide doping range and the observed incommensurate modulation will be discussed in terms of a stripe-like arrangement in Chapter 6.

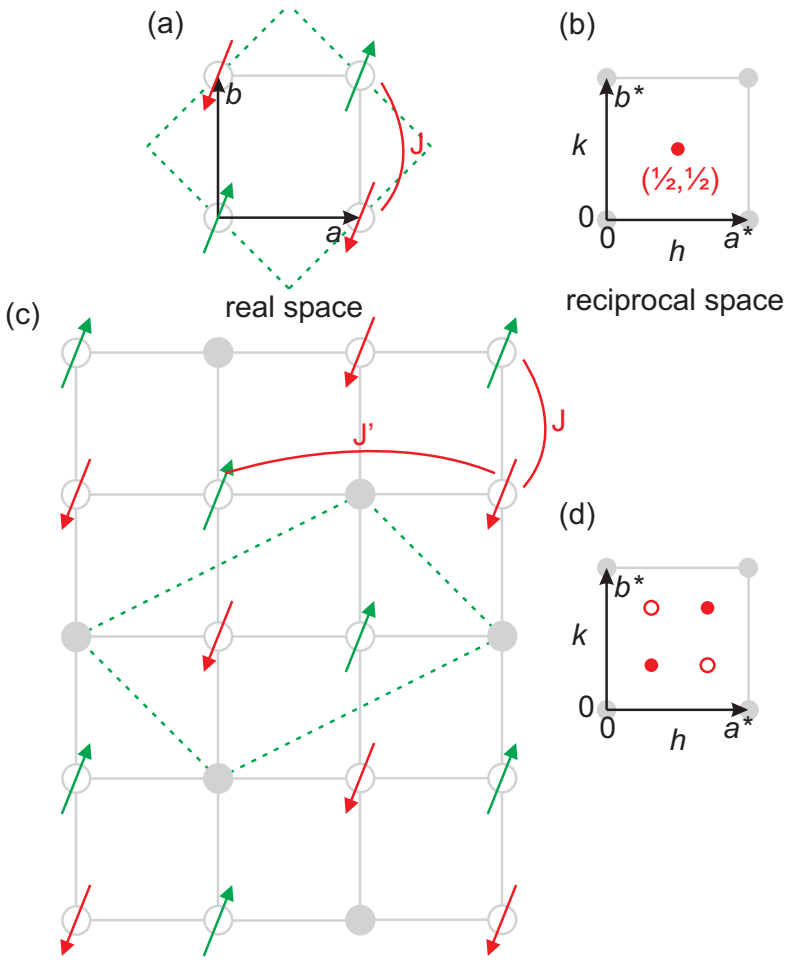

Figure 2.10.: Modulation of the antiferromagnetic spin order in a site-centered stripe arrangement on an ideal two-dimensional square lattice. (a) An antiferromagnetic nearest-neighbor coupling J between spins of a transition metal ion (empty circle) stabilizes a real space spin arrangement, which is commensurate to the tetragonal unit cell. The magnetic unit cell is represented by dashed lines. (b) The magnetic superstructure reflection $(\frac{1}{2}, \frac{1}{2})$ in reciprocal space is denoted by a red circle. (c) Site-centered hole localization (filled circles) in a stripe-like arrangement for a hole concentration $\frac{1}{3}$, as proposed for $La_{5/3}Sr_{1/3}NiO_4$ [167]. An inter-stripe next-nearest neighbor coupling J' and intra-stripe nearest neighbor coupling J are shown. (d) The modulation of the undoped spin arrangement induces satellite reflections (filled circles) away from $(\frac{1}{2}, \frac{1}{2})$. In tetragonal symmetry, the energetically equivalent twin arrangement rotated by 90° induces satellite reflections represented by empty circles.

3. Experimental Details

In this chapter, the experimental methods used for this thesis will be introduced. To investigate the temperature dependence, the doping dependence, dynamical aspects, and interrelations of the structural and magnetic properties of $La_{2-x}Sr_xCoO_4$ in detail, we used x-ray and neutron-scattering techniques. The choice of techniques and instruments with their advantages and disadvantages strongly depends on the scientific objectives. The interactions of an x-ray and neutron beam with a crystalline sample and therefore the available information about the physical properties is fundamentally different. While x-rays primarily interact with the electrons in a crystal within a scattering experiment, neutrons interact with the atomic nuclei, and via the magnetic dipole-dipole interaction, with magnetic moments. The combination of both probes provides information about static and dynamic aspects of charge, nucleus and spin distribution in materials. This chapter is divided in three major parts: the structure determination of $La_{2-x}Sr_xCoO_4$ by x-ray diffraction, the charge-order investigation by neutron diffraction, and the analysis of antiferromagnetic correlations by neutron-scattering experiments. Emphasis will be laid on the special setup to analyze the interplay between structural and magnetic properties by chemical pressure, variation of temperature, and hole doping.

3.1. Sample Synthesis

Bulk polycrystalline samples of $La_{2-x}Sr_xCoO_4$ ($0.15 \leq x \leq 1.1$) were prepared by a solid-state reaction of appropriate amounts of La_2O_3, $SrCO_3$, and Co_3O_4 powders. Depending on the doping level, the calcination was carried out several times in air or argon atmosphere in the temperature region 1050-1410 °C for 24 h, thoroughly grinding the material in between. The preparation is described in detail in literature [94, 135, 168]. Phase equilibria studies are given in Refs. [169, 170]. Single crystals of $La_{2-x}Sr_xCoO_4$ ($0.2 \leq x \lesssim 1$) were grown by the traveling floating zone method in a flow of argon or oxygen gas. Polycrystalline samples with low Sr doping were prepared and characterized by M. Haider [94] and single crystals were grown by M. Benomar [135] or M. Reuther [168]. All single crystals and powder samples were homogeneous and single phase as determined by the Rietveld analysis [171] of the powder x-ray diffraction (PXD) patterns using *FullProf* [172]. The cation composition of the samples was controlled by energy dispersive x-ray microanalysis (EDX) by I. Simons and atomic-absorption spectroscopy (AAS) by A. Möller and P. Kliesen at the Department of Inorganic Chemistry at the University of Cologne. The results are given in Fig. A.1 in the Appendix.

3.2. Structure Determination

3.2.1. X-Ray Powder Diffraction

$La_{2-x}Sr_xCoO_4$ exhibits a single-layered perovskite structure with a tetragonal lattice structure at higher temperatures (HTT). With decreasing temperature a phase transition to a so-called low temperature orthorhombic (LTO) phase occurs for low doping levels. To determine the lattice parameters and the phase boundary of HTT and LTO states of the layered $La_{2-x}Sr_xCoO_4$ compounds precisely, x-ray powder diffraction measurements were carried out using a Siemens XP-18 diffractometer with a rotating copper-anode as x-ray source. The experimental setup and procedure of this standard method can be found in detail, for example, in Refs. [94, 173]. The layout of a conventional x-ray powder diffractometer is very simple. In a $\theta - 2\theta$ setup with Bragg-Brentano geometry, a polycrystalline powder sample on a flat object holder is placed in reflection position to an x-ray detector in the center of the diffractometer. The x-ray detector rotates around the sample, tracing a circle, and collects the diffracted beam over a wide 2θ range, while the sample is rotated by θ. The position and intensity distribution of reflections in a powder diffraction pattern can be calculated using Bragg's law and the refinement of atomic positions in a structure model via the Rietveld method [171]. To satisfy Braggs law for a large number of reflections, single-crystal samples are well ground for the random distribution of crystallites. The loss of three-dimensional information through this is the main disadvantage of the method, which hinders an accurate structure solution, so that a structure model is needed in the Rietveld refinement process. The advantage of an x-ray powder diffractometer lies in a very high angle resolution, by what it is well suited for the analysis of lattice constants and structural phase transitions. A further important application of the method is the quantitative analysis of different crystalline phases in the specimen used for the characterization of newly synthesized samples. Room-temperature lattice parameters of the available doping series $La_{2-x}Sr_xCoO_4$ were examined using a series of diffractograms. A typical measurement lasts 12 h with an angle resolution of 0.02° in the 2θ-range from 10° to 120°. The temperature dependence of the lattice parameters and the HTT-LTO transition temperature was investigated with a Siemens D5000 diffractometer using monochromized Cu K_α radiation. With the combined usage of a ^{4}He evaporation cryostat and a *Paar* high-temperature camera the temperature region 10 K $\leq T \leq$ 1050 K is covered.

3.2.2. Single-Crystal X-Ray Diffraction

In contrast to an x-ray powder diffractometer, the relative Bragg reflection intensity can be integrated very precisely for a large number of reciprocal lattice points using a single-crystal x-ray diffractometer. The relative Bragg intensities provide information about the electron-density distribution in a sample through the structure factor F, by what the relative atomic positions can be calculated. The structure factor is given by

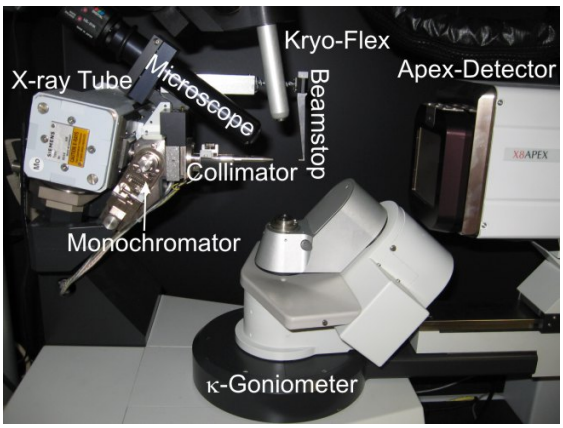

Figure 3.1.: Setup of the X8 Apex single-crystal diffractometer with CCD area detector, κ-goniometer, and *Kryo-Flex* low temperature device.

$F(\vec{G}) = \sum_i^n f_i \exp(2\pi i \vec{r_i} \cdot \vec{G})$ with the atomic form factor f_i, the position $\vec{r}_i = (x_i, y_i, z_i)$ of atom i in the unit cell, and the reciprocal lattice vector $\vec{G} = (h, k, l)$. The total number of atoms is n. The observed reflection intensity is $I \approx |F|^2$. In principle, the electron density of the crystal can be calculated by the Fourier transformation $\rho(\vec{r}) = \frac{1}{V} \sum_{hkl} F(\vec{G}) \exp(-2\pi i \vec{G} \cdot \vec{r})$. The phase $\Phi(\vec{G})$ of the structure factor $|F(\vec{G})| \cdot e^{i\Phi)}$ is not experimentally achievable, which is the phase problem of x-ray crystallography. A set of theoretical methods exists to partly recover the phase information in an experiment. In the case of doped single-layered cobaltates, the starting point of the structure model was given by the reported neutron scattering investigation on La_2CoO_4 [65]. To collect a large number of Bragg intensities in the three-dimensional reciprocal lattice, the specimen can be rotated around three independent angles and the detector on the 2θ circle in a so-called four-circle diffractometer. The main disadvantage of this method lies in the less precise analysis of lattice constants and structural phase transitions in comparison to a powder x-ray diffraction. The use of powder x-ray diffraction lattice constants for the calculation structure parameters in absolute lengths, for example bond lengths, is advisable. Within the scope of this thesis, an X8 Apex single-crystal diffractometer by *Bruker* with a CCD area detector and a *Kryo-Flex* low-temperature device was put in operation at the Institute of Physics II (see Fig. 3.1). The experimental setup comprises an x-ray ceramic tube with 0.4×0.8 mm fine-focus area, molybdenum-anode ($\lambda_{K\alpha 1} = 0.7093$ Å, $\lambda_{K\alpha 2} = 0.71359$ Å), short cooling head, and a maximum power of 2000 W. The white beam of the Mo tube is monochromized by using the (0,0,2) reflection of a pyrolytic graphite crystal (12×6 mm, 0.4° mosaic spread). As per manufacturer's specifications, the positioning accuracy of the sample is $\pm 0.015°$ for φ, $\pm 0.010°$ for κ, ω, and a 2θ resolution of 0.0003° for the detector circle. X-ray intensity data were collected by an Apex CCD detector with an active area of 62×62 mm and a resolution of 15 μm. By using an optimized phosphor layer, a sensitivity of 160 e^- per Mo-photon and a readout time of $t < 0.2$ s is reached. The realization of temperature dependent measurements

at an x-ray four-circle diffractometer is still difficult, unsatisfactorily. Closed cryostat configurations for low-temperature measurements constrict the angle variability, Be or Kapton polyimide film windows obscure the view of the crystal and enhance background scattering. Therefore nitrogen-gas stream cooling equipment with the temperature limit of liquid nitrogen is the standard laboratory technique. Inside a laminar nitrogen flow with an ambient dry air stream of the *Kryo-Flex* low-temperature device, sample cooling down to $T \sim 90$ K is possible. The open construction can lead to the formation of ice close to the sample in a long-run experiment, which increases background scattering and provides second phase reflections. The appearance of ice at the sample position for long-run measurements (3-5 days) was minimized using ϕ-scans at high κ angles and a highly efficient air dryer.

Single crystals of the $La_{2-x}Sr_xCoO_4$ series exhibit a relatively high linear absorption factor μ in the doping region $\mu = \mu_m/\rho = 26.81$ mm^{-1} for $La_{1.8}Sr_{0.2}CoO_4$ and $\mu = 30.01$ mm^{-1} for $La_1Sr_1CoO_4$ with respect to Mo-K_α photon energies and the density ρ at room temperature. To optimize the semiempirical multi-scan absorption corrections using the software program *SADABS* [174], all crystals were ground to nearly spherical shape, typical $\varnothing \sim 100$ μm in diameter. A picture of the custom-built single-crystal ball mill is shown in Fig. 3.2 and the design drawing can be found in the Appendix B.1. The construction was supported by P. Held and L. Bohatý from the Institute of Crystallography at University of Cologne. Crystals rotate around a vertical axis in a cylindrical chamber through a continuous air stream. Sandpaper on the seam provides the required abrasion. A filter (52 μm pore) at the exhaust in the cask cover encloses crystals of designated size. The surface texture and nearly ($\Delta r \sim 50$ μm) spherical shape was checked by a Leica MZ16 stereomicroscope. As $La_{2-x}Sr_xCoO_4$ crystals exhibit a relatively enhanced hardness for a layered system, very fine sandpaper (600-grit) can be used for a long grinding time of several hours in a weak air stream. This improves the crystal surface smoothness markedly. For the x-ray data collection the sample is fixed in the tip of a Boro-silicate glass capillary on a goniometer head.

The data collection strategy, analysis, and reflection integration is based on the *Apex* software collection. After the determination of the orientation matrix, a collection strategy was optimized concerning completeness, redundancy and time by the *COSMO* software. The maximal 2θ angle achievable within an experiment was $\sim$120 °, which corresponds to a resolution of $d \sim 0.41$Å. Data were integrated using *Saint*, providing periodic refinements for different runs and a global refinement of unit cell parameters and instrumental errors. The sample absorption μ is modeled via spherical harmonic functions [175] of the beam direction cosines of eighth order as the crystals are strongly absorbing. The error analysis and derivation of correct standard uncertainties in the absorbtion correction is described in the *SADABS* user guide [174]. The typical correction factor 0.0015 for Mo $\lambda/2$ contamination [176] was tested and used throughout the measurements. The structure model was refined with *Jana2000* [177]. Reflections with $I < 3\sigma$ were considered as unobserved and all observed reflections were accounted for without averaging

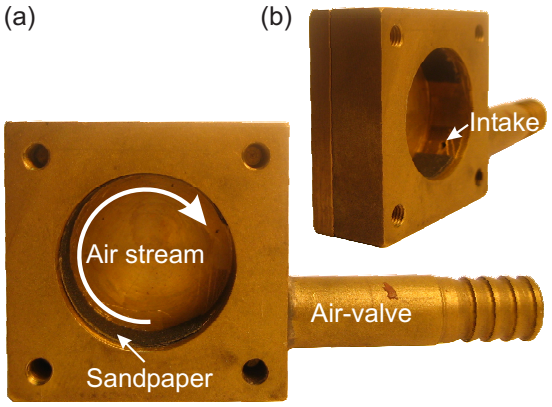

Figure 3.2.: To optimize multi-scan absorption correction for the strong absorbing material $La_{2-x}Sr_xCoO_4$, single-crystals where grinded to nearly spherical shape. For this purpose, a single-crystal ball mill was constructed. The crystals rotate around a vertical axis in a cylindrical chamber through a continuous air stream. The cask cover with a filter exhaust is not shown.

over symmetry equivalents. All structure refinements were based on F^2. An isotropic type I extinction correction with Gaussian contribution [178] was applied on the data during crystal structure refinement. An extinction correction helps avoiding the effect of the reflection of a significant fraction from the primary x-ray beam by outer lattice planes [179]. Deeper lying planes contribute less to the diffracted intensity through the weakened primary radiation. In the definition of Zachariasen the extinction depends only on the mosaic spread in comparison to the mosaic block size for type I [180]. Atomic displacement parameters were calculated in harmonic approximation. The stoichiometry was calculated via refinements of the occupation factors a_i of La/Sr and oxygen sites.

3.2.3. Criteria of Fit and Model Analysis

To judge the structural model refinement of a diffraction experiment, a variety of criteria of fit has to be taken into account. This numerical criteria indicate the adequacy of the structure model, counting statistics, reflection-profile agreement, etc.. The definition of the criteria of fit depends on the refinement against the structure factor F or intensities $I \propto F^2$. Powder and single-crystal structure refinements in this work are based on F^2, where intensities I are measured with the estimated standard deviation $\sigma(I)$. Residuals of refinements against F^2 are typically two or three times higher than those for refinements against F. The weight w of the structure refinement is given by

$$w = \frac{1}{4F_o^2} \frac{1}{(\sigma^2 + (uF_o)^2)} \tag{3.1}$$

with standard deviation σ and the instability factor u. The corresponding minimized function is

$$P = \sum w(F_o^2 - F_c^2)^2. \tag{3.2}$$

The instability factor u represents systematic errors depending on the instrument and sample, which contribute to the estimated standard deviations of intensities. u was unac-

counted for in the weighting scheme to keep datasets from different crystals comparable. Typical values of $u = 0.01$ for systematic instrumental errors showed no improvements to the compared statistical quantities. The Goodness-of-Fit S is defined by

$$S = \sqrt{\left(\frac{\sum_i w(F_{o,i}^2 - F_{c,i}^2)^2}{m - n} \right)} \tag{3.3}$$

with the number of reflections m and the number of refined parameters n. S is close to unity when systematic errors are insignificant, the weights are correctly determined, and the structure model is accurate. Small deviations from 1 may still indicate an accurate structure model, as further details of the anharmonics, bonding electrons, etc., are neglected [177]. Note, the weighted R-factor wR can be a few times higher for a refinement against F^2 and a value $wR < 0.15$ should be reached for a good dataset [181].

3.2.4. Neutron Powder Diffraction

The HTT/LTO instability in single-layered cobaltates is characterized by a cooperative tilt of CoO_6 octahedra. Weak oxygen displacements are difficult to detect for compounds with electron dense constituents in a standard x-ray diffraction experiment. This problem can be solved by using neutron diffraction techniques. As mentioned above, the interaction of neutrons with a crystalline sample is fundamentally different in comparison to x-ray scattering and is based on nuclear and magnetic scattering. The coherent scattering is not proportional to the atomic number Z and enables to localize light constituents although electron dense constituents are present in a compound. Neutron diffraction experiments were carried out to determine the low-temperature structure of $La_{2-x}Sr_xCoO_4$ ($x = 0.2, 0.4, 0.8$). Neutron powder diffraction data were collected for these samples at 10 K on the high-resolution diffractometer 3T2 at the Orphée reactor, Laboratoire Léon Brillouin (Saclay, France), with an incident neutron wavelength of 1.225 Å. The powder sample was placed in a vanadium cup and kept in an He gas-flow cryostat. The intensities were measured by a bank of 20 ^{3}He counters. A range of $6 \leq 2\theta \leq 126$ ° was covered in the diffraction patterns.

The neutron powder diffraction profiles were fitted using a Rietveld-type method implemented in the program *Fullprof* [172]. The observed profiles were described using a Thompson-Cox-Hastings pseudo-Voigt function and instrumental broadening was accounted through U, V, W parameters in the Caglioti formula [182]. Since the octahedral tilting angle and the concomitant x displacement of the La/Sr ion are small, no significant superstructure reflections such as $(0, 3, 1)_{Bmab}$ were found for $La_{1.8}Sr_{0.2}CoO_4$. As for x-ray diffraction patterns, we used the Rietveld method to refine the structure model. The estimation of the background was performed using a refinable background polynomial function.

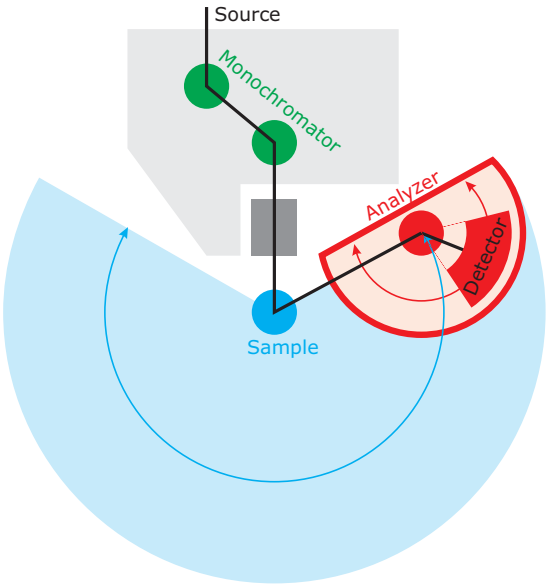

Figure 3.3.: Schematic of a triple-axis neutron spectrometer with independently adjustable monochromator, sample, and analyzer axis. The monochromator, sample, and analyzer crystal angles define the energy and momentum of the incident and scattered neutron beam. The scattering function $S(\mathbf{Q},\omega)$ can be investigated in the wide range in energy and momentum space of the sample by the variability of angles and neutron wavelengths.

3.3. Charge- and Spin-Order Determination

Charge-order instabilities and static spin correlations in $La_{2-x}Sr_xCoO_4$ were studied by triple-axis neutron spectrometer. In addition, the charge-order superstructure in $La_{1.5}Sr_{0.5}CoO_4$ was investigated on four-circle neutron diffractometers. A triple-axis neutron spectrometer is the most versatile tool when performing inelastic scattering to investigate lattice dynamics, magnetic excitations, spin-waves, diffuse scattering, etc. in condensed matter, see for example [183]. A very good signal-to-noise ratio of a triple-axis spectrometer and the flexibility in the choice of beam collimation, neutron energies, and analyzer reflections also help to characterize weak elastic scattering, *i.e.* spin or charge order in case of the single-layered cobaltates. The schematic layout of a three-axis instrument is shown in Fig. 3.3. The monochromator, analyzer, and sample axis can be moved individually. Monochromator and analyzer crystals are used to define the energy of incident and scattered neutrons in the experiment. Generally, by defining a precise energy transfer $\hbar\omega$ and momentum transfer $\hbar\mathbf{Q}$ to the sample, the scattering function $S(\mathbf{Q},\omega)$ can be investigated in the wide range in energy and momentum space predetermined by the spectrometer and sample characteristics. The main disadvantage of a triple-axis spectrometer is that only one position for $S(\mathbf{Q},\omega)$ can be achieved at a time. Cold, thermal, and hot spectrometers are distinguished by the choice of wavelength $\lambda > 4.0$ Å, $\lambda \sim 2$ Å, and $\lambda < 2$ Å. Using the relations $T = 11.605E$ and $\lambda = 9.044/\sqrt{E}$ between temperature T (K), Energy E (meV), and neutron wavelength λ (Å), neutrons of the thermal regime correspond to 290 K$\sim$ 25 meV$\sim$ 1.8 Å. Of course, the $\mathbf{Q}$ resolution for cold neutrons is increased, but the absolute neutron flux and the obtainable section in

momentum and energy space is reduced in comparison with a thermal spectrometer. A general disadvantage of a triple-axis spectrometer is, that the size of cryostats, furnaces, and magnets restricts the experiment to a nearly fixed scattering plane of the reciprocal space. Two-circle goniometers with a small angle range are commonly used for the sample alignment. Charge-order superstructure reflections in $La_{1.5}Sr_{0.5}CoO_4$ were investigated by hot four-circle neutron diffractometers. With the smaller wavelength and variable crystal orientation, the Bragg intensities can be accurately integrated in a larger section of the reciprocal lattice.

3.4. Antiferromagnetic Correlations in $La_{2-x}Sr_xCoO_4$

Scientific objectives in case of $La_{2-x}Sr_xCoO_4$ are to investigate the coupling between the antiferromagnetic correlations, the structural anomalies, and charge order instabilities. A basic characterization of magnetic correlations for the whole series ($0.2 \leq x \leq 1.0$) was provided by the magnetic susceptibility measurements. Field-cooled and zero-field-cooled magnetic susceptibility of $La_{2-x}Sr_xCoO_4$ was measured by M. Benomar [135] and N. Hollmann [154], the former using a SQUID (Superconducting Quantum Interference Device) magnetometer and the latter a VSM (Vibrating Sample Magnetometer).

To determine static and dynamic spin correlations, elastic and inelastic neutron scattering experiments were performed using the triple-axis spectrometers 1T1, G43, 4F1, 4F2 at the Orphée reactor, Laboratoire Léon Brillouin (Saclay, France), *Unidas* at the FRJ2 (Jülich, Germany), and *PUMA* at the FRMII (München, Germany). Details to basic techniques of using magnetic neutron scattering with a triple-axis spectrometer can be found in Refs. [44, 183]. In contrast to optical spectroscopy, collective excitation like phonons and spin waves, *i.e.* atomic displacements and spin deviations in a magnetic system, can be studied for a defined energy transfer $\hbar\omega$ and momentum transfer $\hbar\mathbf{Q}$. The analysis of the spin-wave dispersion reveals the magnetic exchange integrals, magnetic moments, and anisotropies in the system.

Using the polarization analysis at 4F1, the magnetic correlations were separated from structural contribution in $La_{1.7}Sr_{0.3}CoO_4$. For all measurements, crystals with cylindrical shape being typically 40 mm in length and 10 mm in diameter were either mounted in an Al can filled with He gas or on a sample stick in a sample well, cooled in a closed-cycle or *Orange* cryostat.

3.5. Analyzing Magnetic Correlations by Neutron Scattering

A polarization analysis in neutron scattering experiments was used to separate magnetic from structural scattering contributions in $La_{1.7}Sr_{0.3}CoO_4$ samples. The main aspects will be briefly introduced in the following. The interaction of the neutron with matter in a scattering experiment is based on both coherent and incoherent scattering of the

neutron on the atom core and on the interaction of its magnetic dipole moment with the magnetic field of the electron density distribution of the atom. Good introductions to the application of spin-polarized neutron scattering can be found in Refs. [183–187].

3.5.1. Nuclear Coherent Scattering

Taking Fermis Golden Rule [188] into account, the double-differential cross section of a scattering experiment can be written as:

$$\left(\frac{d^2\sigma}{d\Omega dE_f}\right)_{\lambda_i\to\lambda_f} = \frac{|\vec{k}_f|}{|\vec{k}_i|}\left(\frac{m}{2\pi\hbar^2}\right)^2 | < \vec{k}_f\lambda_f|V|\vec{k}_i\lambda_i > |^2\delta(E_{\lambda_i} - E_{\lambda_f} + E_i - E_f). \quad (3.4)$$

By the interaction of the neutron with the scattering system through the potential V, the initial state of the system λ_i, with starting energy E_{λ_i}, is transferred to the final state λ_f with energy E_{λ_f}. The wave vector $\vec{k}_i$ and the energy E_i of the neutron before the scattering result in $\vec{k}_f$ and E_f (let $\Delta E_n = E_i - E_f = \hbar\omega$).

Following the terminology in Ref. [183], Equation (3.4) can be generalized for the interaction of the magnetic dipole moment of the neutron with the magnetic field of the atom core and the electron shell via the dipole-dipole interaction to

$$\left(\frac{d^2\sigma}{d\Omega dE_f}\right)_{s_i\to s_f} = \frac{|\vec{k}_f|}{|\vec{k}_i|}\sum_{i,f} P(\lambda_i)\left|\left\langle \lambda_f \left| \sum_l e^{i\vec{Q}\cdot\vec{r}_l} U_l^{s_i s_f} \right| \lambda_i \right\rangle\right|^2 \delta(E_{\lambda_i} - E_{\lambda_f} + \Delta E_n). \quad (3.5)$$

The sum in Equation 3.5.1 is counting over the total arrangement of atoms in the unit cell at distinct sites l with corresponding positions $\vec{r}_l$. $P(\lambda_i)$ denotes the statistical weighting factor of the initial state λ_i and $U_l^{s_i s_f}$ denotes the scattering amplitude from spin state s_i of the neutron to the spin state s_f at site l:

$$U_l^{s_i s_f} =< s_f|b_l - p_l\vec{S}_{\perp l}\cdot\boldsymbol{\sigma} + B_l\mathbf{I}_l\cdot\boldsymbol{\sigma}|s_i > . \quad (3.6)$$

Let b_l be the coherent scattering amplitude of the atom core, B the spin dependent scattering amplitude of the core, $\mathbf{I}$ the core spin operator, $\vec{S}_\perp$ the magnetic interaction vector perpendicular to $\vec{Q}$, and $\boldsymbol{\sigma}$ the spin operator of the electron shell. The magnetic scattering amplitude p is proportional to the magnetic form factor $F(\vec{Q})$ and the magnetic moment of the electrons, composed of spin and orbital contributions.

The question arises how nuclear and electron contributions change the spin-state of the neutron in a scattering process, which can by determined by the polarization analysis. For purely coherent scattering of spinless atomic nuclei ($I = 0$) Equation (3.6) can be written as

$$U_l^{s_i s_f} =< s_f|b_l|s_i >= b_l < s_f|s_i >= \begin{cases} b_l, & \text{non-spin-flip} \\ 0, & \text{spin-flip,} \end{cases} \quad (3.7)$$

if the change of the spin state[1] is analyzed regarding to only one chosen axis during the experiment, *e.g.* if a direction reversal (spin-flip) or no direction reversal (non-spin-flip) of the expectation value of the spin operator occurs. There are no spin-flip scattering contributions for coherent scattering with spinless atomic nuclei.

3.5.2. Magnetic Scattering

If atom core contributions to the scattering are neglected, the scattering amplitude in Equation 3.6 can be simplified to

$$U_l^{s_i s_f} =< s_f | p_l \vec{S}_{\perp l} \cdot \boldsymbol{\sigma} | s_i >= p_l \sum_\gamma \vec{S}_{\perp l,\gamma} < s_f | \boldsymbol{\sigma}_\gamma | s_i > . \tag{3.8}$$

With the Pauli-Spin-matrices

$$\boldsymbol{\sigma}_x = \begin{pmatrix} 0 & 1 \\ 1 & 0 \end{pmatrix}, \boldsymbol{\sigma}_y = \begin{pmatrix} 0 & -i \\ i & 0 \end{pmatrix}, \boldsymbol{\sigma}_z = \begin{pmatrix} 1 & 0 \\ 0 & -1 \end{pmatrix} \tag{3.9}$$

and the neutron spin direction 'up' $|+ >= \binom{1}{0}$ and 'down' $|- >= \binom{0}{1}$ a distinction between the following cases for spin-flip and non-spin-flip scattering can be made:

$$U_l^{s_i s_f} = p_l \cdot \begin{cases} -\vec{S}_{\perp l,z}, & + \rightarrow + \quad \text{Non-Spin-Flip} \\ \vec{S}_{\perp l,z}, & - \rightarrow - \quad \text{Non-Spin-Flip} \\ -(\vec{S}_{\perp l,x} + i\vec{S}_{\perp l,y}), & + \rightarrow - \quad \text{Spin-Flip} \\ -(\vec{S}_{\perp l,x} - i\vec{S}_{\perp l,y}), & - \rightarrow + \quad \text{Spin-Flip.} \end{cases} \tag{3.10}$$

If $\vec{Q}$ is chosen parallel to the polarization direction, $\vec{S}_{\perp l,z} = 0$ is obtained and therefore only an intensity contribution during the spin-flip measurement. For $\vec{Q}$ perpendicular and $\vec{S}$ parallel to the polarization direction follows $\vec{S}_{\perp l,x} = \vec{S}_{\perp l,y} = 0$ and only an intensity contribution in the non-spin-flip channel is observed.

$\vec{S}_\perp$ can be written as the component perpendicular to the unit vector $\widehat{Q}$, see Ref [187]:

$$\vec{S}_\perp = \widehat{Q} \times (\vec{S} \times \widehat{Q}) \tag{3.11}$$

$$= \vec{S} - \widehat{Q}(\widehat{Q} \times \vec{S}). \tag{3.12}$$

The square of $\vec{S}_\perp$ is

$$|\vec{S}_\perp|^2 = \sum_{\alpha\beta} \left(\delta_{\alpha\beta} - \frac{Q_\alpha Q_\beta}{|\vec{Q}|^2} \right) S_\alpha^* S_\beta \qquad (\alpha, \beta = x, y, z). \tag{3.13}$$

[1] The spin operator $\mathbf{s} = \frac{1}{2}\boldsymbol{\sigma}$ for the spin-$\frac{1}{2}$ particle is composed by the Pauli-Spin-matrices. For the polarization vector follows $\vec{P} =< \boldsymbol{\sigma} >$.

The magnetic cross section is frequently attributed to a Fourier transformation of the spin-correlation function $S_{\alpha\beta}(\vec{Q},\omega)$, see literature [189].

Equation (3.5) can be simplified in combination with Equation (3.13) to

$$\left(\frac{d^2\sigma}{d\Omega dE_f}\right) = \frac{k_f}{k_i} r_0^2 F^2(\vec{Q}) \sum_{\alpha\beta} \left(\delta_{\alpha\beta} - \frac{Q_\alpha Q_\beta}{|\vec{Q}|^2}\right) S_{\alpha\beta}(\vec{Q},\omega). \tag{3.14}$$

Here, $F(\vec{Q})$ is the magnetic form factor and r_0 the classical electron radius. The spin-correlation function is proportional to the imaginary part of the dynamic magnetic susceptibility, according to the fluctuation-dissipation theorem:

$$S_{\alpha\beta}(\vec{Q},\omega) \propto \frac{1}{1 - exp(-\hbar\omega/k_B T)} Im\chi_{\alpha\beta}(\vec{Q},\omega). \tag{3.15}$$

If the magnetic cross section is separated in a polarization analysis, the magnetic susceptibility can be directly calculated.

Nuclear Incoherent Scattering

When neutrons are scattered by atom cores with spin $I \neq 0$ and magnetic contributions of the electron shell are neglected, Equation (3.6) is reduced to

$$U_l^{s_i s_f} =< s_f | b_l + B_l \mathbf{I}_l \cdot \boldsymbol{\sigma} | s_i > . \tag{3.16}$$

By utilizing Pauli-Spin-matrices it follows

$$U_l^{s_i s_f} = p_l \cdot \begin{cases} b_l + B_l \mathbf{I}_{l,z}, & \begin{cases} + \rightarrow + & \text{Non-Spin-Flip} \\ - \rightarrow - & \text{Non-Spin-Flip} \end{cases} \\ B_l(\mathbf{I}_{l,x} + i\mathbf{I}_{l,y}), & \begin{cases} + \rightarrow - & \text{Spin-Flip} \\ - \rightarrow + & \text{Spin-Flip.} \end{cases} \end{cases} \tag{3.17}$$

The coherent scattering length b_l vanishes for purely incoherent scattering and one obtains for the scattering cross section per atom in thermal equilibrium with $< I_x^2 >=< I_y^2 >=< I_z^2 >= \frac{1}{3} I(I+1)$

$$\frac{d\sigma}{d\Omega}^{\text{Non-Spin-Flip}} = \frac{1}{3} < B^2 I(I+1) > \tag{3.18}$$

$$\frac{d\sigma}{d\Omega}^{\text{Spin-Flip}} = \frac{2}{3} < B^2 I(I+1) > . \tag{3.19}$$

1/3 of the total spin-incoherent scattering intensity is measured in the non-spin-flip channel and 2/3 in the spin-flip channel.

$\vec{P}$	Spin-Flip	Non-Spin-Flip
$\vec{P}\parallel\vec{Q}$	$\sigma_{mag} + \frac{2}{3}\sigma_{\mathrm{inc}} + \sigma_U$	$\sigma_{coh} + 0\sigma_{mag} + \frac{1}{3}\sigma_{inc} + \sigma_U$
$\vec{P}\perp\vec{Q}$	$\frac{1}{2}\sigma_{mag} + \frac{2}{3}\sigma_{\mathrm{inc}} + \sigma_U$	$\sigma_{coh} + \frac{1}{2}\sigma_{mag} + \frac{1}{3}\sigma_{inc} + \sigma_U$

Table 3.1.: Comparison of magnetic contributions σ_{mag}, coherent contributions σ_{coh}, and incoherent contributions σ_{inc} to the total scattering intensity for different polarization directions in a spin-flip or non-spin-flip mode. σ_U accounts for the background scattering.

3.5.3. Separation of Magnetic and Nuclear Contributions

The magnetic contributions σ_{mag}, coherent contributions σ_{coh}, and incoherent contributions σ_{inc} to the total scattering intensity for different polarization directions in a spin-flip or non-spin-flip mode can be summarized as done in Table 3.1.

Therefore, the magnetic contribution can be separated by

$$\frac{d\sigma}{d\Omega}_{mag} = 2\left(\frac{d\sigma}{d\Omega}_{\perp}^{\text{Non-Spin-Flip}} - \frac{d\sigma}{d\Omega}_{\parallel}^{\text{Non-Spin-Flip}}\right) \tag{3.20}$$

$$= 2\left(\frac{d\sigma}{d\Omega}_{\parallel}^{\text{Spin-Flip}} - \frac{d\sigma}{d\Omega}_{\perp}^{\text{Spin-Flip}}\right) \tag{3.21}$$

from all other contributions.

4. Crystal Structure of $La_{2-x}Sr_xCoO_4$

The doping and temperature dependence of structural parameters in $La_{2-x}A_xCoO_{4+\delta}$ with A = Ba, Sr, Ca was investigated by means of powder x-ray diffraction, single-crystal x-ray diffraction, and neutron diffraction. With respect to the stability of the crystal structure over a wide Sr doping region ($0.05 \leq x \lesssim 1.0$), the influence of chemical pressure and hole doping is determined in detail and provides valuable information about the coupling to spin degrees of freedom and frustration effects in the system. Structural distortions are common in layered perovskites and reduce the lattice symmetry. We investigated the low-temperature orthorhombic (LTO) distortion at low doping levels and the variation of atomic positions on further doping in the high-temperature tetragonal (HTT) phase of $La_{2-x}Sr_xCoO_4$. In particular, Co-O bond-length anisotropies were analyzed accounting for internal structural strains, LTO-phase instabilities, and magnetoelastic coupling. An analysis of the structural degrees of freedom of $La_{2-x}Sr_xCoO_4$ and a comparison to isostructural $La_{2-x}Sr_xCuO_4$ (LSCuO) and $La_{2-x}Sr_xNiO_4$ (LSNiO) gives insight in the anomalies present in layered cobaltates. An anomalous decrease of the Co-O_{apical} bond length near $x \sim 0.4$ and the high-temperature thermal expansion of in-plane and out-of-plane lattice constants at half doping suggest a Co^{3+} spin-state transition.

4.1. Introduction

The $La_{2-x}Sr_xCoO_4$ crystal structure is classified as a single-layered perovskite of the K_2NiF_4-type. The interesting physics of this material class is governed by the presence of multiple degrees of freedom. Within the complex interplay of lattice, spin, and charge degrees of freedom, a rich variety of ordering phenomena like stripe phases [4, 5, 130, 190], checkerboard-like charge order at half doping [6–8, 191], and high-temperature superconductivity in cuprates [161] occur. In particular, the lattice dynamics of cuprates obtained a renewed interest. High-temperature superconductivity is located between the long-range antiferromagnetic order and the metallic state in the generic phase diagram. The influence of fluctuating order in stripe phases [62, 162, 192, 193] and electron-lattice interactions [194–197] on the mechanism of superconductivity is still an open issue. By the comparative study of the doping dependence of structural distortions and lattice dynamics one gains insight into the coupling of the crystal lattice to these phenomena [75, 198–201].

The doped single-layered perovskite systems $La_{2-x}Sr_xMO_{4+\delta}$ (M=Co, Ni, Cu) are structurally, magnetically, and electronically closely related. All undoped parent compounds exhibit an orthorhombic distortion from the tetragonal structure at room temperature. Uniform M-O_6 octahedra-tilt instabilities cause a symmetry reduction from a high-temperature tetragonal (HTT) to a low-temperature orthorhombic (LTO) and a low-temperature tetragonal (LTT) phase at low doping levels. These tilt instabilities are typically ascribed to structural tensile and compressive strains resulting from a bond-length mismatch for quasi close-packed atoms. The parent compound La_2CoO_4 exhibits a strong bond-length mismatch, resulting in the largest LTO distortion in the series [11, 65, 70, 73]. The intercalation of excess oxygen on interstitial sites reduces the internal strains in the system. This is a known problem for layered compounds [202] during the preparation process and leads to topotactic oxidation at room temperature for $La_2CoO_{4+\delta}$ [66]. A-site substitution with Sr or the intercalation of interstitial oxygen δ in the A_2BX_4-type structure varies the bond-length mismatch and phase boundaries are correspondingly shifted. All three parent compounds exhibit long-range antiferromagnetic order in the orthorhombic phase. While the nearest-neighbor interaction between M^{2+} ions (M = Co [11], Ni [127, 203], Cu [204, 205]) combined with a finite interlayer coupling or an Ising-like anisotropy stabilizes the Néel state in the LTO distorted parent compounds, a four-fold symmetry for B-sites is found in charge and spin ordered half-doped compounds (M = Mn [6], Co [7, 8], Ni [206]). Starting with a relatively high optical energy gap of $E_g = 5 - 6$ eV for La_2CoO_4 [13] in comparison to 4 eV in La_2NiO_4 [207] and 2 eV in La_2CuO_4 [208], $La_{2-x}Sr_xCoO_4$ is a charge-transfer insulator which remains insulating up to $x = 1.5$ Sr doping [22]. Within the strong-correlation limit, a natural possibility for a Wigner crystal state is found on the square lattice at half doping for two-dimensional systems [191, 209, 210]. The finite charge-order correlation length in this material class may result from the quenched disorder of the dopant ions and the strong anisotropy of the layered structure [211]. Topological interlayer frustration suppresses three-dimensional long-range order, which could be induced by a monoclinic distortion of the tetragonal unit cell [212]. In the intermediate doping range a phase separation going from a stable Wigner state towards a stripe formation was found in nickelates [191] and cuprates [121]. The influence of elastic effects on the stabilization of stripes was theoretically proposed by Khomskii *et al.* [213]. Additionally, in experiments, the pinning of stripes to lattice instabilities was observed in cuprates [214–216]. So far, little is known about the HTT-LTO phase boundary, the antiferromagnetic coupling at half-doping, and stripe instabilities for $x < 0.5$ in single-layered cobaltates. Especially in the case of cobaltates, this may result from the difficulties with stoichiometry at low doping levels. More detailed analyses of structural parameters and the lattice symmetry of doped single-layered cobaltates are needed to reveal the relation between crystal structure, the doping dependency of the antiferromagnetic coupling, and charge order instabilities.

Particular interest is focussed on cobaltates with Co^{3+} ions because of the possible spin-

states and their influence on the crystal lattice and on the magnetic order. A Co^{3+} spin-state transition was suggested in the three-dimensional analogue, the $LCoO_3$ (L = La, Pr, Nd) perovskites [217]. Susceptibility and thermal expansion measurements [32, 140, 218] on $LaCoO_3$ indicate a thermally driven transition from a non-magnetic insulator with Co^{3+} in the low-spin state ($t_{2g}^6 e_g^0$, $S = 0$) to a paramagnetic insulator with Co^{3+} in the intermediate ($t_{2g}^5 e_g^1$, $S = 1$) or high-spin state ($t_{2g}^4 e_g^2$, $S = 2$). The intermediate-spin state is, however, controversially discussed [33–36]. Unlike the high-spin state, the intermediate-spin state with partially filled e_g band is believed to be Jahn-Teller active [37, 219], but this matter is still under consideration [33, 34, 220–222]. The monoclinic distortion of $LaCoO_3$ found by Maris *et al.* is ascribed to a cooperative Jahn-Teller distortion ($I2/a$) of the rhombohedral structure ($R\bar{3}c$). Calculating structure factors with the given structure parameters, the distortion should be verifiable with standard laboratory powder x-ray diffraction, but, to our knowledge, it was never reported in literature. For review articles with a different experimental points of view see Refs. [223, 224]. Twinning hinders the differentiation of Co-O bond lengths in pseudocubic perovskites.

In the single-layered perovskites the intrinsic difficulty of crystal twinning is less developed. Thus, the influence of the Co^{3+} spin-state degree of freedom is of interest and may be directly differentiated in the charge-ordered phase of this mixed-valence system. The spin arrangement of $La_{1.5}Sr_{0.5}CoO_4$ was suggested to be antiferromagnetic on a strongly frustrated square lattice [7]. Critical frustration between nearest- and next-nearest Co^{2+} neighbors may induce a spin-glass phase with a strongly reduced spin freezing temperature $T_{SO} \approx 30$ K in comparison to the charge-order transition with a very high transition temperature $T_{CO} = 825(27)$ K [8]. Both interactions were proposed to exhibit exchange integrals of equal magnitude accounting for the number of neighbors. The interaction energies of the sublattices cannot be simultaneously minimized and a glass transition temperature is found at low temperatures. Up to now, a detailed analysis of the antiferromagnetic coupling and the influence of the Co^{3+} spin-state degree of freedom at half doping is missing. In addition, the charge ordering in cobaltates is anomalous; short-range charge order with in-plane correlation length $\xi_{\parallel} = 26(2)$ and $\xi_{\perp} = 8.1(7)$ was verified in $La_{1.5}Sr_{0.5}CoO_4$ [8]. Basal and apical oxygens are displaced in Co-O bond directions accompanying the charge-order modulation and following a breathing type-mode of the CoO_6 octahedra. In contrast to the glass-type order, the activation energy of $E_a \sim 6000$ K [27] of the electrical conductivity is surprisingly high. The question arises why static charge correlations are less defined at half doping in contrast to the relative high transition temperature $T = 825(27)$ K. Is there a coupling between the doping dependent changes in the antiferromagnetic exchange on the MO_2 square lattice and the lifting of the LTO distortion, *i.e.* a lifting of the in-plane anisotropies? Depending on the experimental techniques, partly controversial spin-state models were proposed for $La_{2-x}Sr_xCoO_{4+\delta}$ [14, 18, 27, 29–31, 225].

Using different preparation methods, the crystal structure of $La_{2-x}Sr_xCoO_{4+\delta}$ can be stabilized over a wide doping range from $x = 0$ up to $x = 2$ [21], where the nominal Co valence changes by $2 + x$, *i.e.* from 2 to 4. Therefore, it is possible to investigate the doping dependent variation of structural parameters and lattice distortions described in the following in detail.

4.2. HTT-LTO Phase Transition and Structural Parameters ($0.05 \leq x \leq 1.1$)

4.2.1. HTT-LTO Transition in Layered Compounds

The lattice parameters and the LTO distortion of $La_{2-x}Sr_xCoO_4$ ($0.05 \leq x \leq 1.1$) were determined by x-ray powder diffraction. Structural parameters were investigated by using the software program *FullProf* [172] by Rodriguez-Carvajal. The structural phase transition is indicated by the splitting of (h, k, l) and (k, h, l) reflections in $Bmab$ notation, going from tetragonal to orthorhombic symmetry. Due to a better resolution at high diffraction angles, the highly-indexed reflections should be chosen to analyze the phase transition. As in nickelates, the (400)/(040) reflections near $2\theta \sim 69°$ are superposed by (208)/(028) reflections [126]. A peak-width analysis of the (200)/(020) splitting in combination with the analysis of the criteria of fit for $Bmab$ and $I4/mmm$ symmetry of the LTO and HTT phases enables the phase determination. To determine the instrumental peak broadening through U, V, W parameters in the Caglioti formula [182], calibration measurements with Si powder samples were carried out. The temperature dependence of the lattice parameters and the HTT-LTO transition temperature were investigated with a Siemens D5000 diffractometer using Cu K_α radiation. With the combined usage of a ^{4}He evaporation cryostat and a *Paar* high-temperature camera, the temperature region 10 K $\leq T \leq$ 1050 K is covered.

Fig. 4.1 shows the orthorhombic splitting ϵ of $La_{2-x}Sr_xCoO_4$ at low doping levels. Doping the parent compounds La_2MO_4 (M=Co, Cu, Ni) with Sr reduces the orthorhombic strain and the HTT phase is stabilized. In comparison to the nickelate [126] and cuprate system [81], no linear dependence between orthorhombic splitting and doping can be seen. In agreement with the size of the orthorhombic distortion of the parent compounds, the LTO-HTT phase boundary is shifted to higher doping levels.

First, to understand the effect of Sr doping, the orthorhombic distortions of the undoped compounds will be considered. The LTO distortions in the parent compounds of the $La_{2-x}Sr_xMO_4$ (M=Co, Cu, Ni) series were studied in [11, 125, 226] (see Fig. 4.10). The crystal structures in Ni and Cu samples were investigated by neutron powder diffraction and the effect of interstitial oxygen was analyzed in detail. Table 4.1 gives a comparison of available structure parameters of the parent compounds. All undoped parent compounds exhibit the LTO distortion with $Bmab$ symmetry already at room

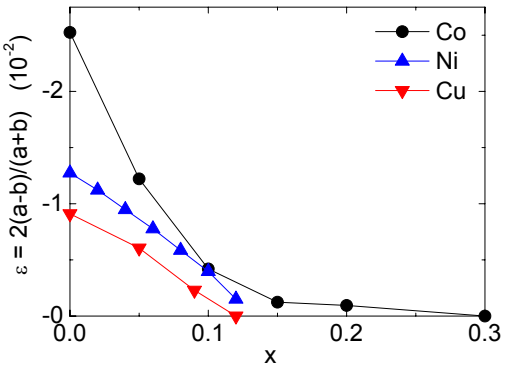

Figure 4.1.: Orthorhombic splitting ϵ in $La_{2-x}Sr_xMO_4$ (M = Co, Ni, Cu) at low doping levels. Cobaltate lattice constants for $x = 0$ are taken from Yamada *et al.* [11] and for $x > 0$ from Haider [94]. For comparison, room temperature data for Ni [126] and Cu [70, 226] are shown.

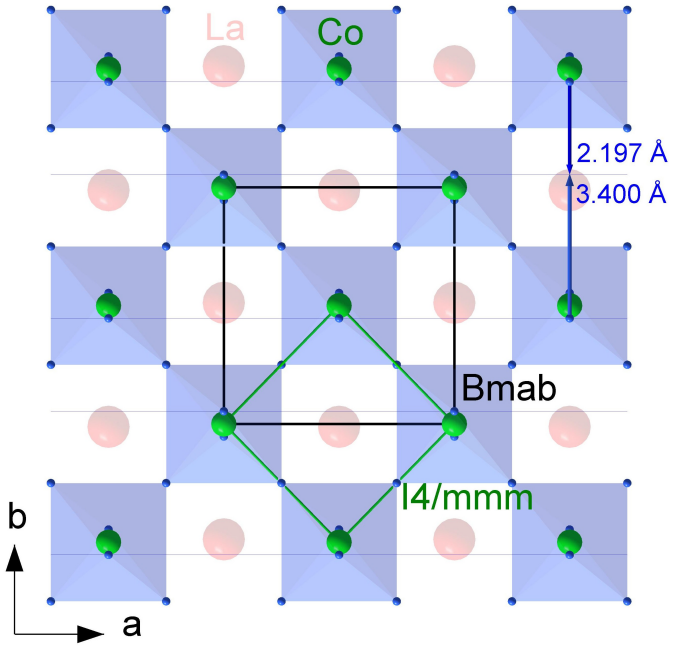

Figure 4.2.: *ab*-plane of La_2CoO_4 in *Bmab* setting at room temperature (atomic positions are taken from [65]). The unit cell of the undistorted structure with $I4/mmm$ symmetry is represented in green, the orthorhombic unit cell in black. The apical oxygen ions of the in *b*-direction tilted CoO_6-octahedra are connected by blue lines. The tilting angle Θ is calculated to 7°. The *b*-axis is consecutively reduced with increasing Sr doping, as the octahedra tilting is vanishing.

Compound	La_2CoO_4 [65]	La_2NiO_4 [73]	La_2CuO_4 [70]	Sr_2RuO_4 [227]
T (K)	RT	250	RT	RT
Symmetry	$Bmab$	$Bmab$	$Bmab$	$F4/mmm$
a (Å)	5.46(1)	5.4499(2)	5.357	5.4744
b (Å)	5.598(1)	5.5275(2)	5.406	-
c (Å)	12.66(3)	12.5118(3)	13.148	12.7397
$\epsilon = (a-b)/(a+b)$	-0.01266	-0.0071	-0.0045	-
$\overline{MO}_{basal}$	1.9621	1.9442	1.904	1.9355
$\overline{MO}_{apical}$	2.301	2.235	2.410	2.0599
$\Delta\overline{MO}/\overline{MO}_{basal}$	0.173	0.15	0.266	0.064
Θ (°)	7	6	3	-
$t = \frac{r_A+r_O}{\sqrt{2}\cdot(r_B+r_O)}$	0.862	0.885	0.868	0.92

Table 4.1.: Comparison of the structure parameters of single-layered perovskite systems. The octahedra tilting angle Θ refers to the out-of-plane oxygen O_{apical} displacement.

temperature [65, 70, 71, 73, 75, 79], where MO_6-octahedra are tilted in the direction of the face diagonal of the HTT unit cell. The anticooperative tilting of corner-sharing octahedra is represented by blue arrows in Fig. 2.4. By the distortion of the octahedra in the displacement, namely the elongation in direction of the apical oxygen ion O_{apical}, the expected shortening of the b lattice constant in orthorhombic $Bmab$ setting is overbalanced. This can be related to the displacement of the La^{3+}/Sr^{2+} ions in the LTO phase and the accompanied displacement of O_{apical} in the anisotropic La coordination, see Fig. 2.5. It follows that $a < b < c$. Since Cu^{2+} $3d^9$ is strongly Jahn-Teller active, the Cu-O bond-length anisotropy and the c/a ratio is significantly enhanced for cuprates. This effect has to be accounted for when discussing structural strains via the bond-length mismatch. All systems show a strong deviation of the tolerance factor from the ideal value. An undoped single-layered perovskite showing no tilt or rotational octahedron distortion away from the ideal tetragonal structure is Sr_2RuO_4. This may be ascribed to the smaller bond-length mismatch between Sr-O and Ru-O (see Tab. 4.1). The structure was investigated by Vogt *et al.* using neutron powder diffraction in the temperature region $0.24 \leq T \leq 295$ K [227]. No long-range structural distortions are present in this temperature region, but the authors report a structural anomaly for the c/a ratio in $I4/mmm$ notation of the HTT phase at the metal-insulator transition at $T = 100$ K. Furthermore, this anomaly was disapproved by a later work. Superstructure reflections, which would indicate a breaking of the lattice symmetry, as well as anomalies in the Ru-O bond-length variation and in the atomic displacement parameters down to 20 K are not observed [228].

The magnitude of the orthorhombic distortion $\epsilon = (a-b)/(a+b)$ and, concomitant, the MO_6 octahedra tilting angle Θ decrease with increasing atomic number of the transition metal ion. The linear-quadratic coupling of ϵ to the order parameter in the fourth-order expansion of the Ginzburg-Landau free energy results in a linear dependence between orthorhombicity and temperature. The variation of ionic radii through doping shifts the HTT/LTO transition temperature systematically, thus one could expect a nearly linear decrease of ϵ at room temperature. The observed deviations for cobaltates are due to an additional mechanism or off-stoichiometry. Of particular importance, for the size of the orthorhombic distortion, is the intercalation of excess oxygen δ in the crystal structure of $La_{2-x}Sr_xCoO_{4+\delta}$ at low doping levels, as discussed in Sec. 2.1.3. Excess oxygen ions on interstitial sites reduce the orthorhombic splitting of the system as long as they do not order. The sample stoichiometry for $0.2 \leq x \leq 1.0$ was investigated by atomic absorption spectroscopy measurements and single-crystal x-ray diffraction. A possible influence of excess oxygen in the powder samples has to be taken into account. From a 'steric' point of view, the HTT-LTO transition would be just slightly increased, since the maximum of incorporable oxygen (δ_{max}) in $La_{2-x}Sr_xCuO_{4+\delta}$ and $La_{2-x}Sr_xNiO_{4+\delta}$ is systematically decreasing with increasing x [126, 134].

4.2.2. Temperature Dependence of the LTO Superstructure Reflections

The temperature dependence of the CoO_6 tilt instability was investigated by single-crystal x-ray diffraction. The symmetry reduction from $I4/mmm$ to $Bmab$ is accompanied by an enlargement of the crystallographic unit cell and superstructure reflections in the reciprocal space are induced. According to the series expansion of the LTO phase transition, the expected superstructure intensity couples quadratically to the order parameter $I \propto Q_2^2$. In particular, superstructure reflections ($h/2$, $k/2$, l) in HTT notation with h, k odd, l even and $l > 0$ are expected to arise in the LTO distorted phase with $Bmab$ symmetry. Depending on the individual structure factor, weak superstructure reflections should be observable in a single-crystal x-ray diffraction experiment for longer counting times. Precession maps at $T = 100$ K and $T = 300$ K were calculated from two single-crystal x-ray datasets for the LTO distorted $x = 0.2$ compound with identical collection strategies. The precession method refers to the undistorted mapping of reciprocal lattice layers, *i.e.* the projection of the dataset on selected symmetry layers. To verify LTO superstructure reflections, the intensities in the (h, k, l) layers were calculated with constant l. $\lambda/2$ contamination with typical 0.15 % intensity in comparison to the main structure reflection was found at small $\mathbf{Q}$ values [176]. Fig. 4.3 shows the temperature dependence of the (h, k, 6) layer for a standard experiment used to determine the main structure. The exposure times were 30 s per frame up to $2\theta = 144.62$ ° with a redundancy of ~ 4 at higher diffraction angles. The map accounts all measured $(h, k, 6)$ reflections projected in a 512x512 pixel area. A cut-off intensity of just 200 counts was chosen to visualize weak reflections. Significant superstructure reflections are found only

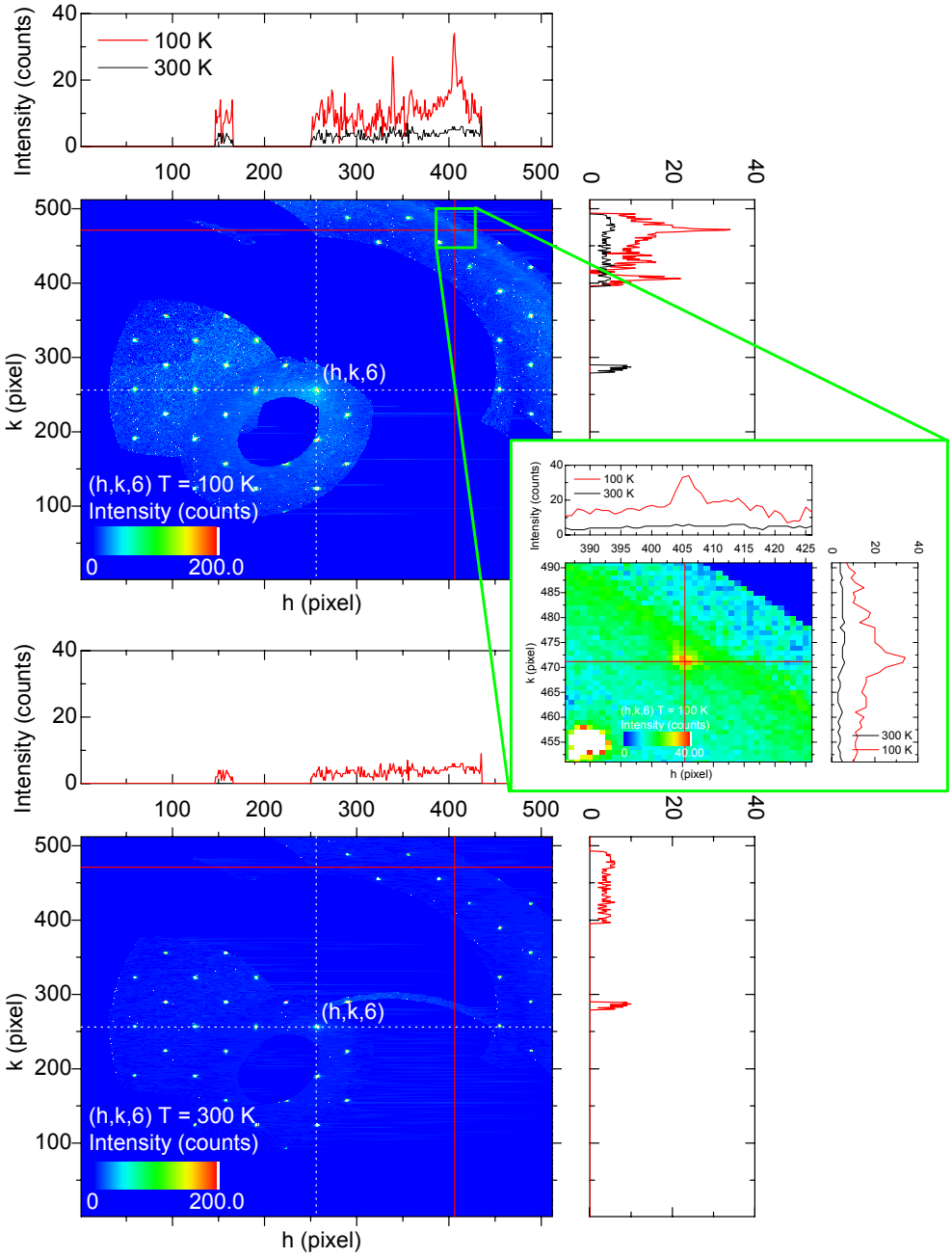

Figure 4.3.: Temperature dependence of the weak LTO superstructure peak (4.5, 6.5, 6) in the (h, k, 6)-plane of $La_{1.8}Sr_{0.2}CoO_4$ from a long-run experiment using a specimen of nearly spherical shape, 140 μm in diameter.

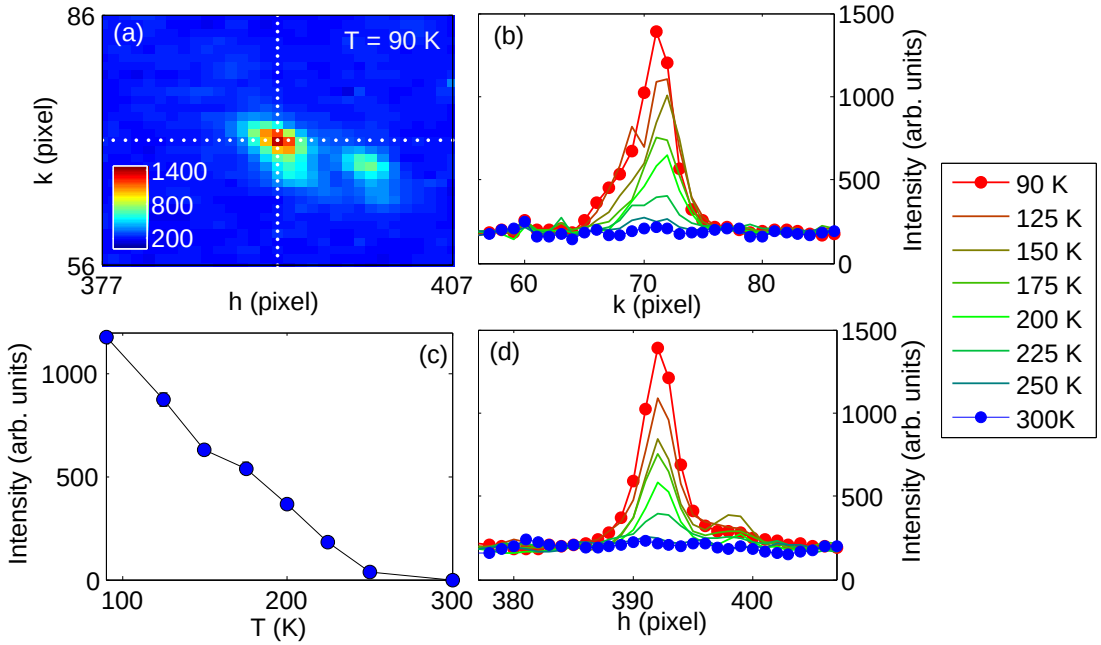

Figure 4.4.: Temperature dependence of the orthorhombic superstructure peak (2.5, 8.5, $\overline{2}$) of $La_{1.7}Sr_{0.3}CoO_4$. (a) The two-dimensional contour plot shows two peak contributions due to a mixture of $K_{\alpha 1}$ and $K_{\alpha 2}$ radiation. Vertical (b) and horizontal (d) scans across the $K_{\alpha 1}$ maximum are shown for different temperatures below and above the HTT/LTO phase transition. (c) Temperature dependence of the maximal peak intensity with subtracted background contribution.

at large $\mathbf{Q}$ values. Small additional scan regions at $T = 300$ K are due to orientational matrix scans and do not contribute to superstructure reflections. Red lines represent slices through the reciprocal lattice across (4.5, 6.5, 6) and the corresponding intensity graphs are given at the border. In comparison, a (4.5, 6.5, 6) contribution is only found at $T = 100$ K. This result is surprising, as the HTT-LTO transition temperature is expected near $T \sim 440$ K from powder x-ray diffraction (see Fig. 4.12). This may be due to an insufficiently small sample size and due to low contributions from the small CoO_6 octahedron tilt to the scattering factor; as expected, oxygen contributions to the total x-ray scattering are weak in comparison to the more electron dense atoms.

In order to investigate the LTO distortion in $x = 0.3$, a large single crystal (volume-factor 3000 larger in comparison to the typical sample size of $r = 35$ μm) was prepared for orientated scans with counting times of 120 s at a small detector distance of $dx = 37.5$ mm. The [2,0,0] direction was set perpendicular both to the x-ray beam and

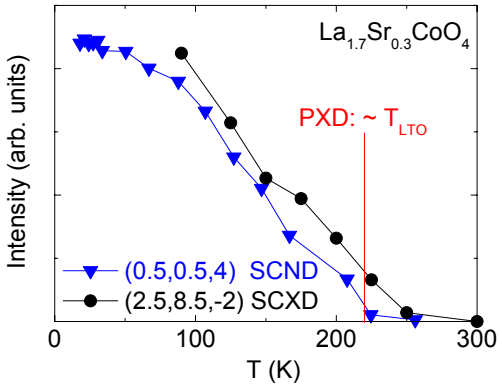

Figure 4.5.: LTO transition temperature in $La_{1.7}Sr_{0.3}CoO_4$, estimated by single-crystal x-ray diffraction (SCXD), single-crystal neutron diffraction (SCND) measurements, and the analysis of the orthorhombic distortion $\epsilon = (a-b)/(a+b)$ in powder x-ray diffraction (PXD) measurements.

the detector direction. The intensity was integrated using a ω-scan of 2° with a fixed detector 2θ position. The observed temperature dependence of a (2.5, 8.5, -2)$_{tetr}$ reflection is shown in Fig. 4.4. Panel 4.4 (a) represents a section of the CCD-detector image with 512x512 superpixel resolution. Beside the calculated reflection position, marked by dotted lines, the $K_{\alpha 2}$ contribution is found. Panel (b) and (d) illustrate vertical and horizontal cuts across (2.5, 8.5, -2)$_{tetr}$ for different temperatures down to liquid nitrogen temperature, limited by the *KryoFlex* stream. The temperature dependence is in agreement with the onset of orthorhombic splitting near $T \sim 220$ K from powder x-ray diffraction measurements (see Fig. 4.5 and Fig. 4.11) with respect to the experimental resolution and the energy window of the x-ray diffractometer. The reflection corresponds to (6, 11, -2) indices, since (11, 6, -2) is forbidden for *Bmab* symmetry. The superstructure intensity is expected to couple quadratically or $\mathbf{Q}_{LTO} \propto (T - T_{LTO})^{2\beta}$ to the order parameter $\mathbf{Q}_{LTO}$ near the phase transition. Owing to a possible Gauss-broadening at the transition temperature due to sample inhomogeneities, the decline may be smeared out. This is similar to the observed temperature dependence of LSCuO [229], where fluctuations are important near the phase transition.

4.2.3. Doping Dependence of Lattice Parameters at Room Temperature

The lattice parameters of $La_{2-x}Sr_xCoO_4$ ($0.05 \leq x \leq 1.1$), shown in Fig. 4.6, at room temperature, determined by the Rietveld method, are in qualitative agreement with literature data [11, 22, 65, 94, 210]. The estimated standard deviations of the least-square refined values lie within the point size. Below $x < 0.3$ the LTO phase with *Bmab* symmetry is stabilized, as discussed in the previous section. Here, the precise doping level of the HTT/LTO phase transition at room temperature is of particular importance for the ascription of structural anomalies. As mentioned before, the LTO phase can be identified in the powder diffractograms by the $(110)_{\mathrm{HTT}}$ splitting or line-width increment to

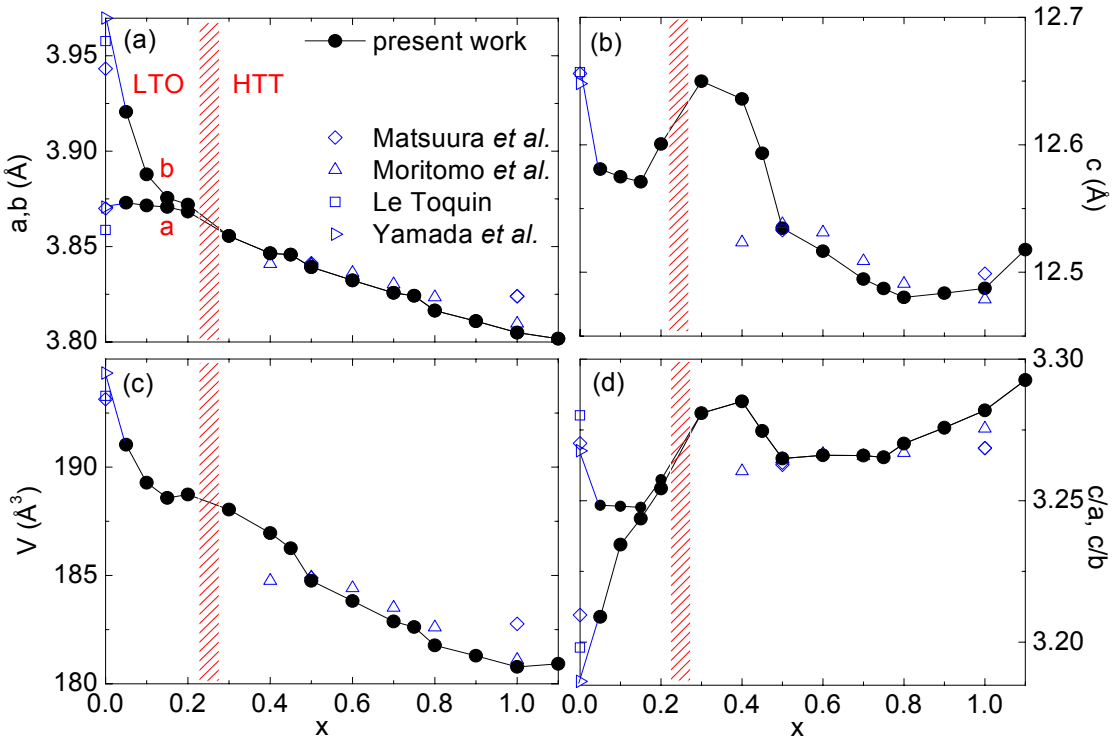

Figure 4.6.: Lattice parameters of $La_{2-x}Sr_xCoO_4$ ($0.05 \leq x \leq 1.1$) at room temperature in $I4/mmm$ notation. For comparison, literature data from [11, 22, 65, 210] are included. For $x < 0.3$, the LTO distortion with $Bmab$ symmetry and $a < b$ is stabilized. Corresponding orthorhombic lattice constants are shortened by a factor $1/\sqrt{2}$. Data for $x < 0.3$ were measured and refined by M. Haider [94]. The dashed region represents the proposed HTT-LTO phase transition at room temperature.

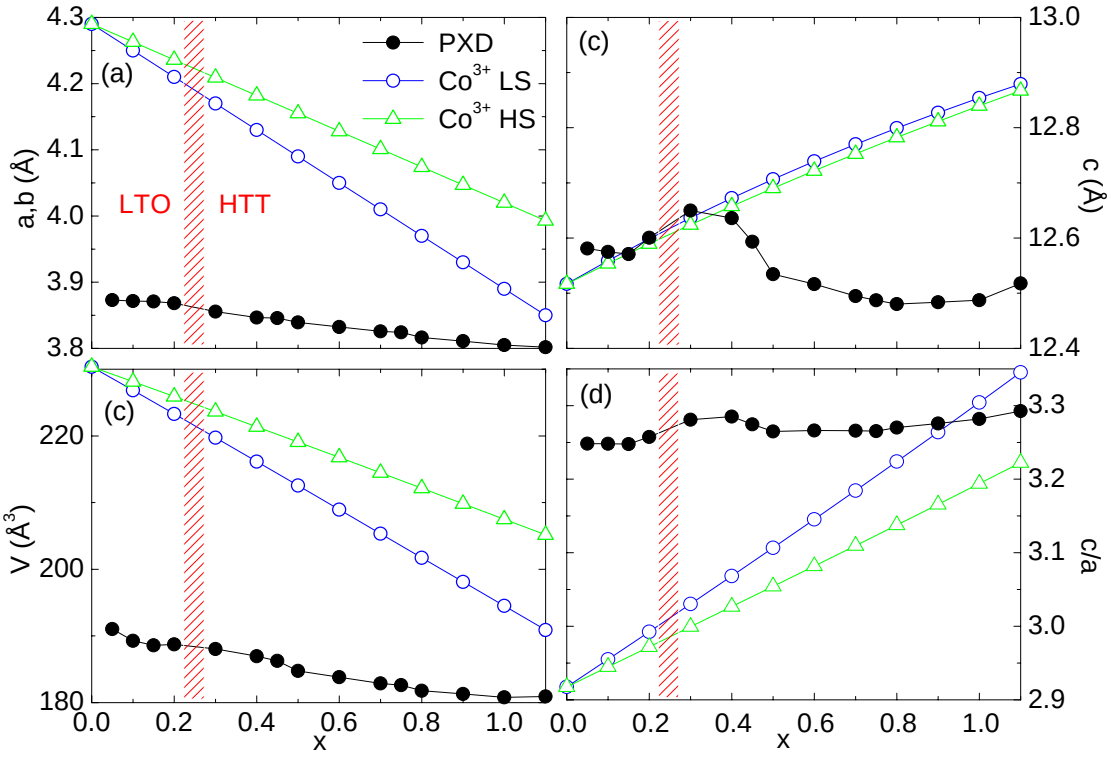

Figure 4.7.: Comparison of lattice constants of $La_{2-x}Sr_xCoO_4$ with an ionic estimation. Basis of this estimation is the undistorted tetragonal structure with $I4/mmm$ symmetry assuming Co^{3+} in the high-spin and low-spin state, respectively (Co^{2+} is always in the high-spin state). The ionic radii are taken from [54].

$(200)_{LTO}$ and $(020)_{LTO}$[1]. The phase transition was also examined through the analysis of the sample dependent linewidth. This analysis of the resolution convoluted linewidth broadening was compared with a Si standard, which provides information about the angle dependence of the instrumental resolution function. The LTO distortion is fully suppressed at $x = 0.3$. For better comparison to the HTT phase, with $I4/mmm$ symmetry above $x = 0.2$, the orthorhombic a and b lattice constants were shortened by $1/\sqrt{2}$.

As expected, the unit cell volume decreases with increasing strontium content up to

[1]Miller indices and lattice constants of the HTT phase are given in the standard setting $I4/mmm$ of space group No. 139. The HTT space group notation in literature often refers to $F4/mmm$, where a,b are rotated by 45° and elongated by $\sqrt{2}$ in comparison to $I4/mmm$. Superstructure reflections with $h + l = 2n$ or h, k odd and l even but $l \neq 0$ ($n \in \mathbb{Z}$) arise below the LTO phase transition with $Bmab$ symmetry.

$x = 1.0$, due to the variation of ionic radii when accounting quasi close-packed spheres. La^{3+} ions are substituted by larger Sr^{2+} ions (see Table 4.2), but concomitantly, the nominal Co-valence v_{Co} changes to $v_{Co} = 2 + x$ by hole doping. Overall, the change in the average Co-ion radius overbalances the changes on the A-site with respect to both Co^{3+} high-spin and Co^{3+} low-spin occupation. To give a first estimation for the internal strains in the systems, the calculated and measured lattice constants are compared in Fig. 4.7. The calculation assumes symmetry constraints of the HTT phase. Due to the smaller ionic La^{3+}/Sr^{2+} radii, in-plane lattice dimensions are defined by the doubled Co-O bond length. The c-value was calculated by $c = 2 \cdot \text{Co-O} + 2 \cdot \text{La-O} + 2\sqrt{\text{La-O}^2 - \text{Co-O}^2}$, where the last addend considers the mismatch between adjacent LaO and CoO_2 layers. For the ideal layered structure with $\text{La-O} = \sqrt{2} \cdot \text{Co-O}$ and $2 \cdot \text{Co-O} = a$ it follows $c = (2 + \sqrt{2}) \cdot a$. Clear deviations, pointing to strain distortions, are seen in the a lattice constant, which is shortened for all doping levels. The sum of changes in La^{3+}/Sr^{2+} and Co^{2+}/Co^{3+} ionic radii tends to increase the out-of-plane lattice constant. While the increase of c is observed at low doping levels, a steep decrease occurs near $x = 0.45$. Overall, the lattice volume V decreases, but stays well below the expectation value with constraints to a HTT phase. As discussed in Sec. 2.1, the bond-length mismatch and the LaO layer repulsion, immanent in the single-layered perovskite structure, are expected to cause some internal strain in the system. Further insight in the nature of the internal strains in cobaltates will be obtained from the analysis of the bond-length anisotropies.

Anomalies can be identified by separating LTO distortional effects. While the orthorhombic splitting $\epsilon = (a - b)/(a + b)$ vanishes at $x = 0.3$, the HTT in-plane lattice constant decreases monotonically upon further doping. Since the b-axis indicates the CoO_6 tilt direction, as shown for La_2CoO_4 in Fig. 4.2, it exhibits the largest changes ($a < b < c$ in $Bmab$ notation). The HTT a-axis represents the doubled Co-O bond length and decreases through the nominal electron removal on Co-sites. Two remarkable anomalies are seen in the c-axis doping dependence: the steep drop near $x = 0.45$ and the increase above $x = 0.8$. The lifting of the tilting distortion in case of rigid octahedra would lead to a maximum near the LTO-HTT phase transition, but the reduction of internal strains is expected to be uniform. Before discussing the anomalies in detail, we can ascribe these to the instabilities found in other Sr doped single-layered perovskites. The structural aspects of strontium doping in the single-layered perovskite system $La_{2-x}Sr_xMO_4$ (M = Co, Cu, Ni) were examined in literature.

The orthorhombic distortion for the parent compound La_2CoO_4 amounts to $\epsilon = (a - b)/(a + b) = -0.0126$, according to lattice constants from Yamada *et al.* [11]. This is in good agreement to $\epsilon = -0.0127$ from single-crystal neutron diffraction measurements determined by Le Toquin [65][2]. The CoO_6-octahedra tilting angle Θ is 7° (see Fig. 4.2),

[2] In comparison, the absolute values of the lattice constants differ in the given references, but the orthorhombic distortions are coinciding. Aberrations from stoichiometry are expected to affect the cooperative octahedra tilting and therefore ϵ. Differences in absolute values may result from wavelength

Ion	CN	Closed shell r (Å)	High-spin state r_{HS} (Å)	configuration	Low-spin state r_{LS} (Å)	configuration
La^{3+}	IX	1.216				
Ca^{2+}	IX	1.18				
Sr^{2+}	IX	1.31				
Ba^{2+}	IX	1.47				
Co^{2+}	VI	-	0.745	$t_{2g}^5e_g^2$, $S = 3/2$	0.650	$t_{2g}^6e_g^1$, $S = 1/2$
Co^{3+}	VI	-	0.610	$t_{2g}^4e_g^2$, $S = 2$	0.545	$t_{2g}^6e_g^0$, $S = 0$
Ni^{2+}	VI	-	0.690	$t_{2g}^6e_g^2$, $S = 1$	-	
Ni^{3+}	VI	-	0.600	$t_{2g}^5e_g^2$, $S = 3/2$	0.560	$t_{2g}^6e_g^1$, $S = 1/2$
Cu^{2+}	VI	-	0.730	$t_{2g}^6e_g^3$, $S = 1/2$	-	
O^{2-}	VIII	1.42				

Table 4.2.: Comparison of the ionic radii with coordination number CN in $La_{2-x}A_xMO_4$ (A = Ca, Sr, Ba; M = Co, Ni, Cu)) from [54]. In case of non-closed shell configuration, ionic radii are given for high-spin (HS) and low-spin (LS) states. The discussion of a Cu^{3+} spin contribution in LSCuO is inadequate, as a so-called Zhang-Rice singlet is formed [230].

calculated by the displacement of the apical oxygen ion O_{apex}. With increasing Sr doping level, the difference between a and b decreases with a decisive decrease of b and vanishes at the phase transition at $x = 0.3$. This is equivalent to the lifting of the cooperative octahedra tilt and a reduction of the octahedral distortion. From a steric point of view, the increase of c with a maximum at the phase transition is induced by the raise of rigid octahedra. As mentioned before, the a lattice constant in the tetragonal phase is twice the size of the Co-O_{basal} bond length. The strictly monotonic decrease in the HTT phase represents the nominal change of the average ionic radius of the cobalt ion.

The coupling of the structure parameters and the LTO/HTT distortion to internal strains or electronic effects of the transition metal ion can be studied by heterovalent or isovalent doping in the single-layered perovskites. Let us now focus on the effect of chemical pressure by the ionic radii variation of the divalent dopant. In order to verify the effect of chemical pressure on the anomalous decrease of the c-axis near $x = 0.4$, additional powder samples of $La_{2-x}A_xCoO_4$ (A = Ca, Ba) near half doping were prepared by M. Benomar [135]. Fig. 4.8 shows the comparison of the measured lattice parameters with literature data. Literature data for Ba samples from Cherepanov *et al.* [92] are in agreement with ours. All samples exhibit the HTT symmetry at room temperature. The lattice constant change for a given doping level belongs to the alkaline-earth ionic radii

gaging in the neutron-scattering experiments and the reduced angle resolution within a four-circle diffractometer experiment.

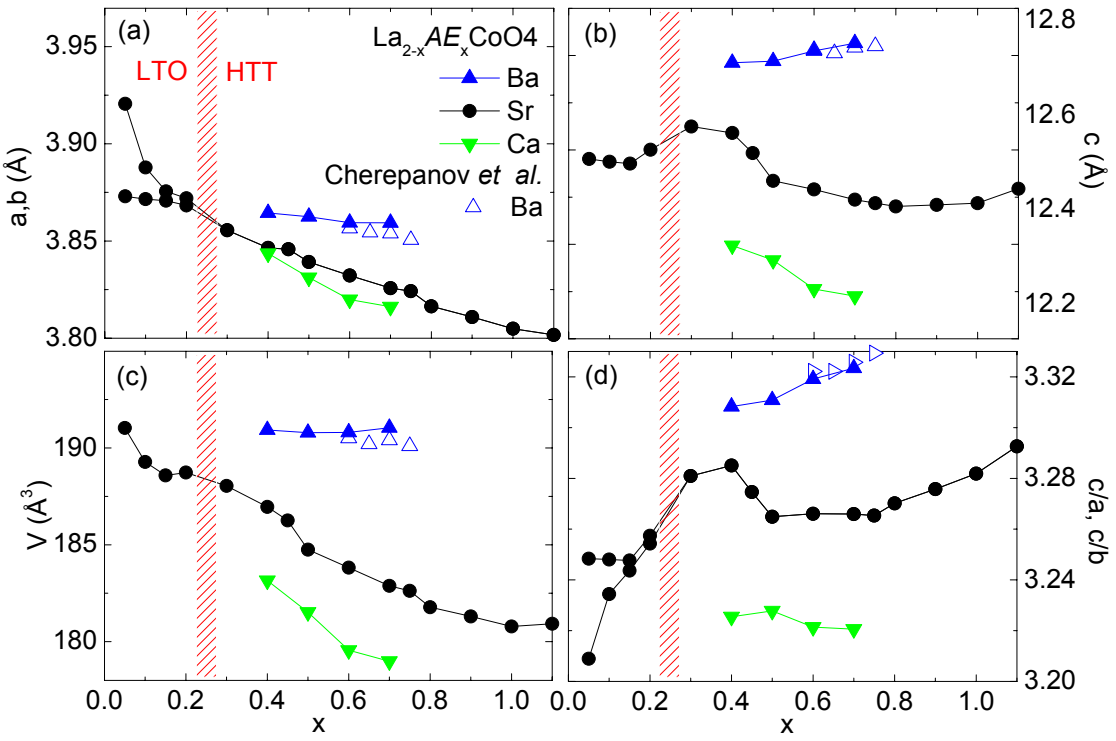

Figure 4.8.: Comparison of the lattice constants of $La_{2-x}A_xCoO_4$ (A = Ca, Sr, Ba) at room temperature in $I4/mmm$ setting with literature data for Ba from [92]. (b) No clear c-axis anomaly is found in Ba and Ca samples in this doping region.

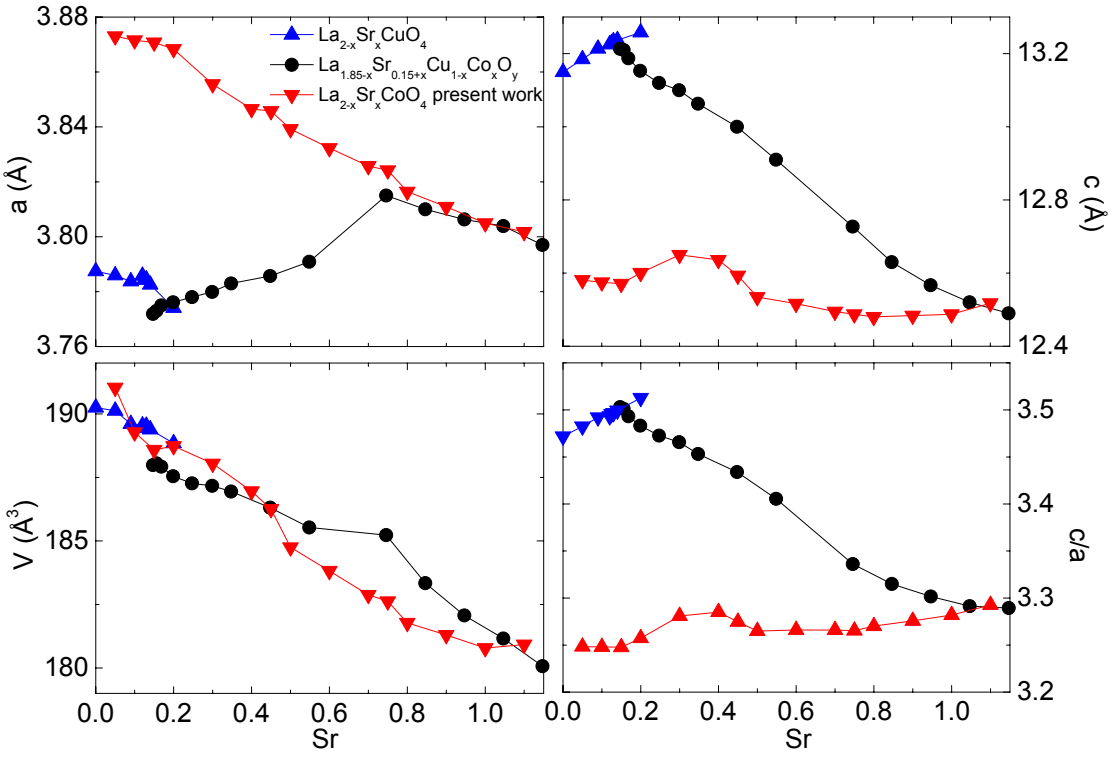

Figure 4.9.: Comparison of lattice constants from co-doped and heterovalent doped cuprates and cobaltates $La_{1.85-x}Sr_{0.15+x}Cu_{1-x}Co_xO_y$ [231].

$r_{Ba} = 1.47$ Å, $r_{Sr} = 1.31$ Å, and $r_{Ca} = 1.18$ Å in ninefold coordination. Interestingly, no indication for an LTO distortion was found for Ca samples, in which an enhanced bond-length mismatch is expected in comparison to $r_{La} = 1.216$ Å. However, the curve progression of Ba and Ca is smooth across half doping with respect to the expected change of the ionic radii, suggesting the reduction or absence of the c-axis anomaly in this doping region. A further investigation of the low- and high-doping region would be very interesting to verify whether the observed anomaly for Sr doped samples is systematically shifted.

A comparison of lattice constants from co-doped and heterovalent doped cuprates and cobaltates $La_{1.85-x}Sr_{0.15+x}Cu_{1-x}Co_xO_y$ [231] is shown in Fig. 4.9. Both the Sr and Co content increases simultaneously in the sample series investigated by Gaojie *et al.*, and therefore, the two systems of Sr doped cuprates and cobaltates are connected. In comparison, the lattice parameters are in good agreement. The increase of a and the decrease of c for $x \leq 0.6$ in $La_{1.85-x}Sr_{0.15+x}Cu_{1-x}Co_xO_y$ at room temperature indicates a significant

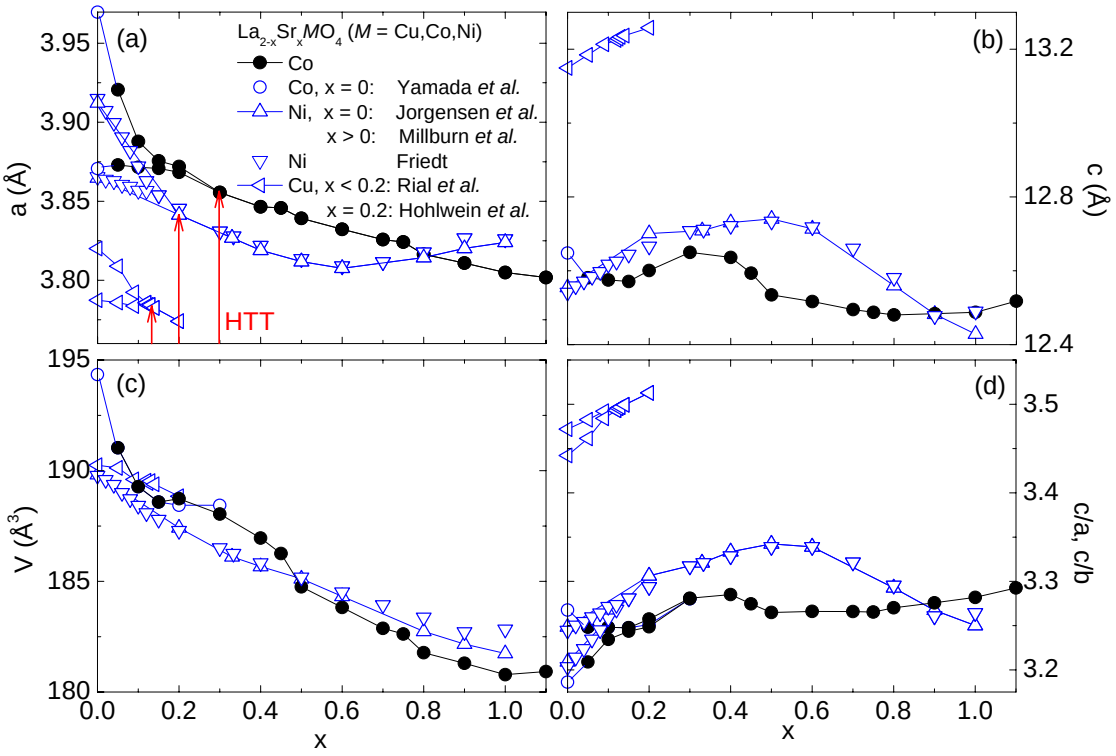

Figure 4.10.: Comparison of the lattice constants of $La_{2-x}Sr_xMO_4$ (M = Co, Cu, Ni) at room temperature in $I4/mmm$ setting. Literature data for Co are taken from [11, 94], for Ni from [125, 232], and for Cu from [202, 226].

reduction of the dominant Jahn-Teller distortion. With the reduction of the octahedra anisotropy, the c/a value decreases. Concomitantly, the authors report an increase of the resistivity for polycrystalline pellets. Beyond $x = 0.6$ the resistivity decreases and the in-plane lattice constant follows the curve progression of $La_{2-x}Sr_xCoO_4$. However, no evidence is found for a c-axis anomaly pointing to the Co^{3+} spin degree of freedom. On the basis of the so far existing data, the $La_{2-x}Sr_xCoO_4$ seems to be unique with the significant structural anomalies in comparison to heterovalent and co-doped cuprates.

A comparison between Sr doped cobaltates, cuprates, and nickelates is shown in Fig. 4.10. The increase of the c-axis constant in the compound with increasing x verifies the reduction of the octahedra tilt. The c value for La_2CoO_4 deviates in literature. This can be associated with the problem to stabilize stoichiometric samples of the pure compound, since it exhibits an unusually fast oxygen transport and spontaneous intercalation of oxygen at room temperature is observed [66]. However, the decrease of the lattice volume

in HTT notation of LSCoO, LSNiO, and LSCuO is similar, although the in-plane and out-of-plane anisotropies differ. A dominant Jahn-Teller distortion in LSCuO leads to a large difference in the lattice constants and, through this, to an enhanced c/a ratio. Neglecting hybridization effects, Ni^{2+} $3d^8$ is not Jahn-Teller active and Co^{2+} $3d^7$, in the high-spin state, is expected to exhibit only a small distortion due to a smaller energy gain in the t_{2g} splitting. This suggests comparable a and c lattice constants of cobaltates and nickelates with respect to ionic radii from Tab. 4.2. For higher Sr doping levels, the increase of a and the decrease of the axial distance above $x = 0.6$ in LSNiO was interpreted as a change in the electronic structure of Ni ions [232]. The orbital character of the occupied states of the e_g levels is proposed to be significantly redistributed from z^2 to $x^2 - y^2$. This agrees with a deviation in the nominal valence calculated in the bond valence sum approach. The volume averages over Jahn-Teller distortions and orbital redistribution making the variation with x comparable to that in cobaltates. An analysis of the Co-O bond-length anisotropy will give insight in the nature of the c axis anomaly in single-layered cobaltates. It is worth to note that the LTO transition is systematically shifted to higher doping levels with increasing atomic number, which has been discussed in Sec. 4.2.1.

4.2.4. Temperature Dependence of Lattice Parameters

Fig. 4.11 shows the low-temperature lattice constants of $La_{2-x}Sr_xCoO_4$ as determined by powder x-ray diffraction in the temperature region $10-300$ K. Small deviations of the PXD data from the room temperature based setup can result from a sample displacement in the helium cryostat or in the high temperature camera. Although this effect is partially accounted for in the refinement process via the displacement parameter d for a $\theta - 2\theta$ diffractometer, the lattice parameters may slightly differ beyond the estimated standard deviation. To compare high, low, and room-temperature measurements systematically, lattice constants were scaled relative to the room temperature values. Systematic experimental errors resulting from d-displacement, sample preparation, and diffractometer calibration were minimized for the long-run room temperature values, as described in Sec. 4.2.3.

The relative changes for the in-plane and out-of-plane lattice constants with temperature are small in comparison to the changes with doping. The LTO b lattice constant for $x = 0.2$ is not shown in Figure 4.11, as the deviation is small. $x = 0.3$ exhibits the HTT-LTO phase transition near $T \sim 220$ K. There were no indications for an LTT phase stabilization in the given temperature region for $x = 0.2$ and $x = 0.3$. No anomalies were found for a further increasing Sr content. The small relative changes of in-plane and out-of-plane lattice constants in this temperature range are similar to the findings in $La_{2-x}Sr_xNiO_4$ (x=0.3,0.4) [233], where the relative changes are $\Delta a = 0.2$ % and $\Delta c = 0.3$ %. This demonstrates the structural proximity of cobaltates and nickelates. While the half-doped cobaltate exhibits the strongest thermal expansion for a by

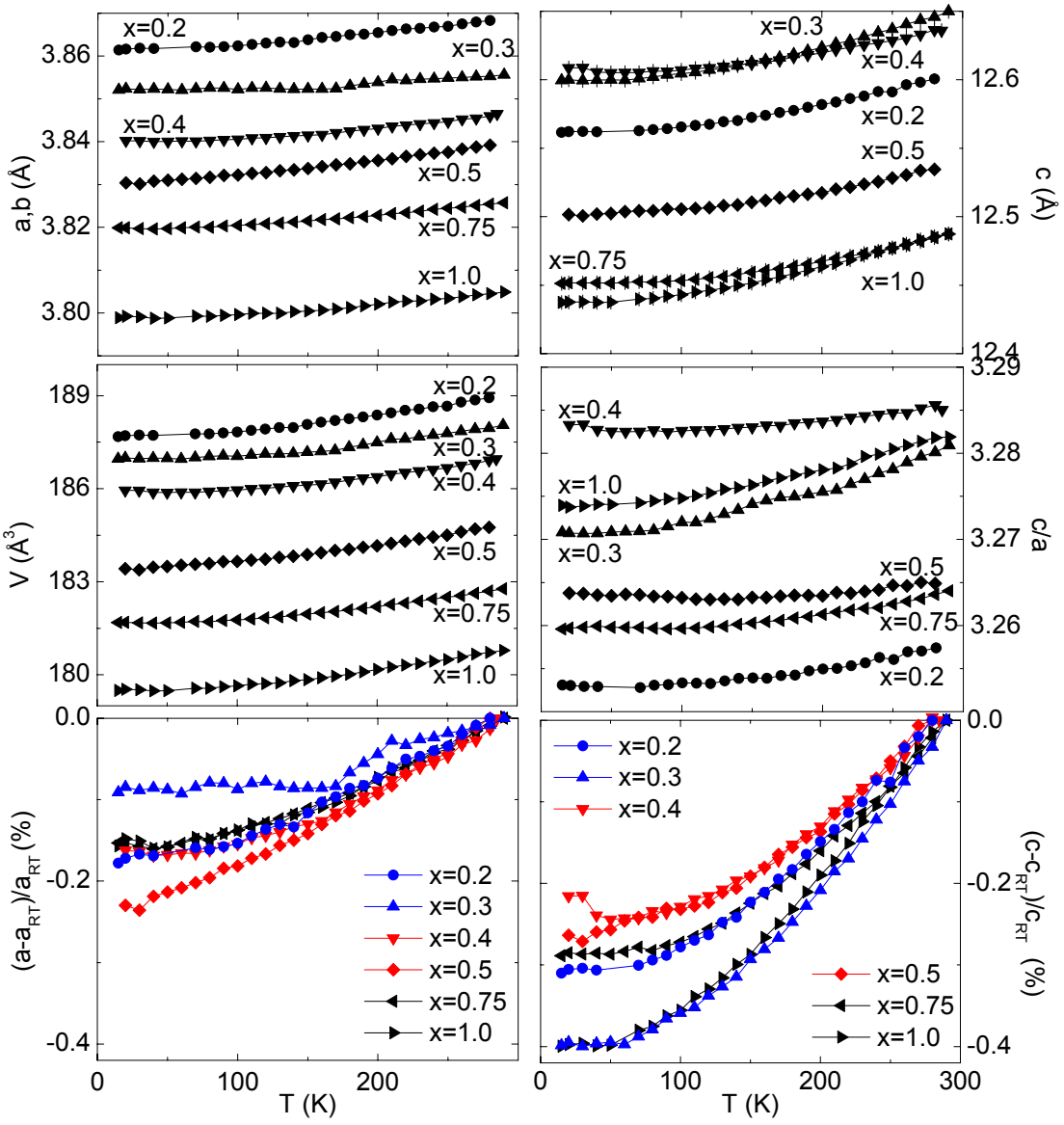

Figure 4.11.: Temperature dependence of the lattice parameters of $La_{2-x}Sr_xCoO_4$ determined by powder x-ray diffraction and neutron diffraction (blue stars) in the temperature region $10-300$ K. Data for $x = 0.2, 0.4, 1.0$ are taken from M. Haider [94].

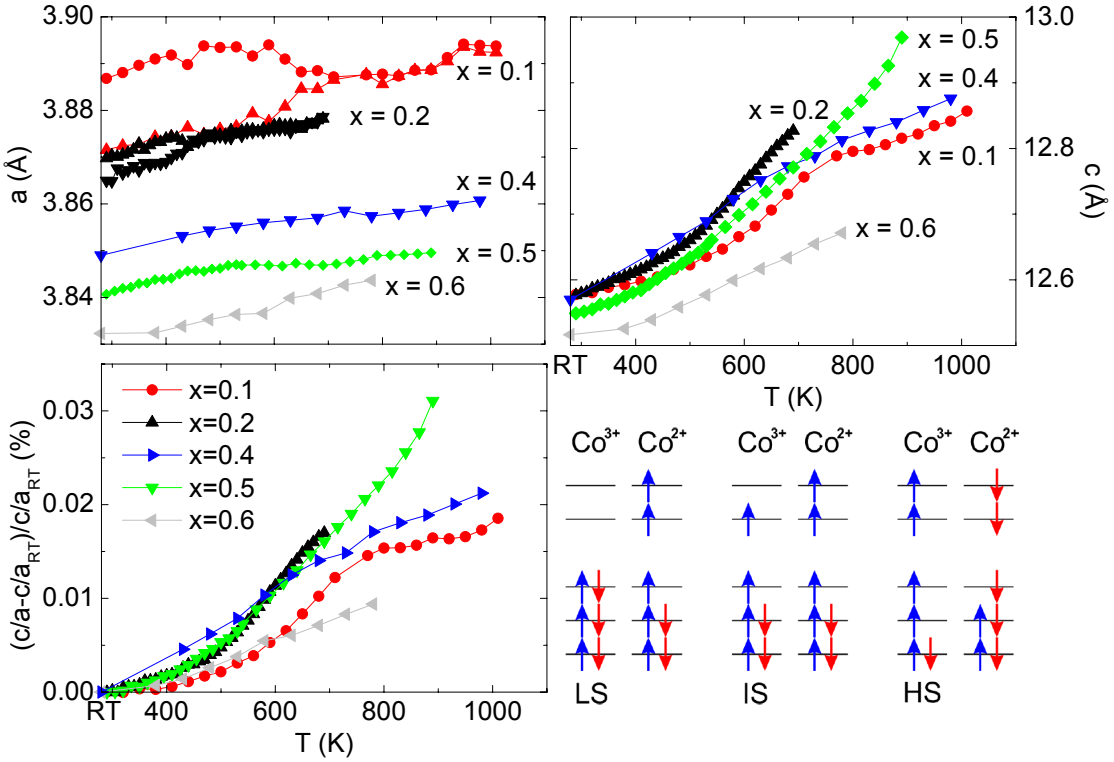

Figure 4.12.: Temperature dependence of the relative lattice parameters of $La_{2-x}Sr_xCoO_4$ determined by powder x-ray diffraction in the temperature region $300 - 1050$ K. Data for $x = 0.1, 0.2, 0.5$ are taken from M. Haider [94]. In the lower right panel possible Co spin states in the system are shown.

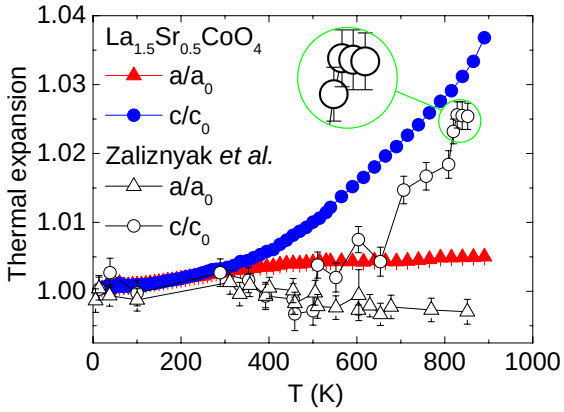

Figure 4.13.: Temperature dependence of the lattice constants in $La_{1.5}Sr_{0.5}CoO_4$ relative to low-temperature values. In comparison to our high-resolution x-ray powder diffraction results, the literature values from single-crystal neutron diffraction on a triple-axis spectrometer, determined by Zaliznyak *et al.*, are shown [8]. A saturation of the c-axis above $T \sim 800$ K was proposed.

~ 0.23 %, it is minimal along the c direction. This effect may be attributed to checkerboard-like charge ordering phenomenon at half doping with a relative high transition temperature $T = 825(27)$ K, proposed in Ref. [8].

Fig. 4.12 shows the high-temperature lattice constants of $La_{2-x}Sr_xCoO_4$. There are no discontinuities in the temperature dependence of a and c in the HTT phase. The HTT-LTO transition for the $x = 0.1$ sample is near $T \sim 700$ K and for the $x = 0.2$ sample near $T \sim 440$ K [94]. While in the $x = 0.4$ and 0.6 compounds a saturation of the c-axis constant is indicated, the increase for $x = 0.5$ is enhanced with increasing temperature. This may be ascribed to an electronic change of the Co^{3+} ions away from the low-spin occupation, as the increase of the in-plane lattice constant becomes less prominent. The possible Co spin states in the system are represented in the lower right panel of Fig. 4.12. A thermal population of the Co^{3+} intermediate-spin or high-spin from a low-spin configuration may be caused by the observed anisotropic changes of the lattice constants. The charge ordering temperature was estimated to be $T_{CO} = 825(27)$ [8] from a extrapolation of the c-axis thermal expansion and the decrease of the charge order scattering intensity. We find no saturation of the thermal expansion of the c-axis at this temperature in our sample, see Fig. 4.13. Thus, the estimation of T_{CO} by Zaliznyak *et al.* [8] is questionable, since a similar charge-order characteristic was found in our half-doped sample by neutron diffraction. The decomposition of the sample may be a relevant factor for the thermal expansion saturation as observed in the previous work. A two-dimensional character of the charge order is pronounced with in-plane correlation length $\xi_{\parallel} = 26(2)$ Å and out-of-plane correlation length $\xi_{\perp} = 8.1(7)$ Å. However, one could imagine a strengthening of the Co-O_{basal} bonds in the charge ordered phase, but the distortion type with respect to Co^{2+} and Co^{3+} ions and the hybridization has to be taken into account. $La_{1.5}Sr_{0.5}CoO_4$ exhibits the highest in-plane and out-of-plane resistivity in comparison to underdoped and overdoped samples (see Fig. 2.7). Through the enhancement of the ionic character, electrons are localized in $d_{3z^2-r^2}$ orbitals.

Overall, the structural changes in the single-layered cobaltate $La_{2-x}Sr_xCoO_4$, at room temperature, can be attributed to the reduction of internal strains arising from a bond-length mismatch and the immanent La-O layer repulsion. After the reduction of the highest orthorhombic distortion in La_2CoO_4, the HTT-LTO transition is shifted systematically with the increase of the atomic number in comparison to LSNiO and LSCuO. The 'normal' structural changes, near half doping in $La_{2-x}A_xCoO_4$ (A = Ca, Ba), suggest an electronic origin for the anomalous decrease of c near $x = 0.45$ for the Sr doped compound, which will be further analyzed by single-crystal x-ray diffraction in Sec. 4.3.

4.3. Structural Parameters

The lattice constants and the LTO phase transition can be determined very precisely in an x-ray powder diffraction experiment of single-layered cobaltates. However, the

$La_{2-x}Sr_xCoO_4$	$x = 0.2$	$x = 0.3$	$x = 0.4$	$x = 0.45$	$x = 0.5$
a (Å)	3.8683(1)	3.8556(1)	3.8465(1)	3.8458(1)	3.8392(1)
c (Å)	12.6006(5)	12.6499(5)	12.6359(4)	12.5934(2)	12.5345(5)
V (Å^3)	188.73(1)	188.04(1)	186.96(1)	186.256(3)	184.75(1)
La (0 0 z)					
z	0.36146(1)	0.36234(1)	0.36220(1)	0.362214(5)	0.361983(3)
U_{11}=U_{22} (Å^2)	0.00744(3)	0.00469(2)	0.00444(2)	0.00695(3)	0.003534(1)
U_{33} (Å^2)	0.00452(2)	0.00181(2)	0.00324(2)	0.00559(3)	0.00165(2)
U_{iso} (Å^2)	0.00647(1)	0.00373(1)	0.00404(1)	0.00650(2)	0.00291(1)
Co (0 0 0)					
U_{11}=U_{22} (Å^2)	0.00331(5)	0.00171(3)	0.00140(3)	0.00380(5)	0.00056(2)
U_{33} (Å^2)	0.00879(7)	0.00489(6)	0.00563(6)	0.00777(7)	0.00328(3)
U_{iso} (Å^2)	0.00514(3)	0.00277(2)	0.00281(3)	0.00512(3)	0.00147(2)
O_{basal} (0 $\frac{1}{2}$ 0)					
U_{11} (Å^2)	0.0073(4)	0.0061(2)	0.0061(2)	0.0079(3)	0.0054(2)
U_{22} (Å^2)	0.0051(4)	0.0037(2)	0.0034(2)	0.0062(2)	0.0034(2)
U_{33} (Å^2)	0.023(6)	0.0130(3)	0.0129(3)	0.0149(3)	0.0095(2)
U_{iso} (Å^2)	0.0118(3)	0.0076(1)	0.0075(2)	0.0097(2)	0.0061(1)
O_{apical} (0 0 z)					
z	0.1750(2)	0.1741(1)	0.1733(1)	0.17194(2)	0.1690(1)
U_{11}=U_{22} (Å^2)	0.035(1)	0.0200(3)	0.0163(3)	0.0195(4)	0.0148(2)
U_{33} (Å^2)	0.017(1)	0.0155(5)	0.0169(5)	0.0191(5)	0.0136(3)
U_{iso} (Å^2)	0.029(1)	0.0185(2)	0.0165(2)	0.0194(2)	0.0144(1)
Bond lengths					
La-O_{basal} (Å)	2.60544(5)	2.59784(4)	2.59442(4)	2.59316(4)	2.58650(7)
La-O_{apical} (Å)	2.349(5)	2.381(2)	2.386(2)	2.399(2)	2.422(1)
La-O_{apical} (Å)	2.7737(1)	2.7651(3)	2.7567(5)	2.7566(3)	2.7443(2)
Co-O_{basal} (Å)	1.9341(1)	1.9278(1)	1.9232(1)	1.9229(1)	1.9196(1)
Co-O_{apical} (Å)	2.206(3)	2.203(2)	2.190(2)	2.165(2)	2.119(1)
Refinement					
R (%)	2.63	1.88	1.79	1.58	2.14
$wR(F^2)$ (%)	6.53	4.62	4.76	4.09	5.10
GooF	1.48	1.29	1.21	1.80	1.47
N_{obs}	3041	5421	3730	2076	6007
N_{ind}	495	485	498	482	494

Table 4.3.: Results of the x-ray single-crystal structure diffraction experiments on $La_{2-x}Sr_xCoO_4$ ($0.2 \leq x \leq 0.5$) with the space group $I4/mmm$ (No. 139) at $T = 295$ K. The refinements are based on F_0^2 using 13 parameters with reflections $F^2 > 3\sigma(F^2)$. The lattice constants were refined from long-run x-ray powder diffraction patterns.

$La_{2-x}Sr_xCoO_4$	$x = 0.6$	$x = 0.7$	$x = 0.8$	$x = 0.9$	$x \sim 1.0$
a (Å)	3.8323(1)	3.8258(1)	3.8164(1)	3.8109(1)	3.8049(1)
c (Å)	12.5165(3)	12.4947(3)	12.4804(2)	12.4837(1)	12.4873(1)
V (Å^3)	183.822(5)	182.879(5)	181.778(3)	181.230(3)	180.785(3)
La (0 0 z)					
z	0.361993(5)	0.361775(6)	0.361712(4)	0.361647(4)	0.36158(1)
U_{11}=U_{22} (Å^2)	0.00461(2)	0.00440(2)	0.00312(1)	0.00314(2)	0.00404(2)
U_{33} (Å^2)	0.00256(2)	0.00334(2)	0.00211(2)	0.00188(2)	0.00297(3)
U_{iso} (Å^2)	0.00392(1)	0.00405(1)	0.00279(1)	0.00272(1)	0.00368(2)
Co (0 0 0)					
U_{11}=U_{22} (Å^2)	0.00187(3)	0.00176(4)	0.00083(2)	0.00118(3)	0.00235(4)
U_{33} (Å^2)	0.00367(5)	0.00419(6)	0.00312(4)	0.00319(4)	0.00448(6)
U_{iso} (Å^2)	0.00247(2)	0.00257(3)	0.00159(2)	0.00185(2)	0.00306(3)
O_{basal} (0 $\frac{1}{2}$ 0)					
U_{11} (Å^2)	0.0068(2)	0.0061(3)	0.0056(2)	0.0061(2)	0.0077(3)
U_{22} (Å^2)	0.0043(2)	0.0039(2)	0.0033(2)	0.0037(2)	0.0047(3)
U_{33} (Å^2)	0.0093(2)	0.0097(3)	0.0088(2)	0.0088(2)	0.0098(3)
U_{iso} (Å^2)	0.0068(1)	0.0066(2)	0.0059(1)	0.0062(1)	0.0074(2)
O_{apical} (0 0 z)					
z	0.1675(1)	0.1670(1)	0.1655(1)	0.1650(1)	0.1650(1)
U_{11}=U_{22} (Å^2)	0.0138(3)	0.0125(3)	0.0116(2)	0.0121(2)	0.0128(3)
U_{33} (Å^2)	0.0130(3)	0.0127(4)	0.0108(2)	0.0097(3)	0.0114(4)
U_{iso} (Å^2)	0.0135(2)	0.0126(2)	0.0113(1)	0.0113(1)	0.0124(2)
Bond lengths					
La-O_{basal} (Å)	2.57981(4)	2.57721(5)	2.57292(3)	2.57173(3)	2.57043(6)
La-O_{apical} (Å)	2.434(1)	2.434(2)	2.449(1)	2.455(1)	2.454(2)
La-O_{apical} (Å)	2.7349(2)	2.7289(2)	2.7199(1)	2.7151(1)	2.7109(2)
Co-O_{basal} (Å)	1.9161(1)	1.9129	1.9082(1)	1.9054(1)	1.9024
Co-O_{apical} (Å)	2.097(1)	2.082(2)	2.065(1)	2.060(1)	2.061(2)
Refinement					
R (%)	1.93	2.00	1.93	1.90	2.40
$wR(F^2)$ (%)	4.94	5.21	4.72	4.14	5.83
GooF	1.23	1.33	1.23	1.32	1.32
N_{obs}	3790	3488	5373	4072	2805
N_{ind}	484	459	474	472	463

Table 4.4.: Results of the x-ray single-crystal structure diffraction experiments on $La_{2-x}Sr_xCoO_4$ ($0.6 \leq x \lesssim 1.0$) with the space group $I4/mmm$ (No. 139) at $T = 295$ K. The refinements are based on F_0^2 using 13 parameters with reflections $F^2 > 3\sigma(F^2)$. The lattice constants were refined from long-run x-ray powder diffraction patterns. Offstoichiometry is indicated by the La/Sr occupation refinement in the nominal $LaSrCoO_4$ compound.

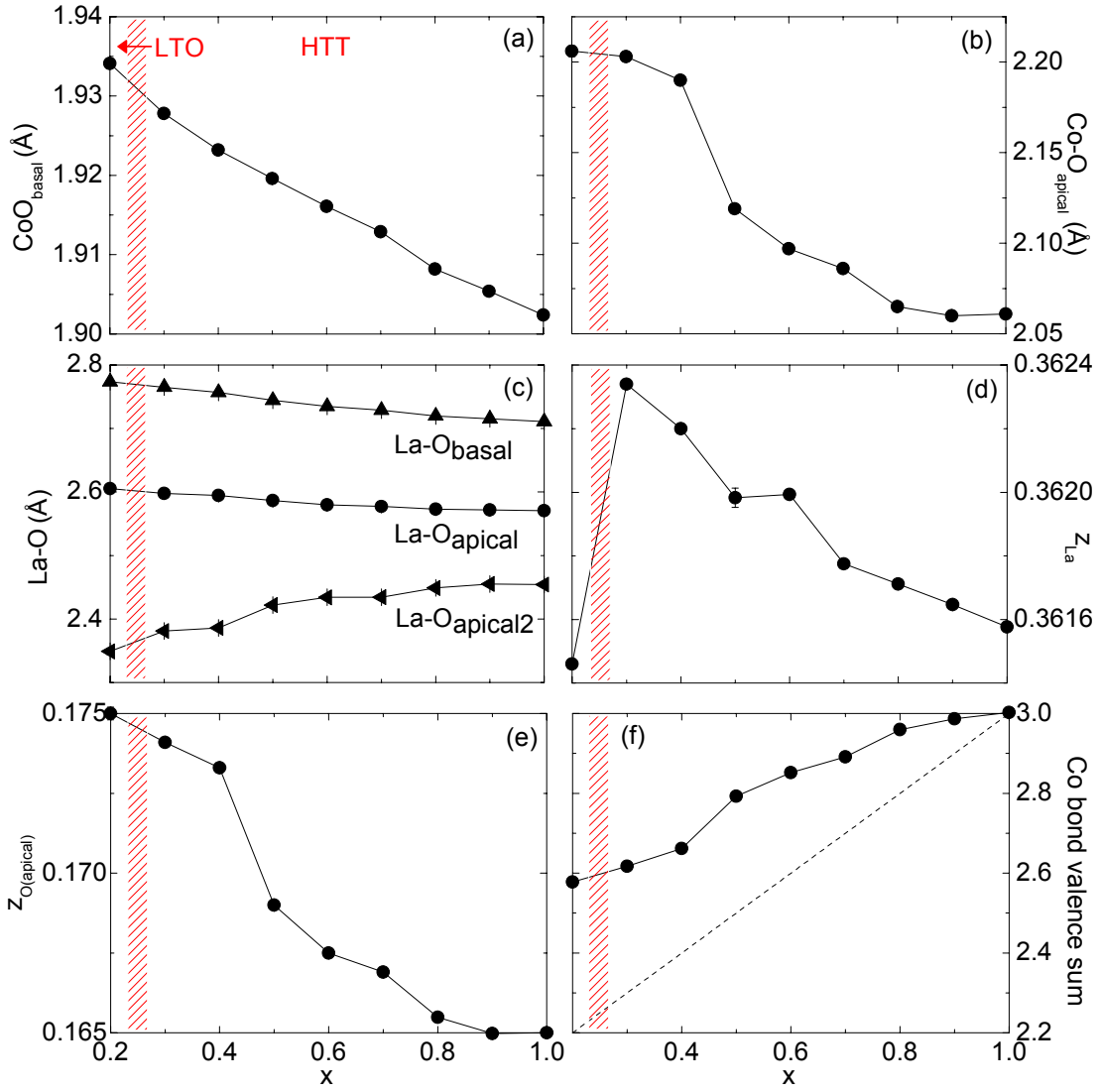

Figure 4.14.: Doping dependent change of atomic positions and bond lengths in $La_{2-x}Sr_xCoO_4$ at room temperature. The structural phase transition from orthorhombic $Bmab$ to tetragonal $I4/mmm$ symmetry is represented by the red line pattern.

loss of three-dimensional information and the weak scattering contributions of oxygen hinders the refinement of all structural parameters. X-ray single-crystal and neutron powder diffraction allow the investigation of all structural parameters. In particular, single-crystal x-ray diffraction was used to investigate the nature of the *c*-axis anomaly of $La_{2-x}Sr_xCoO_4$. To minimize errors, arising from an aspherical absorption correction, and to improve the comparability, the crystals were ground in a single-crystal ball mill to nearly spherical shape with similar radii. Figure 4.14 shows the doping dependency of the atomic positions and bond lengths in $La_{2-x}Sr_xCoO_4$ at room temperature. The lattice constants determined by x-ray powder diffraction were used for the single-crystal refinement and the calculation of the bond-lengths (see chapter 4.2)). The LTO distortion for $x = 0.2$ is small at room temperature. To avoid problems arising from the orientation-matrix determination and the integration process, only the main structure reflections corresponding to HTT symmetry were used. This provides a good bond-length comparability to higher doping levels, since errors, due to the additional structural degrees of freedom for La/Sr and oxygen, are small[3]. Table 4.3 and 4.4 give all structural parameters. From the HTT *a*-axis data it is clear that the Co-O_{basal} bond length is nearly linearly decreasing with doping. In contrast to the CoO_6 octahedron distortion, the coordination anisotropy of the La ion is continuously reduced with increasing x (see Fig. 4.14 (c)). Note that the shortest La-O bond length is the one between the apical oxygen ion at approximately (0, 0, 0.17) and the La ion just above at approximately (0, 0, 0.36), see Fig. 2.5. The *c* axis anomaly originates from the decrease of the Co-O_{apical} bond length and not from the doping dependent structural changes in the (La,Sr)O layers. A steep decrease of 3.81 % between $x = 0.3$ and $x = 0.5$ reflects the *c*-axis decrease. This is indicated by the drop of the relative $z_{O(apical)}$ parameter in comparison to z_{La}, too.

The bond-valence model is a valuable tool to characterize structural strains. A comparison of the bond-valence sum for Co^{2+x} ions with the nominal value $v_{Co} = 2 + x$ is shown in Fig. 4.14 (f). In Pauling's electrostatic-valence approach, a bond valence V_i is attributed to each bond and the bond-valence sum is calculated by summing over the bonds R_{ij}:

$$V_i = \sum_j e^{((R_0^{Co2+} - R_{ij})/b)}. \tag{4.1}$$

Here, R_0^{Co2+} and b are empirical parameters determined for the Co^{2+} coordination in several well known compounds.

In the LSCoO series we find a clear deviation of the calculated bond-valence sum, using $b = 0.37$ and $R_0^{Co2+} = 1.692$ for Co^{2+}-O^{2-} bonds [234, 235], from the nominal $v = 2 + x$ valency at low doping levels. With increasing Sr content, the bond-valence sum gets closer to the expectation value and coincides with it at $x \sim 1$. The anomalous drop of the Co-

[3] For an octahedra tilting of $\Theta \sim 1^\circ$ follows a relative Co-O bond-length change of $\cos 1 \approx 0.02$ % for $x = 0.2$ at room temperature.

O_{apical} bond length beyond $x \sim 0.4$ leads to an increase of the bond-valence sum, *i.e.* an increase of the structural strain. The enhanced bond-valence values must be ascribed to internal strains changing the equilibrium bond length anisotropically at low doping levels. A decrease of the bond-length mismatch upon Sr substitution lifts the structural strains. Therefore, the above described bond-length anomaly may not be of structural origin. It is worth to note that the Co^{3+} contribution is neglected in equation 4.1. There are no spin state dependent R_0^{Co3+} values reported in literature. Because of the strong difference in the existing values for this oxidation state $R_0^{Co3+} = 1.7, 1.680, 1.670, 1.637$ [236], the Co^{3+} spin-state degree of freedom is neglected in our calculation. In comparison to single-layered cobaltates and nickelates [232], the bond-valence sum for Cu in $La_{2-x}Sr_xCuO_{4+\delta}$ agrees surprisingly well with the increase of the nominal value calculated for different charge-carrier concentrations [237]. Starting with a strain induced δv_{Cu} deviation of 0.43 in La_2CuO_4 at room temperature, the Cu valency increases with 0.009 in $La_2CuO_{4.005}$ and 0.107 in $La_{1.87}Sr_{0.13}CuO_4$, which is similar to the hole concentration $n_h = x + 2\delta$ in the systems. This implies that the entire induced charge carriers cause the changes in Cu-O bonding lengths and therefore bond-length mismatch driven strains remain constant.

Let us now focus on La^{3+}/Sr^{2+} disorder and thermal motion of atoms in the single-layered cobaltates. An analysis of the atomic displacement parameters gives insight into thermally induced atomic motion and static displacive disorder (see for example [238]). Due to the short time scale of the x-ray and lattice interaction in comparison to the oscillation period of an atom around the equilibrium position, disorder or thermal motion lead to a similar decrease of the structure factor. A study of the temperature dependence of atomic displacement parameters can provide information to distinguish between static disorder and thermal motion, as the phonon contribution increases with their thermal excitation. However, disorder may also be temperature dependent. Both, displacive and magnetic correlations in single-layered perovskites and the diffuse scattering arising from intralayer and interlayer disorder are analyzed in Ref. [239].

The atomic displacement parameters of $La_{2-x}Sr_xCoO_4$ at room temperature are shown in Fig. 4.15. The isotropic Gaussian displacement parameters are nearly independent on doping in the HTT phase. As $x = 0.2$ is refined with $I4/mmm$ constraints, an increased U_{33} value of the O_{basal} ion and an increased value of $U_{11}(=U_{22})$ of the O_{apical} reflects the CoO_6 octahedra tilt at room temperature. To analyze anisotropies in the system, a comparison of the LTO distorted and undistorted single-layered perovskites is given in Tab. 4.5. In general, the cobaltate atomic displacement parameters are in qualitative agreement with the parameters of the parent compound La_2CoO_4 [65] at room temperature (see Tab. 4.5, too). In detail, the in-plane parameters of Co in $La_{1.5}Sr_{0.5}CoO_4$ are strongly reduced. This is interesting, as one would expect an increase of Co-O bonding with increasing charge in the series Cu^{2+}, Co^{2+x}, Ru^{4+}. The anisotropy reflects the MO_6 octahedron distortion, *i.e.* the Co-O_{basal} and Co-O_{apical} bond-length anisotropy, which is more pronounced in La_2CuO_4 and less in Sr_2RuO_4. The thermal ellipsoids of O_{apical} and O_{basal} indicate no octahedra tilt instability in the HTT phase.

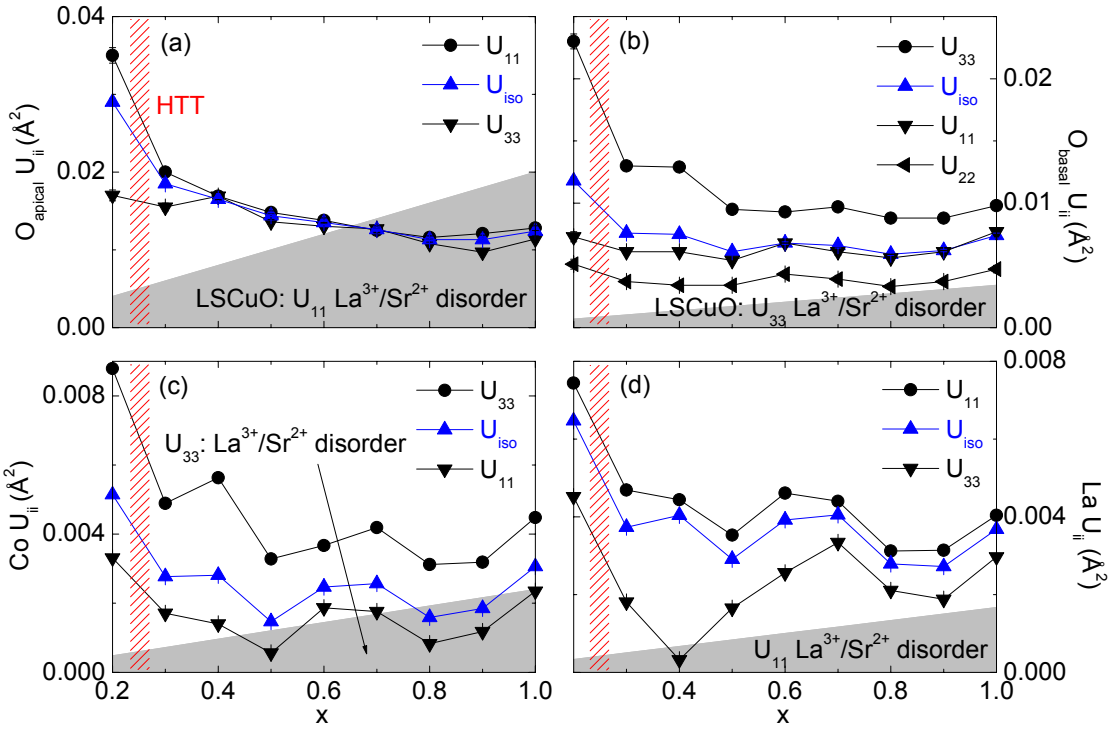

Figure 4.15.: Atomic displacement parameters of $La_{2-x}Sr_xCoO_4$ at room temperature, calculated from harmonic refinement. The grey area represents the linear extrapolation of the La^{3+}/Sr^{2+} disorder contribution to the atomic displacement parameters in $La_{1.85}Sr_{0.15}CuO_4$ at $T = 200$ K [240].

While the successive reduction of U_{33}, U_{22}, and U_{11} for O_{basal} is in agreement with the increase of the bond strength, the U_{33} parameter of O_{apical} is unusually high.

To account for the effect of disorder in the system, we may compare results of LSCuO with LSCoO. The influence of La/Sr dopant disorder in $La_{1.85}Sr_{0.15}CuO_4$ was simulated via an interaction-potential model using distinct potentials for the La-O and Sr-O interaction and distinct charges. A large number of super cells ($4 \times 4 \times 4$ in $F4/mmm$ notation) were constructed with a random arrangement of La and Sr ions for the given doping level. Positional displacements result from the variation of the local interatomic potentials, whose squares are averaged over the super cells. In addition to the phonon contribution to the atomic displacement parameters, the disorder contributions at $T = 200$ K are largest for $U_{11,disorder} = 0.003$ of O_{apical} and $U_{33,disorder} = 0.00051$ of O_{basal}. The linearly extrapolated disorder contribution for higher Sr doping levels in LSCuO is represented by a grey area in Fig. 4.15. The La^{3+}/Sr^{2+} disorder is maximal for a random distribution at $x = 1$ in $La_{2-x}Sr_xCoO_4$. The comparison of atomic displacement pa-

A_2BO_4	$La_{1.5}Sr_{0.5}CoO_4$ $I4/mmm$	La_2CoO_4 [65] $Bmab$	La_2CuO_4 [74] $Bmab$	Sr_2RuO_4 [228] $I4/mmm$
A				
U_{11} (Å^2)	0.003534(1)	0.007(1)	0.0071(2)	0.00678(8)
U_{22} (Å^2)	$=U_{11}$	0.007(1)	0.0062(1)	$=U_{11}$
U_{33} (Å^2)	0.00165(2)	0.0053(5)	0.0044(1)	0.00488(9)
U_{23} (Å^2)	-	0.0011(5)	-0.0004(1)	-
B				
U_{11} (Å^2)	0.00056(2)	0.00663(1)	0.0033(2)	0.00227(9)
U_{22} (Å^2)	$=U_{11}$	0.00663(1)	0.0028(1)	$=U_{11}$
U_{33} (Å^2)	0.00328(3)	0.0066(1)	0.0088(2)	0.0036(1)
O_{basal}				
U_{11} (Å^2)	0.0054(2)	0.0047(5)	0.0068(2)	0.0112(1)
U_{22} (Å^2)	0.0034(2)	0.0047(5)	0.0055(1)	0.0031(1)
U_{33} (Å^2)	0.0095(2)	0.0164(5)	0.0143(2)	0.0111(1)
O_{apical}				
U_{11} (Å^2)	0.0148(2)	0.027(2)	0.0208(3)	0.0097(1)
U_{22} (Å^2)	$=U_{11}$	0.009(1)	0.0157(2)	$=U_{11}$
U_{33} (Å^2)	0.0136(3)	0.009(1)	0.0066(2)	0.0046(1)
U_{23} (Å^2)	-	-0.0017(8)	0.0009(1)	-

Table 4.5.: Atomic displacement parameters of $La_{1.5}Sr_{0.5}CoO_4$ in comparison to single-layered perovskites A_2BO_4 with and without BO_6 tilt and rotational instabilities.

rameters for O_{basal}, Co and La/Sr is in agreement with the order of magnitude for the phonon contribution, but the increase with increasing x is not statistically significant. The strongest disorder induced change is expected for the atomic displacement parameter U_{11} of O_{apical}, which clearly differs from the observation. However, a quantitative comparison of the LSCuO and LSCoO for high doping levels may be misleading, because of the different force constants and local deviations from the random arrangement of Sr ions.

Fig. 4.16 shows the comparison of room-temperature M-O bond lengths found in $La_{2-x}Sr_xMO_4$ (M = Co, Ni). Due to the similar ionic sizes of $Co^{2+/3+}$ and $Ni^{2+/3+}$ ions (see Tab. 4.2), the resulting bond-length anisotropy and its doping dependence are comparable. As already discussed in Sec. 4.2.1, anomalies in the Ni-O bond lengths at $x = 0.6$ were ascribed to an orbital redistribution from z^2 to $x^2 - y^2$ orbitals by Millburn *et al.* [232]. Ni^{2+} ($3d^8$) is Jahn-Teller inactive, while Ni^{3+} ($3d^7$) exhibits a spin

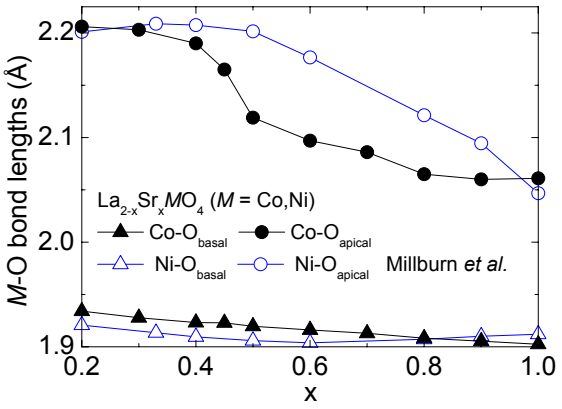

Figure 4.16.: Observed doping dependence of the M-O bond lengths in $La_{2-x}Sr_xMO_4$ (M = Co, Ni) at room temperature. Data for Ni are taken from Millburn *et al.* [232].

degree of freedom and may show Jahn-Teller activity. The observed structural changes are proposed to result from a change from a Jahn-Teller active polaron to a Jahn-Teller inactive polaron. In a simple ionic picture the steep decrease of Co-O_{apical} also has an electronic origin, where the Co^{3+} spin state changes from high-spin to a low-spin occupation near $x = 0.45$. For a detailed discussion of this idea see Sec. 7.1.

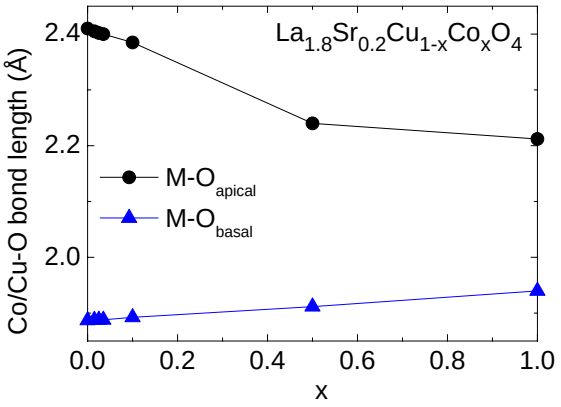

Figure 4.17.: Doping dependence of the Co/Cu-O bond lengths in $La_{1.8}Sr_{0.2}Cu_{1-x}Co_xO_4$ at room temperature in I4/mmm setting. Data for $x < 1.0$ are taken from Hohlwein *et al.* [95].

The effect of Co codoping in $La_{1.8}Sr_{0.2}Cu_{1-x}Co_xO_4$ ($x = 0, 0.015, 0.025, 0.035, 0.1, 0.5$) was investigated by Hohlwein *et al.* [95]. The authors used high-resolution powder diffraction to analyze the room temperature structure in detail. No superstructure reflections of the LTO phase were found for all doping levels. The doping dependence of in-plane and out-of-plane *M-O* bonds is shown in Fig. 4.17. Including our data, a systematic decrease of the bond-length anisotropy is observed with increasing Co doping. The increase of U_{33} for O_{basal} and U_{11} for O_{apical} suggests the onset of the short-range octahedra tilt instability at $x = 0.5$: the Jahn-Teller distortion of CuO_6/CoO_6-octahedra is systematically reduced with increasing x.

The analysis of the different Co-O bond-lengths in $La_{2-x}Sr_xCoO_4$ ($0.2 \leq x \lesssim 1.0$)

in comparison to nickelates and co-doped cuprates suggests an electronic nature of the steep decrease of Co-O_{apical} near $x \sim 0.45$. As indicated by the atomic displacement parameters, no CoO_6 tilt instabilities are present at higher doping levels.

4.3.1. Comparison of Bond Lengths in $La_{2-x}Sr_xCoO_4$ from Single-Crystal and Powder Experiments

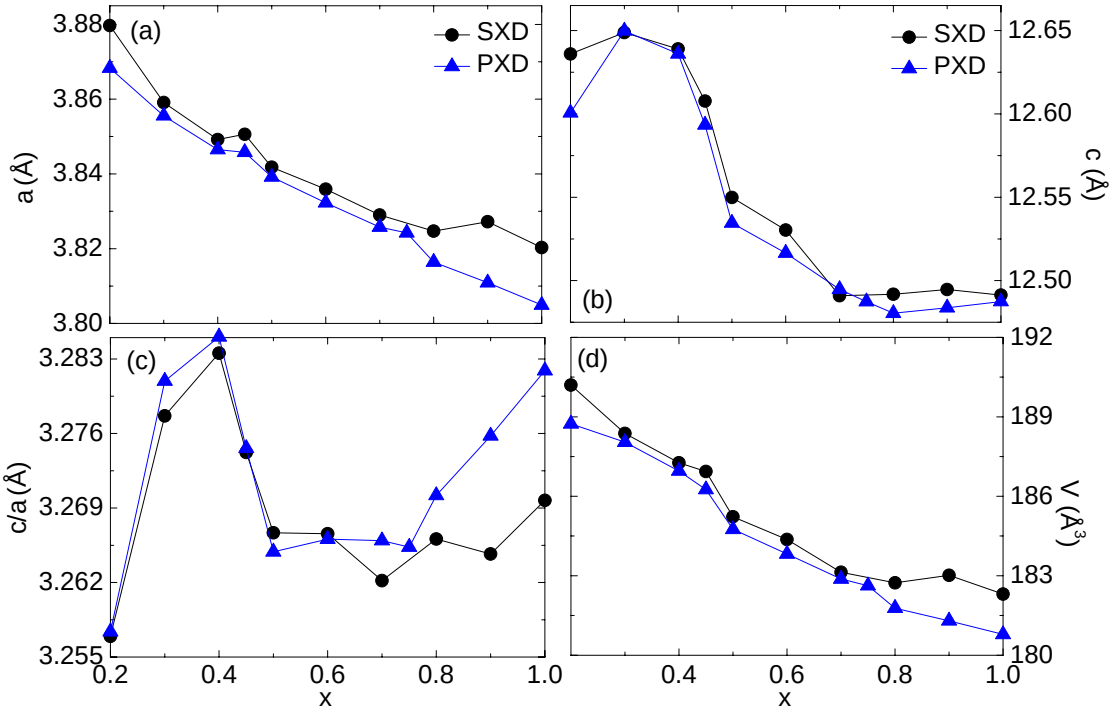

Figure 4.18.: Doping dependence of the lattice parameters of $La_{2-x}Sr_xCoO_4$ at room temperature. In comparison, results from single-crystal and powder x-ray experiments.

Due to the higher angle resolution, lattice constants from powder x-ray diffractometer measurements were taken to determine the Co-O bond lengths given in Tab. 4.3 and 4.4. Large single crystals of cylindrical shape, having typically 50 mm length and 8 mm diameter, were prepared by a floating zone method in a mirror furnace. To analyze sample inhomogeneities along the specimen in the standard characterization using x-ray powder diffraction, the lattice constants of slices above and below the single-crystal were compared. Powder and single-crystal samples originate from the same slice. To neglect crystal inhomogeneities perpendicular to the growing direction, the structure parameters were calculated using lattice constants from the single-crystal x-ray experiments (see

$La_{2-x}Sr_xCoO_4$	$x = 0.2$	$x = 0.3$	$x = 0.4$	$x = 0.45$	$x = 0.5$
a (Å)	3.8797(4)	3.8591(1)	3.8492(1)	3.8506(1)	3.8418(1)
c (Å)	12.636(1)	12.6488(5)	12.6390(4)	12.6077(5)	12.5499(2)
V (Å^3)	190.20(4)	188.38(2)	187.26(1)	186.93(2)	185.23(1)
La (0 0 z)					
z	0.36146(1)	0.36234(1)	0.36220(1)	0.36221(5)	0.361983(3)
U_{11}=U_{22} (Å^2)	0.00749(3)	0.00470(2)	0.00445(2)	0.00689(2)	0.003534(1)
U_{33} (Å^2)	0.00455(2)	0.00180(2)	0.00324(2)	0.00553(3)	0.00166(2)
U_{iso} (Å^2)	0.00651(1)	0.00373(1)	0.00405(1)	0.00644(1)	0.00292(1)
Co (0 0 0)					
U_{11}=U_{22} (Å^2)	0.00334(5)	0.00172(3)	0.00140(3)	0.00398(3)	0.00055(2)
U_{33} (Å^2)	0.00884(7)	0.00488(6)	0.00562(6)	0.00800(6)	0.00329(3)
U_{iso} (Å^2)	0.00517(3)	0.00277(2)	0.00281(3)	0.00532(3)	0.00147(2)
O_{basal} (0 $\frac{1}{2}$ 0)					
U_{11} (Å^2)	0.0073(4)	0.0062(2)	0.0061(2)	0.0081(3)	0.0054(2)
U_{22} (Å^2)	0.0051(4)	0.0037(24)	0.0034(2)	0.0064(2)	0.0034(2)
U_{33} (Å^2)	0.023(6)	0.0130(3)	0.0129(3)	0.0152(3)	0.0096(2)
U_{iso} (Å^2)	0.0118(3)	0.0076(1)	0.0075(2)	0.0099(2)	0.0061(1)
O_{apical} (0 0 z)					
z	0.1750(2)	0.1741(1)	0.1733(1)	0.17194(2)	0.1690(1)
U_{11}=U_{22} (Å^2)	0.035(1)	0.0200(3)	0.0163(3)	0.0198(4)	0.0148(2)
U_{33} (Å^2)	0.018(1)	0.0155(5)	0.0170(5)	0.0194(5)	0.0136(3)
U_{iso} (Å^2)	0.023(1)	0.0185(2)	0.0165(2)	0.0197(2)	0.0144(1)
Bond lengths					
La-O_{basal} (Å)	2.6130(1)	2.59902(9)	2.59570(8)	2.59316(4)	2.58650(7)
La-O_{apical} (Å)	2.355(5)	2.381(4)	2.389(3)	2.399(2)	2.422(1)
La-O_{apical} (Å)	2.782(1)	2.7674(6)	2.7583(5)	2.7566(3)	2.7443(2)
Co-O_{basal} (Å)	1.9398(4)	1.9295(1)	1.9246(1)	1.9253(1)	1.9209(1)
Co-O_{apical} (Å)	2.212(5)	2.202(4)	2.189(3)	2.168(2)	2.121(1)
Refinement					
R (%)	2.63	1.88	1.79	1.58	2.14
$wR(F^2)$ (%)	6.53	4.63	4.76	4.09	5.10
GooF	1.48	1.29	1.21	1.80	1.47
N_{obs}	3041	5421	3730	2076	6007
N_{ind}	495	485	498	482	494

Table 4.6.: Results of the x-ray single-crystal structure diffraction experiments on $La_{2-x}Sr_xCoO_4$ ($0.2 \leq x \leq 0.5$) with the space group $I4/mmm$ (No. 139) at $T = 295$ K. The refinements base on F_0^2 using 13 parameters with reflections $F^2 > 3\sigma(F^2)$.

$La_{2-x}Sr_xCoO_4$	$x = 0.6$	$x = 0.7$	$x = 0.8$	$x = 0.9$	$x \sim 1.0$
a (Å)	3.8359(1)	3.8290(5)	3.8247(1)	3.8272(5)	3.8203(4)
c (Å)	12.5303(3)	12.4909(17)	12.4918(2)	12.4946(17)	12.4913(13)
V (Å^3)	184.4(1)	183.13(4)	182.734(6)	183.02(6)	182.30(5)
La (0 0 z)					
z	0.361993(5)	0.361776(6)	0.361712(4)	0.361647(4)	0.36158(1)
U_{11}=U_{22} (Å^2)	0.00462(2)	0.00441(2)	0.00312(1)	0.00319(2)	0.00410(2)
U_{33} (Å^2)	0.00256(2)	0.00333(2)	0.00211(2)	0.00186(2)	0.00295(3)
U_{iso} (Å^2)	0.00393(1)	0.00405(1)	0.00279(1)	0.00275(1)	0.00372(2)
Co (0 0 0)					
U_{11}=U_{22} (Å^2)	0.00187(3)	0.00177(4)	0.00083(2)	0.00120(3)	0.00238(4)
U_{33} (Å^2)	0.00368(5)	0.00419(6)	0.00312(4)	0.00317(4)	0.00448(6)
U_{iso} (Å^2)	0.00248(2)	0.00257(3)	0.00159(2)	0.00186(2)	0.00308(3)
O_{basal} (0 $\frac{1}{2}$ 0)					
U_{11} (Å^2)	0.0068(2)	0.0061(3)	0.0056(2)	0.0062(2)	0.0078(3)
U_{22} (Å^2)	0.0043(2)	0.0039(2)	0.0033(2)	0.0037(2)	0.0048(3)
U_{33} (Å^2)	0.0094(2)	0.00965(3)	0.0088(2)	0.0087(2)	0.0098(3)
U_{iso} (Å^2)	0.0068(1)	0.0066(2)	0.0059(1)	0.0062(1)	0.0074(2)
O_{apical} (0 0 z)					
z	0.1675(1)	0.1670(1)	0.1655(1)	0.1650(1)	0.1650(1)
U_{11}=U_{22} (Å^2)	0.0138(3)	0.0125(3)	0.0116(2)	0.0122(2)	0.0130(3)
U_{33} (Å^2)	0.0130(3)	0.0127(4)	0.0108(2)	0.0097(3)	0.0114(4)
U_{iso} (Å^2)	0.0135(2)	0.0126(2)	0.0113(1)	0.0114(1)	0.0124(2)
Bond lengths					
La-O_{basal} (Å)	2.58242(8)	2.57802(11)	2.57706(8)	2.57879(8)	2.57654(10)
La-O_{apical} (Å)	2.437(3)	2.434(3)	2.451(2)	2.458(2)	2.456(3)
La-O_{apical} (Å)	2.7375(3)	2.7312(4)	2.7257(3)	2.7266(3)	2.7217(4)
Co-O_{basal} (Å)	1.9179(1)	1.9145(5)	1.9123(1)	1.9136(5)	1.9101(4)
Co-O_{apical} (Å)	2.099(3)	2.085(3)	2.067(2)	2.061(2)	2.061(3)
Refinement					
R (%)	1.93	2.00	1.93	1.90	2.40
$wR(F^2)$ (%)	4.94	5.21	4.72	4.14	5.83
GooF	1.23	1.33	1.23	1.32	1.32
N_{obs}	3790	3488	5373	4072	2805
N_{ind}	484	459	474	472	463

Table 4.7.: Results of the x-ray single-crystal diffraction experiments on $La_{2-x}Sr_xCoO_4$ ($0.6 \leq x \lesssim 1.0$) with the space group $I4/mmm$ (No. 139) at $T = 295$ K. The refinements base on F_0^2 using 13 parameters with reflections $F^2 > 3\sigma(F^2)$.

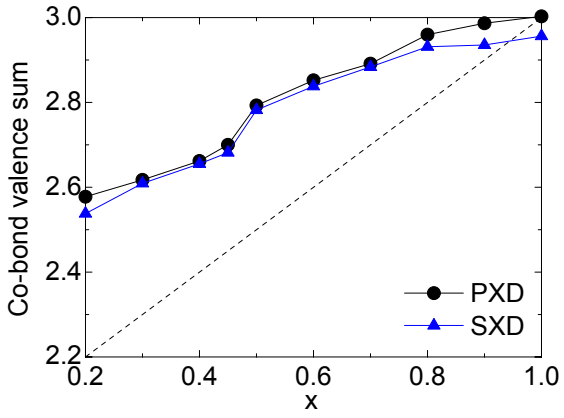

Figure 4.19.: Co-bond-valence sum determined by refined bond lengths from single-crystal and powder experiments.

Tab. 4.6, Tab. 4.7, Fig. 4.18). The largest differences are appearing for $x = 0.2$ and $x \geq 0.8$. To investigate a possible off-stoichiometry in the sample, the occupation of La/Sr and oxygen sites was refined for the single-crystal data. At $x = 0.9$, we found a significant improvement of the refinement from $S = 1.32$, $R = 2.39$, and $wR = 5.81$ to $S = 1.23$, $R = 2.20$, and $wR = 5.40$ with redistribution of the La/Sr ratio to a Sr doping level of $x = 0.77$. This is in contrast to the lattice constant progression, as the $x = 0.77$ sample would exhibit a larger in-plane lattice constant. The refinement of the site occupation for the $x = 0.9$ sample provides no improvement of the global criteria of the fit. The modification of absolute values has no significant influence on the bond-valence sum, as can be seen in Fig. 4.19. However, site occupation refinement indicates no off-stoichiometry at low doping levels and the observed anomaly in the Co-O_{apical} at intermediate doping stays the same.

4.4. Temperature Dependence of the Structure Parameters

The structural parameters of $La_{2-x}Sr_xCoO_4$ ($x = 0.2, 0.4, 0.8$), determined by powder neutron diffraction at $T = 10$ K, can be found in Tab. 4.8. A large amount of well ground powder (~ 5 g) was used on the high resolution neutron powder diffractometer 3T2 at the Laboratoire Léon Brillouin in Saclay. The progression of the lattice constants qualitatively agrees with the low-temperature powder diffraction data. The c-axis value at $x = 0.4$ and atomic displacement parameters U_{22} for O_{basal} are significantly decreased. For $x = 0.2$, a weak second phase contribution was found at $2\theta = 14.28°$ using $\lambda = 1.2251$ Å. This contribution originates neither from educts, (327)-structure phases nor from a simple antiferromagnetic superstructure reflection. The Co-O bond-lengths become successively more equal with increasing x.

$La_{2-x}Sr_xCoO_4$	$x = 0.2$	$x = 0.4$	$x = 0.8$
Symmetry	$Bmab$	$I4/mmm$	$I4/mmm$
a (Å)	5.4599(2)	3.84149(9)	3.81420(3)
b (Å)	5.4660(1)	$= a$	$= a$
c (Å)	12.5573(2)	12.5445(4)	12.4411(1)
V (Å^3)	374.76(2)	185.116(9)	180.994(2)
La (0 0 z)			
z	0.36171(9)	0.3621(1)	0.36155(7)
U_{iso}	0.0029(2)	0.0022(3)	0.0007(2)
Co (0 0 0)			
U_{iso}	0.0029(7)	0.006(1)	0.0084(8)
O_{basal}			
U_{11}	0.001(2)	0.0014(9)	0.0023(6)
U_{22}	0.000(2)	0.0004(8)	-0.0010(6)
U_{33}	0.027(1)	0.030(1)	0.0104(7)
U_{13}	-0.0005(5)	=0	=0
U_{iso}	0.010(2)	0.011(1)	0.0039(6)
O_{apical} (0 0 z)			
z	0.1696(2)	0.1679(2)	0.1649(1)
U_{11}	0.029(4)	0.0112(6)	0.0037(4)
U_{22}	0.029(4)	$= U_{11}$	$= U_{11}$
U_{33}	0.024(1)	0.032(1)	0.0157(6)
U_{iso}	0.027(3)	0.0180(8)	0.0077(5)
Bond Lengths			
La-O_{basal}	2.5973(8)	2.5851(9)	2.5698(6)
La-O_{apical}	2.412(2)	2.436(3)	2.447(2)
La-O_{apical}	2.7581(3)	2.7422(4)	2.7170(2)
Co-O_{basal}	1.931447(8)	1.92073(1)	1.907099(3)
Co-O_{apical}	2.130(2)	2.106(2)	2.051(1)
Refinement			
wR/R_{exp}	7.165/2.803	8.793/3.761	6.854/3.232

Table 4.8.: Results of the powder neutron diffraction (PND) experiments on $La_{2-x}Sr_xCoO_4$ at $T = 10$ K.

$La_{1.8}Sr_{0.2}CoO_4$					
T (K)	100	150	200	250	293
a (Å)	3.8644(2)	3.8649(1)	3.8652(1)	3.8672(1)	3.8693(1)
c (Å)	12.6098(6)	12.6140(5)	12.6212(5)	12.6355(4)	12.6476(4)
V (Å^3)	188.31(2)	188.42(1)	188.56(1)	188.97(1)	189.36(1)
La (0 0 z)					
z	0.362010(6)	0.362006(6)	0.361994(6)	0.361980(6)	0.361953(6)
U_{11}=U_{22} (Å^2)	0.00469(3)	0.00530(3)	0.00606(3)	0.00720(3)	0.00788(3)
U_{33} (Å^2)	0.00110(4)	0.00172(4)	0.00249(4)	0.00312(4)	0.00351(4)
U_{iso} (Å^2)	0.00350(2)	0.00411(2)	0.00487(2)	0.00584(2)	0.00642(2)
Co (0 0 0)					
U_{11}=U_{22} (Å^2)	0.00275(6)	0.00290(5)	0.0321(5)	0.00383(5)	0.00409(5)
U_{33} (Å^2)	0.00265(8)	0.00367(8)	0.00490(8)	0.00600(8)	0.00688(9)
U_{iso} (Å^2)	0.00272(4)	0.00316(4)	0.00380(4)	0.00455(4)	0.00502(4)
O_{basal} (0 $\frac{1}{2}$ 0)					
U_{11} (Å^2)	0.0051(4)	0.0059(4)	0.0063(4)	0.0077(4)	0.0082(4)
U_{22} (Å^2)	0.0052(4)	0.0053(3)	0.0054(3)	0.0063(3)	0.0065(3)
U_{33} (Å^2)	0.0139(5)	0.0147(5)	0.0155(5)	0.0162(5)	0.0177(5)
U_{iso} (Å^2)	0.0081(3)	0.0086(2)	0.0090(2)	0.0101(2)	0.0108(3)
O_{apical} (0 0 z)					
z	0.1752(3)	0.1749(3)	0.1756(3)	0.1750(3)	0.1751(3)
U_{11}=U_{22} (Å^2)	0.0231(8)	0.0233(8)	0.0230(8)	0.0260(8)	0.0277(9)
U_{33} (Å^2)	0.0190(10)	0.0188(9)	0.0206(10)	0.0193(9)	0.0202(9)
U_{iso} (Å^2)	0.0217(5)	0.0218(5)	0.0222(5)	0.0237(5)	0.0252(5)
Bond lengths					
La-O_{basal} (Å)	2.60021(5)	2.60081(5)	2.60169(5)	2.60388(5)	2.60600(5)
La-O_{apical} (Å)	2.356(4)	2.359(4)	2.352(4)	2.363(3)	2.363(3)
La-O_{apical} (Å)	2.7725(6)	2.7725(6)	2.7740(6)	2.7742(6)	2.7759(6)
Co-O_{basal} (Å)	1.9322(2)	1.9324(1)	1.9326(1)	1.9336(1)	1.9346(1)
Co-O_{apical} (Å)	2.209(4)	2.207(4)	2.216(4)	2.211(3)	2.215(3)
Refinement					
R (%)	2.54	2.42	2.59	2.39	2.51
$wR(F^2)$ (%)	6.57	6.16	6.55	6.13	6.24
GooF	1.81	1.83	1.83	1.63	1.73
N_{obs}	1765	1760	1766	1791	1783

Table 4.9.: Results from the single crystal x-ray diffraction experiments on $La_{1.8}Sr_{0.2}CoO_4$ in $I4/mmm$ setting (Nr. 139) for different temperatures. The refinements base on F_0^2 using 13 parameters with reflections $F^2 > 3\sigma(F^2)$.

$La_{1.7}Sr_{0.3}CoO_4$					
T (K)	100	150	200	250	293
a (Å)	3.8560(5)	3.8565(3)	3.8571(3)	3.8583(2)	3.8588(1)
c (Å)	12.607(2)	12.615(1)	12.627(1)	12.6397(6)	12.6488(4)
V (Å^3)	187.45(7)	187.62(5)	187.85(4)	188.16(3)	188.35(1)
La (0 0 z)					
z	0.362366(5)	0.362364(5)	0.362358(4)	0.362336(4)	0.362313(5)
U_{11}=U_{22} (Å^2)	0.00468(2)	0.00557(2)	0.00625(2)	0.00698(2)	0.00787(2)
U_{33} (Å^2)	0.00323(2)	0.00366(2)	0.00421(2)	0.00472(2)	0.00550(2)
U_{iso} (Å^2)	0.00420(1)	0.00493(1)	0.00557(1)	0.00623(1)	0.00708(1)
Co (0 0 0)					
U_{11}=U_{22} (Å^2)	0.00318(3)	0.00365(3)	0.00389(3)	0.00419(3)	0.00465(3)
U_{33} (Å^2)	0.00451(5)	0.00529(5)	0.00633(5)	0.00732(5)	0.00864(5)
U_{iso} (Å^2)	0.00362(2)	0.00420(2)	0.00470(2)	0.00523(2)	0.00598(2)
O_{basal} (0 1/2 0)					
U_{11} (Å^2)	0.0060(2)	0.0068(3)	0.0075(2)	0.0085(2)	0.0094(3)
U_{22} (Å^2)	0.0056(2)	0.0061(2)	0.0063(2)	0.0064(2)	0.0065(2)
U_{33} (Å^2)	0.0136(3)	0.0142(3)	0.0143(3)	0.0148(3)	0.0165(3)
U_{iso} (Å^2)	0.0084(2)	0.0090(2)	0.0094(1)	0.0099(1)	0.0108(2)
O_{apical} (0 0 z)					
z	0.1756(2)	0.1752(2)	0.1753(2)	0.1753(2)	0.1755(2)
U_{11}=U_{22} (Å^2)	0.0217(5)	0.0212(4)	0.0213(4)	0.0217(4)	0.0231(4)
U_{33} (Å^2)	0.0181(5)	0.0189(5)	0.0178(5)	0.0192(5)	0.0189(5)
U_{iso} (Å^2)	0.0205(3)	0.0204(3)	0.0201(2)	0.0209(2)	0.0217(2)
Bond lengths					
La-O_{basal} (Å)	2.59383(4)	2.59487(4)	2.59612(3)	2.59795(3)	2.59917(4)
La-O_{apical} (Å)	2.354(2)	2.361(2)	2.362(2)	2.364(2)	2.3624(19)
La-O_{apical} (Å)	2.7684(4)	2.7679(4)	2.7685(3)	2.7695(3)	2.7703(3)
Co-O_{basal} (Å)	1.928(5)	1.9282(3)	1.9285(3)	1.9291(2)	1.9294(1)
Co-O_{apical} (Å)	2.214(2)	2.211(2)	2.213(2)	2.216(2)	2.2204(19)
Refinement					
R (%)	2.09	2.13	2.05	2.05	2.09
$wR(F^2)$ (%)	4.93	4.96	4.65	4.71	4.71
GooF	1.57	1.45	1.48	1.46	1.49
N_{obs}	3106	3090	3073	3233	3029

Table 4.10.: Results from the single crystal x-ray diffraction experiments on $La_{1.7}Sr_{0.3}CoO_4$ in $I4/mmm$ setting (Nr. 139) for different temperatures. The refinements base on F_0^2 using 13 parameters with reflections $F^2 > 3\sigma(F^2)$.

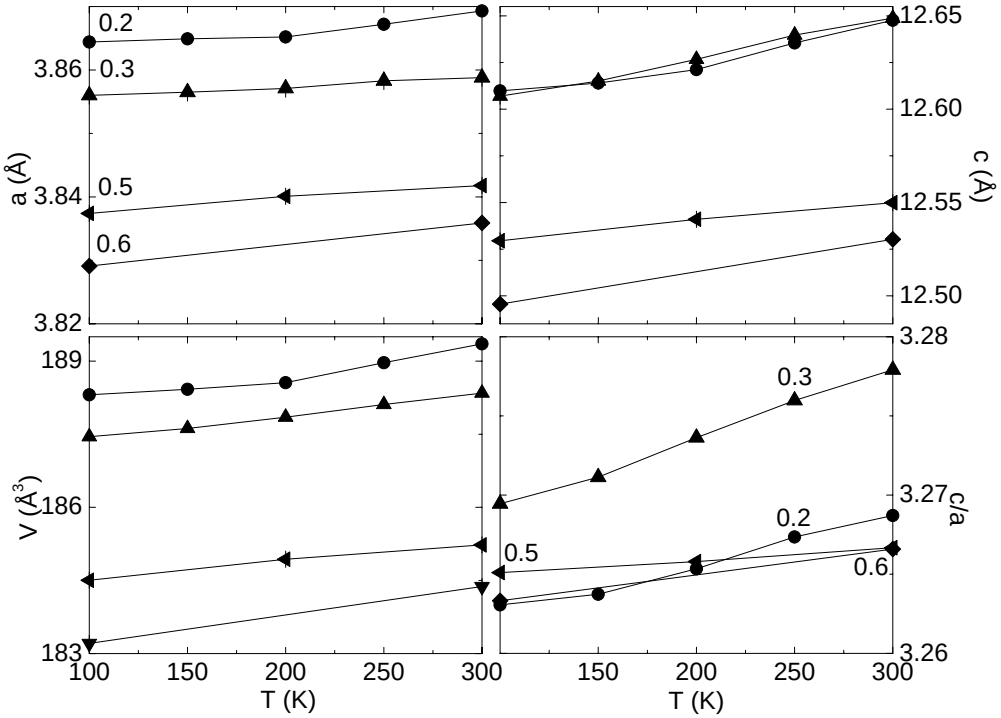

Figure 4.20.: Temperature dependence of the lattice parameters of $La_{2-x}Sr_xCoO_4$ ($x = 0.2, 0.3, 0.5, 0.6$) determined by single-crystal x-ray diffraction in the temperature region $100 - 300$ K.

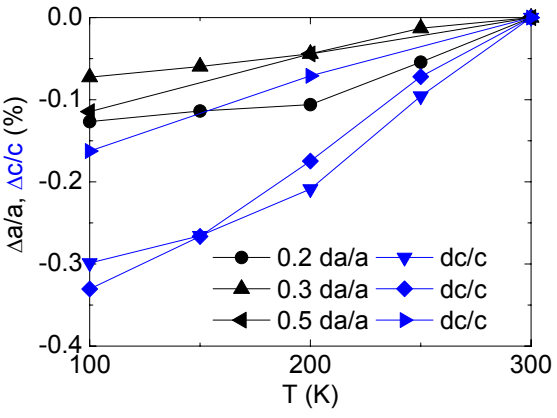

Figure 4.21.: Relative thermal expansion of $La_{2-x}Sr_xCoO_4$ ($x = 0.2, 0.3, 0.5, 0.6$) lattice constants determined by single-crystal x-ray diffraction in the temperature region $100 - 300$ K.

Using the *KryoFlex* cooling system, structural parameters of several cobaltate samples $La_{2-x}Sr_xCoO_4$ ($x = 0.2, 0.3, 0.5, 0.6$), below and above the Co-O_{apical} bond-length decrease, were investigated at low temperatures. For comparability reasons, the collection strategy and scan parameters were kept equal. The temperature dependence of the lattice parameters is shown in Fig. 4.20 and 4.21. The relative change of HTT a and c axes qualitatively agrees with the changes from powder x-ray diffraction. However, deviations may be due to the low angle resolution of a single-crystal diffractometer. The structure parameters are given in Tab. 4.4. For low-temperature x-ray single-crystal experiments, the emergence of ice near the sample position has to be taken into account. Although a nitrogen stream embedded in dry air of the *KryoFlex* device was used, the adsorption of ice between sample and goniometer head during long-run measurements could not be fully prevented. This can be seen in the background-intensity distribution in the calculated precision maps. The additional diffuse intensities have a strong influence on the atomic displacement parameters. We neglect a detailed discussion on the atomic displacement parameters for higher doping levels at this point, since some samples exhibit a non-positive harmonic-displacement tensor for the Co ion at $T = 100$ K.

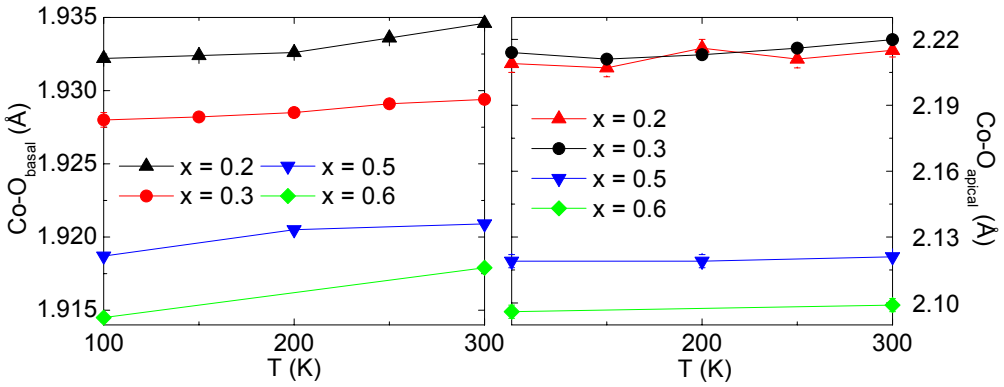

Figure 4.22.: Temperature dependence of the Co-O bond lengths of $La_{2-x}Sr_xCoO_4$ ($x = 0.2, 0.3, 0.5, 0.6$) determined by single-crystal x-ray diffraction in the temperature region $100 - 300$ K.

In the comparison of the temperature dependent structural changes and the atomic displacement parameters between $La_{1.8}Sr_{0.2}CoO_4$ and $La_{1.7}Sr_{0.3}CoO_4$, no obvious changes were found. Both the La and Co coordination anisotropy are decreasing with decreasing temperature. Noteworthy are the oxygen atomic displacement parameters related to the CoO_6 octahedra tilt, *i.e.* U_{33} of O_{basal} and $U_{11} = U_{22}$ of O_{apical}. These parameters decrease just slightly, which we attribute to the enhanced CoO_6 octahedron tilt appearing for decreasing temperatures. The constraints to HTT symmetry increase the atomic displacement parameters, associated with the tilt direction, and the tilt is expected to increase with decreasing temperatures. To Co-O bond lengths decrease with decreasing

$La_{1.5}Ca_{0.5}CoO_4$			
T (K)	100	200	280
a (Å)	3.8268(3)	3.8288(1)	3.8299(1)
c (Å)	12.344(1)	12.3527(4)	12.3949(3)
V (Å^3)	180.77(4)	181.09(2)	181.81(1)
La (0 0 z)			
z	0.361884(6)	0.361870(6)	0.36186(1)
U_{11}=U_{22} (Å^2)	0.00351(2)	0.00503(2)	0.00643(2)
U_{33} (Å^2)	0.00404(3)	0.00458(2)	0.00546(2)
U_{iso} (Å^2)	0.00369(1)	0.00488(1)	0.00611(1)
Co (0 0 0)			
U_{11}=U_{22} (Å^2)	0.00182(5)	0.00184(3)	0.00231(3)
U_{33} (Å^2)	0.00502(7)	0.00535(5)	0.00675(6)
U_{iso} (Å^2)	0.00288(3)	0.00301(2)	0.00379(2)
O_{basal} (0 $\frac{1}{2}$ 0)			
U_{11} (Å^2)	0.0047(2)	0.0053(2)	0.0070(2)
U_{22} (Å^2)	0.0041(2)	0.0042(2)	0.0046(2)
U_{33} (Å^2)	0.0125(3)	0.0127(3)	0.0153(3)
U_{iso} (Å^2)	0.0071(2)	0.0074(1)	0.0090(2)
O_{apical} (0 0 z)			
z	0.1703(1)	0.1704(1)	0.1703(1)
U_{11}=U_{22} (Å^2)	0.0156(3)	0.0166(3)	0.0187(3)
U_{33} (Å^2)	0.0111(4)	0.0110(3)	0.0116(4)
U_{iso} (Å^2)	0.0141(2)	0.0147(2)	0.0163(2)
Bond lengths			
La-O_{basal} (Å)	2.56276(5)	2.56443(5)	2.56884(5)
La-O_{apical} (Å)	2.3644(5)	2.3647(4)	2.374(1)
La-O_{apical} (Å)	2.735(1)	2.7366(6)	2.7374(2)
Co-O_{basal} (Å)	1.9134(3)	1.9144(1)	1.9149(1)
Co-O_{apical} (Å)	2.103(2)	2.105(1)	2.112(1)
Refinement			
R (%)	2.22	1.93	1.98
$wR(F^2)$ (%)	5.58	4.61	4.64
GooF	1.20	1.35	1.32
N_{obs}	3228	3287	3303

Table 4.11.: Results from the single crystal x-ray diffraction experiments on $La_{1.5}Ca_{0.5}CoO_4$ in tetragonal $I4/mmm$-setting (No. 139) at $T = 100, 200, 280$ K. The refinement procedure included 13 variables against F_0^2 and reflection intensities $F^2 > 3\sigma(F^2)$.

temperatures, as shown in Fig. 4.22.

To investigate the effect of chemical pressure at half doping, Ca and Sr doped single crystals were prepared. We studied the temperature dependent structure modifications between $100 \leq T \leq 295$ K on a piece of a large single-crystal of $La_{1.5}Ca_{0.5}CoO_4$. The lattice volume is strongly reduced through the reduction of the alkaline-earth radius [54], as indicated by the powder x-ray diffraction patterns. However, the difference between room temperature CoO_6 bond lengths is only slightly reduced in comparison to the Sr doped sample with $x = 0.5$. This is an important observation, as it suggests only weak influence from the ionic radii of the dopant on the coordination anisotropy of cobalt. The isotropic atomic displacement parameters are increased in comparison to $x = 0.5$ Sr doping at room temperature, which may be caused by a charge ordering phenomenon, found by resistivity measurements (M. Benomar [135]). Another possibility is a dynamic CoO_6 tilt instability. While U_{33} is enhanced for the in-plane oxygen ion, the thermal ellipsoid of O_{apical} is nearly isotropic. A detailed analysis of superstructure reflections using neutron diffraction would give further insight.

4.5. Conclusions

The structural parameters of $La_{2-x}RE_xCoO_4$ (RE= Ca, Sr, Ba) were studied in detail by means of single-crystal x-ray, powder x-ray, and powder neutron diffraction. The parent compound exhibits an orthorhombic distortion of the K_2NiF_4-type structure, the so-called low-temperature orthorhombic phase, already at room temperature with the largest distortion compared to La_2NiO_4 and La_2CuO_4. The LTO distortion decreases with increasing dopant concentration and is fully suppressed above $x = 0.3$ at room temperature. Furthermore, the LTO transition temperature is successively reduced. The temperature dependence of LTO superstructure reflections for $T < 220$ K in $La_{1.7}Sr_{0.3}CoO_4$ suggests a gauss-broadened phase transition. The stabilization of the HTT phase and the decrease of the lattice volume in $La_{2-x}Sr_xCoO_4$ at further doping can be fully explained through the reduced internal strains implied by the ionic radii. The comparative studies of LSCoO with LSCuO and LSNiO give also insight in steric effects and anomalies. The HTT/LTO phase transition is systematically shifted to higher doping levels at room temperature according to internal strains, induced by the bond-length mismatch. The strength of internal strains in single-layered cobaltates is indicated by a strong deviation of the calculated bond-valence sum from the nominal value at low doping levels, which decreases upon increasing dopant concentration.

An anomalous decrease of the HTT c-axis was found near $x \sim 0.45$ in $La_{2-x}Sr_xCoO_4$, which could be ascribed to the reduction of the CoO_6 octahedron elongation. Also, the bond-length differences of the ninefold La coordination are smoothly lowered over the doping range $0.2 \leq x \lesssim 1.0$. The reduced or absent anomaly in Ca and Ba doped samples near half doping suggests a significant shift or suppression with changing chemical pres-

sure on the single-layered perovskite structure. The half-doped compound with $x = 0.5$ exhibits the largest relative decrease of the in-plane lattice constant and the smallest relative decrease of the out-of-plane lattice constant of the series in the low-temperature region $10 - 300$ K. This change of the thermal expansion with doping may be attributed to the onset of charge order, since it is indicated by the maximum of the in-plane and out-of-plane resistivity at $x = 0.5$. The short-range spin and charge order was verified in this half-doped single-layered cobaltate [7]. An anomalous increase of the c-axis length and a saturation of the a-axis length at higher temperatures ($300 - 850$ K) were found in this compound. This anomalous thermal expansion at $x = 0.5$ suggests an electronic origin, *i.e.* an orbital redistribution, for the steep increase of the c-axis in $La_{1.5}Sr_{0.5}CoO_4$. The temperature dependence of the lattice constants exhibits no change at the recently proposed charge-order transition temperature $T = 825(27)$ K [8]. In contrast to this neutron diffraction analysis of Zaliznyak *et al.*, there is no indication for a saturation of the c-axis length at this temperature in our data.

Overall, the doping and temperature dependence of structural parameters in the $La_{2-x}Sr_xCoO_4$ compounds and the interrelation to the isostructural LSNiO and LSCuO systems is well described in the bond-length mismatch model. The steep decrease of the Co-O_{apical} bond length near $x \sim 0.45$ and the increase of the out-of-plane lattice constant at $x = 0.5$ is attributed to an electronic origin. A model for a doping dependent and thermally induced Co^{3+} spin-state transition will be discussed later in Sec. 7.1.

5. Charge Ordering in $La_{1.5}Sr_{0.5}CoO_4$

The checkerboard-like charge order in $La_{1.5}Sr_{0.5}CoO_4$ has been studied by means of x-ray diffraction and of single-crystal neutron diffraction at room temperature. Since the x-ray structure factor is small for oxygen, no indications for a charge-order superstructure were found in standard single-crystal x-ray diffraction experiments. Neutron diffraction on three large samples revealed weak superstructure reflections, which were modeled by a breathing-type distortion of CoO_6 octahedra.

5.1. Introduction

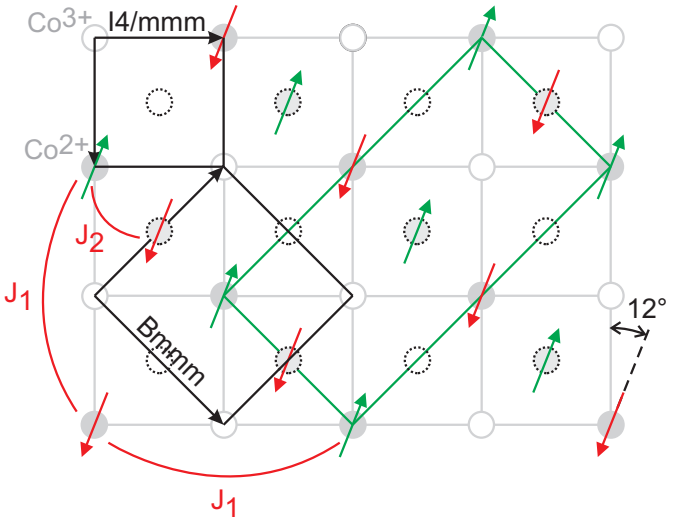

Figure 5.1.: Scheme of the spin and the charge order in $La_{1.5}Sr_{0.5}CoO_4$ within the *ab*-plane of the HTT unit cell with $I4/mmm$ symmetry. Dashed circles represent the positions of the Co ions in adjacent layers. Charge order reduces the HTT lattice symmetry to the space group $Bmmm$. The magnetic unit cell is indicated by green color. The antiferromagnetic spin correlations will be discussed in Chap. 6.

Cooperative charge- and spin-ordered phases are common in doped transition metal oxides with layered perovskite structure. Especially in case of half-doping, the charge disproportionation may provide a commensurate phase on the square lattice and a simple arrangement of differently charged ions, although the underlying interactions may be complex. Checkerboard-like charge ordering was found in the half-doped single-layered perovskite systems $La_{0.5}Sr_{1.5}MnO_4$ [6, 210], $La_{1.5}Sr_{0.5}CoO_4$ [8], and $La_{1.5}Sr_{0.5}NiO_4$ [158, 191, 206]. In the strong-correlation limit, there is a natural possibility for a stable Wigner

crystal state [241, 242] on the square lattice in two-dimensional systems, *i.e.* for the single-layered cobaltate with an equal number of Co^{2+}/Co^{3+} ions at $x = 0.5$. A Wigner crystal is a crystalline phase of an electron system, which can be stabilized through strong electron correlations in comparison with their kinetic energy. Correlation effects can be enhanced when the electron density or the dimensionality is reduced. So, the minimal dimensionality of single-layered perovskite systems in the Ruddlesden-Popper series favors the stabilization of charge order. For the single-layered perovskites, the interlayer frustration may play a crucial role to prevent long-range three-dimensional ordering [212]. The local oxygen displacements in a CoO_6 octahedron, due to the periodical modulation of the nominal Co charge, may provide valuable information about the Co^{3+} spin-state degree of freedom. This motivates the detailed analysis of the charge-order superstructure of $La_{1.5}Sr_{0.5}CoO_4$. Only few superstructure reflections were analyzed in a previous characterization of the charge ordered phase by a triple-axis neutron diffraction investigation [8].

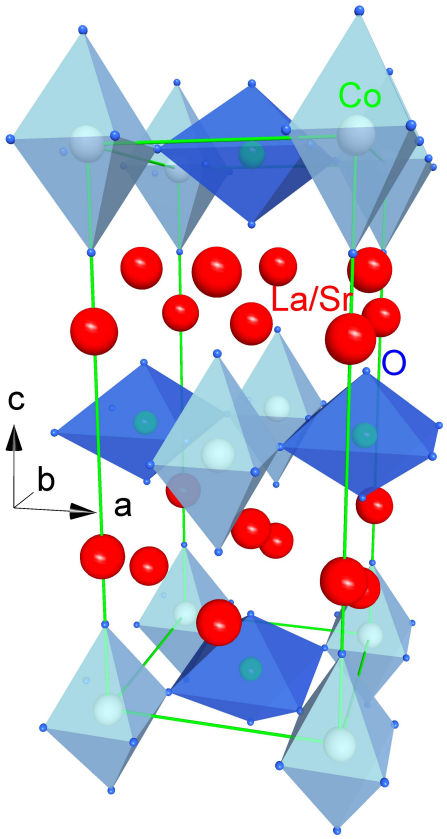

Figure 5.2.: Breathing-type distortion of CoO_6 octahedra in checkerboard-like charge ordered $La_{1.5}Sr_{0.5}CoO_4$ as proposed by Zaliznyak *et al.* [8]. The HTT space group symmetry $F4/mmm$ is broken by the modulated displacement of in-plane O_{basal} and out-of-plane oxygen O_{apical}. The authors attribute this Jahn-Teller compatible distortion to a Co^{3+} intermediate-spin state.

The transition temperatures for checkerboard-like charge order in $La_{0.5}Sr_{1.5}MnO_4$ [210] with $T_{co} \sim 217$ K [6] and in $La_{1.5}Sr_{0.5}NiO_4$ [206] with $T_{co} \sim 480$ K are nearly identical.

The stabilization of charge order affects the magnetic ordering type at lower temperatures by defining the spin sublattices and determining the effective exchange paths. Vice versa, the antiferromagnetic spin interaction may stabilize charge order [243]. In $La_{2-x}Sr_xNiO_4$, the combined spin and charge order was discussed in terms of a stripe model [158], where at $n_h = 1/3$ the periodicities of spin and charge order exactly correspond to each other; the wavelength of the charge ordering is exactly half that of the spin ordering, or the charge-order propagation vector $\mathbf{q}_{co}$ is twice as large as that of the spin order $\mathbf{q}_{so}$, $\mathbf{q}_{co} = 2\mathbf{q}_{co}$. In the intermediate hole doping region $1/3 \leq n_h \leq 0.5$, the stripe order consists of the mixture of $n_h = 1/3$ stripe order and $n_h = 1/2$ charge/spin order [158]. At half doping, all nearest-neighbor sites of Ni^{2+} are occupied by holes and effective exchange interactions between spins are reduced. In comparison to nickelates and manganites, a higher charge order transition temperature $T_{co} = 825(27)$ K and short-range spin order below $T_{so} \sim 30$ K were determined in $La_{1.5}Sr_{0.5}CoO_4$ [7, 8]. The half-doped cobaltate exhibits incommensurate spin order with the propagation vector $\mathbf{Q}_s = (\frac{1}{2} + \epsilon, 0, 1)$, $\epsilon = -0.008$, in $F4/mmm$ setting of the non-ordered crystal. In our measurements, the in-plane correlation length of the spin order is $\xi_{||} = 68(3)$ Å, and the out-of-plane correlation length is $\xi_{\perp} = 9.9(3)$ Å. Only adjacent CoO_2 layers are coupled through this small out-of-plane correlation length. Coexistent checkerboard-like charge order was proposed to be stabilized up to $T_{co} = 825(27)$ K in Ref. [8]. The large difference in the ordering temperatures ($T_{so} \ll T_{co}$) was ascribed to an effective decoupling of both phenomena in contrast to $T_{co} = 217$ K and $T_{so} = 110$ K in $La_{0.5}Sr_{1.5}MnO_4$ [6]. Charge-ordering superstructure reflections exhibit a finite in-plane correlation length $\xi_{||} = 26(2)$ Å and a diffuse broadening along the out-of-plane lattice direction, leading to $\xi_{\perp} = 8.1(3)$ Å. Corresponding reflections were found at positions $\tau \pm \mathbf{Q}_c$ with $\mathbf{Q}_c = (1, 0, l)$ and $(0, 1, l)$ for $l = 0, 1$ in $F4/mmm$ notation. Note that typically the alternative setting $F4/mmm$ is chosen in a neutron diffraction experiment, where the unit cell is rotated by 45° and lattice constants are elongated by $\sqrt{2}$. In view of the stripe-ordered phase in nickelates one would expect a direct correspondence between the periodicity of spin and charge order and thus incommensurate charge order reflections with $\epsilon_{co} = 2\epsilon_{so}$. The deviation of the spin-order periodicity from a commensurate value with $\epsilon_{so} = -0.008$ is small. Due to the short correlation length and therefore the large peak width in reciprocal space, the charger-order reflections appear to be commensurate. The combined spin and charge ordering scheme is shown in Fig. 5.1. Neutron diffraction with polarization analysis on antiferromagnetic Bragg peaks revealed that the spin moment lies nearly within the CoO_2 layers (standard error for the out-of-plane displacement $\Delta c \sim 5°$) [244]. The antiferromagnetic sublattices are rotated by 12° to the Co-O_{basal} bonds. The standard setting of the non-ordered crystal structure is $I4/mmm$ (No. 139). Charge ordering breaks the translation symmetry of the HTT lattice and superstructure reflections can be observed.

A quantitative analysis of the observed charge-order reflections by the scattering func-

tion $S(\mathbf{Q}, 0)$ for specific $\mathbf{Q}$ values with finite correlation lengths suggests a harmonic modulation of in-plane and out-of-plane oxygen displacements. This modulation is directly coupled to the Co ion oxidation and spin state, *i.e.* a breathing-type distortion of the $Co^{2+}O_6$ and $Co^{3+}O_6$ octahedra is found. Zaliznyak *et al.* obtained oxygen displacements $\varepsilon_{a,b} = 0.012(1)$ and $\varepsilon_c = -0.0058(4)$ in lattice units [8]. The proposed breathing-type distortion is shown in Fig. 5.2. Due to the increase of superstructure intensities with increasing $|\mathbf{Q}|$ in a diffraction experiment with thermal neutrons, only few charge-order reflections at large $\mathbf{Q}$ values were collected in this triple-axis diffractometer experiment. To determine the charge order distortion in $La_{1.5}Sr_{0.5}CoO_4$ in detail, experiments were carried out on neutron four-circle single diffractometers using three well-characterized samples.

5.2. Checkerboard Charge Ordering at Half Doping

For a detailed crystallographic analysis of the charge-order superstructure the number of reflections has to be several times greater than the number of structural parameters. The choice of the neutron diffraction instrument is of importance for this purpose. The disadvantage of a standard thermal triple-axis spectrometer for a structural analysis is the constraint to a scattering plane. Only few superstructure reflections can be collected and the integrated intensity, needed for the structure refinement, is difficult to determine. A four-circle diffractometer at a hot neutron source is the instrument to precisely integrate a large number of reflection intensities in reciprocal space.

Synchrotron x-ray scattering studies have provided evidence for spatial modulations of charge densities in nickelates and cuprates [245, 246]. As presented above, $La_{1.5}Sr_{0.5}CoO_4$ exhibits a charge order instability with a nominal checkerboard-like arrangement of Co^{2+}/Co^{3+} ions within the CoO_2 layer. We found no indications for this charge ordering in the half-doped cobaltate in a standard single-crystal x-ray diffraction experiment. Precession maps were calculated from a long-run experiment (∼4 d) on a sample, nearly spherical in shape with $r \sim 80$ μm. Details of the single-crystal diffractometer can be found in Sec. 3.2.2. Despite the high transition temperature in comparison to the half-doped manganite and nickelate, no superstructure reflections were seen. Charge- and spin-order correlation lengths and transition temperatures were characterized on a triple-axis neutron diffractometer, which will be discussed in Chap. 6. The spin-glass transition temperature and the correlation lengths are in good agreement with data from Zaliznyak *et al.* previously published [7, 8]. Main structure and charge-order superstructure reflections in $La_{1.5}Sr_{0.5}CoO_4$ were collected for three samples on the hot neutron four-circle diffractometers 5C2 at the Laboratoire Léon Brillouin in Saclay, France and *HEIDI* at the Forschungsreaktor München II in Garching, Germany. Cu-(220) monochromated radiation with $\lambda = 0.87$ Å was used and higher order contamination was suppressed using an Er-filter (intensity ratio $I(\lambda/2)/I(\lambda) = 0.0113$). Structure model refinements of the

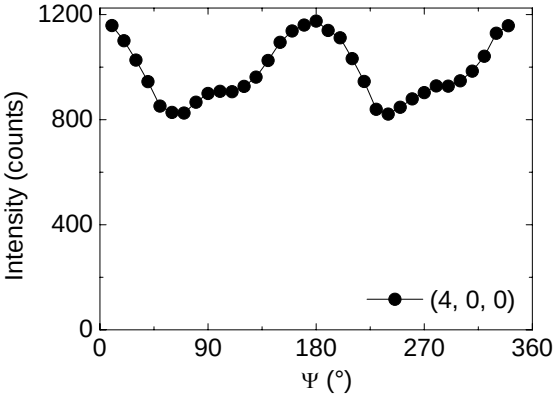

Figure 5.3.: (4,0,0) Ψ scan for the single-crystal neutron diffraction on $La_{1.5}Sr_{0.5}CoO_4$ at room temperature. An intensity variation of 33 % is due to a strong extinction in the sample.

main structure base on the data integration using *Pron2k* by M. Meven [247, 248] and the software program *Jana2000* [177]. A Gauss grid integration [249] in *datap* was used for the absorption correction.

Sample I: For the analysis of the main structure, 1216 reflections of the HTT phase in $F4/mmm$ notation in the angle region $7.61° \leq 2\theta \leq 96.38°$ were collected on 5C2. *Sample II:* For the collection of charge order superstructure reflections, a well characterized single crystal was used. It was cut along the $I4/mmm$ lattice directions to a cuboid with $2 \times 2 \times 1$ mm^3 edge lengths with mosaic spread $\lesssim 0.13°$ and mounted on *HEIDI*. A set of 550 main structure reflections was collected. Systematic instrumental errors were accounted for by a McCandlish factor 0.031. Systematic errors due to absorption and extinction are indicated through so-called Ψ-scans, where intensities for reflections with χ angles near 90° are measured for different Ψ angles [250]. While the scattering condition is fulfilled for all Ψ, the rotation against the azimuthal angle tests different transmission paths through the crystal. A Ψ scan for (4, 0, 0) reflection in $F4/mmm$ notation is shown in Fig. 5.3. In comparison with x-ray diffraction, absorption is less pronounced for neutron scattering. The absorption coefficient of $La_{1.5}Sr_{0.5}CoO_4$ is calculated to 0.026789 mm^{-1} for $\lambda = 0.87$ Å. The importance of extinction in our sample was investigated with Ψ-scans of the (400) reflection. The crystal structure refinement is hindered by extinction through an intensity variation of ~ 33 %. The sample was too small to collect a larger set of superstructure reflections with $I > 3\sigma(I)$.

Sample III: A crystal, being ∼50 times larger than sample II with cylindrical shape (6 mm in diameter and 7 mm in length), was chosen to determine charge order superstructure reflections in a second attempt. A set of 179 $F4/mmm$ main structure reflections and 194 superstructure reflections according to $Bmmm$ symmetry in the angle range $10.06° \leq 2\theta \leq 89.64°$ was collected on *HEIDI*. The best description of the profile shapes for the superstructure reflections is given by lattice Lorentzians, corresponding to a finite-range harmonic modulation in real space. Some additional weak reflections, breaking the B extinction rule, were collected. These are ascribed to a charge order twin structure

which is rotated by 90° in the *ab*-plane. Data were integrated and Lorentz corrected, including a McCandlish coefficient 0.01 of instability considered in the weighting scheme of the refinement using the program *Pron2k* [247].

A comparison between the structure parameters of $La_{1.5}Sr_{0.5}CoO_4$ in $I4/mmm$ and $F4/mmm$ settings at room temperature, *i.e.* for a non-ordered description of the main-structure reflections, is given in Tab. 5.1. For sample I, reflections were averaged over symmetry equivalent positions. Relative atomic positions of sample I and II in the neutron diffraction experiment and the x-ray sample are in good agreement. Atomic displacement parameters strongly depend on the 2θ angle region (see datasets for sample II), underlining the influence of extinctions in the sample. Since isotropic parameters are enhanced for all samples in neutron diffraction experiments, the influence of extinction is expected. In comparison with an x-ray diffraction experiment, the additional contribution of oxygen disorder to the atomic displacement parameters is measurable more precisely. The atomic scattering factors are not electron density dependent, but nucleus, i.e. scattering length dependent. The atomic scattering lengths[1] are of the same magnitude for neutron diffraction.

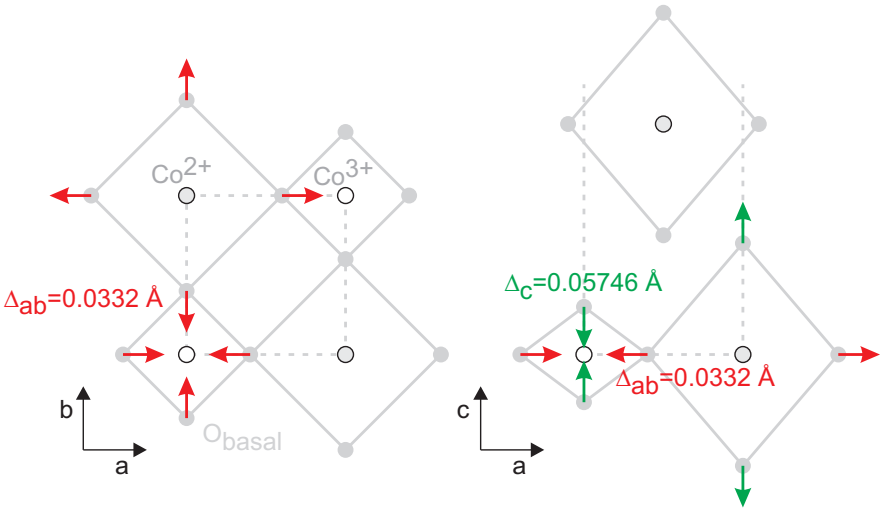

Figure 5.4.: Scheme of the in-plane and out-of-plane breathing type distortion observed in charge ordered $La_{2-x}Sr_xCoO_4$ at room temperature in $I4/mmm$ notation. The modulation is similar to a simple enlargement and shrinking of the CoO_6 octahedra, which is not Jahn-Teller active.

Breathing-type charge ordering corresponds to a symmetry reduction from $F4/mmm$ to $Bmmm$ (No. 65 D_{2h}^{19}). The displacement of the in-plane oxygen ion and the modu-

[1] La b_{coh} = 8.24 fm, Sr b_{coh} = 7.02 fm, Co b_{coh} = 2.49 fm, and O b_{coh} = 5.803 fm [251]

$La_{1.5}Sr_{0.5}CoO_4$	5C2 Sample I I4/mmm	HEIDI Sample II F4/mmm	HEIDI Sample II F4/mmm	XSCD F4/mmm
2θ region (°)	7.61 - 96.38	7.95 - 114.96	7.95-70	
a (Å)	3.82(2)	5.435(9)	5.435(9)	5.4294(1)
c (Å)	12.52(8)	12.56(1)	12.56(1)	12.5345(3)
V (Å^3)	182.9	371.0(1)	371.0(1)	369.50(2)
La/Sr (0,0,z),z =	0.36190(5)	0.36182(8)	0.36198(8)	0.361983(3)
U_{11}=U_{22} (Å^2)	0.0123(2)	0.0072(4)	0.0074(5)	0.00354(2)
U_{33} (Å^2)	0.0101(2)	0.068(4)	0.0069(7)	0.00165(2)
U_{iso} (Å^2)	0.0116(1)	0.0071(2)	0.0072(3)	0.00291(1)
Co (0,0,0)				
U_{11}=U_{22} (Å^2)	0.0101(5)	0.0023(9)	0.003(1)	0.00056(2)
U_{33} (Å^2)	0.0120(7)	0.009(1)	0.013(2)	0.00328(3)
U_{iso} (Å^2)	0.0107(3)	0.0045(6)	0.0063(9)	0.00147(2)
O_{basal} $(\frac{1}{4},\frac{1}{4},0)_{F4/mmm}$, $(0,\frac{1}{2},0)_{I4/mmm}$				
U_{11} (Å^2)	0.0137(3)	0.0075(5)	0.0090(6)	0.0044(1)
U_{33} (Å^2)	0.0120(3)	0.0142(6)	0.0116(7)	0.0096(2)
U_{12} (Å^2)	-	-0.0009(4)	-0.0010(4)	-0.0010(1)
U_{iso} (Å^2)	0.0143(2)	0.0097(3)	0.0099(4)	0.0061(1)
O_{apical} (0,0,z),z =	0.1694(1)	0.1698(2)	0.1698(1)	0.1690(1)
U_{11}=U_{22} (Å^2)	0.0229(3)	0.0162(6)	0.0182(6)	0.0148(2)
U_{33} (Å^2)	0.0189(4)	0.0169(8)	0.0142(9)	0.0136(3)
U_{iso} (Å^2)	0.0216(2)	0.0165(4)	0.0169(4)	0.0144(1)
Bond lengths				
La-O_{basal} (Å)	2.5770(4)	2.5892(8)	2.5879(7)	2.58411(3)
La-O_{apical} (Å)	2.409(1)	2.412(2)	2.413(2)	2.419(1)
La-O_{apical} (Å)	2.7315(2)	2.7463(3)	2.7467(3)	2.7424(2)
Co-O_{basal} (Å)	1.911(5)	1.922(5)	1.922(5)	1.9195(1)
Co-O_{apical} (Å)	2.120(1)	2.132(2)	2.1331(18)	2.119(1)
Refinement				
R (%)	5.44	5.15	3.16	5.11
$wR(F^2)$ (%)	7.65	13.13	7.94	2.15
N_{obs}	1216	550	541	6007
N_{ind}	193	176	226	494

Table 5.1.: Results of the x-ray and neutron single-crystal structure refinement of $La_{1.5}Sr_{0.5}CoO_4$ in $I4/mmm$ or $F4/mmm$ notation (No. 139) at $T = 295$ K. The refinement bases on F_0^2 using 13 parameters with reflections $F^2 > 2\sigma(F^2)$. Reflections for the first two refinements were averaged over equivalents to minimize the strong extinction.

Atom	Wyckoff		Atom	Wyckoff	
La1/Sr1	4*i*	(0, 0, *z*)	La2/Sr2	4*j*	(0, 0.5, *z*)
Co1	2*a*	(0, 0, 0)	Co1b	2*c*	(0.5, 0.5, 0)
O1a	8*o*	(0.25-ϵ, 0.25-ϵ, 0)			
O2a	4*i*	(0, 0, $z-\epsilon$)	O2b	4*j*	(0.5, 0.5, $z+\epsilon$)

Table 5.2.: Atomic position in the breathing-type distorted $La_{1.5}Sr_{0.5}CoO_4$ with $Bmmm$ (No. 65 D_{2h}^{19}) symmetry.

lation of O_{apical} positions for the checkerboard-like arrangement of Co^{2+}/Co^{3+} ions lifts the face centering F. The staggered stacking of adjacent CoO_2 layers breaks the fourfold rotational symmetry. Our data-collection strategy accounted not only for breathing-type mode superstructure reflections at large $\mathbf{Q}$ values, but also for further symmetry positions, to test more complex displacement modulations. We found reflections, which we mainly ascribe to the equivalent charge-order twin with an in-plane charge arrangement rotated by 90°. For a total number of 548 collected reflections, 57 weak reflections (h, k, l) with h even, k even, and l odd or h odd, k odd, and l even are not compatible with $Bmmm$ even when including twinning. This may indicate a more complex distortion pattern. The refinement of a centrosymmetric $Bmmm$ structure model is based on F^2, considering intensities with $F^2 > 3\sigma(I)$. Reflections were not averaged for the refinement procedure. The results of the refinement are given in Tab. 5.3.

The observed variation of z coordinates of O2a and O2b corresponds to a modulation $\widetilde{z} \pm \varepsilon_z$ with $\varepsilon_z = 0.0046$ around the average position $\widetilde{z} = 0.1700(1)$, as it is determined in the refinement of the $F4/mmm$ structure model with the fundamental reflections. Concomitantly, the in-plane bond length Co-O_{basal} is modulated by the oxygen displacement (0.25-ε_a, 0.25-ε_b, 0) with ε_a=0.0037(4) and ε_b=0.0050(3). The z position of La2/Sr2 is shifted by $-0.00095(8)$ relative to the $F4/mmm$ symmetry position (0,0.5,0.5-z_{La1}). The criteria of the fit are $R = 6.87$ (%) and wR=22.52 (%). wR is typically enhanced by extinction effects in the high-quality crystal.

The charge order superstructure, refined with our large data set, disagrees to the distortion proposed by Zaliznyak *et al.*. In their model the Co-site with shorter in-plane Co-bonds exhibits an elongated Co-O_{apical} bond, suggesting a Jahn-Teller active Co^{3+} intermediate-spin state. In contrast our model yields a shorter Co-O_{apical} bond for the Co-site with shorter in-plane bond. The real space CoO_6 octahedra modulation anisotropy of $\Delta_c = 0.0575$ Å in c-direction, $\Delta_a = 0.020(2)$ Å in a-direction, and $\Delta_a = 0.027(2)$ Å in b-direction around the average positions is found. The bond-valence sums $v_{Co1} = 3.07$ and $v_{Co2} = 2.49$ indicate the suitable charge segregation. The CoO_6 octahedra are elongated along the out-of-plane direction by the reduction of internal strains in the single-layered perovskite system. The observed modulation provides no further multiplet splitting

Atom	U_{11}	U_{22}	U_{33}	U_{12}
La1/Sr1 (0, 0, z) z =0.36114(8)	0.0044(2)	0.0044(2)	0.0025(4)	-
La2/Sr2 (0, 0.5, z) z =0.13791(8)	=U_{11} La1	=U_{22} La1	=U_{33} La1	-
Co1 (0, 0, 0)	0.0041(6)	0.0041(6)	0.0016(8)	-
Co2 (0.5, 0.5, 0)	=U_{11} Co1	=U_{22} Co1	=U_{33} Co1	-
O1 (x, y, 0) x =0.2463(4) y =0.2450(3)	0.0034(3)	0.0034(3)	0.0115(4)	-0.0012(2)
O2a (0, 0, z) z=0.1654(1)	0.0137(3)	0.0137(3)	0.0078(5)	-
O2b (0.5, 0.5, z) z=0.1745(1)	0.0137(3)	0.0137(3)	0.0078(5)	-
Co1-O1 = 1.88766 Å Co1-O2a = 2.07524 Å Co2-O1 = 1.95407 Å Co2-O2b = 2.19016 Å				
R=6.87 (%), wR=22.52 (%), $g_{11} = 1.89 \cdot 10^{-6}$, $g_{22} = 2.38 \cdot 10^{-6}$, $g_{33} = 1.14 \cdot 10^{-6}$, $10.06° \leq 2\theta \leq 89.64°$				

Table 5.3.: Model of the charge-ordered structure in $La_{1.5}Sr_{0.5}CoO_4$ in space group $Bmmm$ at room temperature. The refinement bases on F^2 with 14 parameters for reflection intensities $F^2 > 3\sigma(I)$.

and cannot be associated with a Co^{3+} intermediate-spin occupation via a Jahn-Teller distortion.

5.3. Conclusions

We presented a detailed study of the charge-ordering distortion in $La_{1.5}Sr_{0.5}CoO_4$ at room temperature by means of single-crystal x-ray and neutron diffraction. The analysis of the local oxygen displacements of the associated $Co^{2+}O_6$ and $Co^{3+}O_6$ octahedra modulation provides valuable information about the Co^{3+} spin-state degree of freedom. Considering the enhanced charge-order transition temperature (T_{co} = 825(27) K [8]) in comparison to nickelates ($T_{co} \sim$ 480 K [206]) and manganites ($T_{co} \sim$ 217 K [6]), charge order is expected to be well stabilized at room temperature. To analyze the charge-order

correlation lengths and the magnetic coupling scheme in $La_{1.5}Sr_{0.5}CoO_4$ in detail, we investigated the spin- and charge-ordering characteristics on different triple-axis neutron spectrometers. The results will be discussed in Chap. 6. At this point, it is mentionable that the static spin- and charge-order correlations found in our measurements on large single-crystals exhibit similar characteristics, *e.g.* the in-plane and out-of-plane correlation lengths fully agree with previous studies [7]. The charge ordering is short-ranged and the peak-shape of superstructure reflections corresponds to so-called factorized lattice Lorentzians, as proposed in Ref. [8]. The quantitative analysis of the displacement modulation of oxygen ions by Zaliznyak *et al.* is based on triple-axis neutron diffraction data of few superstructure reflections. Our experiment on the hot four-circle neutron diffractometer *HEIDI* allowed the collection and accurate integration of a large set of superstructure reflections. We find a breathing-type modulation of the CoO_6 octahedra with the same sign for O_{basal} and O_{apical} distortions. Therefore, O_{basal} and O_{apical} ions approach Co^{3+} ions and move away from Co^{2+} ions. Additional weak superstructure reflections, which should be systematically extinct in $Bmmm$ settings of the distortion, were mostly ascribed to the equivalent charge-order twin. The observed displacement modulation is in contrast to the previously proposed modulation of Zaliznyak *et al.* and the proposed Co^{3+} intermediate-spin state [8]. We find no indication for a Jahn-Teller like distortion on the Co^{3+} site and, therefore, no indication for an intermediate-spin occupation at room temperature. Both Co^{3+} low-spin ($t_{2g}^6 e_g^0$) and high-spin occupation ($t_{2g}^4 e_g^2$) are in agreement with our results. The strong anomalies of the thermal expansion at high temperatures suggest a stabilization of the low-spin state, being the ground state of the system only at low temperatures.

6. Magnetism in $La_{2-x}Sr_xCoO_4$

This chapter presents the static and dynamic spin correlations in $La_{2-x}Sr_xCoO_4$ (x=0.3, 0.4, 0.45, 0.5, 0.6), which have been studied by means of single-crystal neutron scattering. The comparison of field-cooled and zero-field-cooled susceptibility measurements indicates a spin-glass behavior with a strong in-plane to out-of-plane anisotropy. Commensurate nearest-neighbor spin correlations are observed in the $x = 0.3$ sample. The commensurate spin correlations are short-ranged but similar to the parent compound La_2CoO_4 with spin moments within the CoO_6 layer and strongly diluted nearest-neighbor spin correlations. Further doping induces an incommensurate modulation of the antiferromagnetic spin correlation, which we attribute to a stripe-like phase. The incommensurability ϵ for $x > 0.3$ is found to change nearly linearly with hole doping $n_h = x + 2\delta$ similar to $La_{2-x}Sr_xNiO_4$ (LSNiO) [158] and $La_{2-x}Sr_xCuO_4$ (LSCuO) [252]. Overall, the effective antiferromagnetic exchange seems to be dominated by Co^{2+} ions ($3d^7$ $S = 3/2$), where the nearest-neighbor interaction is replaced by a next-nearest-neighbor interaction with respect to charge ordering. Combining the magnon dispersion analysis with the structural studies as functions of T and x of Chapters 4 and 5, we obtain an evidence, that Co^{3+} in $La_{1.5}Sr_{0.5}CoO_4$ is in the low-spin state.

6.1. Introduction

Doped transition metal oxides with layered crystal structures show a rich variety of unusual ordering phenomena. Among these phenomena, a segregation of holes into so-called stripes, forming antiphase-domain walls between antiferromagnetic domains, has been experimentally observed in cuprates and nickelates [130, 191, 209, 253, 254] and attracts great interest due to its interrelation to high-temperature superconductivity [4]. From a theoretical point of view, stripes have been proposed as a result of competing interactions [255], Hartree-Fock calculations [256], and Monte Carlo simulations [257]. The question whether stripes are induced by elastic, magnetic, or electronic interactions is still open [213]. Elastic and inelastic neutron scattering are ideal probes to study the nature of stripes in layered perovskite systems [62, 252, 258]. Due to the structural and magnetic similarities to the cuprate and nickelate system and the possible influence of the Co^{3+} spin-state degree of freedom, the study of magnetic correlations in the cobaltate system $La_{2-x}Sr_xCoO_4$ is of particular interest.

In general, the lattice dimensionality d and the dimensionality of the effective exchange integrals of a system play a crucial role for the magnetic ground state. Single-layered

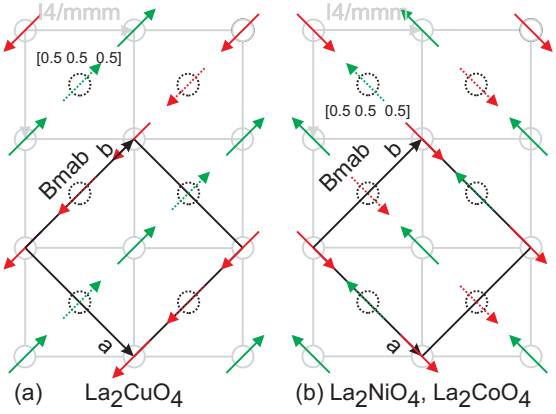

Figure 6.1.: Schematic representation of the three-dimensional spin order of La_2MO_4 (M = Cu, Ni, Co) within the ab-plane in $Bmab$ setting. Circles with solid lines represent M^{2+} ions of one MO_2 plane, circles with dashed lines ions of the adjacent plane below or above. (a) The antiferromagnetic propagation vector $\mathbf{Q}_m$ of La_2CuO_4 is parallel to the [100]-direction, perpendicular to the direction of the spin moment $\mathbf{S} \parallel [010]$, and perpendicular to the tilting direction of the CuO_6 octahedra [262]. (b) For La_2MO_4 (M = Ni,Co) $\mathbf{Q}_m \parallel \mathbf{S}$ [11, 127].

perovskites represent a nearly two-dimensional square-lattice system, where the dimensionality of the magnetic exchange is essential for long-range order at finite temperatures [259]. According to the Mermin-Wagner theorem [260], long-range order is excluded for an isotropic Heisenberg model with three-dimensional exchange integrals $J_x = J_y = J_z \neq 0$ in two lattice dimensions. Within an XY model ($J_x = J_y \neq 0, J_z = 0$), there is also no finite transition temperature to conventional long-range order [260], but topological order (Kosterlitz-Thouless transition) below a critical temperature [261] exists. For an Ising model with ($J_x = J_y = 0, J_z \neq 0$), *i.e.* only one spin component coupled, there exists long-range order at finite temperatures $T > 0$ K for the two-dimensional lattice. In real systems three-dimensional order usually occurs, however, also in XY and Heisenberg systems. The reason is the interlayer coupling J_{perp} or the Ising anisotropy in single-layered transition metal oxides. The effective model can be investigated by the critical exponents in the temperature dependence of the sublattice magnetization and the spin-correlation function.

Remarkable similarities are found for the undoped case in the generic phase diagram of single-layered perovskites. The parent compounds La_2MO_4 (M = Co, Cu, Ni) are isostructural and exhibit long-range antiferromagnetic order with similar spin structures in the LTO phase [11, 73, 74, 262, 263]. A schematic representation of the observed spin arrangement within the idealized MO_2 square lattice is shown in Fig. 6.1. Circles with solid lines represent M ions of one MO_2 plane, while dashed circles symbolize the ions of the adjacent plane above or below. The lattice constants of the LTO phase with $Bmab$ symmetry are along the face diagonal of the former HTT unit cell in $I4/mmm$ notation. In general, the spin moments $\mathbf{S}$ tend to lie in the MO_2 planes for all these

	Co	Ni	Cu
S	3/2	1	1/2
$\vec{Q}_m$	[100]	[100]	[100]
$\vec{Q}_S$	[100]	[100]	[010]
T_N (K)	275	330	312
$T_{I4/mmm \rightarrow Bmab}$ (K)	900	780	530

Table 6.1.: Antiferromagnetic spin structures of La_2MO_4 (M=Co, Cu, Ni) after [11, 117, 126, 127, 271–273]. Given directions refer to orthorhombic $Bmab$ symmetry.

compounds. Nearest neighbors of Co^{2+} ions in the high-spin state ($3d^7$, $S = 3/2$) are coupled antiferromagnetically in La_2CoO_4 [11]. The spin structure with $T_N = 275$ K can be characterized by a propagation vector $\mathbf{Q}_m = [1, 0, 0]$ and parallel spin direction $\mathbf{S} = [1, 0, 0]$ within the ab-plane of the orthorhombic $Bmab$ unit cell. Note that the propagation vector is determined by the spin arrangement of the adjacent layers in the three-dimensional Néel state. The spin structure is equal to the structure in La_2NiO_4, shown in panel 6.1 (b). For La_2CuO_4, the spin direction is rotated by 90° in the MO_2-plane and canted 0.17° out of the plane, due to the Dzyaloshinsky-Moriya interaction [264, 265] in the LTO phase [266]. Spin canting perpendicular to the CuO_2 planes is induced by spin-orbit coupling in the LTO phase with tilted CuO_6 octahedra. The characteristics of the parent compounds are summarized in Tab. 6.1. The nominal spin moment S on the quasi square lattice is systematically decreasing with increasing atomic number. The Néel temperatures are comparable in the series with decreasing bond-length mismatch, but the LTO phase-transition temperatures are reduced. La_2CuO_4 is a model system for a two-dimensional Heisenberg antiferromagnet with a weak interlayer coupling ($J_\perp/J \simeq 2 \cdot 10^{-5}$) [266]. La_2CoO_4 and La_2NiO_4 are proposed to be realizations of the two-dimensional Ising model [11]. As in the cuprate [162] and the nickelate system [267, 268], long-range magnetic order is suppressed in $La_{2-x}Sr_xCoO_4$ by strontium doping (see Ganguly *et al.* [155] and Y. Moritomo *et al.* [27]). This may be ascribed to an effective dilution of transition-metal spins below the square-lattice percolation threshold $x_c \sim 0.41$ of holes [269]. Diagonal and parallel stripe-order modulations in cuprates and nickelates are induced at low doping levels [158, 159] well below the percolation limit. Interestingly, incommensurate parallel spin-density modulation is destroyed in $La_{2-x}Sr_xCu_{1-y}Ni_yO_4$ by Ni substitution near $x = y$ and bulk three-dimensional antiferromagnetic order is reestablished [270].

In order to investigate the magnetic coupling scheme in the half-doped cobaltate and to understand the crossover from commensurate ($x = 0.3$) to checkerboard order ($x = 0.5$), *i.e.* the evolution of the static spin correlations in the spin-glass phase, large single crystals of $La_{2-x}Sr_xCoO_4$ (x=0.3, 0.4, 0.45, 0.5, 0.6) were investigated by elastic and

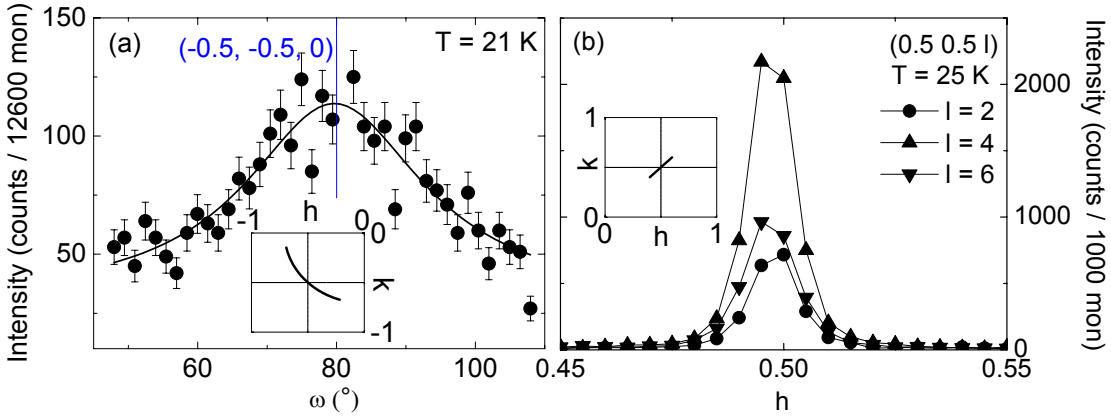

Figure 6.2.: Antiferromagnetic and LTO superstructure reflections of $La_{1.7}Sr_{0.3}CoO_4$. (a) Rocking scan along the commensurate antiferromagnetic reflection (-0.5, -0.5, 0) in $I4/mmm$ notation. (b) Scans in (x, x, 0)-direction across LTO superstructure reflections ($\frac{1}{2}$, $\frac{1}{2}$, l) with l even, $l > 0$. Cooperative CoO_6 tilting reduces the lattice symmetry to $Bmab$.

inelastic neutron scattering. In case of $x = 0.3$, a polarization analysis was used to separate structural and magnetic contributions.

6.2. Commensurate Spin Correlations in $La_{2-x}Sr_xCoO_4$ (x = 0.3, 0.5)

The spin correlations in the $La_{2-x}Sr_xCoO_4$ for $x = 0.3, 0.4, 0.45, 0.5$, and 0.6 were investigated on large single-crystals by elastic and inelastic neutron scattering. The static spin correlations were found to be near to a commensurate value for the $x = 0.3$ and $x = 0.5$ samples. Let us first compare the fundamental differences in the spin arrangement, if the charge order is accounted for and the LTO distortion is lifted.

6.2.1. Antiferromagnetic Spin Correlations in $La_{1.7}Sr_{0.3}CoO_4$

Antiferromagnetic and structural reflections from the symmetry reduction (HTT to LTO) in $La_{1.7}Sr_{0.3}CoO_4$ were primarily investigated in (1,1,0)/(0,0,1) and (1,0,0)/(0,1,0) orientation on the cold triple-axis spectrometer G43 at the Laboratoire Léon Brillouin. According to integral and zonal extinction rules, the transition from $I4/mmm$ to $Bmab$ symmetry leads to additional structure reflections ($h/2$, $k/2$, l). Indices are restricted to h, k odd and l even but $l \neq 0$ in the HTT notation. For single face centering B in the orthorhombic Bravais lattice, general reflection conditions with $h + l = 2n$ arise.

Gliding planes a along (0,1,0) and b along (0,0,1) lead to special conditions $h = 2n$ for $(h, 0, l)$ and $k = 2n$ for $(h, k, 0)$. Examples of superstructure reflections at $T = 25$ K are shown in Fig. 6.2 (b). The observed peak width is the same for HTT and LTO reflections. With the momentum resolution of our experiment, orthorhombic lattice constants were not resolvable. Even under consideration of structural twinning, superstructure reflections ($\frac{1}{2}$, $\frac{1}{2}$, l) with odd l should be absent. Weak reflections of the latter (factor ~ 20 lower), scaling with the temperature dependence of reflections with even l, were observed and can be attributed to the Renninger effect in high-quality single crystals for $l > 0$ [274, 275]. The Renninger effect describes multiple diffraction, when two reciprocal lattice points (h_1, k_1, l_1) and (h_2, k_2, l_2) pass the surface of the Ewald sphere simultaneously. The diffracted beam of the first plane is again diffracted on the second plane. For a given space group, a Renninger reflection may be misleadingly attributed to a reflection $(h_1 - h_2, k_1 - k_2, l_1 - l_2)$, which may be systematically extincted in the real space group, and has to be taken into account for high-quality crystals. The Renninger effect can be analyzed by the angle dependence of the reflection intensity for azimuthal scans [179]. Such scans were not accessible in the given experimental setup. A monoclinic distortion of the crystal lattice due to an additional octahedron distortion by the apical oxygen displacement was reported in La_2CuO_4 [74], but the ($\frac{1}{2}$, $\frac{1}{2}$, l) reflections with odd l in $La_{1.7}Sr_{0.3}CoO_4$ scale perfectly with reflections with even l . An elastic rocking scan across the antiferromagnetic zone center (-$\frac{1}{2}$, -$\frac{1}{2}$, 0) (see Fig. 6.2 (a)) reveals a broad maximum, suggesting short-range spin correlations at $T = 21$ K. For weak scattering contributions a rocking scan avoids intensity variations due to the enhanced background scattering near the primary beam. Longitudinal, transverse, (x, 0, 0), and (0, x, 0) Q-scans across (-$\frac{1}{2}$, -$\frac{1}{2}$, 0) reveal no splitting or incommensurate shift of the superstructure reflections. Superstructure reflections ($\frac{1}{2}$, $\frac{1}{2}$, l) with even l are shown in Fig. 6.2 (b).

In order to verify the magnetic nature of the ($\frac{1}{2}$, $\frac{1}{2}$, 0) reflection, spin-polarized neutron scattering measurements were carried out at the cold triple-axis spectrometer 4F1 at the Laboratoire Léon Brillouin. The reflections ($\frac{1}{2}$, $\frac{1}{2}$, l) with $l > 0$, l even are structural in nature with an intensity variation according to the orthorhombic CoO_6-octahedra tilt distortion. As suggested by the previous measurements, the reflection (0.5, 0.5, 0) is purely magnetic due to short-range antiferromagnetic spin correlations. Fig. 6.3 (a) shows the spin-flip (SF) and non-spin-flip (NSF) scattering for neutron polarization $\mathbf{P}$ parallel or perpendicular to the scattering vector $\mathbf{Q}$ along ($\frac{1}{2} \pm x$, $\frac{1}{2} \pm x$, 0) at $T = 1.5$ K. Due to the SF intensity for neutron polarization $\mathbf{P} \parallel \mathbf{Q}$ and the missing contribution in the NSF channel, the measured intensity is of magnetic origin [187]. The magnetic spin-flip intensity contribution for $\mathbf{P} \perp \mathbf{Q}$ is restricted to the $\mathbf{P} \parallel \mathbf{y}$ channel. Comparing the intensity distributions from different polarization directions allows the determination of the spin direction by selection rules (see Sec. 3.5). The scattering plane is defined by the [1, 1, 0] and [0, 0, 1] directions. Together with the former results this gives a spin moment lying within the CoO_2 layers. Due to the short-range correlation it is not possible to differentiate between $\mathbf{Q}_m \| \mathbf{Q}_S$ of the orthorhombic phase or $\mathbf{Q}_m \perp \mathbf{Q}_S$ with

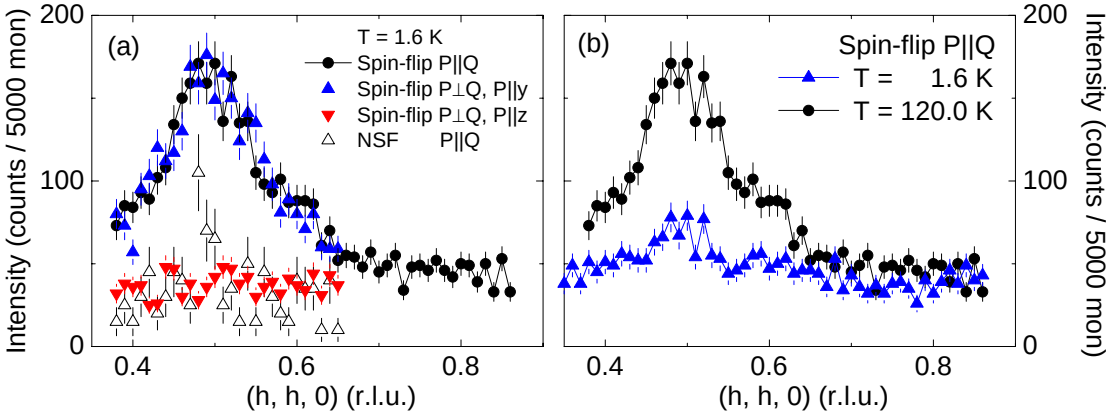

Figure 6.3.: Analysis of the spin direction by the comparison of the spin-flip and non-spin-flip scattering intensity for the $(\frac{1}{2}, \frac{1}{2}, 0)$ reflection in $La_{1.7}Sr_{0.3}CoO_4$ with different neutron polarizations $\mathbf{P}$. (a) Comparison of the spin-flip and non-spin-flip scattering at $T = 1.6$ K. Thus the Moment lies within the CoO_2 plane (for explanation see text). (b) Comparison of spin-flip scattering with $\mathbf{P}||\mathbf{Q}$ at $T = 1.6$ K and near the transition temperature $T = 120$ K.

spin direction $\mathbf{Q}_s$ rotated by 90° to the propagation vector $\mathbf{Q}_m$ of the low-temperature tetragonal phase [11] (see Table 6.1). The static magnetic correlations vanish almost fully at $T = 120$ K (see Fig. 6.3 (b)). Transverse and longitudinal scans revealed no discommensurations. Magnetic correlation lengths of the spin correlations can be deduced from the half peak width at half maximum for a Lorentzian shape function of reflections in reciprocal space, when the convoluted instrumental-resolution contribution is separated appropriately from the total peak width. With respect to the relatively small in-plane correlation length of $\xi_{||} \sim 5$ Å, the commensurate correlations would agree with dilute nearest-neighbor spin correlations within the CoO_2 layers, but one has to account for the difference between mobile holes at sufficiently high temperatures and doping levels and immobile non-magnetic impurities in the system. The site-percolation threshold on a square lattice with only nearest-neighbor interaction is $p_c = 0.593$ for a non-magnetic dilution [269]. Therefore, in the case of a non-magnetic dopant, the critical doping level is $x_c = 1 - p_c \approx 0.4$, and commensurate spin correlations at $x = 0.3$ are well in the undercritical region. The suppression of magnetic order in the two-dimensional Ising system $K_2(Co_{1-x}Mg_x)F_4$ at $x_c = 0.41$ agrees perfectly with the site-percolation theory [276].

The influence of immobile impurities and mobile holes can be compared with the doped La_2CuO_4 system. In 2D Heisenberg systems as $La_2Cu_{1-y}Zn_yO_4$, the critical doping level $y \sim 0.26$ is lower than the expected threshold [204]. However, the three-dimensional antiferromagnetic state in $La_{2-x}Sr_xCuO_4$ is destroyed by a small amount of holes ($x =$

0.02) [277] leading to a spin-glass regime. In this insulating spin-glass region $0.02 \leq x \leq 0.055$, incommensurate satellite reflections, indicating a diagonal spin modulation, were observed [159]. With respect to the effective suppression of antiferromagnetic correlations by mobile holes, the stability of commensurate nearest-neighbor correlations in single-layered cobaltates up to the hole doping level $x = 0.3$ is surprising. On the one hand, this may be ascribed to an effect of the Co^{3+}-Co^{2+} exchange coupling, when Co^{3+} ions are supposed to be magnetic and an antiferromagnetic nearest-neighbor interaction is assumed. On the other hand, the instability towards quasi-metallic conductivity may be important, which is shifted in cobaltates to $x = 1.5$ [22] in comparison to $x = 1$ in LSNiO [278] and the quasi metallic state above T_c in LSCuO, existing already at $x > 0.05$.

The temperature dependencies of the maximum of the structural and magnetic superstructure intensities are shown in Fig. 6.5. The transition temperatures of the orthorhombic distortion T_o and local magnetic order T_s are observed at $T_s \sim 130$ K and at $T_o \sim 220$ K in linear approximation of the temperature dependence of $(\frac{1}{2}, \frac{1}{2}, 0)$ and $(\frac{1}{2}, \frac{1}{2}, 4)$, see Fig. 6.5. The temperature dependence qualitatively agrees with the temperature dependence of (2.5, 8.5, -2) from a single-crystal x-ray diffraction experiment and the onset of the orthorhombic splitting ϵ at $T \sim 220$ K from the powder x-ray diffraction analysis. The superstructure reflection intensity in LSCuO was described by a power law behavior $(T_0 - T)^{2\beta}$ [229]. We find no indications for a power law behavior of the reflection intensities in $La_{1.7}Sr_{0.3}CoO_4$ for the given smeared-out transition temperature. Further analysis of the magnetic and structural phase transition including a Gaussian broadening cannot improve the approximation. Conclusively, $La_{1.7}Sr_{0.3}CoO_4$ exhibits short-range antiferromagnetic spin correlations ($\xi \simeq 5$ Å) in the orthorhombically distorted phase. Both, the CoO_6-octahedra tilting and the antiferromagnetic spin arrangement within the CoO_2 planes correspond to the arrangements found in the parent compound La_2CoO_4. Long range magnetic order is suppressed and the HTT/LTO transition temperature reduced through Sr doping.

Let us now focus on the dynamic spin correlations in $La_{1.7}Sr_{0.3}CoO_4$. The low-energy spin-wave dispersion was studied on the cold triple-axis spectrometer 4F2. Fig. 6.4 (a) shows a scan in $(x, -x, 0)$-direction across the antiferromagnetic superstructure reflection $(\frac{1}{2}, \frac{1}{2}, 0)$ of $La_{1.7}Sr_{0.3}CoO_4$ at $T = 20$ K. Under consideration of the instrumental resolution, the analysis of the Lorentz-type reflection profile yields an in-plane correlation length $\xi_{ab} = 5.0(1)$ Å. The energy dependence of magnetic correlations near $(\frac{1}{2}, \frac{1}{2}, 0)$ up to a neutron energy gain of 2 THz = 8.3 meV is presented in Fig. 6.4 (b). Due to the large **q**-width of these signals these scans do not allow one to separate the two modes dispersing along $\pm[1,\bar{1},0]$-directions. This indicates a steep increase of the dispersion near the zone center and, therefore, a strong nearest-neighbor exchange interaction. Higher energies were not accessible with the cold-neutron scattering experiment.

To study the spin-wave dispersion in the ab-plane up to higher energies, we used a large single-crystal (cylindrical shape, 40 mm length, 8 mm in diameter) on the thermal triple-axis spectrometer 1T1. Typical Q-scans along $[0.5 + x, 0.5 - x, 0]$ for different

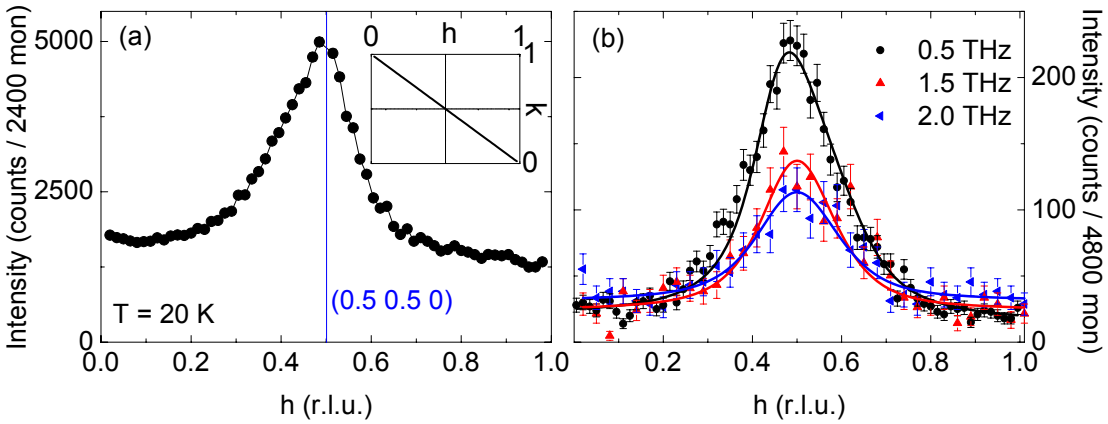

Figure 6.4.: Magnetic superstructure reflection ($\frac{1}{2}$, $\frac{1}{2}$, 0) of $La_{1.7}Sr_{0.3}CoO_4$ at $T = 20$ K measured in (100)/(010)-orientation. (a) The elastic scan in [x, -x, 0]-direction yields an in-plane correlation length $\xi_{ab} = 5.0(1)$ Å. (b) Energy dependence of magnetic correlations near ($\frac{1}{2}$, $\frac{1}{2}$, 0) for the same scan direction at $T = 20$ K.

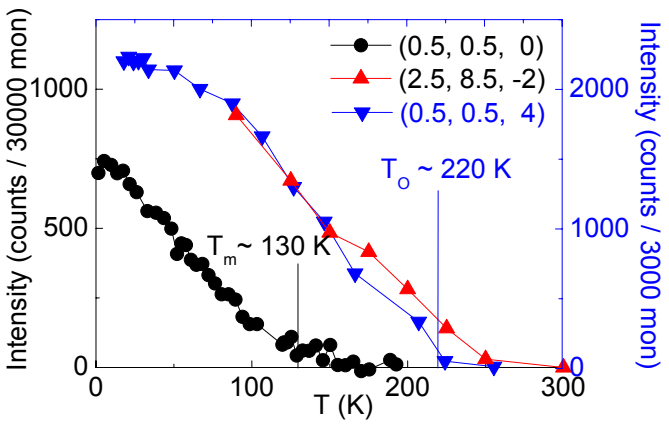

Figure 6.5.: Comparison of the temperature dependence of the antiferromagnetic superstructure reflection ($\frac{1}{2}$, $\frac{1}{2}$, 0) and of the orthorhombic superstructure reflection ($\frac{1}{2}$, $\frac{1}{2}$, 4) of $La_{1.7}Sr_{0.3}CoO_4$. The magnetic intensity was determined by Spin-Flip scattering in a polarized-neutron experiment at the triple-axis spectrometer 4F1.

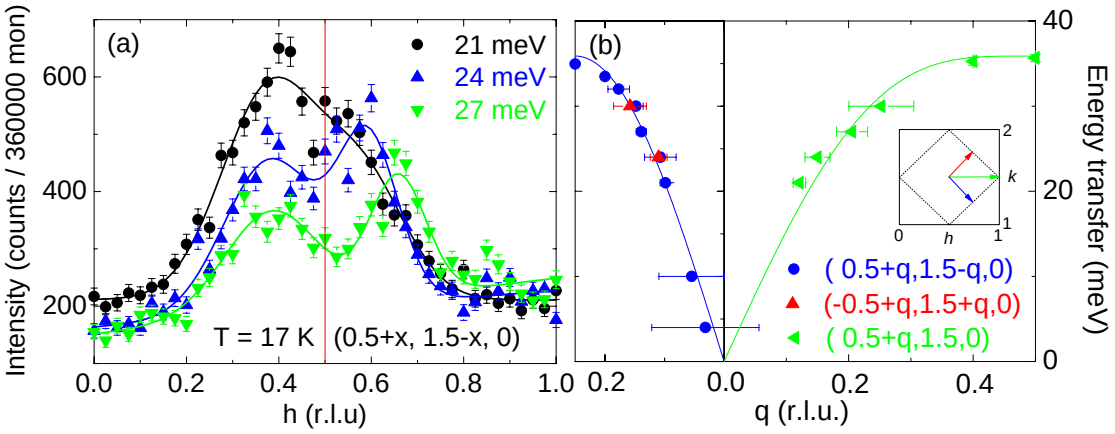

Figure 6.6.: Spin-wave dispersion in $La_{1.7}Sr_{0.3}CoO_4$ at $T = 17$ K. (a) Typical const-E-scans for different energy transfers. (b) Isotropic dispersion of the magnetic in-plane excitations. The solid lines are calculated using Eq. 6.2.

energy transfers at $T = 17$ K are shown in Fig. 6.6 (a). The resulting spin-wave dispersion along different symmetry directions is shown in Fig. 6.6 (b). We started with an antiferromagnetic Hamiltonian

$$H = J \sum_{i,j} S_i S_j + K \sum_i S_i^2 \tag{6.1}$$

to model the dispersion. The first summation describes the exchange interaction between nearest Co^{2+} neighbors and the second summation a small single-ion anisotropy. This model assumes a homogenous magnetic square lattice thus ignoring the locally different magnetic character at the Co^{3+} sites. Using standard linear spin-wave theory, the resulting dispersion relation is

$$E(Q) = zJS\sqrt{\left(1 + \frac{2K}{zJ}\right)^2 - \left(\frac{1}{2}\left(\cos\left(k_x\right) + \cos\left(k_y\right)\right)\right)^2} \tag{6.2}$$

with $J = 5.97(8)$ meV, $S = 3/2$, $K \sim 0$, and the number of nearest neighbors $z = 4$. The dispersion is isotropic along in-plane directions. For the given short correlation length, the peak-width analysis of the low-energy dispersion yields enlarged errors bars. But we find no indications for an anisotropy gap in contrast to the Ising-like anisotropy in La_2CoO_4 [11]. The temperature dependence of the scans for 21 meV and 27 meV is shown in Fig. 6.7. While dynamic spin correlations are still observable at $T = 200$ K, no well defined spin waves exist.

The in-plane dispersion is well described by accounting for only one effective nearest-neighbor exchange integral. On the basis of the present data, the contribution of the

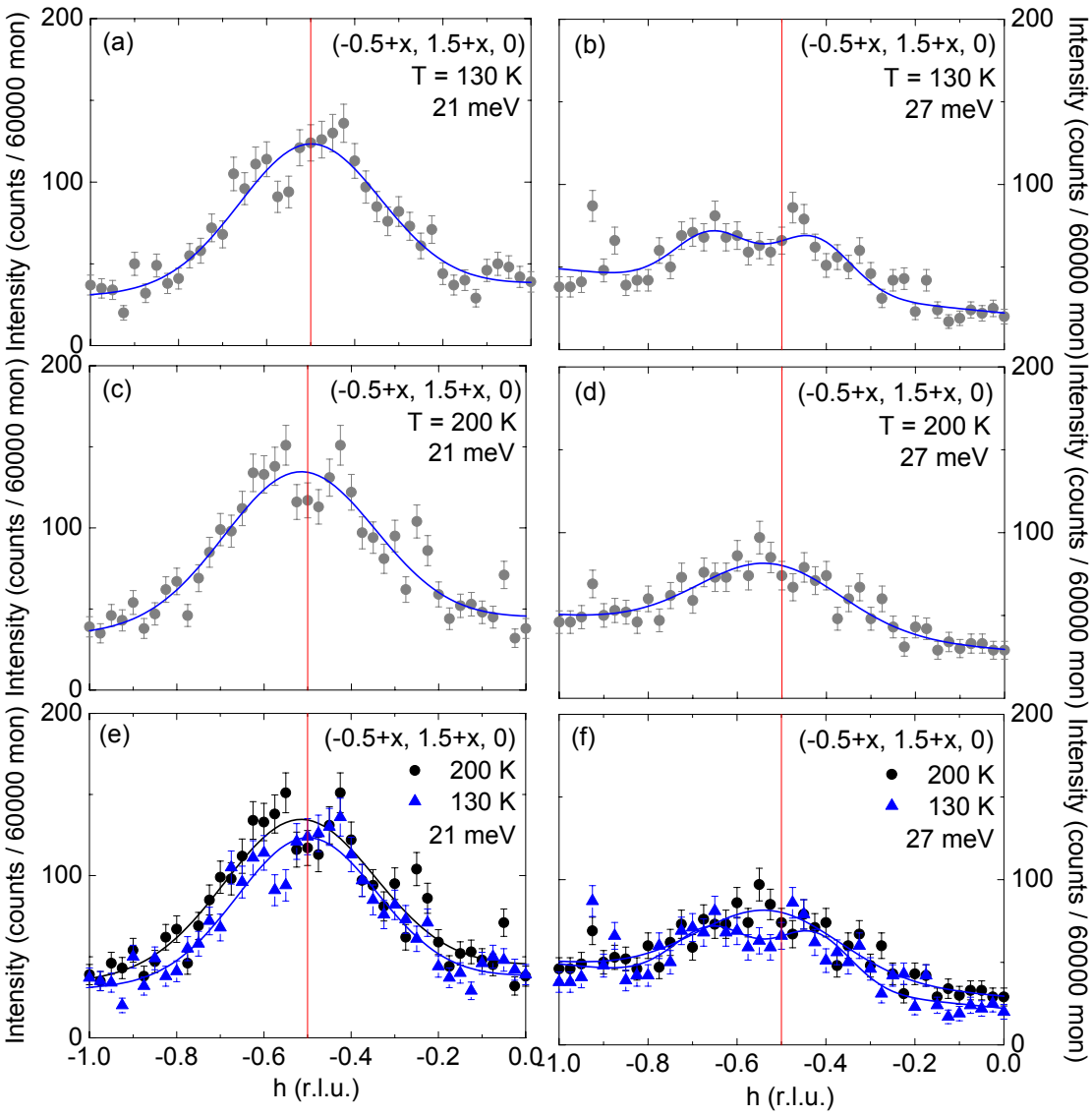

Figure 6.7.: Temperature dependence of magnetic excitations in $La_{1.7}Sr_{0.3}CoO_4$ for 21 meV and 27 meV. Dynamic spin correlations are still observable at $T = 200$ K, but no well defined spin waves exist.

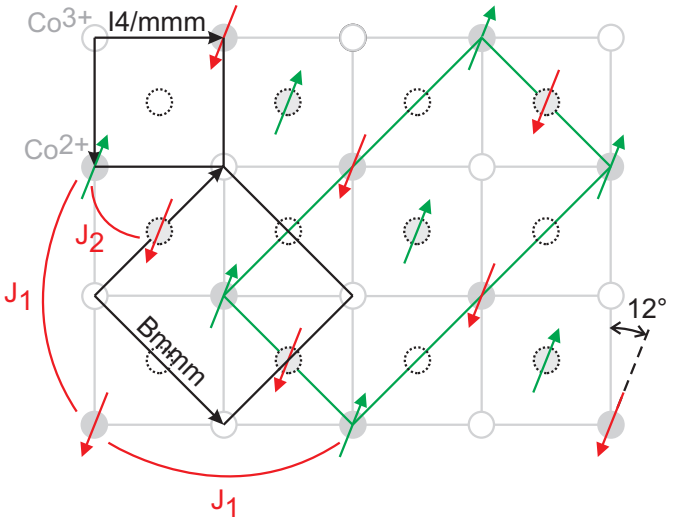

Figure 6.8.: Scheme of the spin and charge order in $La_{1.5}Sr_{0.5}CoO_4$ within the *ab*-plane of the tetragonal unit cell in $I4/mmm$ notation. Dashed circles represent the position of the Co ions in the adjacent layers. The charge-order unit cell exhibits $Bmmm$ symmetry. The magnetic unit cell is indicated by green color. Two effective exchange integrals between next-nearest Co^{2+} neighbors in the *ab*-plane and between nearest Co^{2+} neighbors of adjacent layers stabilize the spin arrangement.

Co^{3+} spin degree of freedom is not detectable. Both, the antiferromagnetic coupling over a high-spin or a dilution of non-magnetic low-spin state ions would coincide in one effective exchange coupling with a finite correlation length. At this point, it must be emphasized that also the Co^{3+} high-spin state in the insulating phase agrees with the observed commensurate nearest-neighbor coupling, as the Co^{2+}-HS-Co^{3+}-HS interaction should be antiferromagnetic.

6.2.2. Spin and Charge Order in $La_{1.5}Sr_{0.5}CoO_4$

The spin and charge order in the half-doped cobaltate $La_{1.5}Sr_{0.5}CoO_4$ was first observed by Zaliznyak *et al.* [7, 8, 211, 279]. A charge glass state with a checkerboard-like arrangement of Co^{2+} and Co^{3+} ions on the two-dimensional square lattice was concluded from superstructure reflections below $T_{CO} = 825(27)$ K. In the former tetragonal notation of the HTT phase, charge order with modulation $\mathbf{q}_{CO} = (1 + 2\epsilon, 0, l)$ and $(0, 1 + 2\epsilon, l)$ $(l = 0, 1)$ occurs. Anisotropic correlation lengths with $\xi_{ab} = 26$ Å and $\xi_c = 8.1(7)$ Å were calculated using factorized lattice Lorentzians similar to [280, 281]. The interplane coupling is small. Slightly incommensurate magnetic modulations with $\mathbf{q}_{SO} = (0.5 + \epsilon, 0, 1)$ $(\epsilon = 0.017)$ are found in the charge ordered phase below $T_{SO} \sim 30$ K. A schematic drawing of the charge and spin order within the *ab*-plane is shown in Fig. 6.8. Filled solid circles indicate Co^{2+} ions and empty solid circles Co^{3+} ions within a CoO_2 plane. Dashed circles represent ions of the adjacent CoO_2 above or below. The antiferromagnetic arrangement of Co^{2+} spins corresponds to diagonal lines of equal spins and Co^{3+}

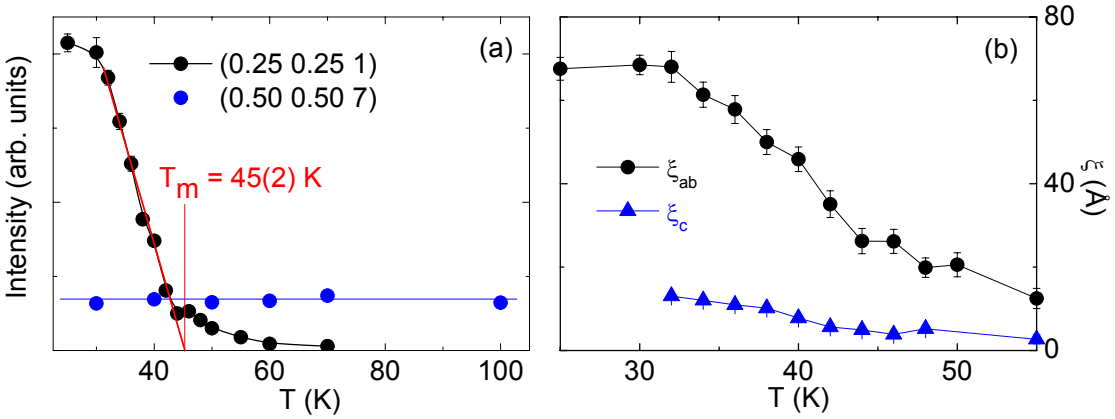

Figure 6.9.: Spin and charge order of $La_{1.5}Sr_{0.5}CoO_4$. (a) Temperature dependence of the magnetic reflection intensity at $(\frac{1}{4}, \frac{1}{4}, 1)$ and the charge order reflection $(\frac{1}{2}, \frac{1}{2}, 7)$. The transition temperature T_m is in linear approximation $T_m = 45(2)$ K, while the structural intensity is not varying. (b) Magnetic in-plane correlation length ξ_{ab} within the CoO_2-planes and perpendicular out-of-plane correlation length ξ_c. Data were measured by D. Senff.

holes along [1,-1,0]. Because of the selection rules for magnetic neutron scattering, the direction of the spin moment can be estimated by the magnetic structure factor. Neutron scattering is only sensitive to the projection $\mathbf{S}_\perp$ perpendicular to the scattering vector $\mathbf{Q}$. A polarization analysis of the magnetic intensities revealed that the spin moment lies within the *ab*-plane at an angle 12° to the Co-O bonds, with a small spin reorientation of 5° above 30 K [244]. In general, satellite positions $(\frac{1}{2} \pm \frac{1}{4}, \frac{1}{2} \pm \frac{1}{4}, 0)$ and $(\frac{1}{2} \pm \frac{1}{4}, \frac{1}{2} \mp \frac{1}{4}, 0)$ are allowed. Neglecting the $\mathbf{Q}$ dependence of the magnetic form factor, one may estimate the reduction of the structure factor due to the spin moment component perpendicular to $\mathbf{Q}$. For $(\frac{3}{4}, \frac{3}{4}, 0)$ the spin moment component is reduced to 54.4% and for $(\frac{1}{4}, \frac{3}{4}, 0)$ to 95.9 %. In our sample, we find the reflections $(\frac{3}{4}, \frac{3}{4}, 0)$ and $(\frac{1}{4}, \frac{1}{4}, 0)$ to be approximately a factor 10 smaller, suggesting a weak interlayer coupling in the system with the spin arrangement shown in Fig. 6.8.

The spin and charge order in $La_{1.5}Sr_{0.5}CoO_4$ was investigated in detail on the triple-axis neutron spectrometer G43 at the Laboratoire Léon Brillouin using a large single crystal (cylindrical shape with 40 mm in length and 10 mm in diameter). Experiments were carried out with the aid of D. Senff. As exemplarily shown in Fig. 6.9, we find characteristic scattering of spin and charge order at half doping, similar to the reported data of Zaliznyak *et al.* [7]. Reflections can be separated by their position and $\mathbf{Q}$-dependence in reciprocal space. According to [6], the magnetic and charge-order structure factor can be easily calculated. For the small nuclear displacement $\mathbf{r}_j = \mathbf{r}_j^0 + \boldsymbol{\epsilon}_j$ due to

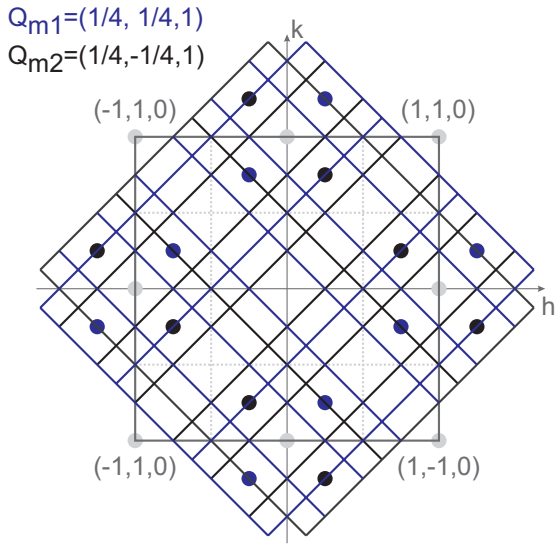

Figure 6.10.: Magnetic Brillouin-zones of $La_{1.5}Sr_{0.5}CoO_4$ within the (h, k, 0)-plane. The two magnetic twins are represented by different colors.

the charge order, the nuclear structure factor is

$$F_{co}(\mathbf{Q}) \propto \sum_j b_j \left\{1 + i\mathbf{Q}\cdot\boldsymbol{\epsilon}_j\right\} e^{i\mathbf{Q}\cdot\mathbf{r}_j^0} e^{-W_j} \Rightarrow I_{co} \propto |\mathbf{Q}\cdot\boldsymbol{\epsilon}_j|^2, \tag{6.3}$$

the magnetic structure factor

$$F_{so}(\mathbf{Q}) \propto \sum_j \left\{\hat{\mathbf{Q}} \times \mathbf{S}_j \times \hat{\mathbf{Q}}\right\} f(\mathbf{Q}) e^{i\mathbf{Q}\cdot\mathbf{r}_j^0} e^{-W_j} \Rightarrow F_{so}(\mathbf{Q}) \overset{|\mathbf{Q}|\to\infty}{\longrightarrow} 0,$$

and the neutron cross section

$$\frac{d\sigma_{co,so}}{d\Omega}(\mathbf{Q}) \propto \sum_{\tau_{co,so}} |F_{co,so}(\mathbf{Q})|^2 \delta(\mathbf{Q} - q_{co,so}). \tag{6.4}$$

While the charge-order intensities I_{co} increase with $|\mathbf{Q}|$, $F_{so}(\mathbf{Q})$ vanishes with increasing $\mathbf{Q}$. The magnetic form factor can be calculated in analytical approximation after Brown [282] (see Fig. C.1). Charge-order reflections (0.5, 0.5, 7) and (0.5, 0.5, 8) in $I4/mmm$ notation with in-plane correlation lengths of $\xi_{ab} \sim 19(1)$ Å are well established and nearly constant in the temperature region $25 \leq T \leq 300$ K. Spin-order correlation lengths of $\xi_{ab} = 68(3)$ Å and $\xi_c = 13.1(4)$ Å are calculated from scans across the (0.25, 0.25, 1) magnetic peak with Lorentzians folded with the instrumental resolution. The spin order was found to be nearly commensurate with $\epsilon = 0.0065(2)$ at $T = 25$ K. The interrelation of ϵ between spin and charge ordering cannot be analyzed due to the short-range character of the charge ordering.

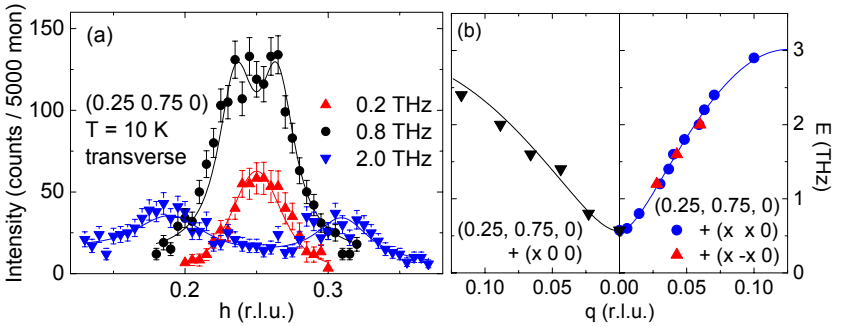

Figure 6.11.: Spin-wave dispersion of $La_{1.5}Sr_{0.5}CoO_4$ at $T = 10$ K as determined around (0.25, 0.75, 0) for different directions at $T = 10$ K.

In order to analyze the antiferromagnetic coupling in $La_{1.5}Sr_{0.5}CoO_4$, we investigated the in-plane spin-wave dispersion on the cold neutron triple-axis spectrometer 4F1 at the Laboratoire Léon Brillouin and on *PUMA* at the Forschungsreaktor München II. The expected magnetic Brillouin zone is schematically shown in Fig. 6.10. Typical constant energy scans across (0.25, 0.75, 0), to analyze the dispersion near the zone center, are shown in Fig. 6.11 (a). Only one gapped dispersion is observed for scans along the symmetry directions $[x, x, 0]$,$[x, -x, 0]$, and $[x, 0, 0]$. We find no evidence for anisotropy in the in-plane spin-wave dispersion. This is surprising, since in general, one would expect differences for scans along $[x, x, 0]$ and $[x, -x, 0]$. A critical frustration due to competing antiferromagnetic nearest-neighbor (J) and next-nearest-neighbor (J_1) interactions of Co^{2+} spins was proposed for $La_{1.5}Sr_{0.5}CoO_4$ by Zaliznyak *et al.* [7]. Scans along $[x, x, 0]$ test the average next-nearest-neighbor interaction J_1 and a ferromagnetic alignment of nearest Co^{2+} spins, while scans along $[x, -x, 0]$ test only J_1. Note that the different magnetic twins can be distinguished by the choice of the superstructure reflection. This may indicate a dominant next-nearest-neighbor interaction J_1 in the system, where interlayer frustration with a small coupling J_2 leads to the observed spin-glass behavior. We modeled the spin-wave dispersion using the Hamiltonian

$$H = \sum_{i,j} J_1 \cdot S_i \cdot S_j + \sum_{i,j} J_2 \cdot S_i \cdot S_j + K \sum_i (S_i^z)^2 \tag{6.5}$$

with the in-plane next-nearest-neighbor exchange integral J_1, the out-of-plane nearest-neighbor exchange integral J_2, and single-ion anisotropy constant K. In all summations the interaction parameters refer to the bonds. The results are given in Tab. 6.2. Since the in-plane dispersion is nearly isotropic, the out-of-plane exchange is small. A finite J_2 is indicated by the energy scans discussed later. Therefore, the nearly isotropic observed in-plane spin-wave dispersion is well described by a simple antiferromagnetic two-lattice model with $S = 3/2$ Co^{2+} high-spin states and non-magnetic Co^{3+} ions. The effective

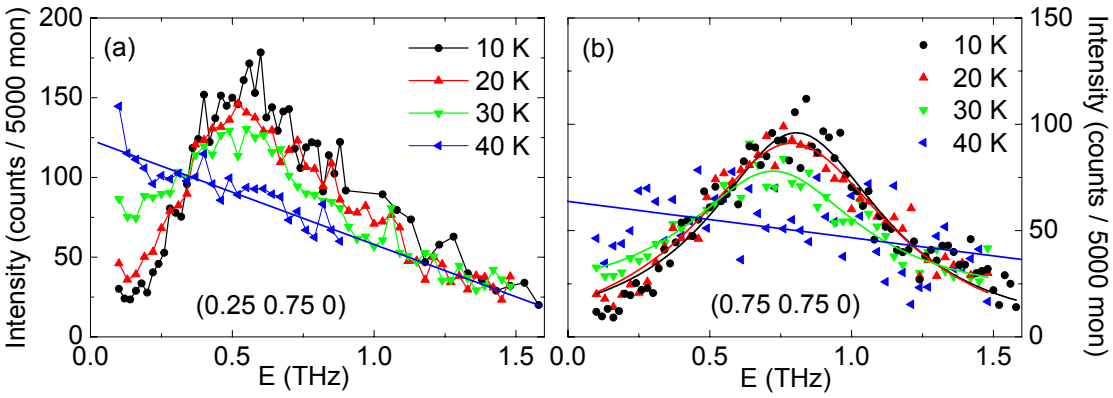

Figure 6.12.: Energy scan for $(\frac{1}{4}, \frac{3}{4}, 0)$ (a) and $(\frac{3}{4}, \frac{3}{4}, 0)$ (b) in $La_{1.5}Sr_{0.5}CoO_4$. Measured intensities are Bose-corrected.

exchange may be mediated via next-nearest neighbor bonds Co^{2+}-O-Co^{3+}-O-Co^{2+} and a weak out-of-plane coupling between nearest Co^{2+} neighbors. In the analysis of magnetic correlations by Helme *et al.* spin waves extend to ∼16 meV [244], which is comparable to our results, but the Brillouin zone was falsely attributed and the zone center was not investigated at all. In comparison to the half-doped LSNiO, the exchange interaction is much weaker but the anisotropy gap in the Co-system is larger.

Bose-corrected energy scans at (1/4, 3/4, 0) and (3/4, 3/4, 0) for different temperatures up to the spin-glass transition temperature are shown in Fig. 6.12. (1/4, 3/4, 0) corresponds to the antiferromagnetic zone center, where we find an anisotropy gap of $E_g \sim 0.57$ THz. The anisotropy gap vanishes upon heating above the spin-glass transition temperature. Since spin-waves are transverse excitations and the spin-moment is orientated within the *ab*-plane, one observes displacements along *c* and in-plane but perpendicular to **Q** in the CoO_2 plane. While the anisotropy gap at (1/4, 3/4, 0) suggests an Ising-like in-plane anisotropy, the increase of the energy gap at (3/4, 3/4, 0) indicates a finite interlayer coupling J_2 in the half-doped compound by the out-of-plane polarization. The estimation via

$$(\hbar\omega_q)^2 = (4SJ(0) + 2SK)^2 - (4SJ(\mathbf{q}))^2 \tag{6.6}$$

with $J(0) = J_1 + J_2$ and $J(\mathbf{q}) = \frac{1}{2}J_1(\cos(2q_x) + \cos(2q_y)) + \frac{1}{2}J_2(\cos(\frac{1}{2}q_x - \frac{1}{2}q_y + \frac{1}{2}q_z) + \cos(\frac{1}{2}q_x - \frac{1}{2}q_y - \frac{1}{2}q_z))$ gives $J_2 \sim 0.04$ meV per bond.

6.3. Incommensurate, Static Spin Correlations

Static spin correlations in $La_{2-x}Sr_xCoO_4$ ($x = 0.4, 0.45, 0.5, 0.6$) were investigated by single-crystal neutron diffraction. Large single crystals of cylindrical shape (typically

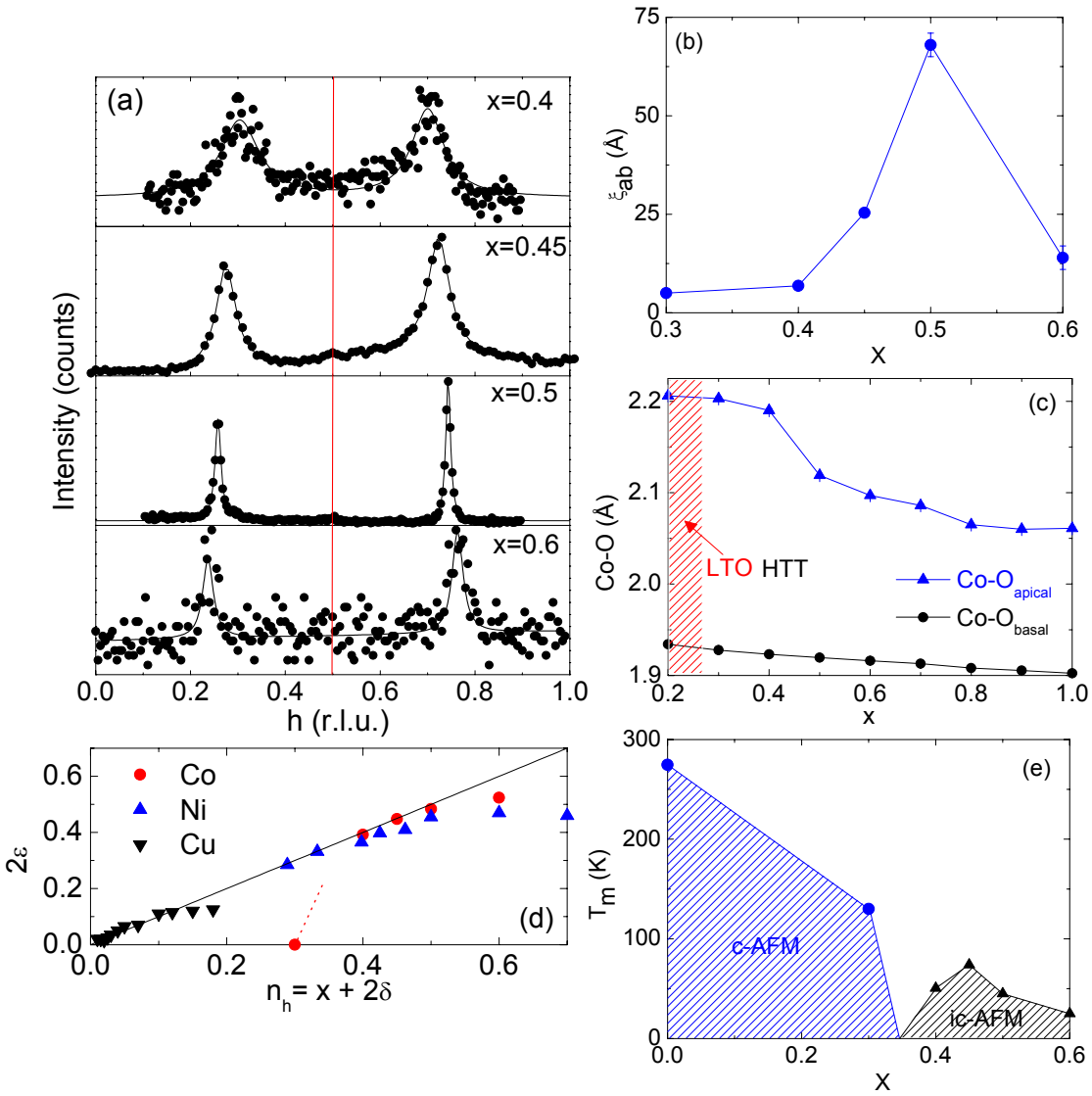

Figure 6.13.: Characteristics of incommensurate spin correlations in $La_{2-x}Sr_xCoO_4$ ($x = 0.4, 0.45, 0.5, 0.6$) at low temperatures. (a) Antiferromagnetic satellite reflections ($\frac{1}{2}\pm\epsilon$, $-\frac{1}{2}\pm\epsilon$, 0). (b) Doping dependence of the in-plane correlation length ξ_{ab}. (c) Co-O bond-length anisotropy. (d) Linear dependence of the incommensurability ϵ with hole doping $n_h = x+2\delta$ in comparison to LSCuO and LSNiO. Data are taken from [158, 252]. (e) Magnetic phase diagram of LSCoO with commensurate AF correlations up to $x = 0.3$ and stripe or checkerboard order in the doping range $0.4 \leq x \leq 0.6$. The highest transition temperature is found near half doping.

	Co	Ni
J_1 (meV)	2.04(9)	5.8(5)
K (meV)	0.074(7)	0.05(2)

Table 6.2.: Comparison of the magnetic exchange and anisotropy parameters of the spin-wave dispersion in $La_{1.5}Sr_{0.5}MO_4$ (M=Co, Ni). Data for M=Ni are taken from [209].

40 mm in length and 10 mm in diameter) were studied on the triple-axis neutron spectrometers *UNIDAS*, *G43* and *1T1* as described in the experimental chapter. Incommensurate satellite reflections ($\frac{1}{2} \pm \epsilon$, $-\frac{1}{2} \pm \epsilon$, 0) and symmetry equivalents were observed within the (100)/(010) scattering plane (see Fig. 6.13 (a)). The satellites were equally displaced from the antiferromagnetic zone center. Note that the reflection profile for one satellite in $x = 0.6$ was investigated in detail with higher counting times in comparison to the long scan across both satellites shown. For better comparison, only the long **Q** scan across both satellites is shown in the panel. The in-plane correlation length ξ_{ab} was calculated by analyzing the Lorentzian peak width of a satellite after the convolution with the gaussian resolution. The results are shown in Fig. 6.13 (b). A maximum of ξ_{ab} is reached at half doping with a nominally equal ratio of Co^{3+} and Co^{2+} ions in the sample. Interestingly, the onset of incommensurability nearly coincides with the largest drop in the Co-O_{apical} bond length as a function of x. As it is illustrated in Fig. 6.13 (d), the incommensurability ϵ is shifted nearly linearly with increasing hole density $n_h = x + 2\delta$. The magnetic transition temperature T_m decreases upon doping the parent compound La_2CoO_4. A similar behavior is found in LSCuO and LSNiO, but at lower doping levels. T_m reaches a maximum at half doping in the incommensurate spin-glass phase.

A possible interpretation of these findings is a spin-stripe model in the spin-glass phase of $La_{2-x}Sr_xCoO_4$. In the LTO phase, commensurate next-nearest neighbor spin correlations are stabilized. An antiferromagnetic superexchange in Co^{2+}-O-Co^{3+} bonds between high-spin ions can stabilize these commensurate spin correlations up to higher doping levels in comparison to LSNiO [158] with $x_c = 0.15$. As indicated by the steep decrease of the Co-O_{apical} bond-length above $x = 0.4$, Co^{3+} ions may exhibit a spin state transition from the high-spin state to the low-spin state as a function of doping. Concomitantly, square-lattice symmetry is found for all temperatures $T > 1.5$ K by the HTT phase for $x \geq 0.4$. The nearly linear shift of the incommensurability denotes that the holes introduced into the system contribute to the modulation of the antiferromagnetic order. This is the expected behavior in a spin-stripe model observed in LSCuO and LSNiO. The charge order near half doping may stabilize the antiferromagnetic interactions between Co^{2+} ions and the in-plane correlation length ξ_{ab} reaches a maximum.

For stripe ordered $La_{2-x}Sr_xCuO_4$, the doping dependence of the in-plane correlation

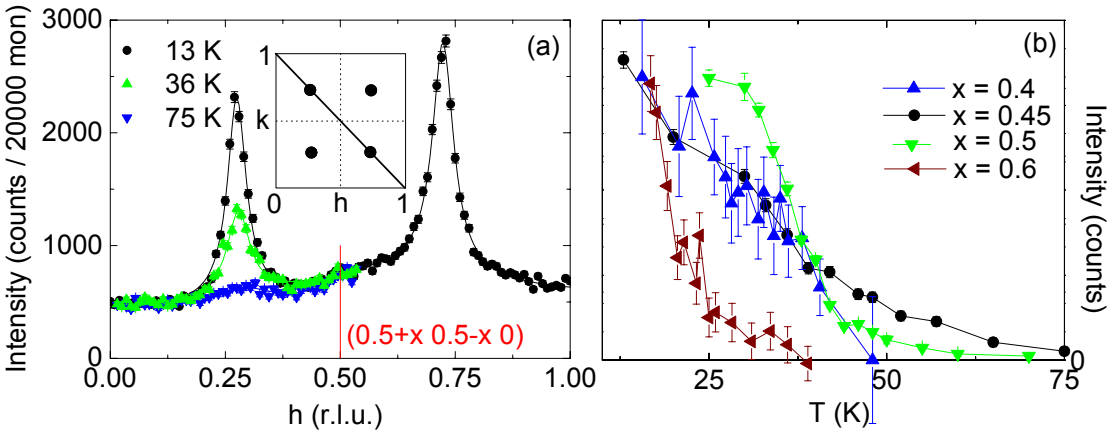

Figure 6.14.: Temperature dependence of antiferromagnetic superstructure reflections in $La_{2-x}Sr_xCoO_4$. (a) Scans along $(0.5 + x, 0.5 - x, 0)$ in $La_{1.55}Sr_{0.45}CoO_4$. (b) Temperature dependence of the maximal peak intensity for $x = 0.4, 0.45, 0.5, 0.6$. Background contributions were subtracted.

length was found to correspond to the mean hole distance $\xi_{ab} \sim a/\sqrt{x}$ [283], where a (~ 3.8 Å) is the mean in-plane lattice constant in HTT notation. For the commensurate order in $La_{1.7}Sr_{0.3}CoO_4$, the expected correlation length would be ~ 6.93 Å, which is near the observed value. The in-plane stripe order in $La_{2-x}Sr_xNiO_4$ ($0.289 \lesssim x \lesssim 0.5$) is well defined with enhanced correlation length [158] and reaches a maximum at $x \sim 1/3$. Together with a maximum in the out-of-plane correlation length ξ_c, this suggests a quasi three-dimensional character of the stripe order. Concomitantly, the spin ordering and charge ordering temperature is maximized. For $La_{2-x}Sr_xCoO_4$, the in-plane correlation length reaches a maximum at half doping, which suggests that the stability of the spin order is enhanced by the charge-glass state of the system. Half doping is equivalent to an alternating occupation of Co-sites with Co^{2+} and Co^{3+} ions. The terminology 'spin stripe' differs from the common definition in this case and for $x > 0.5$, since antiferromagnetic domains would be one-dimensional spin lines.

The temperature dependence of static spin correlations in the investigated compounds $La_{2-x}Sr_xCoO_4$ ($x = 0.4, 0.45, 0.5, 0.6$) is shown in Fig. 6.14. Examples of scans across one magnetic satellite (0.276, 0.724, 0) along the [x,-x,0] direction for $La_{1.6}Sr_{0.4}CoO_4$ are represented in Fig. 6.15 panel (a). The variation of maximal peak intensity with temperature for the given samples is shown in panel (b). The maximum of the spin-order temperature is slightly shifted to $x = 0.45$ in a linear approximation, which may be due to the enhanced energy integration of the triple-axis spectrometer used in comparison to other doping levels. One could expect a higher stability of the antiferromagnetic spin arrangement assisted by the checkerboard-like charge order.

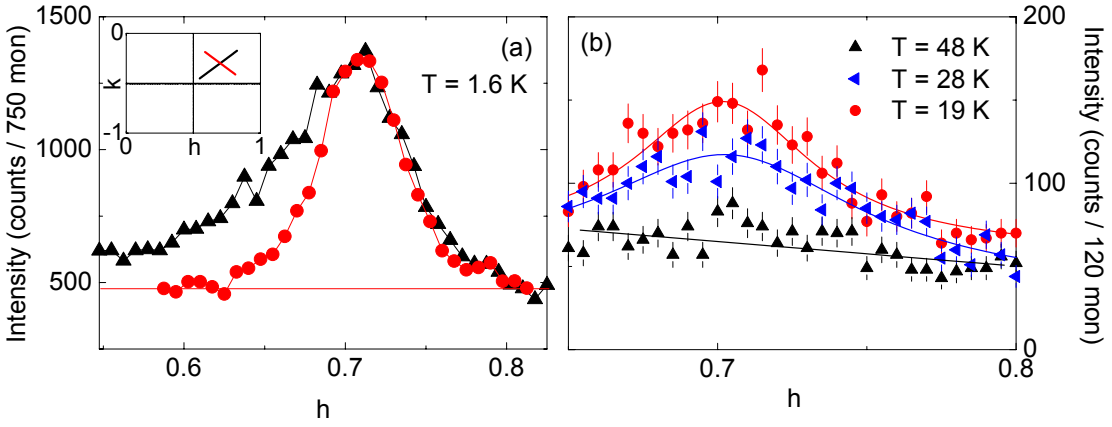

Figure 6.15.: Incommensurate antiferromagnetic reflection (0.7031, -0.3031, 0) of $La_{1.6}Sr_{0.4}CoO_4$. (a) Longitudinal and transverse scan within the CoO_2-plane. The in-plane correlation length is $\xi_{ab} = 29.9(5)$ Å at $T = 1.6$ K. (b) Scans in $[x, x, 0]$-direction across the magnetic reflection reveal no apparent change of the incommensurability for different temperatures.

6.3.1. Magnetic Excitations in the Incommensurate Spin-Glass Phase

Attempts to investigate the dynamic spin correlations in the incommensurate phase were carried out on samples with $x = 0.4$ and $x = 0.6$. To investigate magnetic excitations in $La_{1.6}Sr_{0.4}CoO_4$ we used the same crystal as for the static spin correlations analysis on the triple-axis spectrometer 4F2 at the Laboratoire Léon Brillouin. We found the same antiferromagnetic satellite reflections and temperature dependence as in the previous measurements. However, we were not able to observe well-defined magnetic excitations with the counting rate of 130 sec per point (see Fig. 6.16). This may result from a small ordered moment in the sample at low temperatures.

In contrast to $x = 0.4$, the collective magnetic excitations seem to be better defined in the $La_{1.4}Sr_{0.6}CoO_4$ compound. Fig. 6.17 shows the spin-wave dispersion in $La_{1.4}Sr_{0.6}CoO_4$ at $T = 19.7$ K, measured across (0.76, 0.24, 0) and (0.76, 0.76, 0) for different symmetry directions. Energy scans, for both (0.76, 0.24, 0) and (0.76, 0.76, 0), reveal no evidence for an anisotropy gap. Furthermore, a **Q**-scan across (1, 0, 0) at 0.5 THz indicates no ferromagnetic correlations in the system. Further experiments on the high-energy part of the dispersion on a thermal triple-axis spectrometer are needed to complete the spin-wave dispersion of $La_{1.4}Sr_{0.6}CoO_4$ and to analyze the magnetic exchange in the incommensurate phase. Based on the existing data, a comparable spin-wave velocity to $La_{1.5}Sr_{0.5}CoO_4$ is observed within the experimental resolution.

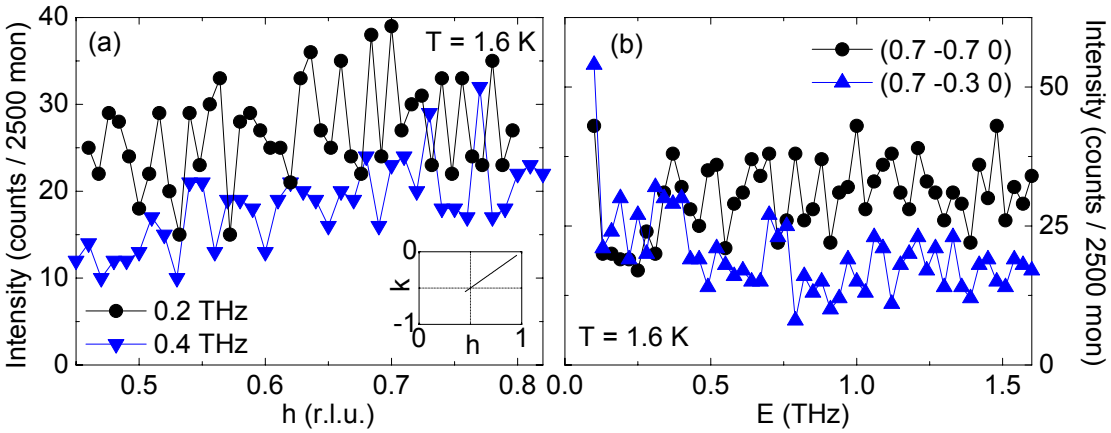

Figure 6.16.: Magnetic excitations in $La_{1.6}Sr_{0.4}CoO_4$. Both in the transverse scan (a) and in the energy scan (b) no correlations are detectable with the chosen monitor counting rate.

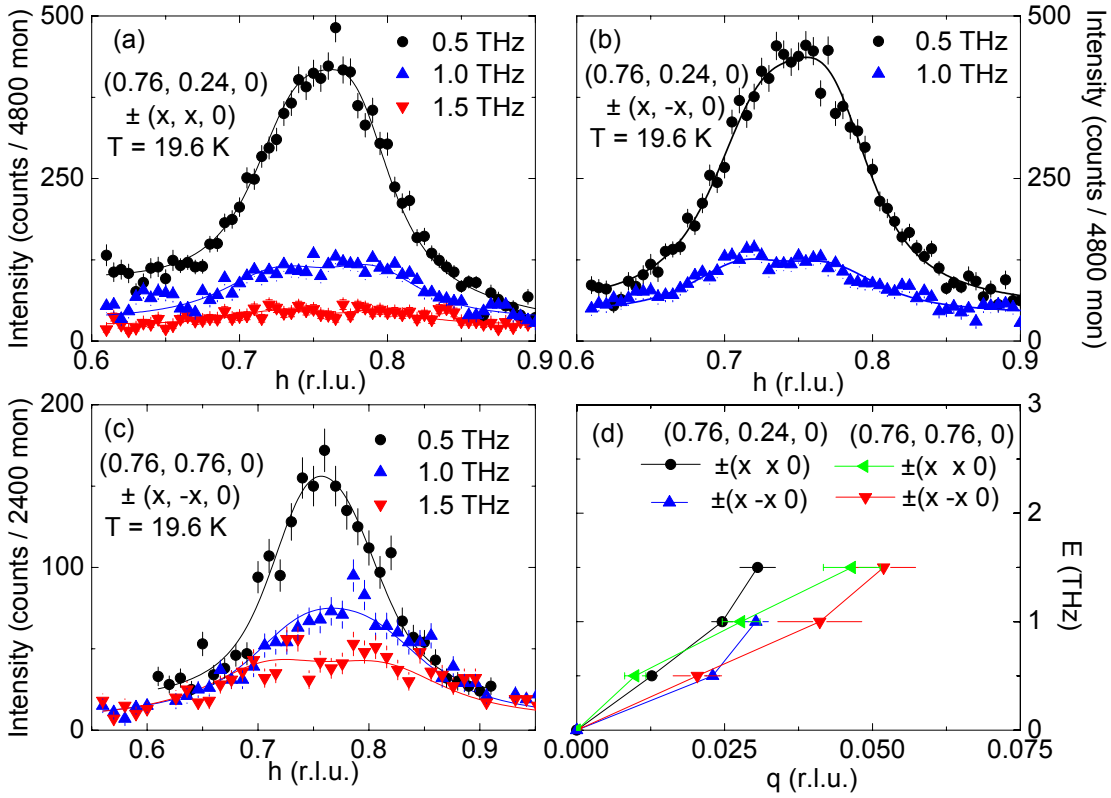

Figure 6.17.: Spin-wave dispersion of $La_{1.4}Sr_{0.6}CoO_4$ at $T = 19.7$ K.

6.4. Discussion of the Co^{3+} Spin Degree of Freedom

Let us now discuss the results in terms of the Co^{3+} spin degree of freedom. Both static and dynamic spin correlations were investigated in detail for the half-doped cobaltate and one may draw conclusions concerning the Co^{3+} spin state in a localized picture. Short-range spin and charge order in half-doped $La_{1.5}Sr_{0.5}CoO_4$ was first observed by Zaliznyak *et al.* [7, 8, 279]. Half doping corresponds to a nominal Co-valence of $v_{Co} = 2.5$ and thus to an equal amount of Co^{2+} and Co^{3+} ions in a fully localized picture. I. A. Zaliznyak *et al.* observed a checkerboard-like charge order within the CoO_2-planes with $T_{CO} = 825(27)$ K and short-range antiferromagnetic spin order with $T_S \lesssim 30$ K. Due to the large difference between the ordering temperatures $T_{CO}/T_S \gtrsim 25$ and a non-detectable anomaly of the charge order intensities at the onset of spin order, the authors point out that both phenomena are completely decoupled. The influence of the Co^{3+} spin-state degree of freedom is unclear. The spin moment of Co^{3+} ions was proposed to be fully quenched by a strong planar anisotropy and the Néel-order is suppressed by the frustration of the nearest and the next-nearest neighbor interaction between Co^{2+} spins. The detailed analysis of the Co^{3+} spin-state degree of freedom and the contribution to the antiferromagnetic coupling in the system is needed and was the starting point of our investigations presented in this chapter. A small set of charge-order superstructure reflections was analyzed in Ref. [8]. From this analysis a Jahn-Teller distortion of the $Co^{3+}O_6$-octahedra [8] is proposed. This would yield a Co^{3+}-intermediate-spin state occupancy at low temperatures. Our data, with a larger set of superstructure reflections, disagree with these results and yield a simple enlargement or shrinking of the different CoO_6 octahedra, which is not a Jahn-Teller active mode. In addition, the magnetic coupling of Co^{3+} and Co^{2+} ions has not been fully characterized and the magnetic coupling scheme between Co^{2+} ions is incomplete. Our analysis of the spin-wave dispersion suggests non-magnetic Co^{3+} ions, which mediate the antiferromagnetic next-nearest neighbor coupling of Co^{2+} spins within the CoO_2 layers. The spin arrangement may be stabilized by the observed weak interlayer coupling. A. Maignan *et al.* studied the coupling scheme of Co^{2+} ions next to Co^{3+} ions for different spin states in $HoBaCo_2O_{5.5}$, proposing the so-called 'spin blockade' [102]. In a localized electronic picture, the substitution of Co^{2+} ions in the high-spin state ($S = 3/2$) into an environment of Co^{3+} ions in the low-spin state disables the electronic transport in the e_g band, because the spin state is not interchangeable by electron hopping. Obversely, the substitution of Co^{3+} ions into an environment of Co^{2+} ions might inhibit a low-spin Co^{3+} ground state in $La_{2-x}Sr_xCoO_4$ for low doping.

It is reasonable to distinguish between different Co^{3+} spin states via the different magnetic coupling schemes between Co^{3+} and Co^{2+} ions. The magnetic coupling between Co^{2+} and Co^{3+} ions at half doping was alternatively studied in other layered mixed-valence cobaltates. For example, the magnetic-coupling scheme for the half-doped compound $Bi_2Sr_2CoO_{6+\delta}$ was investigated by single-crystal neutron scattering with polarization analysis [100]. At $\delta \sim 0.25$ an equal amount of Co^{2+} and Co^{3+} ions is expected.

Co^{3+} is proposed to be in an intermediate-spin state, which causes a ferromagnetic interaction to Co^{2+} in the high-spin state. Ferromagnetic coupling in $La_{2-x}Sr_xCoO_4$ was proposed by the analysis of nuclear magnetic resonance studies for ($x \geq 0.6$) [19], but no evidence was found in the magnetic susceptibility experiments by N. Hollmann [154]. Within a mean-field model, the analysis of χ yields an effective antiferromagnetic coupling. Overall, the results suggest a Co^{3+} low-spin state for $x \geq 0.4$.

6.5. Conclusions

Static and dynamic spin correlations in $La_{2-x}Sr_xCoO_4$ (x=0.3, 0.4, 0.45, 0.5, 0.6) have been studied by means of single-crystal neutron scattering. Commensurate antiferromagnetic spin correlations between nearest neighbors were found at the relatively high Sr doping level $x = 0.3$. The doping level is well below the percolation threshold $x_c \approx 0.4$ for non-magnetic impurity dilution on a square lattice [269]. For the antiferromagnetic order in LSCuO and LSNiO a spin-glass phase is induced at low doping levels. Above $x = 0.024$ in LSCuO [159] and above $x = 0.135$ in LSNiO [5, 190, 284] doped charges localize in stripe ordered phases, but mobile hole doping is expected to suppress antiferromagnetic order effectively. On the basis of the existing data for $La_{1.7}Sr_{0.3}CoO_4$, we can not distinguish whether the random distribution of effectively immobile charge carriers or whether the possible Co^{3+} high-spin state supports the commensurate nearest neighbor-interaction by coupling antiferromagnetically to the Co^{2+} ions. A Co^{3+} high-spin state would not disagree with our observations.

Further doping induces an incommensurate modulated structure, which is indicated by satellite reflections away from the antiferromagnetic (0.5, 0.5, 0) position in tetragonal notation. The incommensurability ϵ increases the distance between satellites and (0.5, 0.5, 0) nearly linearly with hole doping concentration $n_h = x$ over a large x-range. Perfect linearity would indicate that all holes contribute to the modulation of the antiferromagnetic spin arrangement. A nearly linear dependence is also observed in stripe ordered phases of cuprates and nickelates. However, the most stable stripe ordering in doped cuprates is found for LBCuO at $x = 1/8$ [62] and in LSNiO at x=1/3 [158]. A saturation of the incommensurability is observed in all three systems above the most stable stripe-order concentration. The dynamic spin correlations were investigated near half doping. The isotropic spin-wave dispersion in $La_{1.5}Sr_{0.5}CoO_4$ is well described in standard spin-wave theory taking only the antiferromagnetic Co^{2+} next-nearest neighbor interaction and a weak interlayer coupling into account. Non-magnetic Co^{3+} ions may bridge the antiferromagnetic exchange between Co^{2+} ions. The Co^{3+} low-spin state model is also supported by other physical findings. The macroscopic magnetic properties of $La_{2-x}Sr_xCoO_4$ were investigated by magnetic susceptibility measurements by N. Hollmann *et al.* [154]. A strongly frustrated spin-glass behavior is found in the system from the comparison of field-cooled and zero-field-cooled measurements. The anisotropy of the

susceptibility was calculated with respect to the crystal-field splitting and the spin-orbit coupling within a cluster calculation. While a Co^{3+} low-spin state is suggested to be stabilized at intermediate doping levels, the high-spin population is indicated up to $x = 0.3$. Further, a Co^{3+} high-spin is also suggested from the soft x-ray absorption measurements with magnetic dichroism analysis at the Co $L_{2,3}$ edge [285].

7. Phase Diagram of $La_{2-x}Sr_xCoO_4$

In this chapter we summarize our experimental observations to obtain the structural and magnetic phase diagram of $La_{2-x}Sr_xCoO_4$ and to discuss their interdependence. The structural and magnetic instabilities can be ascribed to the doping dependent changes typical for single-layered compounds. We may attribute these changes to the variation of the ionic radii, the structural anisotropy, and the transition metal spin moment in the interplay of structural, magnetic, and charge degrees of freedom. In contrast to LSCuO and LSNiO, we found additional anomalies, which indicate the importance of the Co^{3+} spin-state degree of freedom in this system. After presenting the phase diagram, we compare our new findings with the spin-state schemes of $La_{2-x}Sr_xCoO_4$ and discuss the anomalies in terms of a new Co^{3+} spin-state transition.

The structural and magnetic phase diagram of $La_{2-x}Sr_xCoO_4$ ($0 \leq x \lesssim 1.0$) is shown in Fig. 7.1 (a), deduced from our measurements and described as follows:

LTO/LTT Distortion The crystal structure of the $La_{2-x}Sr_xCoO_4$ compounds is classified in the Ruddlesden-Popper series $A_{n+1}B_nX_{3n+1} = (AX)(ABX_3)_n$ with $n = 1$ for the single-layered perovskites. CoO_2 layers are separated by adjacent rocksalt-like layers of LaO. The ideal single-layered perovskite possesses a body-centered structure in the high-temperature tetragonal phase and undergoes structural phase transitions upon cooling for low doping levels. Structural distortions in single-layered perovskites are commonly attributed to internal strains due to a bond-length misfit of the ionic radii of the constituents [10, 75]. The internal strains can be reduced by the variation of the c/a ratio, the distortion of the CoO_6 octahedron, and the cooperative tilt of CoO_6 octahedra. The phase transition of the structural tilt instabilities are well described within the Ginzburg-Landau theory through a two-component order parameter $\mathbf{Q} = (Q_1, Q_2)$ [72, 83] with Q_1 and Q_2 associated to two orthogonal octahedra tilting modes. The low-temperature orthorhombic ($Q_1 = 0, Q_2 \neq 0$) and the low-temperature tetragonal distortion ($Q_1 = Q_2 \neq 0$) will be taken into account for the single-layered cobaltate in the following[1].

The variation of structural parameters and the lattice symmetry upon doping, including the HTT-LTO transition at low doping levels, were studied in $La_{2-x}Sr_xCoO_4$ in Chapter 4. The undoped parent compound La_2CoO_4 exhibits the LTO distortion below

[1] Further distortions, for example a second orthorhombic phase LTO2 with $Q_1 \neq Q_2 \neq 0$, are observed in cuprates and nickelates. Such instabilities were not observed in single-layered cobaltates and will be neglected for the comparison with nickelates and cuprates.

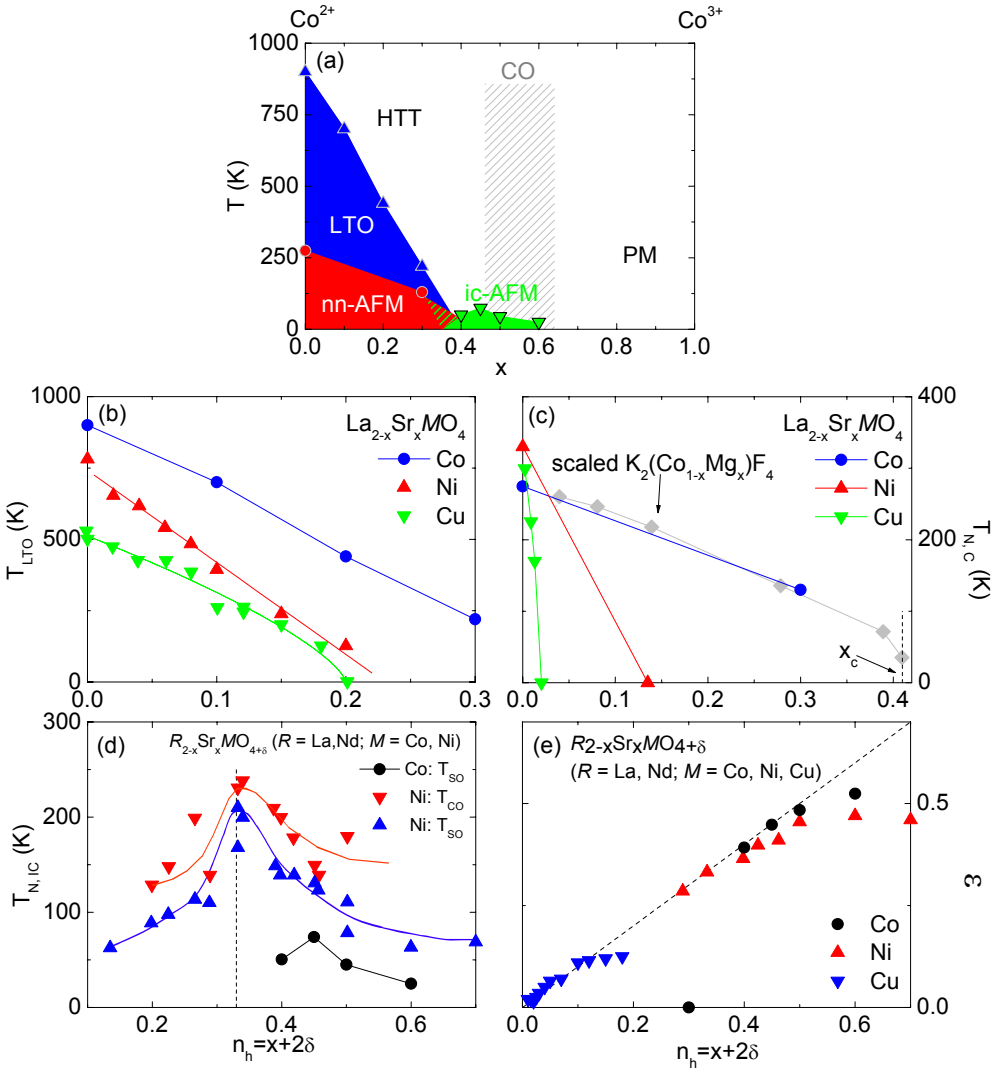

Figure 7.1.: (a) Structural and magnetic phase diagram of $La_{2-x}Sr_xCoO_4$ ($0 \leq x \lesssim 1$). The low temperature orthorhombic (LTO) distortion is lifted below $x = 0.4$. Concomitant static nearest-neighbor (nn) spin correlations vanish and incommensurate (ic) antiferromagnetic spin correlations emerge. Charge order (CO) was investigated in $x = 0.5$ and $x = 0.6$. (b) HTT/LTO phase-transition temperatures in $La_{2-x}Sr_xMO_4$ (M = Co, Ni [126], Cu [286]). The HTT/LTO phase-transition temperature is linearly reduced with increasing Sr doping. The doping dependence of T_{LTO} in LSCuO near the phase transition was approximated via $T_{LTO} \propto (x_{LTO} - x)^{2\beta}$. (c) Transition temperatures $T_{N,C}$ for commensurate antiferromagnetic correlations. Néel temperatures of $K_2(Co_{1-x}Mg_x)F_4$ from Ref. [276] were scaled to $T_N(x = 0)$ of La_2CoO_4 [11]. The T_N reduction in $K_2(Co_{1-x}Mg_x)F_4$ follows the prediction of magnetic dilution on a 2D square lattice with a site-percolation threshold $x_c \sim 0.41$ [269]. (d) Transition temperature $T_{N,IC}$ of incommensurate spin correlations in $R_{2-x}Sr_xMO_{4+\delta}$ (R= La,Nd; M=Co,Ni). The stripe order (charge order) transition temperature $T_{N,IC}$ ($T_{CO,IC}$) in nickelates is maximized at $x \sim 1/3$. Data for Ni are taken from Ref. [206]. (e) Hole doping ($n_h = x + 2\delta$) dependence of the incommensurability ϵ. Data for Ni are taken from Ref. [206] and for Cu from Ref. [252].

Table 7.1.: Comparison of the structural transition temperatures, the magnetic transition temperatures, and the critical doping levels in Sr doped single-layered oxides.

$La_{2-x}Sr_xMO_4$			
$M=$	Co	Ni	Cu
Temperature dependence for $x = 0$:			
$T_{\mathrm{I4/mmm\rightarrow Bmab}}$ (K)	900 [273]	770 [73]	520 [74, 287]
$T_{\mathrm{Bmab\rightarrow P4_2/ncm}}$ (K)	135 [11]	70 [203]	- [288]
long range AFM T_N (K)	275 [11]	330 [73, 203]	325 [204, 289]
Doping dependence $T \simeq 10$ K			
x $Bmab \rightarrow I4/mmm$	$\simeq 0.4$		0.21 [79]
x c $\rightarrow$ ic correlations	0.3	0.2 [268]	0.02^a [214]
x diagonal$\rightarrow$ collinear stripes	-	-	0.055 ± 0.005 [159]

[a] In LSCuO commensurate order is suppressed already at very low doping $x \sim 0.02$. At higher values there is a spin-glass phase with incommensurate ordering, interpreted in terms of a diagonal stripe phase.

$T_{LTO} \sim 900$ K [273]. This LTO distortion exhibits a strong dependence on excess oxygen and the topotactic oxidation and oxygen diffusion constant in La_2CoO_4 is enhanced [66]. Therefore, stoichiometry is important to discuss the structural variation upon Sr doping. The influence of excess oxygen on the atomic parameters in $La_2CoO_{4+\delta}$ was studied in Ref. [65] at room temperature. Comparing the results for La_2CoO_4 with undoped single-layered perovskites La_2MO_4 ($M=$ Ni,Cu) with nominal increasing ionic radii [54], the coupling of LTO to the bond-length mismatch can be studied. The tilt distortion with $\Theta \sim 7$ ° [65] is enhanced in comparison to 6° in La_2NiO_4 [73] and 3° in La_2CuO_4 [70]. This can be ascribed to a strong mismatch between La-O and Co-O bonds. As denoted in Tab. 7.1, the HTT/LTO phase-transition temperature T_{LTO} is lowered in the parent compounds, accompanying the reduction of Θ across the Co, Ni, Cu series.

At low temperatures, indications for an LTT phase ($P4_2/ncm$ symmetry, No. 138) in La_2CoO_4 were found near $T \sim 135$ K [11]. Again, the LTT instability is suppressed in the undoped single-layered perovskites with increasing ionic radius and the reduction of the bond-length mismatch. While in La_2NiO_4 the $T_{LTT} = 70$ K is observed [203], no tetragonal low temperature phase was found in La_2CuO_4 [288]. The LTT phase transition in LSNiO is characterized to be first order with an order parameter $\mathbf{Q} = (Q_1, Q_2)$, $Q_1 = Q_2 \neq 0$, *i.e.* a variation of the NiO_6 octahedra tilt arrangement about 45° to LTO or along a HTT in-plane axis.

The influence of chemical pressure on the octahedral tilt instability can be investigated by the substitution of La^{3+} with larger Sr^{2+} ions. While the structure $La_{2-x}Sr_xCuO_4$ can

be stabilized up to $x \sim 0.2$ [75], the variation of structural parameters in $La_{2-x}Sr_xCoO_4$ can be studied over a wide doping range ($0 \leq x \leq 2$)[21, 25, 65]. We presented the characterization of the HTT/LTO phase transition in $La_{2-x}Sr_xCoO_4$. The ratio of La^{3+}/Sr^{2+} ionic radii and the removal of electrons from CoO_2 layers reduce the bond-length mismatch in the system with increasing dopant concentration. Simultaneous with the reduction of the CoO_6 octahedra tilt, the HTT-LTO transition temperature T_{LTO} is linearly lowered. As shown in Fig. 7.1 (b), T_{LTO} is nearly linearly reduced with x in all three systems. Near the critical doping concentration (x_{LTO}) a doping dependence of $T_{LTO} \propto (x_{LTO} - x)^{2\beta}$ in LSCuO is found. In comparison with LSCuO and LSNiO, the LTO-phase boundary of LSCoO is shifted to higher doping levels ($x \sim 0.35$), which reflects the steric nature of the tilt instability. In the Landau free-energy expansion, the tilt angle Θ in the LTO phase is proportional to the magnitude of the order parameter component Q_2. Therefore, a $(T_{LTO} - T)^{\frac{1}{2}}$ and a $(x_{LTO} - x)^{\frac{1}{2}}$ dependence of the Θ is expected near the phase transition regarding temperature and doping. The orthorhombic strain is quadratically coupled to Q_2. Thus, a linear reduction with T and x follows. In contrast to LSCuO and LSNiO, the reduction of the orthorhombicity in LSCoO is not linear. This may be due to excess oxygen or a further mechanism of strain release.

No indications for an LTT phase, *i.e.* $|Q_2| = |Q_1|$, were found at low temperatures for any of the doped cobaltate samples. Also in LSCuO, the LTT distortion is absent but can be induced by additional Nd doping [290, 291]. In contrast, the LTT phase of LSNiO is observed up to $x = 0.15$ [126]. Whether the LTO/LTT transition in LSNiO and LSCuO is related to a further strain reduction by a bond-length mismatch [126, 292] or to a partial $T \rightarrow T'$ phase transition [291] is unclear.

Antiferromagnetic Spin Correlations A long-range Néel state is stabilized in the parent compound La_2CoO_4 below $T = 275$ K [11] in the LTO phase. Interplanar nearest neighbors of Co^{2+} spins are antiferromagnetically coupled. The direction of the antiferromagnetic propagation vector of the three-dimensional spin structure is determined by the spin direction in adjacent layers. Similar to the spin structure in La_2NiO_4, the spin moment lies within the CoO_2 layers parallel to the antiferromagnetic propagation vector [11]. While the magnetism of La_2CuO_4 is close to the realization of an ideal two-dimensional $S = 1/2$ Heisenberg antiferromagnet, both La_2NiO_4 [127] and La_2CoO_4 exhibit a 2D Ising critical behavior [11]. A finite interlayer coupling stabilizes the three-dimensional long-range order in La_2CuO_4, while long-range order in the nickelate and cobaltate is driven by the Ising-anisotropy and the interlayer coupling of the spin moments. At low temperatures, the LTT transition in La_2CoO_4 is accompanied by a spin rotation of 90° with the spin moment being perpendicular to the antiferromagnetic propagation vector. The spin direction rotates in alternate layers according to the La_2CuO_4 type.

Hole doping and non-magnetic dilution of the system suppresses three-dimensional antiferromagnetic order in a single-layered perovskite system, see Fig. 7.1 (c). Mobile

holes [277] suppress commensurate antiferromagnetism more effectively (Sr: $x_c \sim 0.02$ [214]) in comparison to non-magnetic co-doping (Zn: $y_c \sim 0.26$) in cuprates [204]. The critical Sr doping level of commensurate spin order is shifted to a higher value $x \sim 0.1$ in nickelates [206]. The antiferromagnetic spin correlations in hole doped $La_{2-x}Sr_xCoO_4$ were investigated in chapter 6. Hole doping induces a spin-glass phase, which is suggested by the comparison of field-cooled and zero-field-cooled magnetic susceptibility [154]. Commensurate antiferromagnetic superstructure reflections were found at $x = 0.3$ below $T_s \sim 130$ K. This is well below the site-percolation threshold $x_p \sim 0.41$ on a square lattice for non-magnetic dilution [269], experimentally found in $K_2(Co_{1-x}Mg_x)F_4$ [254]. The finite correlation length of $\xi_{ab} = 5.0(1)$ Å would roughly agree with a random distribution holes in the system, leading to $\xi \propto a/\sqrt{x}$. An analysis of the isotropic spin-wave dispersion suggests a nearest-neighbor coupling of $J = 5.97(8)$ meV in $La_{1.7}Sr_{0.3}CoO_4$. The polarization analysis of the superstructure reflection reveals a spin moment within the CoO_2 planes, similar to the undoped compound. Since the transition temperature $T_s \sim 130$ K is increased in comparison to the $x = 0.3$ expectation value from a linear approximation of the reduction between $T_s = 275$ K at $x = 0$ and x_p, this may indicate an influence of the Co^{3+} spin state. This will be discussed in the following section in comparison to the indications from alternative physical properties. At this point, no differentiation between a static dilution of the antiferromagnetic order of Co^{2+} spins with essentially non-magnetic Co^{3+} ions and the stabilization of commensurate spin correlations by a magnetic Co^{3+} ions can be made.

Incommensurate Spin Order Further doping induces an incommensurate antiferromagnetic phase in $La_{2-x}Sr_xCoO_{4+\delta}$ ($x =$ 0.4, 0.45, 0.5, 0.6); $\left(\frac{1}{2} \pm \epsilon, \frac{1}{2} \mp \epsilon, 0\right)$ satellite reflections are observed around the antiferromagnetic Bragg point $\left(\frac{1}{2}, \frac{1}{2}, 0\right)$. The incommensurability ϵ is nearly linear to the hole density $n_h = x + 2\delta$, see Fig. 7.1 (e). A similar modulation and linearity of ϵ is observed for a so-called stripe-ordering of spins and charges on the square lattice. Charge carriers segregate into one-dimensional lines, building antiphase domain walls of the antiferromagnetic spin arrangement. The structure modulation of stripe order in LSCuO and LSNiO induces also superstructure reflections around $\left(\frac{1}{2}, \frac{1}{2}, 0\right)$, where the direction depends on the magnetic modulation vector, being parallel or diagonal to the HTT lattice. This observation of incommensurate spin correlations is the first indication of stripe-order in $La_{2-x}Sr_xCoO_4$. The nearly linearity of ϵ in $n_h = x + 2\delta$ suggests that the induced charge carriers contribute to the stripe formation in the CoO_2 layer. The arrangement of the satellite reflections indicates a diagonal stripe arrangement, similar to LSNiO ($0.135 \leq x \leq 0.5$) [158, 293] and to LSCuO at low doping levels ($0.02 \leq x \leq 0.053$) [214]. The in-plane correlation length reaches a maximum $\xi_{ab} \sim 25$ Å in the checkerboard-like charge ordered compound with $x = 0.5$. Since the maximum of the in-plane correlation length in LSNiO is observed at $x = 1/3$ [158], accompanied by a maximum of the spin and charge ordering temperatures,

the stripe order is most stable at this fraction, see Fig. 7.1 (d). Therefore, the stripe order in LSCoO would be best defined near the checkerboard arrangement of charges. In detail, a saturation of the incommensurability in cuprates [280] and nickelates [158] is found beyond optimal doping. This is also found in $La_{2-x}Sr_xCoO_4$ beyond $x = 0.5$. We find charge order superstructure reflections still in $La_{1.4}Sr_{0.6}CoO_4$ at room temperature. These charge order is short ranged and the reciprocal lattice reflections are too broad to verify a satellite splitting, expected for a charge order modulation concomitant to spin order modulation. Overall, we found indications for a stripe-like spin order modulation in $La_{2-x}Sr_xCoO_4$ for $0.4 \leq x \leq 0.6$, most stable at half-doping.

7.1. Co^{3+} Spin-State Transition Scheme

We found indications for a Co^{3+} spin-state transition in $La_{2-x}Sr_xCoO_4$ by analysis of the HTT lattice constants, the Co-O bond-lengths, the CoO_6 octahedra modulation at $x = 0.5$, and the antiferromagnetic spin correlations. Co^{2+} is considered to stay always in the high-spin state $S = 3/2$. As the crystal-field splitting is lowered with decreasing oxidation state, the stabilization of the $S = 3/2$ high-spin state is favored for Co^{2+} ($3d^7$) ions through Hunds' rule exchange in comparison to the low-spin state $S = 1/2$.

The analysis of the Co^{3+} spin state in a hole-doped mixed-valence system, such as $La_{2-x}Sr_xCoO_4$, is subtle and leads to a variety of proposed transitions. A charge ordering instability enables the investigation of nominally distinguishable lattice sites for the Co ions. First, the controversially proposed pictures of Co^{3+} spin states and spin-state transitions in $La_{2-x}Sr_xCoO_4$, as summarized in Tab. 7.2, are introduced.

Moritomo *et al.* analyzed the inverse magnetic susceptibility χ^{-1} of $La_{2-x}Sr_xCoO_4$ ($0.4 \leq x \leq 1.0$) in terms of a Curie-Weiss law and derived an effective magnetic moment μ_{eff} per Co site [27]. The decrease of the effective moment from 3.4 μ_B to 2.6 μ_B upon doping beyond $x = 0.7$ combined with the decrease of the in-plane resistivity ρ_{ab} by one order of magnitude at $T = 400$ K was interpreted in terms of a Co^{3+} spin-state transition from the high-spin to the intermediate-spin state. In comparison, our samples exhibit similar doping and temperature dependencies for ρ_{ab} and χ^{-1}. But the derivation of an effective magnetic moment is questionable, since the inverse susceptibility is not linear in the paramagnetic region and the system exhibits strong two-dimensional coupling. Itoh *et al.* determined the hyperfine coupling constant by a comparison of the ^{59}Co Knight shift *versus* magnetic susceptibility between $0.5 \leq x \leq 1.0$ and observed a decrease near $x = 0.75$ [30]. Co^{3+} spin states and two spin-state transitions in the doping region $0 < x < 1.1$ were also theoretically predicted by an unrestricted Hartree-Fock approximation. For $0 < x < 0.39$, an antiferromagnetic high-spin state, for $0.39 \leq x < 0.52$, a ferromagnetic high-spin state and for $0.52 \leq x < 1.1$, a ferromagnetic high-spin-low-spin ordered state is proposed [29]. However, we find no indications for a spin-state transition near $x = 0.75$ from our structural and magnetic investigations.

Estimated from	Doping level	Co^{3+} Spin state	Reference
χ	$x \sim 0.7$	HS $\rightarrow$ IS	[27]
χ	$x = 1$	LS, HS mixture for $20K \leq T \leq 400K$	[18]
χ,ρ,ΔCo-O	$1 \leq x \leq 1.5$	IS	[25, 89]
$\sigma(\omega)$	$x = 1$	HS, LS mixture	[210]
ρ	$x = 0.5$, $x = 1$	HS	[31]
^{59}Co NMR	$x \sim 0.75$	HS $\rightarrow$ IS	[30]
HFA	$0.00 < x < 0.39$	antiferromagnetic HS	[225]
	$0.39 \leq x < 0.52$	ferromagnetic HS	
	$0.52 \leq x < 1.1$	ferromagnetic HS-LS ordered state	

Table 7.2.: Proposed Co^{3+} spin states and spin-state transitions in $La_{2-x}Sr_xCoO_4$ by the analysis of different physical properties, *i.e.* the magnetic susceptibility χ, the optical conductivity $\sigma(\omega)$, the electrical conductivity ρ, and the bond-length anisotropy ΔCo-O. Unrestricted Hartree-Fock approximation was used to estimate different magnetic structures.

The suggestion of a Co^{3+} spin-state transition at $x \sim 0.4$ is based on the steep decrease of the Co-O_{apical} bond length near $x = 0.45$, the structural distortion of $Co^{2+}O_6$ and $Co^{3+}O_6$ octahedra at half doping, the c/a anomaly at high temperatures, the line-shape variation of the Co-L2, 3 edge in an XAS spectrum [285], the anisotropy of the magnetic susceptibility [154], and a good description of the magnon dispersion in $La_{1.5}Sr_{0.5}CoO_4$, when considering only Co^{2+}. The steep decrease of the Co-O_{apical} bond length near $x \sim 0.45$ can neither be attributed to the HTT/LTO phase boundary between $0.2 < x < 0.3$ nor to the reduction of the bond-length mismatch in an ionic model, since the La coordination anisotropy is smoothly decreased with Sr doping for $0.2 \leq x \leq 1.0$. Bond-length mismatch induced strains in the single-layered structure are indicated by the bond-valence sum deviations from the nominal value, which is systematically reduced with increasing x. The decrease between $x = 0.4$ and $x = 0.5$ is ΔCo-$O_{apical} = 0.071(2)$ Å and qualitatively agrees with the reduction of the ionic radii of $\Delta r_{HS,LS} = 0.065$ Å, when the difference between the in-plane and out-of-plane Co-O bond length and the nominal Co^{3+} concentration is taken into account. The Co^{2+} ion is little Jahn-Teller active. In the case of the single-layered cobaltate, a strong octahedral distortion of ~ 12 % partially lifts the t_{2g} and e_g degeneracy. Analyzing the atomic displacement parameters in the HTT phase, we find no signs for short range tilt instabilities, *i.e.* for a symmetry reduction. Also a $Co^{3+}O_6$ cluster calculation is difficult, as the distinct coordination of Co^{2+} and Co^{3+} ions is not known. The reduction of the out-of-plane Co-O bond length indicates a transition from a 'higher' to a 'lower' spin state. This agrees with the anomalous

increase of the out-of-plane lattice constant at $x = 0.5$, *i.e* a thermal population of a 'higher' spin state. A thermally induced spin-state transition for the pure Co^{3+} system $LaSrCoO_4$ was proposed by Demazeau *et al.* [18]. An equal ratio of high-spin and low-spin ions are ordered within the CoO_2 layers. Above 400 K, a low-spin to high-spin transition is proposed, while at 700 K, the high-spin state is stabilized for all cobalt ions. A Co^{3+} high-spin to low-spin transition near $x = 0.4$ is also supported by soft x-ray absorption measurements with magnetic circular dichroism (XMCD) and magnetic linear dichroism (XMLD) on $La_{2-x}Sr_xCoO_4$ (x = 0.3, 0.5, 0.8) by Z. Hu and H. Tjeng [285]. XMCD experiments were carried out at the European Synchrotron Radiation Facility in Grenoble, France, and XMLD experiments at the National Synchrotron Radiation Research Center in Hsinchu, Taiwan. XMCD data at the Co-$L_{2,3}$ edge at photon energies 770-810 eV indicate a significant shift in the spectral weight for Co^{3+} between $x = 0.3$ and $x = 0.5$, while the spectra characteristics are unchanged between $x = 0.5$ and $x = 0.8$. This qualitatively agrees with a Co^{3+} spin-state transition from HS to LS for the former doping range and an LS occupation for the latter doping range. A quantitative analysis using cluster calculation is needed for verification. Our analysis of the weak charge-order superstructure reflections in $La_{1.5}Sr_{0.5}CoO_4$ results in an average ionic radius difference of $r_{Co3+} = 0.530(1)$ Å and $r_{Co2+} = 0.613(1)$ Å, assuming $r_{O2-} = 1.42$ Ås [54]. The nominal Co^{3+} low-spin radius estimated by Shannon *et al.* is $r_{Co3+} = 0.545$ Å [54], but the Co^{2+} high-spin radius $r_{Co2+} = 0.745$ Å is too large. Also internal strains of the single-layered structure, which are not reduced by an octahedral tilt but by the tetragonal distortion, have to be accounted for. An intermediate spin-state occupation is expected to exhibit a remarkable Jahn-Teller activity [37], but the observed octahedra modulation does not suggest a Jahn-Teller active mode. In terms of the charge ordering phenomenon at half doping, the over and underdoped samples exhibit a saturation of the *c*-axis length. The anisotropy $\chi_{ab} > \chi_c$ of the magnetic susceptibility in $La_{2-x}Sr_xCoO_4$ was analyzed by Hollmann *et al.* [154] in terms of a cluster calculation. The anisotropic crystal field and spin-orbit coupling were calculated with respect to a Co^{2+} high-spin state and the Co^{3+} spin degree of freedom. At high doping levels, the observed anisotropy with a larger moment in the *ab*-plane corresponds to the primary Co^{2+} contribution. A less pronounced anisotropy at $x = 0.3$ is somehow surprising and may be attributed to a Co^{3+} high-spin state. Again, a Co^{3+} high-spin state is indicated at $x = 0.3$ and a low-spin state predicted at higher doping levels.

The stabilization of the antiferromagnetic nearest-neighbor interaction up to a hole doping level of $x = 0.3$ is surprising, but the hole mobility has to be taken into account. This doping level is well below the site-percolation threshold for magnetic dilution on the square lattice, but long-range antiferromagnetic order is more effectively suppressed by mobile holes in LSCuO and LSNiO. Short-range antiferromagnetic correlations in the spin-glass phase $0.02 < x < 0.05$ (see Fig. 7.1 (e)) of LSCuO are incommensurate and change the modulation direction near the superconducting phase boundary. Commensurate nearest-neighbor coupling in the spin-glass phase of LSNiO is stabilized up to

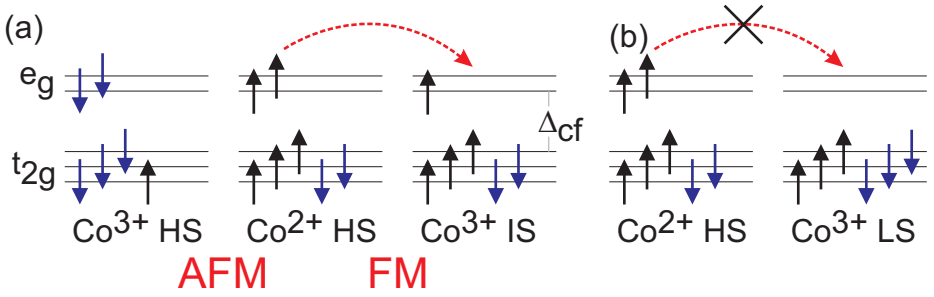

Figure 7.2.: Electron hopping scenarios in $La_{2-x}Sr_xCoO_4$. (a) While electron hopping via t_{2g} states between Co^{2+}-Co^{3+} high-spin ions would favor a ferromagnetic exchange coupling in the metallic and an antiferromagnetic one in the insulating state, exchange between Co^{2+} in the high-spin state and Co^{3+} in the intermediate-spin state is expected to be ferromagnetic. (b) e_g hopping to Co^{3+} neighbors in the low-spin state necessitate additional spin flips, which will be energetically unfavorable. The concept of immobilized Co^{2+} electrons was proposed for $HoBaCo_2O_{5.5}$ as a spin blockade [102].

$x = 0.1$. Therefore, on the one hand, the nearest-neighbor coupling without a charge segregation instability in single-layered cobaltates can be supported up to $x = 0.3$ by an antiferromagnetic exchange coupling between Co^{2+} and Co^{3+}, but, on the other hand, the hole mobility in comparison to the former systems is reduced. The Co^{3+} high-spin state is expected to couple antiferromagnetically to the Co^{2+} high-spin state in the insulating phase; this is in agreement with our spin-state scenario. The onset of incommensurate order at $x = 0.4$ for low temperatures would agree in a stripe scenario with the stabilization of the Co^{3+} low-spin state. Since the Co^{3+} low-spin state is not magnetic, a stripe instability could tend to a segregation of antiferromagnetic Co^{2+} domains via an antiphase boundary.

The question arises what causes the stabilization of the Co^{3+} high-spin state for $x \leq 0.4$. Illustratively, Co^{3+} ions are introduced in a background of Co^{2+} ions. The Co^{3+} spin degrees of freedom may be distinguishable from the magnetic exchange coupling and transport properties. Different electron hopping scenarios are shown in Fig. 7.2. (a) Electron hopping via t_{2g} states between Co^{2+}-Co^{3+} high-spin ions interchanges the spinstructure Co^{2+}-Co^{3+}→Co^{3+}-Co^{2+} and favors an antiferromagnetic exchange coupling in the insulating phase. The exchange between Co^{2+} in the high-spin state and Co^{3+} in the intermediate-spin state is expected to be ferromagnetic. (b) e_g hopping to Co^{3+} neighbors in the low-spin state necessitates additional spin flips, which will be energetically unfavorable. Co^{3+} low-spin ions would only bridge the antiferromagnetic exchange between Co^{2+} ions. The concept of immobilized Co^{2+} electrons was proposed for $HoBaCo_2O_{5.5}$ as a spin blockade [102]. In the case of $La_{2-x}Sr_xCoO_4$, one could think

of a magnetically stabilized high-spin or intermediate-spin state for Co^{3+} in the doping induced spin-glass phase. The Co^{3+} low-spin stabilization, at half doping, is in contrast to the analysis of the magnetic susceptibility from Moritomo *et al.* [27].

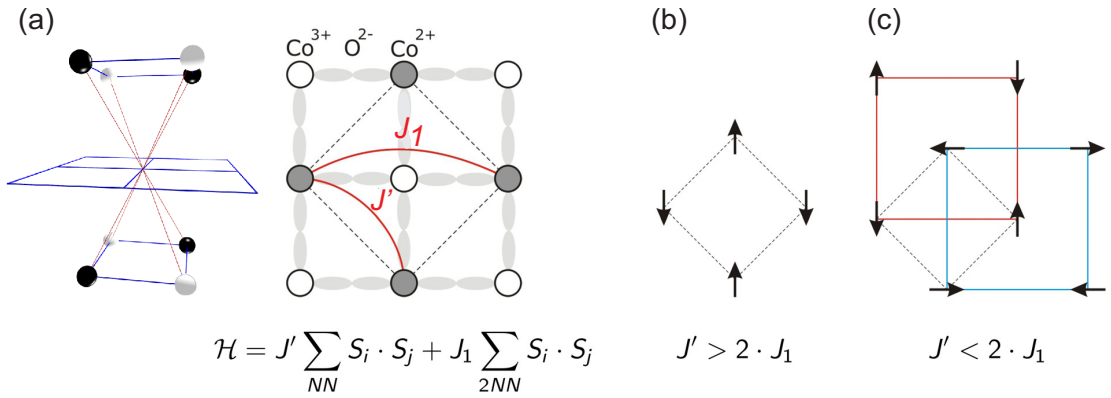

Figure 7.3.: Frustration in single-layered K_2NiF_4-type perovskites: (a) Interlayer charge and spin frustration. Due to the body-centered structure, the both spin- and charge-order interlayer couplings are fully frustrated for only nearest-neighbor coupling. Depending on the relative exchange integrals of effective nearest-neighbor J' and next-nearest-neighbor coupling J_1 the antiferromagnetic exchange leads to a simple coalignement of spins along Co^{2+}-O-Co^{3+}-O-Co^{2+} bonds (b) or decoupled antiferromagnetic sublattices (c).

The existence of a spin- and charge-glass phase in doped single-layered perovskites is, however, understandable, since frustration is expected to have a great influence on spin and charge order. The interlayer frustration, resulting from the body-centering of the lattice, is shown in Fig. 7.3. If only nearest-neighbor coupling is taken into account, both spin and charge order are purely two-dimensional and the CoO_2 layers are perfectly decoupled (Fig. 7.3 (a)). In the case of a charge-ordered state with non-magnetic ions, the spin frustration can be lifted. Within a CoO_2 layer, Co^{2+} spins along the tetragonal [1, 1, 0] direction are antiparallel aligned in the observed spin ordered phase of $La_{1.5}Sr_{0.5}CoO_4$, while along the [1, $\bar{1}$, 0] direction spins are parallel aligned. The spin frustration is lifted by the equal spin directions. Therefore, the observed finite interlayer coupling $J_2 \sim 0.04$ meV may stabilize the observed spin arrangement of the half doped cobaltate. This coupling also links the independent antiferromagnetic sublattices in a next-nearest neighbor coupling J_1 scenario. The relative magnitude of antiferromagnetic nearest-neighbor J' and next-nearest-neighbor J_1 coupling determines the resulting spin arrangement. For $J' > 2 \cdot J_1$, where the factor 2 considers the number of effective in-plane bonds of a tetragonal unit cell, nearest-neighbors of Co^{2+} spins are antiferromagnetically aligned (Fig. 7.3 (b)). For $J' < 2 \cdot J_1$ the sublattices of antiferromagnetically aligned

spins are decoupled (Fig. 7.3 (c)). Zaliznyak *et al.* proposed an equal magnitude of J' and J_1 for $La_{1.5}Sr_{0.5}CoO_4$ [7]. The antiferromagnetic spin arrangement shown in Fig. 6.8 is only energetically favorable with respect to both the interlayer coupling J_2 and next-nearest neighbor coupling J_1.

Ferromagnetic and antiferromagnetic exchanges between Co^{2+} and Co^{3+} ions were proposed for $Bi_2Sr_2CoO_{6+\delta}$ ($\delta \sim 0.25$) [100]. The authors refer to an octahedral coordination of the Co ion, for which the system is comparable to the single-layered perovskite. Due to the intersection of two BiO layers, the CoO_2 interlayer coupling should be less pronounced in comparison to the single-layered cobaltate. The system exhibits a predominant ferromagnetic behavior for $\delta = 0.25$, where a nominal equal ratio of Co^{2+}/Co^{3+} ions is expected. The absence of a ferromagnetic coupling probably gives further support for the picture of a Co^{3+} low spin occupation in half-doped $La_{1.5}Sr_{0.5}CoO_4$.

8. Summary

The structural and magnetic properties of alkali-earth doped single-layered perovskites $La_{2-x}A_xCoO_4$ (A = Ca, Sr, Ba) were investigated by means of x-ray and neutron scattering. To understand the remarkable physical properties of the material class of single-layered perovskites, like static incommensurate order in nickelates and high-temperature superconductivity in cuprates, the detailed analysis of the relevant lattice, spin, and charge degrees of freedom is an important issue. In comparison to the isostructural $La_{2-x}Sr_xCuO_4$ and $La_{2-x}Sr_xNiO_4$ systems, the Co^{3+} spin degree of freedom is of particular importance for the magnetic exchange coupling and for structural variations with doping in cobaltates.

The high-temperature tetragonal (HTT) and the low-temperature orthorhombic (LTO) phase at low Sr-dopant concentrations of the $La_{2-x}Sr_xCoO_4$ ($0.05 \leq x \leq 1.1$) crystal structure were investigated. In general, the temperature and doping dependence of the structural instabilities can be ascribed to steric effects in an ionic picture. All compounds $La_{2-x}Sr_xMO_4$ (M = Co, Ni, Cu) exhibit the LTO distortion at low doping levels. With increasing Sr doping, the mismatch between La/Sr-O and Co-O bond-lengths is reduced and the LTO distortion vanishes between $0.2 < x < 0.3$ at room temperature. We found no indications for the re-entry of a tetragonal phase at low temperatures, the so-called LTT phase, for the doped samples in the investigated temperature region. The high value of the HTT/LTO transition temperature of the parent compound, the shift of the phase boundary to higher Sr doping levels, and the large tilt angle in La_2CoO_4 agree with an increase of internal strains across the series of systems $La_{2-x}Sr_xMO_4$ with M = Cu, Ni, Co. The LTO distortion is induced by a cooperative buckling of corner-sharing CoO_6 octahedra. The reduction of La and Co coordination anisotropies in the HTT phase on further doping agrees with the reduction of internal strains. The difference between the calculated Co bond-valence sum and the nominal value $v_{Co} = 2 + x$ decreases. We found a steep decrease of the Co-O_{apical} bond length near $x \sim 0.45$, which is decoupled from the HTT phase stabilization. This anomalous Co-O bond-length reduction, *i.e.* the reduction of the CoO_6 octahedron elongation, must be attributed to an electronic effect, *i.e.* it originates from a Co^{3+} high-spin to low-spin state transition. The ratio c/a of the half-doped compound with $x = 0.5$ varies anomalously with increasing temperature. While the c-axis exhibits an enhanced increase above room temperature, the in-plane lattice constant is nearly constant in this temperature range. In contrast, the increase of the c/a-ratio of the $x = 0.4$ and $= 0.6$ compound is reduced at high temperatures. The checkerboard-like charge-order state and the concomitant maximal resistivity for the

half-doped compound support the segregation of charges and therefore the effect of the thermal population of a higher Co^{3+} spin state on the lattice constants.

The checkerboard-like charge order of $La_{1.5}Sr_{0.5}CoO_4$ was investigated via single-crystal neutron diffraction at room temperature. This temperature is well below the charge-order proposed transition temperature of $T = 825(27)$ K, reported by Zaliznyak *et al.* [8]. The charge order is short range in nature with a finite in-plane correlation length of $\xi_{ab} = 19(1)$ Å and nearly decoupled CoO_2 layers ($\xi_c = 8.1(3)$ Å). This is due to the charge frustration in the body-centered crystal structure of the HTT phase, when accounting for nearest-neighbor interactions only. Four direct Co neighbors in adjacent layers with a nominal equal ratio of Co^{2+} and Co^{3+} ions lead to an interlayer frustration of the charge arrangement. The analysis of the charge-order superstructure, *i.e.* the oxygen-displacement modulation in neutron diffraction experiments, determines the exact coordination parameters of the thusly distinct Co sites and provides information about a possible Co^{3+} spin-state degree of freedom. A breathing-type modulation was reported on the basis of few superstructure reflections collected on a triple-axis spectrometer [8]. In our experiments, we collected a large set of superstructure reflections with respect to the proposed breathing-type distortion and also accounting for more complex oxygen-displacement schemes. We found a distortion mode which is in contrast to the reported Jahn-Teller-like elongation and compression of the CoO_6 octahedra along the c-direction. A simple shrinking and enlargement of alternate $Co^{3+}O_6$ and $Co^{2+}O_6$ octahedra was observed. This modulation is not Jahn-Teller active and agrees with the proposed Co^{3+} low-spin state at this temperature as suggested from the powder and single-crystal x-ray analyses.

All three parent compounds La_2CoO_4, La_2NiO_4, and La_2CuO_4 exhibit a Néel ordered state with antiferromagnetic nearest-neighbor coupling and spin moments lying within the MO_2 layers. While the long-range order in the Heisenberg system $LaCuO_4$ is stabilized via a finite interlayer coupling, long-range order in La_2CoO_4 and La_2NiO_4 can be stabilized by an Ising-type anisotropy and a finite interlayer coupling. Hole doping suppresses long-range order and induces a spin-glass phase in the single-layered compounds. The static and dynamic spin correlations in high-quality single crystals of $La_{2-x}Sr_xCoO_4$ ($x = 0.3$, 0.4, 0.45, 0.5, 0.6) were investigated by elastic and inelastic neutron scattering. The comparison of field-cooled and zero-field-cooled magnetic susceptibility suggests a spin-glass-like freezing transition of the investigated samples at low temperatures. A short-range antiferromagnetic nearest-neighbor interaction was found in the $x = 0.3$ sample in the LTO distorted phase. Similar to the parent compound La_2CoO_4, the spin moment lies within the CoO_2 layers, as verified by a polarization analysis. The magnetic layers are effectively decoupled and, therefore, the magnetic system can be considered to be two-dimensional. The doping level $x = 0.3$ is below the site-percolation threshold $x_c \sim 0.41$ [269] of non-magnetic dilution on a square lattice, but the high concentration with stable commensurate antiferromagnetic correlations is surprising with regard to the effective reduction of antiferromagnetic correlations through mobile holes

in $La_{2-x}Sr_xCuO_4$ and $La_{2-x}Sr_xNiO_4$. While the Co^{3+} low-spin state is non-magnetic, the high-spin state is expected to couple antiferromagnetically to Co^{2+} neighbors in the insulating phase. We cannot distinguish between a Co^{3+} low-spin or high-spin occupation at this point, but found indication for the latter in the doping dependence of the crystal structure. The observation of antiferromagnetic nearest-neighbor coupling agrees with the high-spin state deduced from the structural analysis. Note that a Co^{3+} intermediate-spin state may favor a ferromagnetic exchange, thereby strongly disturbing the commensurate antiferromagnetic order. Further hole doping induces an incommensurate modulation of the antiferromagnetic spin arrangement. The incommensurability ϵ is found to increase nearly linearly with hole density $n_h = x$. A maximum of the in-plane correlation length is found at half doping. The maximum of the spin-freezing temperature is found near half doping. In contrast to the most stable stripe order in $La_{2-x}Sr_xNiO_4$ at $x = 1/3$ [158], this suggests a stabilization of the spin arrangement by the charge-order instability near half doping. The dynamic spin correlations were investigated for $x = 0.3, 0.5, 0.6$. The in-plane dispersion is found to be isotropic in all cases and well described by a simple spin Hamiltonian accounting for one in-plane exchange interaction and an additional intra-plane interaction for $x = 0.5$. For the nearest-neighbor interaction at $x = 0.3$ we found an exchange integral $J = 5.97(8)$ meV for $S = 3/2$ and the number of nearest neighbors $z = 4$ in linear spin-wave theory. The spin-wave dispersion in $La_{1.5}Sr_{0.5}CoO_4$ is well described by an effective next-nearest-neighbor exchange between Co^{2+} spins with respect to the spin arrangement. Non-magnetic Co^{3+} ions in the low-spin state bridge the antiferromagnetic exchange. A finite interlayer coupling was observed and stabilizes a propagation vector $\mathbf{Q}_s = (1/4, 1/4, 1)$. The Co^{3+} spin-state transition near $x = 0.4$ is also supported by the analysis of the anisotropy of the magnetic susceptibility by N. Hollmann [154]. At high doping levels, the observed anisotropy corresponds to the expected Co^{2+} anisotropy, suggesting Co^{3+} ions in a non-magnetic state. With a decreasing number of holes and a decreasing nominal Co^{3+} density, the anisotropy is reduced at $x = 0.3$. This indicates a Co^{3+} magnetic state via the spin-orbit coupling. Furthermore, a spectroscopic study of the soft x-ray absorption using magnetic dichroism at the Co-$L_{2,3}$ edge indicates a redistribution of spectral weight for Co^{3+} from $x = 0.3$ to $x = 0.5$ according to the here proposed spin-state transition. In analogy to $La_{2-x}Sr_xCuO_4$ and $La_{2-x}Sr_xNiO_4$, we attribute the incommensurability above $x = 0.3$ to a stripe-like modulation instability of the spin arrangement, where all induced holes contribute to the modulation for $\epsilon \propto n_h$. However, due to the short-range nature of static correlations, an incommensurability of the charge-carrier order, coupled to the spin incommensurability, was not detectable in our experiments. Although further investigations are needed, a first indication for stripe-like order is found in single-layered cobaltates .

A. Sample Characterization

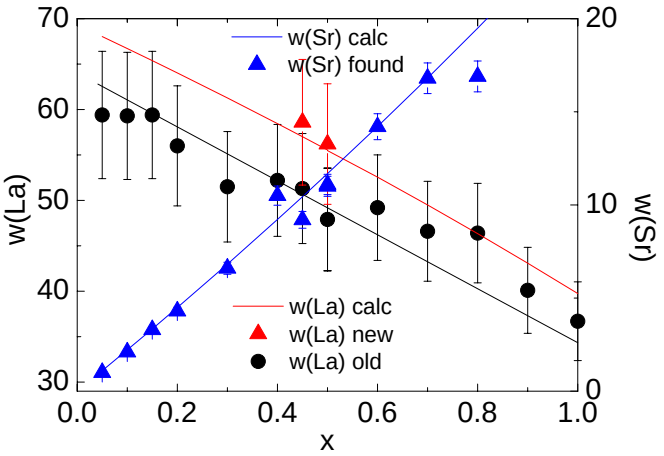

Figure A.1.: Atomic absorption spectroscopy of $La_{2-x}Sr_xCoO_4$ with the calculated and observed constituent weight w.

x	XPD Sample	SXD Sample	NPD Sample	SCNDT Instrument	INS Instrument	SCND Instrument
Sr						
0.05	MHA033					
0.10	MHA034					
0.15	MHA035					
0.2	MB25		MB25			
0.3	MB7	MB7		G4.3	4F1,4F2,1T1	
0.4	MB15	MB15	MB15	Unidas	4F2	
0.45	MA345	MA345			1T1	
0.5	MB1	MB1,MBII		G4.3	4F1, 1T1, PUMA	HEIDI,5C2
0.6	MB17	MB17		G4.3	4F2	
0.7	MB17	MB17				
0.75	LH210	LH210				
0.8	MB11	MB11	MB11			
0.9	N.N.	N.N.				
1.0	MA310	MA310				
1.1	N.N.					
Ca						
$x = 0.5$	MB40	MB40				

Table A.1.: Listing of the $La_{2-x}A_xCoO_4$ samples (A = Sr, Ca) used in this work. X-ray powder diffraction (XPD), single-crystal x-ray diffraction (SXD), neutron powder diffraction (NPD), single-crystal neutron diffraction on a triple-axis spectrometer (SCNDT), inelastic neutron scattering (INS) and single-crystal neutron diffraction (SCND) experiments on four-circle diffractometers were performed within this thesis.

B. X8 Apex Single-Crystal Ball Mill

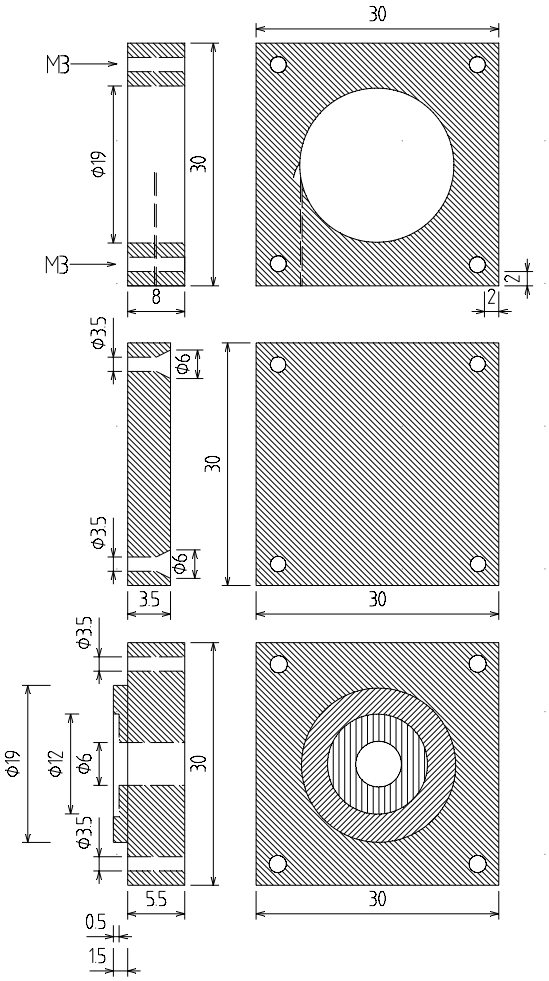

Figure B.1.: Design drawing of the single-crystal ball mill. Dimensions are given in mm. Brass was used as the standard material. The air stream input was optimized by a welded tube connection.

C. Magnetic Form Factor of Co Ions

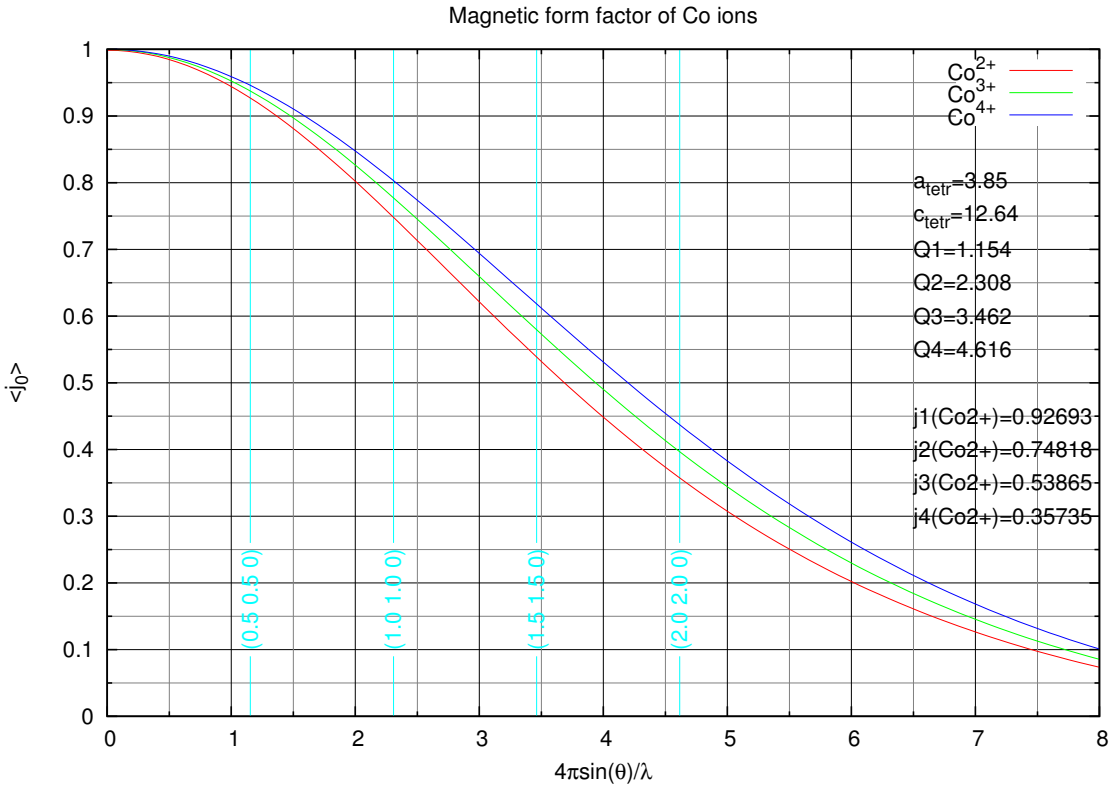

Figure C.1.: Magnetic form factor of Co ions. The **Q**-dependence of the scattering amplitude for a single ion can be calculated in analytical approximation after Brown [282]. Typical reciprocal lattice points for the single-layered cobaltate are represented in light blue.

List of Figures

List of Tables

Bibliography

The numbers at the end of each entry refer to the corresponding pages of occurrence.

[1] Johann Wolfgang von Goethe, *Faust, Der Tragödie erster Teil*, http://www.digbib.org/ (1749). 5

[2] D. Balz and K. Blieth, *Die Struktur des Kaliumnickelfluorids, K_2NiF_4*, Z. Elektrochem. **59**, 545 (1955). 9

[3] J. G. Bednorz and K. A. Müller, *Possible High T_c Superconductivity in the Ba-La-Cu-O System*, Z. Physik B **64**, 189 (1986). 9, 16

[4] J. M. Tranquada, B. J. Sternlieb, J. D. Axe, Y. Nakamura, and S. Uchida, *Evidence for stripe correlations of spins and holes in copper oxide superconductors*, Nature **375**, 561 (1995). 9, 16, 27, 41, 93

[5] J. M. Tranquada, D. J. Buttrey, and V. Sachan, *Incommensurate Stripe Order in $La_{2-x}Sr_xNiO_4$ with $x = 0.225$*, Phys. Rev. B **54**, 12318 (1996). 9, 16, 41, 114

[6] B. J. Sternlieb, J. P. Hill, U. C. Wildgruber, G. M. Luke, B. Nachumi, Y. Moritomo, and Y. Tokura, *Charge and Magnetic Order in $La_{0.5}Sr_{1.5}MnO_4$*, Phys. Rev. Lett. **76**, 2169 (1996). 9, 41, 42, 83, 84, 85, 91, 104

[7] I. A. Zaliznyak, J. P. Hill, J. M. Tranquada, R. Erwin, and Y. Moritomo, *Independent Freezing of Charge and Spin Dynamics in $La_{1.5}Sr_{0.5}CoO_4$*, Phys. Rev. Lett. **85**, 4353 (2000). 9, 10, 21, 41, 42, 43, 81, 85, 86, 92, 103, 104, 106, 113, 127

[8] I. A. Zaliznyak, J. M. Tranquada, R. Erwin, and Y. Moritomo, *Spin-entropy-driven melting of the charge order in $La_{1.5}Sr_{0.5}CoO_4$*, Phys. Rev. B **64**, 195117 (2001). 9, 10, 21, 41, 42, 43, 60, 61, 81, 83, 84, 85, 86, 91, 92, 103, 113, 130

[9] P. G. Freeman, A. T. Boothroyd, D. Prabhakaran, D. González, and M. Enderle, *Spin reorientation in the incommensurate stripe-ordered phase of $La_{3/2}Sr_{1/2}NiO_4$*, Phys. Rev. B **66**, 212405 (2002). 9

[10] Y. T. Zhu and A. Manthiram, *Role of bond-length mismatch in $L_{2-x}Ce_xCuO_4$ (L=lanthanide)*, Phys. Rev. B **49**, 6293 (1994). 9, 17, 117

[11] K. Yamada, M. Matsuda, Y. Endoh, B. Keimer, R. J. Birgenau, S. Onodera, J. Mizukawa, T. Matsuura, and G. Shirane, *Successive antiferromagnetic phase transition in single-crystal La_2CoO_4*, Phys. Rev. B **39**, 2336 (1989). 9, 10, 16, 19, 20, 25, 27, 42, 44, 45, 50, 51, 53, 57, 94, 95, 98, 101, 118, 119, 120

[12] J. Zaanen, G. A. Sawatzky, and J. W. Allen, *Band Gaps and Electronic Structure of Transition-Metal Compounds*, Phys. Rev. Lett. **55**, 418 (1985). 10, 21

[13] S. Uchida, H. Eisaki, and S. Tajima, *Electron correlation and optical conductivity in high-T_c copper oxides - origin of the mid-infrared absorption band*, Physica B **186-188**, 975 (1993). 10, 22, 42

[14] Y. Moritomo, T. Arima, and Y. Tokura, *Electronic Structure of Layered Perovskite $LaSr\mathrm{M}O_4$ (*M=*Cr, Mn, Fe, Co)*, J. Phys. Soc. Japan **64**, 4117 (1995). 10, 22, 43

[15] M. Dlouhá, S. Vratislav, A. Chichev, and Z. Jirák, *Neutron diffraction study of layered perovskite $La_{0.6}Sr_{1.4}CoO_4$*, Acta Physica Slovaca **56**, 181 (2006). 10

[16] S. Castro-García, M. Sánchez-Andújar, C. Rey-Cabezudo, M. A. Senarís-Rodríguez, and C. Julien, *IR characterization of $Ln_{2-x}Sr_xCoO_4$ ($x \geq 1$; Ln=La, Nd) oxides*, J. of Alloys and Compounds **323-324**, 710 (2001). 10

[17] A. Rabenau and P. Eckerlein, *Die K_2NiF_4-Struktur beim La_2NiO_4*, Acta. Cryst. **11**, 304 (1958). 10, 16

[18] G. Demazeau, P. Courbin, G. le Flem, M. Pouchard, P. Hagenmuller, J. L. Soubeyroux, I. G. Main, and G. A. Robins, *Propriétés structurales et magnétiques de $SrLaCoO_4$. Une discussion de la structure électronique du cobalt trivalent*, Nouveau Journal de Chimie **3**, 171 (1979). 10, 43, 123, 124

[19] Y. Furukawa, S. Wada, and Y. Yamada, *Phase Transition from Antiferromagnetic Insulator to Ferromagnetic Metal in $La_{2-x}Sr_xCoO_4$ -Magnetization and NMR Studies-*, J. Phys. Soc. Japan **62**, 1127 (1993). 10, 25, 114

[20] J. Matsuno, Y. Okimoto, M. Kawasaki, and Y. Tokura, *Variation of the Electronic Structure in Systematically Synthesized $Sr_2\mathrm{M}O_4$ (*M = *Ti, V, Cr, Mn, and Co)*, Phys. Rev. Lett. **95**, 176404 (2005). 10, 19

[21] J. Matsuno, Y. Okimoto, Z. Fang, X. Z. Yu, Y. Matsui, N. Nagaosa, M. Kawasaki, and Y. Tokura, *Metallic Ferromagnet with Square-Lattice CoO_2 Sheets*, Phys. Rev. Lett. **93**, 167202 (2004). 10, 44, 120

[22] T. Matsuura, J. Tabuchi, J. Mizusaki, S. Yamauchi, and K. Fueki, *Electrical Properties of $La_{2-x}Sr_xCoO_4$-I: Structure, Electrical Conductivity, and Seebeck Coefficient of Single Crystals (x = 0.0, 0.5, 1.0, and 1.5)*, J. Phys. Chem. Solids **49**, 1403 (1988). 10, 16, 42, 50, 51, 99

[23] T. R. S. Prasanna and A. Navrotsky, *Energetics of $La_{2-x}Sr_xCoO_{4-y}$ (0.5≤ x ≤1.5)*, J. of Solid State Chem. **112**, 192 (1994). 10

[24] M. Sánchez-Andújar and M. A. Señarís-Rodríguez, *Synthesis, structure and microstructure of the layered compounds $Ln_{1-x}Sr_{1+x}CoO_4$ (Ln: La, Nd and Gd)*, Sol. State Sciences **6**, 21 (2004). 10

[25] Y. Shimada, S. Miyasaka, R. Kumai, and Y. Tokura, *Semiconducting ferromagnetic states in $La_{1-x}Sr_{1+x}CoO_4$*, Phys. Rev. B **73**, 134424 (2006). 10, 120, 123

[26] X. L. Wang and E. Takayama-Muromachi, *Magnetic and transport properties of the layered perovskite system $Sr_{2-y}Y_yCoO_4$ ($0 \leq y \leq 1$)*, Phys. Rev. B **72**, 064401 (2005). 10, 19

[27] Y. Moritomo, K. Higashi, K. Matsuda, and A. Nakamura, *Spin-state transition in layered perovskite cobalt oxides: $La_{2-x}Sr_xCoO_4$ (0.4≤ x ≤1.0)*, Phys. Rev. B **55**, R14725 (1997). 10, 25, 43, 95, 122, 123, 126

[28] X. Yang, L. Luo, and H. Zhong, *Structure of $La_{2-x}Sr_xCoO_{4\pm\lambda}$ ($x = 0.0 - 1.0$) and their catalytic properties in the oxidation of CO and C_3H_8*, Applied Catalysis A **272**, 299 (2004). 10, 16, 20

[29] J. Wang, W. Zhang, and D. Y. Xing, *Magnetic structure of the layered perovskite $LaSrCoO_4$*, Phys. Rev. B **62**, 14140 (2000). 10, 25, 43, 122

[30] M. Itoh, M. Mori, Y. Moritomo, and A. Nakamura, *NMR study of the spin state and magnetic properties of layered perovskite cobalt oxides $La_{2-x}Sr_xCoO_4$*, Physica B **259-261**, 997 (1999). 10, 25, 43, 122, 123

[31] T. Matsuura, J. Tabuchi, J. Mizusaki, S. Yamauchi, and K. Fueki, *Electrical Properties of $La_{2-x}Sr_xCoO_4$-II: Models and Analysis of the Relationship between Cobalt 3d Electron State and Structural, Electrical and Magnetic Properties*, J. Phys. Chem. Solids **49**, 1409 (1988). 10, 43, 123

[32] C. Zobel, M. Kriener, D. Bruns, J. Baier, M. Grüninger, T. Lorenz, P. Reutler, and A. Revcolevschi, *Evidence for a low-spin to intermediate-spin state transition in $LaCoO_3$*, Phys. Rev. B **66**, 020402 (2002). 11, 24, 43

[33] M. W. Haverkort, Z. Hu, J. C. Cezar, T. Burnus, H. Hartmann, M. Reuther, C. Zobel, T. Lorenz, A. Tanaka, N. B. Brookes, H. H. Hsieh, H.-J. Lin, C. T. Chen, and L. H. Tjeng, *Spin State Transition in $LaCoO_3$ Studied Using X-ray Absorption Spectroscopy and Magnetic Circular Dichroism*, Phys. Rev. Lett. **97**, 176405 (2006). 11, 24, 43

[34] M. Medarde, C. Dallera, M. Grioni, J. Voigt, A. Podlesnyak, E. Pomjakushina, K. Conder, Th. Neisius, O. Tjernberg, and S. N. Barilo, *Low-temperature spin-state transition in $LaCoO_3$ investigated using resonant x-ray absorption at the Co K edge*, Phys. Rev. B **73**, 054424 (2006). 11, 43

[35] G. Vankó, J.-P. Rueff, A. Mattila, Z. Németh, and A. Shukla, *Temperature- and pressure-induced spin-state transitions in $LaCoO_3$*, Phys. Rev. B **73**, 024424 (2006). 11, 24, 43

[36] K. Knízek, P. Novák, and Z. Jirák, *Spin state of $LaCoO_3$: Dependence on CoO_6 octahedra geometry*, Phys. Rev. B **71**, 054420 (2005). 11, 43

[37] G. Maris, Y. Ren, V. Volotchaev, C. Zobel, T. Lorenz, and T. T. M. Palstra, *Evidence for orbital ordering in $LaCoO_3$*, Phys. Rev. B **67**, 224423 (2003). 11, 23, 24, 43, 124

[38] J. B. Goodenough and J. M. Longo, *Landolt-Börnstein - Group III Condensed Matter*, Volume New Series III/4a, chapter 3. Crystallographic and magnetic properties of perovskites and perovskite-related compounds, pages 126–266. Springer Verlag, Berlin / Heidelberg (1970). 13

[39] M. Marezio, J. P. Remeika, and P. D. Dernier, *The Crystal Chemistry of the Rare Earth Orthoferrites*, Acta. Cryst. B **26**, 2008 (1970). 13

[40] S. Geller, *Crystal Structure of Gadolinium Orthoferrite $GdFeO_3$*, Journal of Chemical Physics **24**, 1236 (1956). 13

[41] M. W. Lufaso and P. M. Woodward, *Jahn-Teller distortions, cation ordering and octrahedral tilting in perovskites*, Acta. Cryst. B **60**, 10 (2004). 13

[42] M. Cwik, T. Lorenz, J. Baier, R. Müller, G. André, F. Bourée, F. Lichtenberg, A. Freimuth, R. Schmitz, E. Müller-Hartmann, and M. Braden, *Crystal and magnetic structure of $LaTiO_3$: Evidence for nondegenerate t_{2g} orbitals*, Phys. Rev. B **68**, 060401 (2003). 13

[43] X. Qiu, Th. Proffen, J. F. Mitchell, and S. J. L. Billinge, *Orbital Correlations in the Pseudocubic O and the Rhombohedral R Phases of $LaMnO_3$*, Phys. Rev. Lett. **94**, 177203 (2005). 13

[44] T. Chatterji, F. Fauth, B. Ouladdiaf, P. Mandal, and B. Gosh, *Volume collapse in $LaMnO_3$ caused by an orbital order-disorder transition*, Phys. Rev. B **68**, 052406 (2003). 13, 36

[45] H. D. Megaw and C. N. W. Darlington, *Geometrical and Structural Relations in the Rhombohedral Perovskites*, Acta. Cryst. A **31**, 161 (1975). 13

[46] A. M. Glazer, *The Classification of Tilted Octahedra in Perovskites*, Acta. Cryst. B **28**, 3384 (1972). 13

[47] A. M. Glazer, *Simple Ways of Determining Perovskite Structures*, Acta. Cryst. A **31**, 756 (1975). 13

[48] P. M. Woodward, *Octahedral Tilting in Perovskites. I. Geometrical Considerations*, Acta. Cryst. B **53**, 32 (1997). 13, 14

[49] P. M. Woodward, *Octahedral Tilting in Perovskites. II. Structure Stabilizing Forces*, Acta. Cryst. B **53**, 44 (1997). 13

[50] V. M. Goldschmidt, *Geochemische Verteilungsgesetze der Elemente VII, VIII. Untersuchungen über Bau und Eigenschaften von Krystallen*, Norsk. Vid. Akad., Math.-Naturvid. Kl. (1926). 14

[51] C. A. Randall, A. S. Bhalla, T. R. Shrout, and L. E. Cross, *Classification and consequences of complex lead perovskite ferroelectrics with regard to B-site cation order*, J. Mater. Res. page 529 (1990). 14

[52] H. D. Megaw, *G. Solids. Crystal structure of barium titanium oxide and other double oxides of the perovskite type*, Trans. Faraday Soc. **42**, A224 (1946). 14

[53] M. W. Lufaso and P. M. Woodward, *Prediction of the crystal structures of perovskites using the software program SPuDS*, Acta. Cryst. B **57**, 725 (2001). 14

[54] R. D. Shannon, *Revised Effective Ionic Radii and Systematic Studies of Interatomie Distances in Halides and Chalcogenides*, Acta. Cryst. A **32**, 751 (1976). 14, 52, 54, 80, 119, 124

[55] P. G. Radaelli and S.-W. Cheong, *Structural phenomena associated with the spin-state transition in $LaCoO_3$*, Mat. Res. Bull. **23**, 501 (1988). 14, 24

[56] H. A. Jahn and E. Teller, *Stability of Polyatomic Molecules in Degenerate Electronic States. I. Orbital Degeneracy*, Proc. Roy. Soc. A **161**, 220 (1937). 15

[57] E. Müller-Hartmann, *Skript zur Vorlesung Theoretische Festkörperphysik II: Modellierung von Übergangsmetalloxidsystemen.* Universität zu Köln, (2003). 15

[58] S. N. Ruddlesden and P. Popper, *New compounds of the K_2NiF_4 type*, Acta. Cryst. **10**, 538 (1957). 16

[59] S. N. Ruddlesden and P. Popper, *The compound $Sr_3Ti_2O_7$ and its structure*, Acta. Cryst. **11**, 54 (1958). 16

[60] Y. Tokura and N. Nagaosa, *Orbital Physics in Transition-Metal Oxidegs*, Science **288**, 462 (2000). 16

[61] E. Dagotto, *Correlated electrons in high-temperature superconductors*, Rev. Mod. Phys. **66**, 763 (1994). 16

[62] J. M. Tranquada, H. Woo, T. G. Perring, H. Goka, G. D. Gu, G. Xu, M. Fujita, and K. Yamada, *Quantum Magnetic Excitations from Stripes in Copper-Oxide Superconductors*, Nature **429**, 534 (2004). 16, 41, 93, 114

[63] N. F. M. Henry and K. Lonsdale, *Internantional Tables For X-Ray Crystallography*, Volume I Symmetry Groups, chapter 6.2, page 548. The Kynoch Press, Birmingham, England (1969). 16

[64] S. K. Yeh, S. Y. Wu, C. S. Lee, and Y. Wang, *Electron-density distribution in a crystal of Dipotassium tetrafluoronickelate, K_2NiF_4*, Acta. Cryst. B **49** (1993). 16

[65] R. Le Toquin, *Réactivité, structure et propriétés physiques de $SrCoO_{2.5+\delta}$ et $La_2CoO_{4+\delta}$. Etude par diffraction des rayons X et des neutrons in situ*, Dissertation, Université de Rennes (2003). 16, 17, 19, 20, 21, 31, 42, 45, 46, 50, 51, 53, 66, 68, 119, 120

[66] A. Nemudry, P. Rudolf, and R. Schöllhorn, *Room temperature topotactic oxidation of lanthanum cobalt oxide $La_2CoO_{4.00}$*, Sol. State Ionics **109**, 213 (1998). 16, 20, 42, 57, 119

[67] R. A. M. Ram, P. Ganguly, and C. N. R. Rao, *Preparation and Characterization of $La_2CoO_{4+\delta}$*, Mat. Res. Bull. **23**, 501 (1988). 16, 20

[68] T. Matsuura, J. Mizusaki, S. Yamauchi, and K. Fueki, *Single Crystal Growth of $La_{2-x}Sr_xCoO_4$ (x=0.0, 0.5, 1.0, and 1.5)*, J. Appl. Phys. **23**, 1143 (1984). 16, 19

[69] U. Lehmann and H. Müller-Buschbaum, *Ein Beitrag zur Chemie der Oxocobaltate(II): La_2CoO_4, Sm_2CoO_4*, Z. anorg. allg. Chem. **470**, 59 (1980). 16

[70] M. Ferretti, E. Magnone, and M. Napoletano, *Structural properties and chemical homogeneity of underdoped $La_{2-x}M_xCuO_4$ cuprates (M = Sr, Ba)*, Int. J. Mod. Phys. **13**, 979 (1999). 16, 42, 45, 46, 119

[71] M. Medarde and J. Rodríguez-Carvajal, *Oxygen vacancy ordering in $La_{2-x}Sr_xNiO_{4-\delta}$ ($0 \leq x \leq 0.5$): the crystal structure and defects investigated by neutron diffraction*, Z. Physik B **102**, 307 (1997). 16, 46

[72] J. D. Axe and M. K. Crawford, *Structural Instabilities in Lanthanum Cuprate Superconductors*, J. Low Temp. Phys. **95**, 271 (1994). 16, 117

[73] J. Rodríguez-Carvajal, M. T. Fernández-Díaz, and J. L. Martínez, *Neutron Diffraction study on structural and magnetic properties of La_2NiO_4*, J. Phys.: Condens. Matter **3**, 3215 (1991). 16, 21, 42, 46, 94, 119

[74] M. Reehuis, C. Ulrich, K. Prokes, A. Gozar, G. Blumberg, Seiki Komiya, Yoichi Ando, P. Pattison, and B. Keimer, *Crystal structure and high-field magnetism of La_2CuO_4*, cond-mat/0601616 (2006). 16, 68, 94, 97, 119

[75] P. G. Radaelli, D. G. Hinks, A. W. Mitchell, B. A. Hunter, J. L. Wagner, D. Dabrowski, K. G. Vandervoort, H. K. Viswanathan, and J. D. Jorgensen, *Structural and superconducting properties of $La_{2-x}Sr_xCuO_4$ as a function of Sr content*, Phys. Rev. B **49**, 4163 (1994). 17, 41, 46, 117, 120

[76] P. Ganguly and C. N. R. Rao, *Crystal Chemistry and Magnetic Properties of Layered Metal Oxides Possessing the K_2NiF_4 or Related Structures*, J. of Solid State Chem. **53**, 193 (1984). 17

[77] A. Manthiram and J. B. Goodenough, *Thermal-Expansion Mismatch and Intergrowth Types in the System $La_{2-y}Nd_yCuO_4$*, J. of Solid State Chem. **92**, 231 (1991). 17

[78] M. Braden, W. Schnelle, W. Schwarz, N. Pyka, G. Heger, Z. Fisk, K. Gamayunov, I. Tanaka, and H. Kojima, *Elastic and inelastic neutron scattering studies on the tetragonal to orthorhombic phase transition of $La_{2-x}Sr_xCuO_{4\pm\delta}$*, Z. Physik B **94**, 29 (1994). 17

[79] H. Takahashi, H. Shaked, B. A. Hunter, P. G. Radaelli, R. L. Hitterman, D. G. Hinks, and J. D. Jorgensen, *Structural effects of hydrostatic pressure in orthorhombic $La_{2-x}Sr_xCuO_4$*, Phys. Rev. B **50**, 3221 (1994). 17, 46, 119

[80] J. D. Axe, A. H. Moudden, D. Hohlwein, D. E. Cox, K. M. Mohanty, A. R. Moodenbaugh, and Youwen Xu, *Structural Phase Transformations and Superconductivity in $La_{2-x}Ba_xCuO_4$*, Phys. Rev. Lett. **62**, 2751 (1989). 18

[81] B. Büchner, *Strukturelle Phasenübergänge und Supraleitung in Selten-Erd-dotiertem (La,Sr)$_2$CuO$_4$*, Dissertation, Universität zu Köln (1994). 18, 44

[82] T. Suzuki and T. Fujita, *Structural phase transition in (La$_{1-x}$Ba$_x$)$_2$CuO$_{4-\delta}$*, Physica C **159**, 111 (1989). 18

[83] Wu Ting, K. Fossheim, and T. Lægreid, *A Landau theoretical study of La$_{2-x}$(Sr,Ba)$_x$CuO$_{4-y}$: Structural phase transitions and related elastic properties*, Sol. State Commun. **75**, 727 (1990). 18, 117

[84] D. M. Hatch, H. T. Stokes, K. S. Aleksandrov, and S. V. Misyul, *Phase transition in perovskite-like A_2BX_4*, Phys. Rev. B **39**, 9282 (1989). 19

[85] J. Petzelt, *Symmetry and lattice-dynamic aspects of structural phase transitions in (CH$_3$NH$_3$)$_2$MNCL$_4$ and related compounds*, J. Phys. Chem. Solids **36**, 1005 (1975). 19

[86] K. S. Aleksandrov and J. Bartolomé, *Octahedral tilt phases in perovskite-like crystals with slabs containing an even number of octahedral layers*, J. Phys. – Condens. Matter **6**, 8219 (1994). 19

[87] Y. Tokura, H. Takagi, H. Watabe, H. Matsubara, S. Uchida, K. Hiraga, T. Oku, T. Mochiku, and H. Asano, *New family of layered copper oxide compounds with ordered cations: Prospective high-temperature superconductors*, Phys. Rev. B **40**, 2568 (1989). 19

[88] C. N. R. Rao and A. K. Ganguli, *Structural Aspects of Superconducting Cuprates*, Acta Cryst. **B51**, 604 (1995). 19

[89] M. Sánchez-Andújar, D. Rinaldi, R. Caciuffo, J. Mira, J. Rivas, and M. A. Señarís-Rodríguez, *Magnetotransport properties of spin-glass-like layered compounds $Ln_{1-x}Sr_{1+x}CoO_4$ ($0 \leq x \leq 0.40$)*, Sol. State Sciences **6**, 21 (2006). 19, 123

[90] M. Sánchez-Andújar, A. Castro-Couceiro, B. Rivas-Murias, J. Mira, J. Rivas, and M. A. Señarís-Rodríguez, *Influence of the dimensionality of the structure and the nature of the rare earth on the magneto-transport properties of $Nd_{1-x}Sr_{1+x}CoO_4$ ($0 \leq x \leq 0.30$)*, Sol. State Sciences **6**, 21 (2006). 19

[91] M. Sánchez-Andújar and M. A. Señarís-Rodríguez, *Magnetic order in the lamellar compounds $La_{1-x}Sr_{1+x}CoO_4$ ($0 \leq x \leq 0.4$)*, Journal of Magnetism and Magnetic Materials **272-276**, 855 (2004). 19

[92] V. A. Cherepanov, L. Ya. Gavrilova, E. A. Filonova, M. V. Trifonova, and V. I. Voronin, *Phase equilibria in the La-Ba-Co-O system*, Mater. Res. Bull. **34**, 983 (1999). 19, 54, 55

[93] L. Ya. Gavrilova, Ya. V. Teslenko, L. A. Bannikch, T. V. Aksenova, and V. A. Cherepanov, *The crytal structure and homogeneity range of the solid solution in La-Sr-Co-Ni-O system*, J. of Alloys and Compounds **344**, 128 (2002). 19

[94] M. Haider, *Strukturuntersuchungen an $La_{2-x}Sr_xCo_{1-y}Ru_yO_4$ und Umbau der XPD Anlagen*, Diplomarbeit, Universität zu Köln, (2005). 19, 29, 30, 45, 50, 51, 57, 59, 60, 61

[95] D. Hohlwein, A. Hoser, R. Sonntag, W. Prandl, W. Schäfer, R. Kiemel, S. Kemmler-Sack, and A. W. Hewat, *Structural changes in superconducting $La_{1.8}Sr_{0.2}CuO_4$ by alloying copper with cobal*, Physica B **156-157**, 893 (1989). 19, 69

[96] R. Kiemel, W. Schäfer, S. Kemmler-Sack, G. Kruschel, and B. Elschner, *Solid solutions in the systems $YBa_2(Cu_{1-x}Co_x)_3O_{7-z}$ and $La_{1.8}Sr_{0.2}Cu_{1-x}Co_xO_{4\pm z}$*, J. Less Common Metals **143**, L11 (1988). 19

[97] Paul Poix, *Etude de la structure K_2NiF_4 par la méthode des invariants, I. Cas des oxydes A_2BO_4*, J. of Solid State Chem. **31**, 95 (1980). 19

[98] R. L. Zhang, J. M. Dai, W. H. Song, Y. Q. Ma, J. Yang, J. J. Du, and Y. P. Sun, *Photoinduced spin-state transition of Co^{3+} in the layered perovskite manganite thin film*, J. Phys. – Condens. Matter **16**, 2245 (2004). 19

[99] O.H. Hansteen and H. Fjellvåg, *Synthesis, Crystal Structure, and Magnetic Properties of $La_4Co_3O_{10+\delta}$ ($0.00 \leq \delta \leq 0.30$)*, J. of Solid State Chem. **141**, 212 (1998). 20

[100] K. J. Thomas, Y. S. Lee, F. C. Chou, B. Khaykovich, P. A. Lee, M. A. Kastner, R. J. Cava, and J. W. Lynn, *Antiferromagnetism, ferromagnetism, and magnetic phase separation in $Bi_2Sr_2CoO_{6+\delta}$*, Phys. Rev. B **66**, 054415 (2002). 20, 113, 127

[101] J. M. Tarascon, P. F. Miceli, P. Barboux, D. M. Hwang, G. W. Hull, M. Giroud, L. H. Greene, Y. LePage, W. R. McKinnon, E. Tselepis, G. Peizier, M. Eibschutz D. A. Neumann, and J. J. Rhyne, *Structure and magnetic properties of nonsuperconducting doped Co and Fe $Bi_2Sr_2Cu_{1-x}M_xO_y$ phases*, Phys. Rev. B **39**, 11587 (1989). 20

[102] A. Maignan, V. Caignaert, B. Raveau, D. Khomskii, and G. Sawatzky, *Thermoelectric Power of $HoBaCo_2O_{5.5}$: Possible Evidence of the Spin Blockade in Cobaltites*, Phys. Rev. Lett. **93**, 026401 (2004). 20, 113, 125

[103] A. A. Taskin, A. N. Lavrov, and Y. Ando, *Transport and magnetic properties of $GdBaCo_2O_{5+x}$ single crystals: A cobalt oxide with square lattice CoO_2 planes over a wide range of electron and hole doping*, Phys. Rev. B **71**, 134414 (2005). 20

[104] A. A. Taskin and Y. Ando, *Electron-Hole Asymmetry in $GdBaCo_2O_{5+x}$: Evidence for Spin-Blockade of Electron Transport in a Correlated Electron System*, Phys. Rev. Lett. **95**, 176603 (2005). 20

[105] C. Frontera, J. L. García-Muñoz, A. E. Carillo, C. Ritter, D. M. y Marero, and A. Caneiro, *Structural and magnetic study of $PrBaCo_2O_{5+\delta}$ ($\delta = 0.75$) cobaltite*, Phys. Rev. B **70**, 184428 (2004). 20

[106] C. Frontera, J. L. García-Muñoz, A. Llobet, and M. A. G. Aranda, *Selective spin-state switch and metal-insulator transition in $GdBaCo_2O_{5.5}$*, Phys. Rev. B **65**, 180405 (2002). 20

[107] F. Fauth, E. Suard, V. Caignaert, and I. Mirebeau, *Spin-state ordered clusters in the perovskite $NdBaCo_2O_{5.47}$*, Phys. Rev. B **66**, 184421 (2002). 20

[108] A. A. Taskin, A. N. Lavrov, and Y. Ando, *Ising-Like Spin Anisotropy and Competing Antiferromagnetic-Ferromagnetic Orders in $GdBaCo_2O_{5.5}$ Single Crystals*, Phys. Rev. Lett. **90**, 227201 (2003). 20

[109] T. Vogt, P. M. Woodward, P. Karen, B. A. Hunter, P. Henning, and A. R. Moodenbaugh, *Low to High Spin-State Transition Induced by Charge Ordering in Antiferromagnetic $YBaCo_2O_5$*, Phys. Rev. Lett. **84**, 2969 (2000). 20

[110] A. Maignan, C. Martin, D. Pelloquin, N. Nguyen, and B. Raveau, *Structural and Magnetic Studies of Ordered Oxygen-Deficient Perovskites* $\mathrm{Ln}BaCo_2O_{5+}$*, Closely Related to the "112" Structure*, J. of Solid State Chem. **142**, 247 (1999). 20

[111] E. Suard, F. Fauth, V. Caignaert, I. Mirebeau, and G. Baldinozzi, *Charge ordering in the layered Co-based perovskite $HoBaCo_2O_5$*, Phys. Rev. B **61**, R11871 (2000). 20

[112] J. S. Gardner, D. McK. Paul, and B. Lebech, *Neutron diffraction study of $La_2CoO_{4.15}$ single crystal*, Physica B **234-236**, 721 (1997). 20

[113] T. Nitadori, M. Muramatsu, and M. Misono, *Valence Control, Reactivity of Oxygen, and Catalytic Activity of $La_{2-x}Sr_xCoO_4$*, Chem. of Materials **1**, 215 (1989). 20

[114] T. Nitadori and M. Misono, *Catalytic Properties of $La_{2-x}Sr_xCoO_4$, a K_2NiF_4-Type Mixed Oxide*, Chem. Lett. **8**, 1255 (1986). 20

[115] L. Borovskikh, G. Mazo, and E. Kemnitz, *Reactivity of oxygen of complex cobaltates $La_{1-x}Sr_xCoO_{3-\delta}$ and $LaSrCoO_4$*, Sol. State Sciences **5**, 409 (2003). 20

[116] V. V. Vashook, H. Ullmann, O. P. Olshevskaya, V. P. Kulik, V. E. Lukashevich, and L. V. Kokhanovskij, *Composition and electrical conductivity of some cobaltates of the type $La_{2-x}Sr_xCoO_{4.5-x/2\pm\delta}$*, Sol. State Ionics **138**, 99 (2000). 20

[117] J. T. Lewandowski, R. A. Beyerleiu, J. M. Longo, and R. A. McCauley, *Nonstoichiometric K_2NiF_4-type Phases in the Lanthanum-Cobalt-Oxygen System*, J. Am. Ceram. Soc. **69**, 699 (1986). 20, 95

[118] M. Huecker, K. Chung, M. Chand, T. Vogt, J. M. Tranquada, and D. J. Buttrey, *Oxygen and strontium codoping of La_2NiO_4: Room-temperature phase diagrams*, Phys. Rev. B **70**, 064105 (2004). 21

[119] P. Gopalan, M. W. McElfresh, Z. Kakol, J. Spalek, and J. M. Honig, *Influence of oxygen stoichiometry on the antiferromagnetic ordering of single crystals of $La_2NiO_{4+\delta}$*, Phys. Rev. B **45**, 249 (1992). 21

[120] T. Freltoft, D. J. Buttrey, G. Aeppli, D. Vaknin, and G. Shirane, *Magnetic correlations and their dependence on excess oxygen in La_2CoO_4*, Phys. Rev. B **44**, 5046 (1991). 21

[121] J. M. Tranquada, Y. Kong, J. E. Lorenzo, D. J. Buttrey, D. E. Rice, and V. Sachan, *Oxygen intercalation, stage ordering, and phase separation in $La_2NiO_{4+\delta}$ with $0.05 \lesssim \delta \lesssim 0.11$*, Phys. Rev. B **50**, 6340 (1994). 21, 42

[122] W. Paulus, A. Cousson, G. Dhalenne, J. Berthon, A. Revcolevschi, S. Hosoya, W. Treutmann, G. Heger, and R. Le Toquin, *Neutron diffraction studies of stoichiometric and oxygen intercalated La_2NiO_4 single crystals*, Sol. State Sciences **4**, 565 (2002). 21

[123] J. E. Lorenzo, J. M. Tranquada, D. J. Buttrey, and V. Sachan, *Neutron-diffraction studies on the time dependence of the oxygen ordering in $La_2NiO_{4.105}$*, Phys. Rev. B **51**, 3176 (1995). 21

[124] S. J. Skinner, *Characterisation of $La_2NiO_{4+\delta}$ using in-situ high temperature neutron powder diffraction*, Sol. State Sciences **5**, 419 (2003). 21

[125] J. D. Jorgensen, B. Dabrowski, Shiyou Pei, D. R. Richards, and D. G. Hinks, *Structure of the interstitional oxygen defect in $La_2NiO_{4+\delta}$*, Phys. Rev. B **40**, 2187 (1989). 21, 44, 57

[126] O. Friedt, *Präparation, Charakterisierung und Struktur von* $La_{2-x}Sr_xNiO_{4+\delta}$, Diplomarbeit, Universität zu Köln, (1998). 21, 44, 45, 47, 95, 118, 120

[127] G. Aeppli and D. J. Buttrey, *Magnetic Correlations in* $La_2NiO_{4+\delta}$, Phys. Rev. Lett. **61**, 203 (1988). 21, 42, 94, 95, 120

[128] T. Hirayama, M. Nakagawa, A. Sumiyama, and Y. Oda, *Superconducting properties in* $La_2CuO_{4+\delta}$ *with excess oxygen*, Phys. Rev. B **58**, 5856 (1998). 21

[129] J. D. Jorgensen, B. Dabrowski, Shiyou Pei, D. G. Hinks, L. Soderholm, B. Morosin, J. E. Schirber, E. L. Venturini, and D. S. Ginley, *Superconducting phase of* $La_2CuO_{4+\delta}$*: A superconducting composition resulting from phase separation*, Phys. Rev. B **38**, 11337 (1988). 21

[130] B. O. Wells, Y. S. Lee, M. A. Kastner, R. J. Christianson, R. J. Birgeneau, K. Yamada, Y. Endoh, and G. Shirane, *Incommensurate Spin Fluctuations in High-Transition Temperature Superconductors*, Science **277**, 1067 (1997). 21, 41, 93

[131] X. Xiong, P. Wochner, S. C. Moss, Y. Cao, K. Koga, and M. Fujita, *Ebvidence of In-Plane Superstructure Formation in Phase-Separated and Staged Single Crystal* $La_2CuO_{4+\delta}$, Phys. Rev. Lett. **76**, 2997 (1996). 21

[132] P. Blakeslee, R. J.Birgeneau, F. C. Chou, R. Christianson, M. A. Kastner, Y. S. Lee, and B. O. Wells, *Electrochemistry and staging in* $La_2CuO_{4+\delta}$, Phys. Rev. B **57**, 13915 (1998). 21

[133] C. Rial, U. Amador, E. Moŕan, M. A. Alario-Franco, and N. H. Andersen, *Evidence of interstitial oxygen in room temperature oxidized* $La_{2-x}Sr_xCuO_{4+y}$ *(0<x<0.1)*, Physica C **234**, 237 (1994). 21

[134] C. Rial, U. Amador, E. Moŕan, N. H. Andersen, and M. A. Alario-Franco, *Structural and physical aspects of room temperature oxidized* $La_{2-x}Sr_xCuO_{4+y}$ *(0<x<0.15)*, Physica C **235**, 561 (1994). 21, 47

[135] M. Benomar, *Einkristallzüchtung und Charakterisierung von dotiertem* $La_{2-x}M_xO_4$ *(*M= *Mn, Ni, Co)*, Dissertation, Universität zu Köln (2007). 22, 23, 25, 29, 36, 54, 80

[136] N. Tsuda, K. Nasu, A. Fujimori, and K. Siratori, *Electronic Conduction in Oxides*, Volume 2nd ed., Springer Verlag, Heidelberg (2000). 23

[137] A. L. Efros, *Coulomb gap in disordered systems*, J. Phys. C **9**, 2021 (1976). 23

[138] G.H. Jonker and J.H. Van Santen, *Magnetic Compounds with Perowskite Structure III.*
Ferromagnetic Compounds of Cobalt, Physica **XIX**, 120 (1953). 23

[139] S. Yamaguchi, Y. Okimoto, H. Taniguchi, and Y. Tokura, *Spin-state transition and high-spin polarons in $LaCoO_3$*, Phys. Rev. B **53**, 2926 (1996). 24

[140] P. M. Raccah and J. B. Goodenough, *First-Order Localized-Electron $\rightleftarrows$ Collective-Electron Transition in $LaCoO_3$*, Phys. Rev. **155**, 932 (1967). 24, 43

[141] M. Itoh, I. Natori, S. Kubota, and K. Motoya, *Spin-Glass Behavior and Magnetic Phase Diagram of $La_{1-x}Sr_xCoO_3$ ($0 \leq x \leq 0.5$) Studied by Magnetization Measurements*, J. Phys. Soc. Japan **63**, 1486 (1994). 24

[142] S. Noguchi, S. Kawamata, K. Okuda, H. Nojiri, and M. Motokawa, *Evidence for the excited triplet of Co^{3+} in $LaCoO_3$*, Phys. Rev. B **66**, 094404 (2002). 24

[143] T. Saitoh, T. Mizokawa, A. Fujimori, M. Abbate, Y. Takeda, and M. Takano, *Electronic structure and temperature-induced paramagnetism in $LaCoO_3$*, Phys. Rev. B **55**, 4257 (1997). 24

[144] M. Itoh, M. Sugahara, I. Natori, and K. Motoya, *Spin State and Hyperfine Interaction in $LaCoO_3$: NMR and Magnetic Susceptibility Studies*, J. Phys. Soc. Japan **64**, 3967 (1995). 24

[145] N. Menyuk, K. Dwight, and P. M. Raccah, *Low Temperature Crystallographic and Magnetic Study of $LaCoO_3$*, J. Phys. Chem. Solids **28**, 549 (1967). 24

[146] G. H. Jonker, *Magnetic and Semiconducting Properties of Perovskites Containing Manganese and Cobalt*, J. Appl. Phys. **37**, 1424 (1966). 24

[147] W. C. Koehler and E. O. Wollan, *Neutron-Diffraction study of the magnetic properties of perovskite-like compounds $LaBO_3$*, J. Phys. Chem. Solids **2**, 100 (1957). 24

[148] M. A. Korotin, S. Y. Ezhov, I. V. Solvyev, V. I. Anisimov, D. I. Khomskii, and G. A. Sawatzky, *Intermediate-spin state and properties of $LaCoO_3$*, Phys. Rev. B **54**, 5309 (1996). 24

[149] R.R. Heikes, R.C. Miller, and R. Mazelsky, *Magnetic and Electrical Anomalies in $LaCoO_3$*, Physica **30**, 1600 (1964). 24

[150] J.B. Goodenough, *An Interpretation of the Magnetic Properties of the Perovskite-Type Mixed Crystals $La_{1-x}Sr_xCoO_3$*, J. Phys. Chem. Solids **6**, 287 (1958). 24

[151] G. Thornton, B. C. Tofield, and A. W. Hewat, *A Neutron Diffraction Study of $LaCoO_3$ in the Temperature Range $4.2 < T < 1248$ K*, J. of Solid State Chem. **61**, 301 (1986). 24

[152] A. Podlesnyak, S. Streule, J. Mesot, M. Medarde, E. Pomjakushina, K. Conder, A. Tanaka, M. W. Haverkort, and D. I. Khomskii, *Spin-State Transition in $LaCoO_3$: Direct Neutron Spectroscopic Evidence of Excited Magnetic States*, Phys. Rev. Lett. **97**, 247208 (2006). 24

[153] S. M. Hayden, G. H. Lander, J. Zarestky, P. J. Brown, C. Stassis, P. Metcalf, and J. M. Honig, *Single crystral growth and magnetic properties of $La_{2-x}MCoO_4$ (M = Ca, Ba)*, Physica B **in preparation** (2006). 24, 26

[154] N. Hollmann, *Magnetische Eigenschaften von Kobaltaten*, Diplomarbeit, Universität zu Köln, (2006). 25, 26, 36, 114, 121, 123, 124, 131

[155] P. Ganguly and S. Ramasesha, *Magnetic Behaviour of La_2CoO_4 and Related Solids*, Magnetism Letters **1**, 131 (1980). 25, 95

[156] J. A. Mydosh, *Spin glasses: an experimental introduction*, Taylor & Francis, London (1993). 25

[157] G. Heber, *Einführung in die Theorie des Magnetismus*, Verlag für Wissenschaft und Forschung, Wiesbaden (1983). 25

[158] H. Yoshizawa, T. Kakeshita, R. Kajimoto, T. Tanabe, T. Katsufuji, and Y. Tokura, *Stripe order at low temperatures in $La_{2-x}Sr_xNiO_4$ with* $0.289 \leq x \leq 0.5$, Phys. Rev. B **61**, R854 (2000). 27, 83, 85, 93, 95, 108, 109, 110, 114, 121, 122, 131

[159] M. Matsuda, M. Fujita, K. Yamada, R. J. Birgeneau, M. A. Kastner, H. Hiraka, Y. Endoh, S. Wakimoto, and G. Shirane, *Static and dynamic spin correlations in the spin-glass phase of slightly doped $La_{2-x}Sr_xCuO_4$*, Phys. Rev. B **62**, 9148 (2000). 27, 95, 99, 114, 119

[160] H. B. Brom and J. Zaanen, *Magnetic Ordering Phenomena and Dynamic Fluctuations in Cuprate Superconsuctors and Insulating Nickelates*, Volume Handbook of Magnetic Materials 15, Elsevier Science B.V., Amsterdam (2003). 27

[161] P. A. Lee, N. Nagaosa, and X.-G. Wen, *Doping a Mott insulator: Physics of high-temperature superconductivity*, Rev. Mod. Phys. **78**, 17 (2006). 27, 41

[162] M. A. Kastner, R. J. Birgeneau, G. Shirane, and Y. Endoh, *Magnetic, transport, and optical properties of monolayer copper oxides*, Rev. Mod. Phys. **70**, 897 (1998). 27, 41, 95

[163] A. W. Overhauser, *Observability of Charge-Density Waves by Neutron Diffraction*, Phys. Rev. B **3**, 3173 (1971). 27

[164] P. M. de Wolff, *The Pseudo-Symmetrie of Modulated Crystal Structures*, Acta. Cryst. A **30**, 777 (1974). 27

[165] V. Petricek and P. Coppens, *Structure Analysis and Displacively Modulated Molecular Crystals*, Acta. Cryst. A **41**, 478 (1985). 27

[166] A. Yamamoto, *Structure Factor of Modulated Crystal Structures*, Acta. Cryst. A **38**, 87 (1982). 27

[167] A. T. Boothroyd, D. Prabhakaran, P. G. Freeman, S. J. S. Lister, M. Enderle, A. Hiess, and J. Kulda, *Spin dynamics in stripe-ordered* $La_{5/3}Sr_{1/3}NiO_4$, Phys. Rev. B **67**, 100407 (2003). 28

[168] M. Reuther, *Züchtung und Charakterisierung von Übergangsmetalloxideinkristallen mit Schichtstruktur*, Dissertation, Universität zu Köln, (in preparation). 29

[169] A. N. Petrov, V. A. Cherepanov, Y. Yu. Zuyev, and V. M. Zhukovsky, *Thermodynamic Stability of Ternary Oxides in* Ln-M-*O (*Ln = *La, Pr, Nd;* M = *Co, Ni, Cu) Sytems*, J. of Solid State Chem. **77**, 1 (1988). 29

[170] J. J. Janecek and G. P. Wirtz, *Ternary Compounds in the System La-Co-O*, J. Amer. Cer. Soc. **61**, 242 (1978). 29

[171] R. A. Young, *The Rietveld Method*, Oxford University Press, New York (1990). 29, 30

[172] J. Rodriguez-Carvajal, *FULLPROF: A Program for Rietveld Refinement and Pattern Matching Analysis* (1990). 29, 34, 44

[173] O. Schumann, *Röntgen- und Neutronenmessungen an Ruthenium-Verbindungen*, Diplomarbeit, Universität zu Köln, (2004). 30

[174] G. M. Sheldrick, *SADABS, Program for Empirical Absorption Correction of Area Detector Data* (1996). 32

[175] R. H. Blessing, *An Empirical Correction for Absorption Anisotropy*, Acta. Cryst. A **51**, 33 (1995). 32

[176] K. Kirschbaum, A. Martin, and A. Alan Pinkerton, $\lambda/2$ *Contamination in charge-coupled-device area-detector data*, J. of Alloys and Compounds **30**, 514 (1997). 32, 47

[177] V. Petricek, M. Dusek, and L. Palatinus, *Jana2000. The crystallographic computing system. Institute of Physics, Praha, Czech Republic* (2000). 32, 34, 87

[178] P. J. Becker and P. Coppens, *Extinction within the limit of validity of the Darwin transfer equations. I. General formalism for primary and secondary extinction and their applications to spherical crystals*, Acta. Cryst. A **30**, 129 (1974). 33

[179] C. Giacovazzo, H. L. Monaco, D. Viterbo, F. Scordari, G. Gilli, G. Zanotti, and M. Catti, *Fundamentals of Crystallography*, Oxford University Press, Oxford (1992). 33, 97

[180] W. H. Zachariasen, *A general theory of X-ray diffraction in crystals*, Acta. Cryst. **23**, 558 (1967). 33

[181] W. Massa, *Kristallstrukturbestimmung*, Teubner Verlag, Stuttgart (2002). 34

[182] G. Caglioti, A. Paoletti, and F. P. Ricci, *Choice of collimators for a crystal spectrometer for neutron diffraction*, Nucl. Instrum. **3**, 223 (1958). 34, 44

[183] G. Shirane, S. M. Shapiro, and J. M. Tranquada, *Neutron Scattering with a Triple-Axis Spectrometer*, Cambridge University Press, Cambridge (2002). 35, 36, 37

[184] T. Brückel, G. Heger, and D. Richter, *Neutron Scattering*, Forschungszentrum Jülich GmbH, Jülich (2000). 37

[185] T. Brückel and W. Schweika, *Polarized Neutron Scattering*, Forschungszentrum Jülich GmbH, Jülich (2002). 37

[186] G. L. Squires, *Introduction to the Theorie of Thermal Neutron Scattering*, Dover Publications Inc., Mineola (1978). 37

[187] R. M. Moon, T. Riste, and W. C. Koehler, *Polarization Analysis of Thermal-Neutron Scattering*, Phys. Rev. **181**, 920 (1969). 37, 38, 97

[188] T. Chatterji, *Neutron Scattering From Magnetic Materials*, chapter 1 Magnetic Neutron scattering, page 7. Elvesier, Amsterdam (2006). 37

[189] W. Marshall and S. W. Lovesey, *Theory of Thermal Neutron Scattering*, Clarendon Press, Oxford (1971). 39

[190] V. Sachan, D. J. Buttrey, J. M. Tranquada, J. E. Lorenzo, and G. Shirane, *Charge and spin ordering in $La_{2-x}Sr_xNiO_{4.00}$ with $x = 0.135$ and 0.20*, Phys. Rev. B **51**, 12742 (1995). 41, 114

[191] C. H. Chen, S.-W. Cheong, and A. S. Cooper, *Charge modulations in $La_{2-x}Sr_xNiO_{4+y}$: Ordering of polarons*, Phys. Rev. Lett. **71**, 2461 (1993). 41, 42, 83, 93

[192] V. Hinkov, S. Pailhes, P. Bourges, Y. Sidis, A. Ivanov, A. Kulakov, C. T. Lin, D. P. Chen, C. Bernhard, and B. Keimer, *Two-dimensional geometry of spin excitations in the high-transition-temperature superconductor $YBa_2Cu_3O_{6+x}$*, Nature **430**, 650 (2004). 41

[193] S. A. Kivelson, I. P. Bindloss, E. Fradkin, V. Oganesyan, J. M. Tranquada, A. Kapitulnik, and C. Howald, *How to detect fluctuating stripes in the high-temperature superconductors*, Rev. Mod. Phys. **75**, 1201 (2003). 41

[194] J. Lee, K. Fujita, K. McElroy, J. A. Slezak, M. Wang, Y. Aiura, H. Bando, M. Ishikado, T. Masui, J.-X. Zhu, A. V. Balatsky, H. Eisaki, S. Uchida, and J. C. Davis, *Interplay of electron-lattice interactions and superconductivity in $Bi_2Sr_2CaCu_2O_{8+\delta}$*, Nature **442**, 546 (2006). 41

[195] A. C. Mclaughlin, F. Sher, and J. P. Attfield, *Negative lattice expansion from the superconductivity-antiferromagnetism crossover in ruthenium copper oxides*, Nature **436**, 829 (2006). 41

[196] D. Reznik, L. Pintschovius, M. Ito, S. Iikubo, M. Sato, H. Goka, M. Fujita, K. Yamada, G. D. Gu, and J. M. Tranquada, *Electron-phonon coupling reflecting dynamic charge inhomogeneity in copper oxide superconductors*, Nature **440**, 1170 (2006). 41

[197] T. P. Devereaux, T. Cuk, Z.-K. Shen, and N. Nagaosa, *Anisotropic Electron-Phonon Interaction in the Cuprates*, Phys. Rev. Lett. **93**, 117004 (2004). 41

[198] T. Fukuda, J. Mizuki, K. Ikeuchi, K. Yamada, A. Q. R. Baron, and S. Tsutsui, *Doping dependence of softening in the bond-stretching phonon mode of $La_{2-x}Sr_xCuO_4$ ($0 \leq x \leq 0.29$)*, Phys. Rev. B **71**, 060501 (2005). 41

[199] A. Lanzara, P. V. Bogdanov, X. J. Zhou, S. A. Kellar, D. L. Feng, E. D. Lu, T. Yoshida, H. Eisaki, A. Fujimori, K. Kishio, J.-I. Shimoyama, T. Noda, S. Uchida, Z. Hussain, and Z.-X. Shen, *Evidence for ubiquitous strong electron-phonon coupling in high-temperature superconductors*, Nature **412**, 510 (2001). 41

[200] H. A. Mook, Pengcheng Dai, F. Dogan, and R. D. Hunt, *One-dimensional nature of the magnetic fluctuations in $YBa_2Cu_3O_{6.6}$*, Nature **404**, 729 (2002). 41

[201] J. D. Jorgensen, H.-B. Schüttler, D. G. Hinks, D. W. Capone, K. Zhang, M. B. Brodsky, and D. J. Scalapino, *Lattice instability and high-Tc superconductivity in $La_{2-x}Ba_xCuO_4$*, Phys. Rev. Lett. **58**, 1024 (1987). 41

[202] C. Rial, E. Moŕan, M. A. Alario-Franco, U. Amador, and N. H. Andersen, *Room temperature chemically oxidized La_2CuO_{4+y}: Phase separation induced by thermal treatment*, Physica C **278**, 122 (1997). 42, 57

[203] K. Nakajima, K. Yamada, S. Hosoya, Y. Endoh, M. Greven, and R. J. Birgeneau, *Spin dynamics and spin correlations in the Spin $S = 1$ two-dimensional square-lattice Heisenberg antiferromagnet La_2NiO_4*, Z. Physik B **96**, 479 (1995). 42, 119

[204] B. Keimer, N. Belk, R. J. Birgeneau, A. Cassanho, C. Y. Chen, M. Greven, M. A. Kastner, A. Aharnony, Y. Endoh, R. W. Erwin, and G. Shirane, *Magnetic excitations in pure, lightly doped, and weakly metallic La_2CuO_4*, Phys. Rev. B **46**, 14034 (1992). 42, 98, 119, 121

[205] T. Freltoft, J. E. Fischer, G. Shirane, D. E. Moncton, S. K. Sinha, D. Vaknin, J. P. Remeika, A. S. Cooper, and D. Harshman, *Antiferrromagnetism and oxygen defiency in single-crystal $La_2CuO_{4-\delta}$*, Phys. Rev. B **36**, 826 (1987). 42

[206] R. Kajimoto, K. Ishizaka, H. Yoshizawa, and Y. Tokura, *Spontaneous rearrangement of the checkerboard charge order to stripe order in $La_{1.5}Sr_{0.5}NiO_4$*, Phys. Rev. B **67**, 014511 (2003). 42, 83, 84, 91, 118, 121

[207] T. Ido, K. Magoshi, H. Eisaki, and S. Uchida, *Opical study of the $La_{2-x}Sr_xNiO_4$ system: Effect of hole doping on the electronic structure of the NiO_2 plane*, Phys. Rev. B **44**, 12094 (1991). 42

[208] S. Uchida, T. Ido, H. Takagi, T. Arima, Y. Tokura, and S. Tajima, *Optical spectra of $La_{2-x}Sr_xCuO_4$: Effect of carrier doping on the electronic structure of the CuO_2 plane*, Phys. Rev. B **43**, 7942 (1991). 42

[209] P. G. Freeman, A. T. Boothroyd, D. Prabhakaran, C. D. Frost, M. Enderle, and A. Hiess, *Spin dynamics of half-doped $La_{3/2}Sr_{1/2}NiO_4$*, Phys. Rev. B **71**, 174412 (2005). 42, 93, 109

[210] Y. Moritomo, Y. Tomioka, A. Asamitsu, Y. Tokura, and Y. Matsui, *Magnetic and electronic properties in hole-doped manganese oxides with layered structures: $La_{1-x}Sr_{1+x}MnO_4$*, Phys. Rev. B **51**, 3297 (1995). 42, 50, 51, 83, 84, 123

[211] O. Zachar and I. Zaliznyak, *Dimensional Crossover and Charge Order in Half-Doped Manganites and Cobaltites*, Phys. Rev. Lett. **91**, 036401 (2003). 42, 103

[212] S. Onoda, Y. Motome, and N. Nagaosa, *Two-Dimensional Charge Order in Layered 2-1-4 Perovskite Oxides*, Phys. Rev. Lett. **92**, 236403 (2004). 42, 84

[213] D. I. Khomskii and K. I. Kugel, *Why stripes? Spontaneous formation of inhomogeneous structure due to elastic interactions*, Europhys. Lett. (2001). 42, 93

[214] M. Fujita, K. Yamada, H. Hiraka, P. M. Gehring, S. H. Lee, S. Wakimoto, and G. Shirane, *Static magnetic correlations near the insulating-superconducting phase boundary in* $La_{2-x}Sr_xCuO_4$, Phys. Rev. B **65**, 064505 (2002). 42, 119, 121

[215] T. Suzuki, T. Goto, K. Chiba, T. Shinoda, T. Fukase, H. Kimura, K. Yamada, M. Ohashi, and Y. Yamaguchi, *Observation of modulated magnetic long-range order in* $La_{1.88}Sr_{0.12}CuO_4$, Phys. Rev. B **57**, R3229 (1998). 42

[216] J. M. Tranquada, J. D. Axe, N. Ichikawa, Y. Nakamura, S. Uchida, and B. Nachumi, *Neutron-scattering study of stripe-phase order of holes and spins in* $La_{1.48}Nd_{0.4}Sr_{0.12}CuO_4$, Phys. Rev. B **54**, 7489 (1996). 42

[217] J.-Q. Yan, J.-S. Zhou, and J. B. Goodenough, *Bond-length fluctuations and the spin-state transition in* $LCoO_3$ *(*L = *La, Pr, and Nd)*, Phys. Rev. B **69**, 134409 (2004). 43

[218] M. A. Señarís-Rodríguez and J. B. Goodenough, $LaCoO_3$ *Revisited*, J. of Solid State Chem. **116**, 224 (1995). 43

[219] G. Maris, *Structural Transitions Induced by Charge and Orbital Ordering in Transition Metal Oxides*, Dissertation, Rijksuniversiteit Groningen (2004). 43

[220] S. K. Pandey, S. Khalid, N. P. Lalla, and A. V. Pimpale, *Local distortion in* $LaCoO_3$ *and* $PrCoO_3$*: EXAFS, XRD and XANES studies*, cond-mat/0610654 (2006). 43

[221] A. Ishikawa, J. Nohara, and S. Sugai, *Raman Study of the Orbital-Phonon Coupling in* $LaCoO_3$, Phys. Rev. Lett. **93**, 136401 (2004). 43

[222] D. Louca, J. L. Sarrao, J. D. Thompson, H. Röder, and G. H. Kwei, *Correlation of local Jahn-Teller distortions to the magnetic/conductive states of* $La_{1-x}Sr_xCoO_3$, Phys. Rev. B **60**, 10378 (1999). 43

[223] M. Kriener, *Spinzustandsänderung, magnetische Ordnung und Metall-Isolator-Übergang in Kobaltaten*, Dissertation, Universität zu Köln (2005). 43

[224] M. Haverkort, *Spin and orbital degrees of freedom in transition metal oxides and oxide thin films studied by soft x-ray absorption spectroscopy*, Dissertation, Universität zu Köln (2005). 43

[225] J. Wang, Y. C. Tao, W. Zhang, and D. Y. Xing, *Theoretical study on the spin-state transition in doped $La_{2-x}Sr_xCoO_4$*, J. Phys. – Condens. Matter **12**, 7425 (2000). 43, 123

[226] C. Rial, E. Moŕan, M. A. Alario-Franco, U. Amador, and N. H. Andersen, *Structural and superconducting properties of $La_{2-x}Sr_xCuO_{4+y}$ ($0<x<0.15$) prepared by room temperature chemical oxidation*, Physica C **254**, 233 (1995). 44, 45, 57

[227] T. Vogt and D. J. Buttrey, *Low-temperature structural behavior of Sr_2RuO_4*, Phys. Rev. B **52**, 9843 (1995). 46

[228] M. Braden, A. H. Moudden, S. Nishizaki, Y. Maeno, and T. Fujita, *Structural analysis of Sr_2RuO_4*, Physica C **273**, 248 (1997). 46, 68

[229] P. Böni, J. D. Axe, G. Shirane, R. J. Birgeneau, D. R. Gabbe, H. P. Jenssen, M. A. Kastner, C. J. Peters, P. J. Picone, and T. R. Thurston, *Lattice instability and soft phonons in single-crystal $La_{2-x}Sr_xCuO_4$*, Phys. Rev. B **38**, 185 (1988). 50, 99

[230] R. L. Zhang and T. M. Rice, *Effective Hamiltonian for the superconducting Cu oxides*, Phys. Rev. B **37**, 3759 (1988). 54

[231] X. Gaojie, M. Zhiqiang, J. Hao, Y. Hongjie, W. Bin, L. Dengpan, and Z. Yuheng, *Transport properties of $La_{1.85-x}Sr_{0.15+x}Cu_{1-x}M_xO_y$ (M=Co,Ga)*, Phys. Rev. B **59**, 12090 (1999). 56

[232] J. E. Millburn, M. A. Green, D. A. Neumann, and M. J. Rosseinsky, *Evolution of the Structure of the K_2NiF_4 Phases $La_{2-x}Sr_xNiO_{4+\delta}$ with Oxidation State: Octahedral Distortion and Phase Separation ($0.2 \leq x \leq 1.0$)*, J. of Solid State Chem. **145**, 401 (1999). 57, 58, 66, 68, 69

[233] G. Wu, J. J. Neumeier, C. D. Ling, and D. N. Argyrious, *Temperature evolution of the crystal structure of $La_{2-x}Sr_xNiO_4$ ($x = \frac{1}{4}$ and $\frac{1}{3}$ as revealed through neutron powder diffraction*, Phys. Rev. B **65**, 174113 (2002). 58

[234] N. E. Brese and M. O'Keeffe, *Bond-Valence Parameters for Solids*, Acta. Cryst. B **47**, 192 (1991). 65

[235] I. D. Brown and D. Altermatt, *Bond-valence parameters obtained from a systematic analysis of the inorganic crystal-structure database*, Acta. Cryst. B **41**, 244 (1985). 65

[236] R. M. Wood and G. J. Palenik, *Bond Valence Sums in Coordination Chemistry. A Simple Method for Calculating the Oxidation State of Cobalt in Complexes Containing Only Co-O Bonds*, Inorg. Chem. **37**, 4149 (1998). 66

[237] M. Braden, P. Schweiss, G. Heger, W. Reichardt, Z. Fisk, K. Gamayunov, I. Tanaka, and H. Kojima, *Relation between structure and doping in $La_{2-x}Sr_xCuO_{4+\delta}$ A neuton diffraction study on single crystals*, Physica C **223**, 396 (1994). 66

[238] J. D. Dunitz, V. Schomaker, and K. N. Trueblood, *Interpretation of Atomic Displacement Parameters from Diffraction Studies of Crystals*, J. Phys. Chem. **92**, 856 (1988). 66

[239] B. J. Campbell, *Diffuse scattering in the layered perovskites*, Z. Kristallogr. **220**, 1088 (2005). 66

[240] M. Braden, M. Meven, W. Reichardt, L. Pintschovius, M. T. Fernandez-Diaz, G. Heger, F. Nakamura, and T. Fujita, *Analysis of the local structure by single-crystal neutron scattering in $La_{1.85}Sr_{0.15}CuO_4$*, Phys. Rev. B **63**, 140510 (2001). 67

[241] E. Wigner, *On the Interaction of Electrons in Metals*, Phys. Rev. **46**, 1002 (1934). 84

[242] E. Wigner, *Effects of the electron interaction on the energy levels of electrons in metals*, Trans. Faraday Soc. **34**, 678 (1938). 84

[243] I. V. Solovyev and K. Terakura, *Magnetic Spin Origin of the Charge-Ordered Phase in Manganites*, Phys. Rev. Lett. **83**, 2825 (1999). 85

[244] L. M. Helme, A. T. Boothroyd, D. Prabhakaran, F. R. Wondre, C. D. Frost, and J. Kulda, *Magnetic excitations in $La_{1.5}Sr_{0.5}CoO_4$*, Physica B **350**, e273 (2004). 85, 104, 107

[245] E. D. Isaacs, G. Aeppli, P. Zschack, S-W. Cheong, H. Williams, and D. J. Buttrey, *Diffuse x-ray scattering from $La_{2-x}Sr_xNiO_4$ and $La_{2-y}Sr_yCuO_4$*, Phys. Rev. Lett. **72**, 3421 (1994). 86

[246] A. Vigliante, M. von Zimmermann, J. R. Schneider, T. Frello, N. H. Andersen, J. Madsen, D. J. Buttrey, Doon Gibbs, and J. M. Tranquada, *Detection of charge scattering associated with stripe order in $La_{1.775}Sr_{0.225}NiO_4$ by hard-x-ray diffraction*, Phys. Rev. B **56**, 8248 (1997). 86

[247] M. Meven, *PRON2K, Data Reduction for* STOE DIF4. 87, 88

[248] M. Meven, *Entwicklung eines hochauflösenden Röngten-Einkristalldiffraktometers und Strukturuntersuchungen an $La_{2-x}Sr_xCuO_4$-Einkristallen*, Dissertation, Rheinisch-Westfälische Technische Hochschule Aachen (2001). 87

[249] P. Coppens, *The Evaluation of Absorption and Extinction in Single-Crystal Structure Analysis*, Volume Crystallogr. Comput., page 255. Munksgaard, Copenhagen (2002). 87

[250] A. C. T. North, D. C. Philipps, and F. Scott Mathews, *A Semi-Empirical Method of Absorption Correction*, Acta. Cryst. A **24**, 351 (1968). 87

[251] V. F. Sears, *Neutron scattering lengths and cross sections*, Neutron News **3**, 29 (1992). 88

[252] K. Yamada, C. H. Lee, K. Kurahashi, J. Wada, S. Wakimoto, S. Ueki, H. Kimura, Y. Endoh, S. Hosoya, G. Shirane, R. J. Birgeneau, M. Greven, M. A. Kastner, and Y. J. Kim, *Doping dependence of the spatially modulated dynamical spin correlations and the superconducting-transition temperature in $La_{2-x}Sr_xCuO_4$*, Phys. Rev. B **57**, 6165 (1998). 93, 108, 118

[253] J. M. Tranquada, *Neutron Scattering Studies of Antiferromagnetic Correlations in Cuprates*, cond-mat/0512115 (2005). 93

[254] S.-W. Cheong, G. Aeppli, T. E. Mason, H. Mook, S. M. Hayden, P. C. Canfield, Z. Fisk, K. N. Clausen, and J. L. Martinez, *Incommensurate magnetic fluctuations in $La_{2-x}Sr_xCuO_4$*, Phys. Rev. Lett. **67**, 1791 (1991). 93, 121

[255] V. J. Emery and S. A. Kivelson, *Frustrated electronic phase separation and high-temperature superconductors*, Physica C **209**, 597 (1993). 93

[256] J. Zaanen and O. Guunarsson, *Charged magnetic domain lines and the magnetism of high-T_c oxides*, Phys. Rev. B **40**, 7391 (1989). 93

[257] T. Giamarchi and C. Lhuillier, *Variational Monte Carlo study of incommensurate antiferromagnetic phases in the two-dimensional Hubbard model*, Phys. Rev. B **42**, 10641 (1990). 93

[258] S. M. Hayden, H. A. Mook, Pengcheng Dai, T. G. Perring, and F. Dogan, *The structure of the high-energy spin excitations in a high-transition-temperature superconductor*, Nature **429**, 531 (2004). 93

[259] L. J. de Jongh ed., *Physics and Chemistry of Materials with Low-Dimensional Structures*, Volume 9 Magnetic properties of Layered Transition Metal Compounds, Kluwer Academic Publishers, London (1990). 94

[260] N. D. Mermin and H. Wagner, *Absence of Ferromagnetism or Antiferromagnetism in One- or Two-Dimensional Isotropic Heisenberg Models*, Phys. Rev. Lett. **17**, 1133 (1966). 94

[261] J. M. Kosterlitz and D. J. Thouless, *Ordering, metastability and phase transitions in two-dimensional systems*, J. Phys. C - Solid State Physics **6**, 1181 (1973). 94

[262] D. Vaknin, S. K. Sinha, D. E. Moncton, D. C. Johnston, J. M. Newsam, C. R. Safinya, and Jr. H. E. King, *Antiferromagnetism in* La_2CuO_{4-y}, Phys. Rev. Lett. **58**, 2802 (1987). 94

[263] S. Wada, T. Kobayashi, M. Kaburagi, T. Kajitani, S. Hosoya, T. Fukuda, S. Onodera, Y. Yamada, K. Shibutani, and R. Ogawa, ^{139}*La NQR Study of antiferromagnetic* $La_2NiO_{4+\delta}$ *and* $La_2CoO_{4-\delta}$, Physica B **165&166**, 1313 (1990). 94

[264] Tôru Moriya, *Anisotropic Superexchange Interaction and Weak Ferromagnetism*, Phys. Rev. **120**, 91 (1960). 95

[265] I. Dzyaloshinsky, *A thermodynamic theory of "weak" ferromagnetism of antiferromagnetics*, J. Phys. Chem. Solids **4**, 241 (1958). 95

[266] T. Thio, T. R. Thurston, N. W. Preyer, P. J. Picone, M. A. Kastner, H. P. Jenssen, D. R. Gabbe, C. Y. Chen, R. J. Birgeneau, and A. Aharony, *Antisymmetric Exchange and its Influence on the Magnetic-Structure and Conductivity of* La_2CuO_4, Phys. Rev. B **38**, 905 (1988). 95

[267] P. G. Freeman, A. T. Boothroyd, D. Prabhakaran, and J. Lorenzana, *Magnetization of* $La_{2-x}Sr_xNiO_{4+\delta}$ *(*$0 \leq x \leq 0.5$*) : Spin-glass and memory effects*, Phys. Rev. B **73**, 014434 (2006). 95

[268] S. M. Hayden, G. H. Lander, J. Zarestky, P. J. Brown, C. Stassis, P. Metcalf, and J. M. Honig, *Incommensurate magnetic correlations in* $La_{1.8}Sr_{0.2}NiO_4$, Phys. Rev. Lett. **68**, 1061 (1992). 95, 119

[269] D. Stauffer and A. Aharony, *Introduction To Percolation Theory*, Volume 2nd ed., Taylor & Francis, London (1992). 95, 98, 114, 118, 121, 130

[270] H. Hiraka, T. Machi, N. Watanabe, Y. Itoh, M. Matsuda, and K. Yamada, *Ni Impurity Effort on Antiferromagnetic Order in Hole-Doped* $La_{2-x}Sr_xCuO_4$, J. Phys. Soc. Japan **74**, 2197 (2005). 95

[271] M. Matsumura, M. Mali, J. Roos, and D. Brinkmann, *Temperature dependence of the sublattice magnetization in the quasi-two-dimensional S=1/2 Heisenberg antiferromagnet La_2CuO_4*, Phys. Rev. B **56**, 8938 (1997). 95

[272] Xun-Li Wang, C. Stassis, D. C. Johnston, T. C. Leung, J. Ye, B. N. Harmon, G. H. Lander, A. J. Schultz, C.-K. Loong, and J. M. Honig, *Neutron-diffraction study of the antiferromagnetic form factor of La_2NiO_4*, Phys. Rev. B **45**, 5645 (1992). 95

[273] T. Kajitani, S. Hosoya, K. Hiraga, and T. Fukuda, *Tetragonal-Orthorhombic Phase Transition of La_2CoO_{4-x}*, J. Phys. Soc. Japan **59**, 562 (1989). 95, 119

[274] J. C. Speakman, *The Renninger effect - an example and its implication*, Acta. Cryst. **18**, 570 (1965). 97

[275] M. Renninger, *„Umweganregung", eine bisher unbeachtete Wechselwirkungserscheinung bei Raumgitterinterferenzen*, Z. Phys. **106**, 141 (1937). 97

[276] S.-W. Cheong, A. S. Cooper, Jr. L. W. Rupp, B. Battlog, J. D. Thomson, and Z. Fisk, *Magnetic dilution study in La_2CuO_4: Comparison with other two-dimensional magnets*, Phys. Rev. B **44**, 9739 (1991). 98, 118

[277] Ch. Niedermayer, C. Bernhard, T. Blasius, A. Golnik, A. Moodenbaugh, and J. I. Budnick, *Common Phase Diagram for Antiferromagnetism in $La_{2-x}Sr_xCuO_4$ and $Y_{1-x}Ca_xBa_2Cu_3O_6$ as Seen by Muon Spin Rotation*, Phys. Rev. Lett. **80**, 3843 (1998). 99, 121

[278] R. J. Cava, B. Batlogg, T. T. Palstra, J. J. Krajewski, Jr. W. F. Peck, A. P. Ramirez, and Jr. L. W. Rupp, *Magnetic and electrical properties of $La_{2-x}Sr_xNiO_{4\pm\delta}$*, Phys. Rev. B **43**, 1229 (1991). 99

[279] I. A. Zaliznyak, J. M. Tranquada, G. Gu, R. Erwin, and Y. Moritomo, *Universal features of charge and spin order in half-doped layered perovskite*, J. Appl. Phys. **95**, 7369 (2004). 103, 113

[280] J. M. Tranquada, J. D. Axe, N. Ichikawa, A. R. Moodenbaugh, Y. Nakamura, and S. Uchida, *Coexistence of, and Competition between, Superconductivity and Charge-Stripe Order in $La_{1.6-x}Nd_{0.4}Sr_xCuO_4$*, Phys. Rev. Lett. **78**, 338 (1997). 103, 122

[281] J. M. Tranquada, N. Ichikawa, and S. Uchida, *Glassy nature of stripe ordering in $La_{1.6-x}Nd_{0.4}Sr_xCuO_4$*, Phys. Rev. B **59**, 14712 (1997). 103

[282] P. J. Brown, *International tables for crystallography*, Volume C, page 391. Kluwer Academic Publishers, Dordrecht (1992). 105, 137

[283] R. J.Birgeneau, D. R. Gabbe, H. P.Jenssen, M. A. Kastner, P. J. Picone, T. R. Thurston, G. Shirane, Y. Endoh, M. Sato, K. Yamada, Y. Hidaka, M. Oda, Y. Enomoto, M. Suzuki, and T. Murakami, *Antiferromagnetic spin correlations in insulating, metallic, and superconducting* $La_{2-x}Sr_xCuO_4$, Phys. Rev. B **38**, 6614 (1988). 110

[284] S.-H. Lee and S-W. Cheong, *Melting of Quasi-Two-Dimensional Charge Stripes in* $La_{5/3}Sr_{1/3}NiO_4$, Phys. Rev. Lett. **79**, 2514 (1997). 114

[285] Z. Hu, *private communication.* 115, 123, 124

[286] R. J. Birgeneau and G. Shirane, *Physical Properties of High-Temperature Superconductors*, Volume I, page 152. World Scientific Publishing, London (1989). 118

[287] D. C. Johnston, J. P. Stokes, D. P. Goshorn, and J. T. Lewandowski, *Influence of oxygen defects on the physical properties of* La_2CuO_{4-y}, Phys. Rev. B **36**, 4007 (1987). 119

[288] M. Sera, M. Maki, M. Hiroi, N. Kobayashi, T. Suzuki, and T. Fukase, *Thermal conductivity and structural instability in La- and Cu-substituted* La_2CuO_4, Phys. Rev. B **52**, R735 (1995). 119

[289] B. Keimer, A. Aharnony, A. Auerbach, R. J. Birgeneau, A. Cassanho, Y. Endoh, R. W. Erwin, M. A. Kastner, and G. Shirane, *Neel transition and sublattice magnetization of pure and doped* La_2CuO_4, Phys. Rev. B **45**, 7430 (1992). 119

[290] B. Büchner, M. Breuer, A. Freimuth, and A. P. Kampf, *Critical Buckling for the Disappearance of Superconductivity in Rare-Earth-Doped* $La_{2-x}Sr_xCuO_4$, Phys. Rev. Lett. **73**, 1841 (1994). 120

[291] M. K. Crawford, R. L. Harlow, E. M. McCarron, W. E. Farneth, J. D. Axe, H. Chou, and Q. Huang, *Lattice instabilities and the effect of copper-oxygen-sheet distortions on the superconductivity in doped* L_2CuO_4, Phys. Rev. B **44**, 7749 (1991). 120

[292] B. Büchner, A. Lang, O. Baberski, M. Hücker, and A. Freimuth, *Transport Properties of Rare Earth Doped* $La_{2-x}Sr_xCuO_4$, J. Low Temp. Phys. **105**, 921 (1996). 120

[293] P. G. Freeman, A. T. Boothroyd, D. Prabhakaran, M. Enderle, and C. Niedermayer, *Spin order and magnetic transitions in* $La_{2-x}Sr_xNiO_4$, Phys. Rev. B **70**, 024413 (2004). 121

List of publications

1. **Crystal structure of the single-layered perovskite $La_{2-x}Sr_xCoO_4$ ($0.15 \leq x \leq 1.1$): Bond-length anisotropies**
   M. Cwik, M. Reuther, M. Benomar, M. Haider, N. Hollmann, P. Kliesen, A. Möller, T. Lorenz, Y. Sidis, F. Bouree, and M. Braden
   in preparation

2. **Static and Dynamic Spin Correlations in the Single-Layered Perovskite $La_{2-x}Sr_xCoO_4$ ($x = 0.3, 0.4, 0.45, 0.5, 0.6$)**
   M. Cwik, M. Benomar, Y. Sidis, K. Hradil, H. Schneider, P. Kliesen, A. Möller, A. Hoser, and M. Braden
   in preparation

3. **Anisotropic susceptibility of $La_{2-x}Sr_xCoO_4$ due to the spin states of cobalt**
   N. Hollmann, M.W. Haverkort, M. Cwik, M. Benomar, and T. Lorenz
   submitted to Phys. Rev. B

4. **Magnetoelastic coupling in $RETiO_3$ (RE = La, Nd, Sm, Gd, Y) investigated with diffraction techniques and thermal expansion measurements**
   A. C. Komarek, H. Roth, M. Cwik, W.-D. Stein, J. Baier, M. Kriener, F. Bouree, T. Lorenz, and M. Braden
   Phys. Rev. B **75**, 224402 (2007)

5. **Raman Scattering in the Mott Insulators $LaTiO_3$ and $YTiO_3$: Evidence for Orbital Excitations**
   C. Ulrich, A. Gössling, M. Grüninger, M. Guennou, H. Roth, M. Cwik, T. Lorenz, G. Khaliullin, and B. Keimer
   Phys. Rev. Lett. **97**, 157401 (2006)

6. **Wechselspiel zwischen Struktur, Spin- und Ladungsordnung in $La_{2-x}Sr_xCoO_4$**
   M. Cwik, M. Benomar, Y. Sidis, T. Lorenz und M. Braden
   Z. Kristallographie Suppl. **22**, 109 (2005)

7. **Determination of the orbital moment and crystal field splitting in $LaTiO_3$**
   M. W. Haverkort, Z. Hu, A. Tanaka, G. Ghiringhelli, H. Roth, M. Cwik, T. Lorenz,

C. Schuessler-Langeheine, S. V. Streltsov, A. S. Mylnikova, V. I. Anisimov, C. de Nadai, N. B. Brookes, H. H. Hsieh, H.-J. Lin, C. T. Chen, T. Mizokawa, Y. Taguchi, Y. Tokura, D. I. Khomskii, and L. H. Tjeng
Phys. Rev. Lett **94**, 056401 (2005)

8. **Struktur und Magnetismus von $LaTiO_3$: Hinweis auf nicht entartete t_{2g}-Zustände**
M. Cwik, T. Lorenz, A. Freimuth, J. Baier, H. Roth, R. Müller, G. Andre, F. Bouree, F. Lichtenberg und M. Braden
Z. Kristallographie Suppl. **21**, 77 (2004)

9. **Structure, magnetization, and resistivity of $La_{1-x}M_xCoO_3$ (M = Ca, Sr, and Ba)**
M. Kriener, C. Zobel, A. Reichl, J. Baier, M. Cwik, K. Berggold, H. Kierspel, O. Zabara, A. Freimuth, and T. Lorenz
Phys. Rev. B **69**, 094417 (2004)

10. **Neutron diffraction study of the nuclear and magnetic structure of the quasi-one-dimensional compound $CuSiO_3$ around $T_N = 8$ K**
H. Wolfram, H. H. Otto, M. Cwik, M. Braden, G. André, F. Bourée, M. Baenitz, and F. Steglich
Phys. Rev. B 69, 144115 (2004)

11. **Crystal and magnetic structure of $LaTiO_3$: Evidence for nondegenerate t_{2g} orbitals**
M. Cwik, T. Lorenz, J. Baier, R. Müller, G. André, F. Bourée, F. Lichtenberg, A. Freimuth, R. Schmitz, E. Müller-Hartmann, and M. Braden
Phys. Rev. B **68**, 060401(R) (2003)

Conference Contributions to

1. Annual Meeting of the Deutsche Physikalische Gesellschaft and DPG - spring meeting of the Division Condensed Matter, Dresden, Berlin, and Regensburg (2003 to 2006)

2. International Workshop of SFB 608 on *Strongly Correlated Transition Metal Compounds*, Cologne (2003)

3. Joint Symposium of SFB 608 and „Graduiertenkolleg“ 549 on *Functional Transition Metal Compounds & Multiferroics*, Cologne (2005)

4. Annual Meeting of the DGK and DGKK, Jena (2004)

5. DPG - spring meeting of the Division Condensed Matter and EPS - 21st General Conference of the Condensed Matter Division, Dresden (2006)

Acknowledgements

At this point, I would like to thank all people who supported this work, first of all the people at the Institute of Physics II in Cologne. In particular, I would like to thank Prof. Dr. M. Braden for the opportunity to perform this Ph.D. thesis, for the introduction to scattering techniques, and for helpful discussions. As well, I would like to thank Prof. Dr. L. H. Tjeng for co-assessing this thesis and Prof. Dr. L. Bohatý for chairing the disputation. M. Benomar, M. Reuther, and M. Haider I would like to acknowledge for the sample preparation, EDX measurements, and additional low-temperature x-ray powder experiments.

Best thanks also go to Dr. A. Möller and P. Kliesen at the Institute of Inorganic Chemistry at the University of Cologne for the atomic-absorption experiments on the single-layered cobaltates.

I deeply appreciate the fruitful discussions with Dr. T. Lorenz on the magnetic susceptibility, the resistivity, and the Co^{3+} spin-state degree of freedom in non-layered and layered cobaltates.

I would like to acknowledge numerous discussions with Prof. Dr. D. I. Khomskii, Prof. Dr. J. Mydosh, Dr. Z. Hu, and Dr. M. Haverkort on the soft x-ray absorption spectroscopy measurements, theoretical aspects of the spin degrees of freedom, and frustration effects in layered systems.

I am very grateful to the instrument scientists Dr. Y. Sidis, Dr. A. Hoser, Dr. D. Lamago, Dr. F. Bourée, Dr. K. Schmalzl, and Dr. K. Hradil at the neutron sources *LLB*, *FRJ-2*, and *FRMII* for supporting the neutron-scattering experiments. Dr. P. Held and Prof. Dr. L. Bohatý I would like to thank for the support to construct the single-crystal ball mill and for helpful suggestions to optimize the single-crystal x-ray structure analysis. I would like to thank Dr. I. Dix for the software installation and the initial operation of the X8 Apex single-crystal diffractometer at the Institute of Physics II. I would like to thank R. Dommel, H. Kierspel, and B. Roden for a continuous supply with liquid helium and nitrogen for our low-temperature measurements. The mechanics at the Institute of Physics II I would like to thank for their excellent work in manufacturing parts for the neutron experiments and the single-crystal diffractometer.

Especially, many thanks to W.-D. Stein, M. Haider, K. Berggold, M. Kriener, M. Valldor, J. Rohrkamp, and C. Hilgers. I greatly enjoyed our discussions.

Finally, I would like to thank my parents and Eva for their continual support and encouragement throughout my years of study.

Kurzzusammenfassung

In der vorliegenden Arbeit wurden die strukturellen und magnetischen Eigenschaften des dotierten, einfach-geschichteten Perowskitsystems $La_{2-x}Sr_xCoO_4$ über einen weiten Dotierungs- ($0.05 \leq x \leq 1.1$) und Temperaturbereich ($1.5 \leq T \leq 1000\ K$) mittels Röntgendiffraktion und Neutronenstreuung untersucht. Das Wechselspiel zwischen strukturellen Verzerrungen, antiferromagnetischen Spinkorrelationen und Ladungsordnung wurde im Detail analysiert und im Hinblick auf die eng verwandten Verbindungen $La_{2-x}Sr_xCuO_{4+\delta}$ und $La_{2-x}Sr_xNiO_{4+\delta}$ diskutiert.

Die sogenannte orthorhombische Tieftemperaturverzerrung (LTO) der tetragonalen (HTT) Struktur vom K_2NiF_4-Typ wird durch $x_{LTO} \sim 0.25$ Sr-Dotierung bei Raumtemperatur aufgehoben. Es wird gezeigt, daß die Variation der Gitterkonstanten nahe der HTT/LTO Phasengrenze auf sterische Effekte zurückgeführt werden kann, d.h. aufgrund einer kooperativen Verkippung über Ecken verbundener CoO_6-Oktaeder induziert wird. Für höhere Sr-Dotierungen wird die HTT Struktur stabilisiert. Die Abnahme des Gittervolumens geht einher mit der Zunahme des chemischen Drucks durch die Substitution von La^{3+}- durch Sr^{2+}-Ionen und der Entnahme von Ladungsträgern aus den CoO_2 Schichten. Während die La-Koordinationsanisotropie gleichmäßig durch Dotierung abgebaut wird, zeigt die Co-O_{apical} Bindungslänge einen starken Abfall bei $x \sim 0.45$. Dieser Abfall kann nicht einer Verringerung struktureller Verspannungen im System, aber einem elektronischen Ursprung zugeschrieben werden. Der Abfall deutet einen dotierungsabhängigen Co^{3+} Spinübergang bei Raumtemperatur vom High-Spin- in den Low-Spin-Zustand an. In $La_{1.5}Sr_{0.5}CoO_4$ wird ein Co^{3+} Low-Spin-Zustand bei Raumtemperatur durch den anomalen Anstieg der Gitterkonstante senkrecht zu den CoO_2-Ebenen und einer Sättigung der Gitterkonstanten in den CoO_2-Ebenen bei hohen Temperaturen unterstützt. Die quantitative Analyse der schachbrettartigen Ladungsordnung in $La_{1.5}Sr_{0.5}CoO_4$ über eine große Anzahl von Überstrukturreflexen zeigt eine Modulation der Sauerstoffpositionen der CoO_6 Oktaeder, die nicht Jahn-Teller aktiv ist. Dies steht im Gegensatz zur bisher in der Literatur angegebenen Modulation der Sauerstoffpositionen und der Co^{3+} Intermediate-Spin-Besetzung. Kommensurable, antiferromagnetische Nächste-Nachbar-Wechselwirkung zwischen Co Spins mit einem Spinmoment innerhalb der CoO_2 Schichten wurde in der Spin-Glass-Phase bis $x = 0.3$ gefunden. Dieser Dotierungsgrad liegt unterhalb der Perkolationsgrenze ($x_c \sim 0.41$) auf Gitterplätzen des Quadratgitters. Die Nächste-Nachbar-Wechselwirkung wird in der isolierenden Phase über einen Co^{3+} High-Spin-Zustand oder durch die Verringerung der Lochmobilität stabilisiert. Weitere Sr Dotierung induziert eine kurzreichweitige, inkommensu-

rable magnetische Ordnung. Die Inkommensurabilität vergrößert sich fast linear mit zunehmender Lochdichte und ein Maximum der Korrelationslänge in den CoO_2-Ebenen wird bei Halbdotierung beobachtet. Erste Anzeichen für eine streifenartige Spinanordnung in einfach-geschichteten Kobaltaten ($0.4 \leq x \leq 0.6$) werden hierdurch gefunden. Eine effektive Co^{2+}-Übernächster-Nachbar Wechselwirkung und eine schwache Zwischenebenenkopplung stabilisieren die Spinordnung in $La_{1.5}Sr_{0.5}CoO_4$.

Abstract

In this thesis the structural and magnetic properties of the single-layered perovskite $La_{2-x}Sr_xCoO_4$ were investigated by means of x-ray diffraction and neutron scattering over a wide doping ($0.05 \leq x \leq 1.1$) and temperature ($1.5 \leq T \leq 1000\ K$) range. The interplay between structural distortions, antiferromagnetic spin correlations, and charge order was studied in detail and is discussed in comparison with the closely related compounds, $La_{2-x}Sr_xCuO_{4+\delta}$ and $La_{2-x}Sr_xNiO_{4+\delta}$.

The so-called low temperature orthorhombic (LTO) distortion of the tetragonal (HTT) K_2NiF_4-type structure is lifted at $x_{LTO} \sim 0.25$ Sr doping at room temperature. It is shown that the variation of the lattice constants near the HTT/LTO phase boundary is due to steric effects, *i.e.* induced by a cooperative tilt of the corner-sharing CoO_6 octahedra. At higher doping the HTT structure is stabilized and the lattice volume decreases according to chemical pressure by the substitution of La^{3+} ions with Sr^{2+} ions and the removal of charge carriers from the CoO_2 layers. While the La coordination anisotropy is smoothly reduced with doping, the Co-O_{apical} bond-length exhibits a steep decrease near $x \sim 0.45$. This decrease cannot be attributed to the reduction of structural strains in the system, but to an electronic origin. The decrease suggests a Co^{3+} spin-state transition from the high-spin to the low-spin state at room temperature with doping. A Co^{3+} low-spin state in $La_{1.5}Sr_{0.5}CoO_4$ at room temperature is supported by the anomalous increase of the out-of-plane and the nearly constant in-plane lattice constant at higher temperatures. The quantitative analysis of the checkerboard-like charge order in $La_{1.5}Sr_{0.5}CoO_4$ on a large set of superstructure reflections reveals a oxygen-displacement modulation of the CoO_6 octahedra, which is not Jahn-Teller active. This is in contrast to the oxygen-displacement modulation and the Co^{3+} intermediate-spin occupation, previously proposed in the literature. Commensurate, antiferromagnetic nearest-neighbor exchange between Co spins with a spin moment within the CoO_2 layer is found in the spin-glass phase up to $x = 0.3$. This doping level is below the site-percolation threshold ($x_c \sim 0.41$) on a square lattice. The nearest-neighbor exchange, similar to the parent compound La_2CoO_4, is stabilized by a Co^{3+} high-spin state in the insulating phase or the reduction of the hole mobility. Further Sr doping induces a short-ranged incommensurate magnetic order. The incommensurability increases nearly linear with increasing hole density and a maximum of the in-plane correlation length at half doping is observed. First indications are thereby found for a stripe-like spin arrangement in single-layered cobaltates with $0.4 \leq x \leq 0.6$. An effective Co^{2+} next-nearest-neighbor exchange and a weak interlayer coupling stabilize the spin order in $La_{1.5}Sr_{0.5}CoO_4$.

Erklärung

Ich versichere, dass ich die von mir vorgelegte Dissertation selbständig angefertigt, die benutzten Quellen und Hilfsmittel vollständig angegeben und die Stellen der Arbeit - einschließlich Tabellen, Karten und Abbildungen -, die anderen Werken im Wortlaut oder dem Sinn nach entnommen sind, in jedem Einzelfall als Entlehnung kenntlich gemacht habe; dass diese Dissertation noch keiner anderen Fakultät oder Universität zur Prüfung vorgelegen hat; dass sie - abgesehen von oben angegebenen Teilpublikationen - noch nicht veröffentlicht worden ist sowie, dass ich eine solche Veröffentlichung vor Abschluss des Promotionsverfahrens nicht vornehmen werde. Die Bestimmungen dieser Promotionsordnung sind mir bekannt. Die von mir vorgelegte Dissertation ist von Prof. Dr. M. Braden betreut worden.

Matthias Cwik